TECHNISCHE UNIVERSITÄT WIEN

DISSERTATION

Growth, Characterization and Application of 2D Pnictogens - Graphene Heterostructures.

ausgeführt zum Zwecke der Erlangung des akademischen Grades
eines Doktors der Technischen Wissenschaften

unter der Leitung von

Univ. Prof. Dominik Eder

and

Dr. Bernhard C. Bayer-Skoff

E-165

Institut für Materialchemie

eingereicht an der Technischen Universität Wien
Fakultät für Technische Chemie

von

M.Tech. Tushar Gupta

11730865

Wien, October 2021

M.Tech. Tushar Gupta

Die approbierte gedruckte Originalversion dieser Dissertation ist an der TU Wien Bibliothek verfügbar.
The approved original version of this doctoral thesis is available in print at TU Wien Bibliothek.
TU Bibliothek Your knowledge hub

माता रामो मत्पिता रामचन्द्रः।

स्वामी रामो मत्सखा रामचन्द्रः।

सर्वस्वं मे रामचन्द्रो दयालुः।

नान्यं जाने नैव जाने न जाने॥३०॥

--॥श्रीबुधकौशिकविरचितं श्रीरामरक्षास्तोत्रं॥

To the nucleus of my existence

"The Almighty & My Family"

Die approbierte gedruckte Originalversion dieser Dissertation ist an der TU Wien Bibliothek verfügbar.
The approved original version of this doctoral thesis is available in print at TU Wien Bibliothek.
TU WIEN Bibliothek Your knowledge hub

Statutory Declaration

This thesis is submitted in partial fulfillments of the requirements for a Doctor of Philosophy degree in Technical Sciences at Faculty of Technical Chemistry, Vienna University of Technology. Except where specific reference is made to work of others, or explicit acknowledgement is given, the contents of this dissertation are the results of my own original work.

Tushar Gupta

Vienna, October 2021

Eidesstattliche Erklärung

Diese Dissertation wird in teilweiser Erfüllung der Anforderungen für den Grad eines Doktors der Philosophie der technischen Wissenschaften an der Fakultät für Technische Chemie der Technischen Universität Wien vorgelegt. Der Inhalt dieser Dissertation ist das Ergebnis meiner eigenen Arbeit, es sei denn, es wird ausdrücklich auf Arbeiten anderer Personen verwiesen oder es wird eine ausdrückliche Danksagung gegeben.

Tushar Gupta

Vienna, October 2021

Die approbierte gedruckte Originalversion dieser Dissertation ist an der TU Wien Bibliothek verfügbar.
The approved original version of this doctoral thesis is available in print at TU Wien Bibliothek.
TU WIEN Bibliothek Your knowledge hub

Acknowledgements

This work in the form of my PhD thesis is a confluence of many great minds. Words will fall short in conveying my gratefulness to people who have been sources of great help, support and motivation towards the successful synthesis and dissemination of fruitful findings to the scientific community as presented though this dissertation. Therefore, as customary I recognize the contributions of following people in the successful completion of this thesis.

I am foremostly thankful to Prof. Dominik Eder for affording me the opportunity to pursue my research plans under his able guidance and resources. That also makes me convey my gratitude to the diverse group of Prof. Eder including both its present and past members, interns etc., for providing me enough space in the group to grow and develop. Equally I am thankful to Prof. Eder for providing the co-supervision of Dr. Bernhard Christian Bayer to me. Working under the daily supervision of Dr. Bayer was a good and enjoyable learning experience for me. This thesis would not have been possible without Dr. Bayer.

Through my supervisors, I had the privilege to meet and associate with some erudite and creative intellectuals during the course of my PhD. In that line, I firstly acknowledge Dr. Kenan Elibol, for sharing his excellently learned skills and for the initial training which helped me gained autonomy quickly. Equivalent acknowledgements go to Prof. Jannik Meyer (now University of Tübingen) and Prof. Jani Kotakoski (University of Vienna) for granting me access to facilities at Physics of Nanostructured Materials, Faculty of Physics, University of Vienna which proved to be vital for gaining deeper understanding of the model systems explored through this dissertation. Sincere recognitions go to Dr. Clemens Manger (University of Vienna) for being my STEM life-line and to Dr. Michael Stöger-Pollach (USTEM, TU Wien) for his immense help with analytical electron microscopy and related spectroscopy and for some truly fertile discussions. I am also thankful to our other internal and external collaborators: Dr. Reinhard Kaindl (Joanneum Research, Austria); Prof. Bernhard Gollas (Graz University of Technology, Austria); Zita Csendes and Prof. Helmuth Hoffmann (Vienna University of Technology, Austria); Anna Niggas and Prof.

Die approbierte gedruckte Originalversion dieser Dissertation ist an der TU Wien Bibliothek verfügbar.
The approved original version of this doctoral thesis is available in print at TU Wien Bibliothek.
TU WIEN Bibliothek Your knowledge hub

Richard A. Wilhelm (Vienna University of Technology, Austria) for providing enough space to contribute my little learned skills in their exciting research.

I am appreciative towards Karin Whitmore (USTEM, Vienna University of Technology), Dr. Karin Wieland (Vienna University of Technology), Dr. Stefan Hummel (University of Vienna), Werner Artner (XRC, Vienna University of Technology) and Dr. Gerlinde Habler (University of Vienna) for organizing my preliminary rendezvous with SEM, Raman spectroscopy, AF-SEM, XRD and FIB respectively and also for helping me out with some intricate measurements and analysis. Sporadic conversations with Prof. Stefan Löffler (USTEM, Vienna University of Technology) and Dr. Thomas Schachinger (USTEM, Vienna University of Technology) regarding microscopic techniques and related data analysis are also cherished.

Company of good colleagues: Dr. Kenan Elibol, Dr. Leonie Deilmann, Dr. Jia Wang, Shaghayegh Naghdi at work; super considerate and caring flatmates: Dr. Jaugen Belagurau, Jozef Vitko, Tomasz Wrzesień at home and dear friends: Deborishi Howladar, Rajendra Singh in Vienna was cherry on cake. I am highly grateful to them for all the nice time via our outings, food and sports in making my stay pleasant and helping me strike work-life balance effectively. I am also thankful to my alma mater friends: Dr. Arpita Saha, Dr. Abhishek Saini, Dr. Anukriti Singh and Dr. Deeksha Gupta for visiting me and for all the amusing moments.

Lately, I got the chance to simulate myself into the role of a daily supervisor while supervising Nicole Rosza for her bachelor thesis. I thank Nicole for her sincerity and hard-work which not only eased her supervision responsibility for me but also facilitated the successful translation of her bachelor thesis results into a decent publication.

Above everything else, I pay my humble obedience to my family and The Lord for always keeping a strong support system constituted around me. I may be too small to describe their greatness and significance in my life but I am tremendously thankful to them for all my possessions (both materialistic and non-materialistic).

Die approbierte gedruckte Originalversion dieser Dissertation ist an der TU Wien Bibliothek verfügbar.
The approved original version of this doctoral thesis is available in print at TU Wien Bibliothek.
TU Bibliothek Your knowledge hub WIEN

Abstract

Two Dimensional (2D) pnictogens are predicted to have thickness dependent transitions in electronic properties and hence constitute key interest in energy and electronics applications. The ultra-smooth surface of 2D materials like graphene facilitates the realization of high lattice mismatched layers to grow atop each other via Van-der-Waals epitaxy. The thus grown polymorphic structures of these pnictogens on graphene have also been found to be superior anode materials for batteries. This study aims to realize such heterostructures and investigate the properties of their rich phases.

Aberration corrected atomically resolved scanning transmission electron microscopy was employed to probe the evolution of structure and morphology at the interfaces in the 2D antimonene (Sb) - graphene heterostructures and bismuthene (Bi) - graphene heterostructures grown via a physical vapor deposition technique of thermal evaporation. These pnictogens were found to simultaneously exist in two different textures of their thermodynamically preferred layered 2D β-phase, namely: β-(001) and β-[2-21] phases on graphene. Importantly, a strong indication for preferred relative crystallographic orientations with respect to the supporting graphene monolayer lattice was observed for both the phases, indicating the existence of rotational Van-der-Waals epitaxy in 2D Sb/Bi - graphene heterostructures. The studies here also highlight other interesting properties of the grown pnictogens: (1) exceptional resilience of both phases against environmental oxidation was revealed via electron energy loss spectroscopy (both low-loss and core-loss); (2) electron beam induced *in situ* crystallizations processes and associated plasmon dynamics were studied with valence electron energy loss spectroscopy etc. Sensitivity of exact Sb / Bi growth results for both phases on graphene on employed processing and substrate properties incl., notably, the nature of the support type underneath the direct graphene support was found. This work thereby provides fundamental insights into the phase wealth and epitaxy landscape in 2D Sb/Bi and 2D Sb/Bi- graphene heterostructures.

Die approbierte gedruckte Originalversion dieser Dissertation ist an der TU Wien Bibliothek verfügbar.
The approved original version of this doctoral thesis is available in print at TU Wien Bibliothek.
TU WIEN Bibliothek Your knowledge hub

As another promising cost-effective and rational technique to scalable synthesize 2D materials, route of liquid phase exfoliation was explored to exfoliate pnictogens, where exfoliation of Bi under the here adopted processing conditions resulted in the synthesis of laterally large 2D sheets of bismuth-oxy-carbonate. The efficacy of five different common solvents in exfoliating Bi was examined. The synthesized exfoliated sheets/flakes of bismuth-oxy-carbonates were later utilized as catalyst component by integrating them with titanium dioxide as photocatalyst via simple mix and match method. The composite showed improved hydrogen evolution rates upon water-splitting as compared to respective individual components. This work thereby further demonstrates the application of bismuth-oxy-carbonate as a catalyst component to drive photocatalytic water splitting reactions to produce hydrogen.

Die approbierte gedruckte Originalversion dieser Dissertation ist an der TU Wien Bibliothek verfügbar.
The approved original version of this doctoral thesis is available in print at TU Wien Bibliothek.
TU WIEN Bibliothek Your knowledge hub

Kurzfassung

Zweidimensionale (2D) Pniktogene haben Lagenanzahl-abhängige Übergänge in ihren elektronischen Eigenschaften und sind daher für Energie- und Elektronikanwendungen von großem Interesse. Die ultraglatte Oberfläche von 2D-Materialien wie Graphen erleichtert die Realisierung von Heterostrukturen mit hoher Gitterfehlanpassung, die mittels Van-der-Waals-Epitaxie übereinander wachsen. Die so auf Graphen gewachsenen polymorphen Strukturen dieser Pniktogene haben sich auch als vielversprechende Anodenmaterialien für Batterien erwiesen. Ziel dieser Untersuchungen ist es, solche Heterostrukturen zu realisieren und die Eigenschaften ihrer reichhaltigen Phasen zu untersuchen.

Aberrations-korrigierte, atomar aufgelöste Rastertransmissionselektronenmikroskopie wurde eingesetzt, um die Entwicklung der Struktur und Morphologie an den Grenzflächen in den 2D-Antimon (Sb) - Graphen-Heterostrukturen und Bismuthen (Bi) - Graphen-Heterostrukturen zu untersuchen, die mittels physikalischer Aufdampfungstechnik gewachsen wurden. Es wurde festgestellt, dass diese Pniktogene in zwei verschiedenen Texturen ihrer thermodynamisch bevorzugten geschichteten 2D-β-Phase ko-existieren, nämlich: β-(001) und β-[2-21] Phasen auf Graphen. Wichtig ist, dass für beide Phasen ein starker Hinweis auf bevorzugte relative kristallografische Orientierungen in Bezug auf das tragende Graphen-Monolagengitter beobachtet wurde, was auf die Existenz von Van-der-Waals-Epitaxie in 2D-Sb/Bi-Graphen-Heterostrukturen hinweist. Die hier durchgeführten Studien heben auch andere interessante Eigenschaften der gewachsenen Pniktogene hervor: (1) Die außergewöhnliche Widerstandsfähigkeit beider Phasen gegen Oxidation durch Umwelteinflüsse wurde mit Hilfe der Elektronen-Energieverlustspektroskopie nachgewiesen; (2) Elektronenstrahlinduzierte in-situ-Kristallisationsprozesse und die damit verbundene Plasmonendynamik wurden mit Hilfe der Valenz-Elektronen-Energieverlustspektroskopie untersucht. Die Abhängigkeit der exakten Sb/Bi-Wachstumsergebnisse für beide Phasen auf Graphen auf die verwendeten Prozess- und Substrateigenschaften, insbesondere die Art des Trägers unter dem direkten Graphen-

Die approbierte gedruckte Originalversion dieser Dissertation ist an der TU Wien Bibliothek verfügbar.
The approved original version of this doctoral thesis is available in print at TU Wien Bibliothek.
TU WIEN Bibliothek Your knowledge hub

Träger, wurde auch untersucht. Diese Arbeit liefert somit grundlegende Einblicke in den Phasenreichtum und die Epitaxielandschaft in 2D Sb/Bi und 2D Sb/Bi Graphen Heterostrukturen.

Als weitere vielversprechende und kostengünstige Technik zur skalierbaren Synthese von 2D-Materialien wurde Flüssigphasenexfoliation untersucht, um Pniktogene zu exfolieren, wobei die Exfoliation von Bi unter den hier verwendeten Bedingungen zur Synthese von lateral großen 2D-Schichten aus Bismut-Oxy-Carbonat führte. Die Wirksamkeit von fünf verschiedenen gängigen Lösungsmitteln bei der Exfoliierung von Bi wurde untersucht. Die synthetisierten Bismut-Oxy-Carbonat-Schichten/-Flocken wurden als Katalysatorkomponente verwendet, indem sie mit Titandioxid als Photokatalysator durch eine einfache Misch- und Anpassungsmethode integriert wurden. Diese Hybride zeigten bei der Wasserspaltung verbesserte Wasserstoffentwicklungsraten im Vergleich zu den jeweiligen Einzelkomponenten. Diese Arbeit demonstriert somit die Anwendung von Bismut-Oxy-Carbonat als Katalysatorkomponente, um photokatalytische Wasserspaltungsreaktionen zur Erzeugung von Wasserstoff anzutreiben.

Die approbierte gedruckte Originalversion dieser Dissertation ist an der TU Wien Bibliothek verfügbar.
The approved original version of this doctoral thesis is available in print at TU Wien Bibliothek.
TU Bibliothek Your knowledge hub WIEN

Table of Contents

Acknowledgements: **IV**

Abstract: **VI**

Kurzfassung: **VIII**

Chapter 1: Prologue **1.1 – 1.8**
- **Chapter Preview** **1.2**
- 1.1 Thesis Framework 1.3
- 1.2 Thesis Structure 1.5
- 1.3 References 1.7

Chapter 2: Background **2.1 – 2.35**
- **Chapter Preview** **2.2**
- 2.1 Context 2.3
- 2.2 Pnictogens 2.3
- 2.3 Antimonene 2.5
  - 2.3.1 Structure 2.5
  - 2.3.2 Properties 2.6
- 2.4 Bismuthene 2.9
  - 2.4.1 Structure 2.10
  - 2.4.2 Properties 2.11
- 2.5 Synthesis of antimonene and bismuthene 2.14
  - 2.5.1 Thermal Evaporation 2.15
  - 2.5.2 Liquid Phase Exfoliation (LPE) 2.19
- 2.6 Photocatalytic water splitting 2.23
- 2.7 Antimonene and Bismuthene as photocatalysts 2.27
- 2.8 Conclusion 2.28
- 2.9 References 2.29

Chapter 3: Experimental Techniques **3.1 - 3.29**
- **Chapter Preview** **3.2**
- 3.1 General Sample preparation 3.3
- 3.2 Deposition/ Growth Methods 3.5
  - 3.2.1 Physical Vapor Deposition 3.5
  - 3.2.2 Liquid Phase Exfoliation 3.7
- 3.3 Characterization Tools 3.9
  - 3.3.1 Transmission Electron Microscopy 3.9
  - 3.3.2 Scanning Electron Microscopy 3.12
  - 3.3.3 Energy Dispersive X-ray Spectroscopy 3.13
  - 3.3.4 Raman Spectroscopy 3.14
  - 3.3.5 Electron Energy Loss Spectroscopy 3.17
  - 3.3.6 Photocatalytic Hydrogen Evolution Reaction 3.20
  - 3.3.7 Scanning Transmission Electron Microscopy 3.22
- 3.4 Miscellaneous Contributions 3.26

Die approbierte gedruckte Originalversion dieser Dissertation ist an der TU Wien Bibliothek verfügbar.
The approved original version of this doctoral thesis is available in print at TU Wien Bibliothek.
TU Bibliothek Your knowledge hub WIEN

3.5 References 3.27

Chapter 4: Antimonene/Graphene Heterostructures 4.1 – 4.33
Chapter Preview 4.2
4.1 Introduction 4.3
4.2 Experimental Procedure 4.5
4.2.1 Growth of 2D Sb on graphene 4.5
4.2.2 Phase and epitaxy analysis of Sb deposits 4.5
4.3 Results and Discussion 4.6
4.3.1 Morphology and Structure 4.6
4.3.2 Van-der-Waals Epitaxy 4.15
4.3.3 Oxidation Susceptibility 4.20
4.3.4 Growth Parameter Space 4.24
4.4 Conclusion 4.27
4.5 References 4.28
Outcome 4.33

Chapter 5: Bismuthene/Graphene Heterostructures 5.1 – 5.34
Chapter Preview 5.2
5.1 Introduction 5.3
5.2 Experimental Procedure 5.5
5.2.1 Growth of 2D Bi on graphene 5.5
5.2.2 Phase and epitaxy analysis of Sb deposits 5.5
5.3 Results and Discussion 5.6
5.3.1 Bi PVD Parameter Space 5.6
5.3.2 RT Bi depositions 5.8
5.3.3 Higher substrate temperature Bi nanoparticles incl. e- beam driven dynamics 5.19
5.3.4 Plasmon Shift during *in situ* Crystallization 5.25
5.4 Conclusion 5.27
5.5 References 5.28
Outcome 5.34

Chapter 6: Liquid Phase Exfoliation of Bi 6.1 – 6.33
Chapter Preview 6.2
6.1 Introduction 6.3
6.2 Experimental Procedure 6.4
6.2.1 Synthesis of 2D $Bi_2O_2CO_3$ nanosheets/-flakes 6.4
6.3 Results and Discussion 6.7
6.3.1 Morphology and Structure 6.7
6.3.2 Discussion of phase analysis of the nanoflakes/-sheets 6.16
6.3.2.1 Top-view TEM (FT) and SAED 6.17
6.3.2.2 XRD 6.21
6.3.3 Discussion of likely reaction pathways of Bi → $Bi_2O_2CO_3$ 6.23
6.3.4 Photocatalytic testing of 2D $Bi_2O_2CO_3$ nanoflakes/nanosheets 6.24
6.4 Conclusion 6.27

Die approbierte gedruckte Originalversion dieser Dissertation ist an der TU Wien Bibliothek verfügbar.
The approved original version of this doctoral thesis is available in print at TU Wien Bibliothek.
TU Bibliothek Your knowledge hub WIEN

6.5 References 6.28
Outcome **6.33**

Chapter 7: Epilogue **7.1 – 7.12**
Chapter Preview **7.2**
7.1 Conclusions 7.3
7.2 Sb Vs Bi on graphene 7.4
7.3 Key findings 7.7
7.4 Outlook 7.10
7.5 References 7.12

CV **XIII - XX**

Die approbierte gedruckte Originalversion dieser Dissertation ist an der TU Wien Bibliothek verfügbar.
The approved original version of this doctoral thesis is available in print at TU Wien Bibliothek.
TU Bibliothek Your knowledge hub WIEN

Chapter 1

Prologue

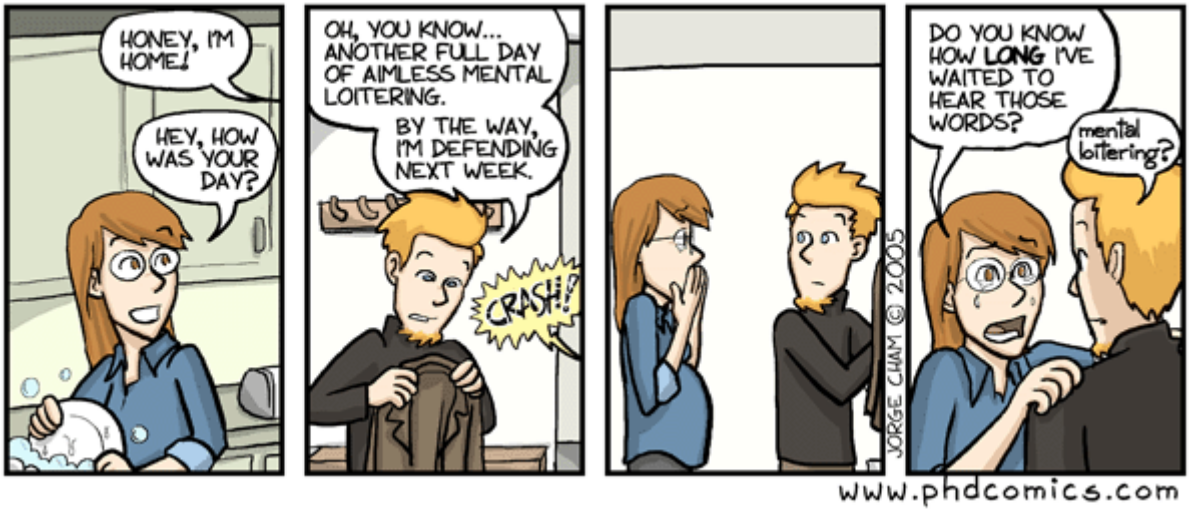

Die approbierte gedruckte Originalversion dieser Dissertation ist an der TU Wien Bibliothek verfügbar.
Wien Vien Bibliothek

Chapter Preview

Chapter 1 *provides an overview of the subjects that form the basis of my investigation and thereby my thesis. The thesis deals with synthesis of pnictogens particularly antimony and bismuth (and their compounds) in low-dimensional form by employing two primary; physical and wet-chemical based synthesis routes. The choice of the selected model systems has been substantiated and a short preface of all the chapters of the thesis has been provided. The figure caption for chapter 1 is an illustration adopted from "**http://phdcomics.com**", whom I have been an ardent follower of, owing to the funny twist they deliver to the day-to-day happenings in any graduate's life during PhD.*

Die approbierte gedruckte Originalversion dieser Dissertation ist an der TU Wien Bibliothek verfügbar.
The approved original version of this doctoral thesis is available in print at TU Wien Bibliothek.
TU Bibliothek Your knowledge hub WIEN

1. Prologue

1.1 Thesis Framework

This doctoral study encompasses the detailed study of low dimensional pnictogens (and also their corresponding compounds). "Pnictogens" is general term use to refer to elements of Group VA, consisting of: Nitrogen (N), Phosphorus (P), Arsenic (As), Antimony (Sb) and Bismuth (Bi). The bulk metallic character increases down the group with N and P being non-metals, As and Sb being semi-metals and Bi being metal.[1] Results regarding their scalable synthesis, outlining their different properties towards successful realization of catalytic applications have been presented and future insights have been postulated. The low-dimensional pnictogens and their compounds were produced via adopting two principal synthesis approaches:

(1) via physical vapor deposition (PVD) route of thermal evaporation

(2) via wet-chemical route of liquid phase exfoliation (LPE)

The choice of pnictogens (and their oxides) to be investigated was kept restricted to antimony and bismuth only. Firstly, this was due to the reported poor ambient stability of few-layered black-phosphorus[2–4], toxicity-related concerns with arsenic[5] and as-of-yet scarcely successful experimental realization of few-layered nitrogen[6–8]. Secondly, the rich allotropic wealth of Sb and Bi remain to be the focus of extensive scientific research because of their remarkable affirmative response towards several electronics and energy related applications, all of which has been discussed in detail in chapter 2.

Three primary model systems have been explored in this thesis, namely:

- Antimonene-graphene heterostructures
- Bismuthene-graphene heterostructures
- 2D (two-dimensional) Bismuth oxycarbonates

To note is that the term "graphene" sometimes has been adopted in place of "monolayer graphene" or "MLG" and that all of them imply the same meaning in the context of this thesis. For the synthesis protocol involving the physical vapor deposition via thermal

Die approbierte gedruckte Originalversion dieser Dissertation ist an der TU Wien Bibliothek verfügbar.
The approved original version of this doctoral thesis is available in print at TU Wien Bibliothek.
TU Bibliothek Your knowledge hub WIEN

evaporation, monolayer graphene was utilized as substrate. This further had two-fold advantages:

(1) Monolayer graphene has already been suggested as a potential substrate for the epitaxial growth of 2D pnictogens by prior DFT study[9]. Additionally, this is also supported by our findings enclosed in the thesis.

(2) Monolayer graphene is also a suitable template for the employed atomic resolution electron microscopic studies as shown by prior studies[10]. This further facilitated the direct assessment of interfacing and epitaxial effects in 2D Sb/Bi - Carbon heterostructures. Our findings therefore could provide productive insights for understanding any potential monolayer graphene related 2D-2D heterostructure model system.

Having stated the choice of research system, the motive behind the carried-out research presented in the form of this thesis was to address some key loopholes in the present state-of-the-art research on 2D pnictogens and 2D pnictogen based compounds, which were:

***clip art adapted from www.slidemodel.com**

- *Outlining the parameter space for the scalable growth/ synthesis of few-layered pnictogens and their compounds.*
- *Providing clearer picture of the phase and epitaxial relationships in 2D pnictogens*
- *Studying their diverse properties including probing some in-situ (e.g.: e- beam induced crystallization) as well as ex-situ (ambient oxidation resilience) processes.*
- *Communicating an application perspective of the studied properties*

Chapters 4-6 address these aforementioned gaps in realizing the motives behind this doctoral study. The three experimental chapters: Chapters 4-6, constitute below mentioned three major highlights of this thesis.

Die approbierte gedruckte Originalversion dieser Dissertation ist an der TU Wien Bibliothek verfügbar.
The approved original version of this doctoral thesis is available in print at TU Wien Bibliothek.
TU WIEN Bibliothek Your knowledge hub

Clear and wealthy insights for phase identification of the grown/synthesized 2D pnictogens (including their compounds) are one of the main highlights of the work carried out in this thesis. The phase analysis presented here removes ambiguities present in some of the prior works (cited in the respective chapters) and presents an all-inclusive approach towards understanding the structural analysis of the few layered pnictogens and their compounds well complemented by the simulated atomic-structural models and corresponding electron diffraction patterns.

PVD employed studies mainly deal with electron microscopy assisted investigations, pointing out the multi-dimensionality of the transmission electron microscopes in gaining understanding about particular model system (including electron beam driven transitions). Information obtained via imaging, diffraction patterns and associated spectroscopic techniques acquired on Transmission Electron Microscopes (TEM) and Scanning Transmission Electron Microscopes ((S)TEM) was paramount in disentangling structural and based complexities and consequently shape the second major highlight of this thesis.

Here reported simple-to-follow strategy for Liquid Phase Exfoliation of Bi resulted into the synthesis of 2D bismuth oxycarbonates possessing ultra-large lateral dimensions, which were established as potential co-catalyst material for steering UV-light driven photo-catalysis. Notably, Photocatalysis remains one of the central strategies for effectively tackling the world's increased energy demands. This enriches the envisaged research on emerging 2D materials in green energy landscape, forming the third highlight of this thesis and further pandiculating the scope of this thesis in the direction of sustainable research.

1.2 Thesis Structure

This thesis comprises of two background chapters and three chapters constituted by the experimental findings of the systems explored. An intro- and outro- chapters are provided at the beginning and the end of the thesis respectively to help reader get a brief overview of the studies performed and also carry with them some outlook for the future

Die approbierte gedruckte Originalversion dieser Dissertation ist an der TU Wien Bibliothek verfügbar.
The approved original version of this doctoral thesis is available in print at TU Wien Bibliothek.
TU Bibliothek Your knowledge hub WIEN

directions given the current state of the art of research on 2D pnictogens and their compounds.

During interpretation and presentation of the introduced methodology, findings etc. as a part of this thesis, wherever required, strong correlation with the prior works has been juxtaposed in order to better explain the significance of the implemented protocol and the obtained results. On that note, following are the brief precaps of the chapters forming part of this thesis:

- ***Chapter 2*** provides background to the field of 2D pnictogens (Sb and Bi, including their compounds), their properties, synthesis techniques and also applications. The chapter also defines a typical process of photocatalysis and sheds some light on its elementary pre-requisites.

- ***Chapter 3*** provides details as well as fundamental working principles of all the instrumentation facilities employed for the synthesis and characterization of the model systems explored in this thesis. Information regarding the general sample preparation and the studies related to testing the quality of the substrates have also been provided. People who have assisted in obtaining specific data have also been kindly acknowledged.

- ***Chapter 4*** explores the model system 1: antimonene-graphene heterostructures, providing insights into the rich phase and epitaxy landscape in 2D Sb and 2D Sb/graphene heterostructures. The findings not only reveal the key influence of direct support under graphene and substrate temperature on the Sb growth but also highlight the good oxidation resilience of the antimonene on graphene.

- ***Chapter 5*** explores the model system 2: bismuthene-graphene heterostructures, providing insights into the structure and morphology evolution of low-dimensional Bi nanostructures onto suspended graphene membranes as a function of substrate temperature. The rich phase and epitaxy landscape in 2D Sb and 2D Sb/graphene heterostructures. The studies uncover some multi-faceted

Die approbierte gedruckte Originalversion dieser Dissertation ist an der TU Wien Bibliothek verfügbar.
The approved original version of this doctoral thesis is available in print at TU Wien Bibliothek.
TU Bibliothek Your knowledge hub WIEN

in-situ electron beam induced atomic dynamics and associated plasmonic property change.

- ***Chapter 6*** explores the wet chemical route of liquid phase exfoliation to obtain low-dimensional pnictogens (Sb and Bi). The chapter however encompasses the results for bismuth only since the exfoliation of antimony was not successful via the followed methodology. On a very interesting note, the chapter introduces the synthesis of unusually large 2D bismuth oxycarbonate $Bi_2O_2CO_3$ nanosheets via the template-free sonochemical approach and highlights the likely reaction pathways for this transition from Bi to $Bi_2O_2CO_3$. Role of nature of 5 different solvents in governing the morphology of exfoliated $Bi_2O_2CO_3$ has been discussed in detail. 2D $Bi_2O_2CO_3$ were then placed as promising catalyst component by revealing their higher response towards hydrogen evolution reaction (HER) with TiO_2 for photocatalytic HER as compared to their individual components.

- ***Chapter 7*** provides future outlook on 2D pnictogens and their compounds-based research centered on the conclusions drawn from the work presented in this thesis.

1.3 References

1. Edwards, P. P. & Sienko, M. J. On the occurrence of metallic character in the periodic table of the elements. *J. Chem. Educ.* **60**, 691 (1983).
2. Wood, J. D. *et al.* Effective Passivation of Exfoliated Black Phosphorus Transistors against Ambient Degradation. *Nano Lett.* **14**, 6964–6970 (2014).
3. Li, L. *et al.* Black phosphorus field-effect transistors. *Nat. Nanotechnol.* **9**, 372–377 (2014).
4. Castellanos-Gomez, A. *et al.* Isolation and characterization of few-layer black phosphorus. *2D Mater.* **1**, 025001 (2014).
5. Farzan, S. F., Karagas, M. R. & Chen, Y. In utero and early life arsenic exposure in relation to long-term health and disease. *Toxicol. Appl. Pharmacol.* **272**, 384–390 (2013).
6. Rouquerol, J., Partyka, S. & Rouquerol, F. Calorimetric evidence for a bidimensional phase change in the monolayer of nitrogen or argon adsorbed on graphite at 77 K. *J. Chem. Soc. Faraday Trans. 1 Phys. Chem. Condens. Phases* **73**, 306–314 (1977).
7. Özçelik, V. O., Aktürk, O. Ü., Durgun, E. & Ciraci, S. Prediction of a two-dimensional crystalline structure of nitrogen atoms. *Phys. Rev. B* **92**, 125420 (2015).

Die approbierte gedruckte Originalversion dieser Dissertation ist an der TU Wien Bibliothek verfügbar.
The approved original version of this doctoral thesis is available in print at TU Wien Bibliothek.
TU WIEN Bibliothek Your knowledge hub

8. Lee, J., Tian, W.-C., Wang, W.-L. & Yao, D.-X. Two-Dimensional Pnictogen Honeycomb Lattice: Structure, On-Site Spin-Orbit Coupling and Spin Polarization. *Sci. Rep.* **5**, 11512 (2015).
9. Wang, G., Pandey, R. & Karna, S. P. Atomically thin group-V elemental films: theoretical investigations of antimonene allotropes. *ACS Appl. Mater. Interfaces* **7**, 11490–11496 (2015).
10. Pantelic, R. S., Meyer, J. C., Kaiser, U. & Stahlberg, H. The application of graphene as a sample support in transmission electron microscopy. *Solid State Commun.* **152**, 1375–1382 (2012).

Die approbierte gedruckte Originalversion dieser Dissertation ist an der TU Wien Bibliothek verfügbar.
The approved original version of this doctoral thesis is available in print at TU Wien Bibliothek.
TU Bibliothek Your knowledge hub WIEN

Chapter 2

Background

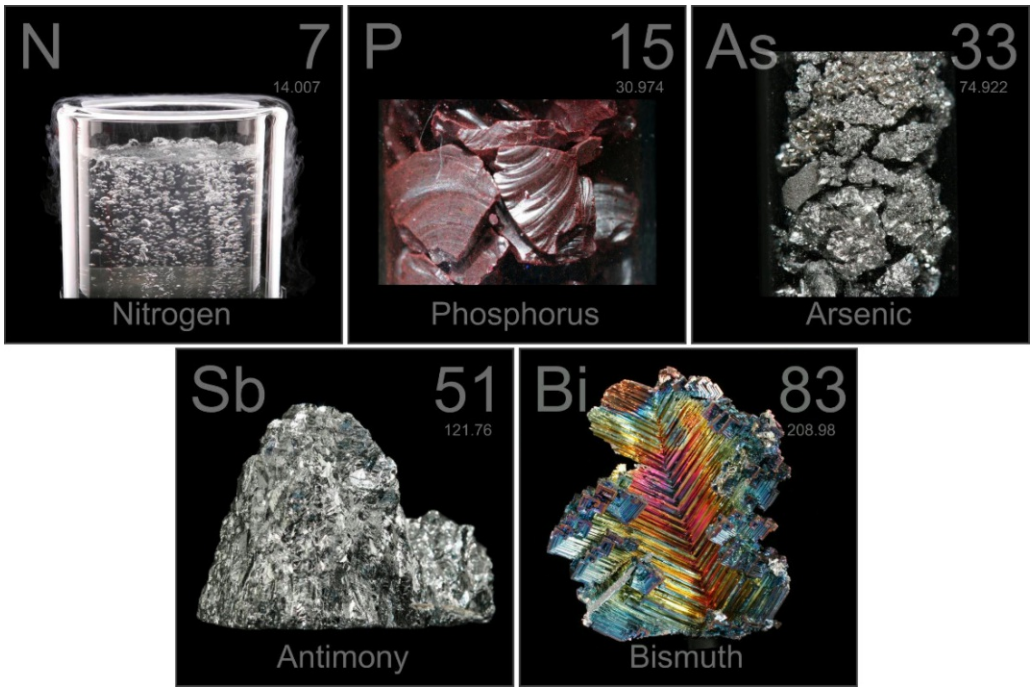

Die approbierte gedruckte Originalversion dieser Dissertation ist an der TU Wien Bibliothek verfügbar.
Your source for knowledge.
TU Bibliothek
WIEN Vien vourknowledge hub

Chapter Preview

Chapter 2 *provides fundamental insights into the world of Pnictogens: dealing with their structure, properties, synthesis methodologies.*

The chapter also introduces the concept of artificial photosynthesis or to say photocatalysis for the production of hydrogen and oxygen from water and finally presents the application prospects of pnictogens in the field of hydrogen evolution reaction via photocatalytic water splitting.

*The caption figure for the chapter 2 shows the different elements in group VA of the periodic table in some of their available forms, adopted from "**http://periodictable.com**"*

Die approbierte gedruckte Originalversion dieser Dissertation ist an der TU Wien Bibliothek verfügbar.
The approved original version of this doctoral thesis is available in print at TU Wien Bibliothek.
TU Bibliothek Your knowledge hub WIEN

2. Background

2.1 Context

Successful realization of graphene and its numerous exciting properties[1] brought an explosive growth of research interest in 2D materials; including the current hot topic MXenes[2]. Consequently many other 2D materials were studied which could compensate for the absence of band gap in intrinsic graphene, among which Transition Metal Di Chalcogenides (TMDCs) were extensively investigated for their exquisite property of thickness, strain and functionality dependent band gap tunability etc.[3] However the limited applicability of these materials in applications requiring lower band gaps (~ 0.1 - 1eV) spurred interest in the then scarcely investigated mono-elemental 2D materials from group 13, 14 and 15 of periodic table[4].

2.2 Pnictogens

Group VA (15) elements, often referred to as pnictogens, namely: Nitrogen (N), Phosphorus (P), Arsenic (As), Antimony (Sb) and Bismuth (Bi) in monolayer form represent an interesting class of 2D materials exhibiting broad range of band gaps and high carrier mobility[5]. These class of materials have shown superior promise towards various energy[6] and electronics[7,8] related applications and have thus gained tremendous amount of research interest.

By means of comprehensive theoretical calculations[5], initially 9 different allotropic forms of group 15 monolayers have been predicted to exist as shown in Figure 2.1. Out of these 9 allotropic forms, 5 are with typical honeycomb structure: α, β, γ, δ, ε and 4 exhibit non-honeycomb structures: ζ, η, θ, ι. However, lately few studies[9] followed a new nomenclature for structural classification for the group 15 monolayers as shown on Figure 2.2. Despite, there exists few structural similarities in both the nomenclatures, namely: β = Buckled (hb) structure, α = Asymmetric-Washboard (aw) structure. Among these different allotropic forms, α-form with puckered structure is the lowest energy

Die approbierte gedruckte Originalversion dieser Dissertation ist an der TU Wien Bibliothek verfügbar.
The approved original version of this doctoral thesis is available in print at TU Wien Bibliothek.
TU WIEN Bibliothek Your knowledge hub

configuration for phosphorene, whereas for the case of arsenene, antimonene and bismuthene, β-form with buckled structure remains the most stable and lowest energy configuration as reported by prior studies[5,10–13].

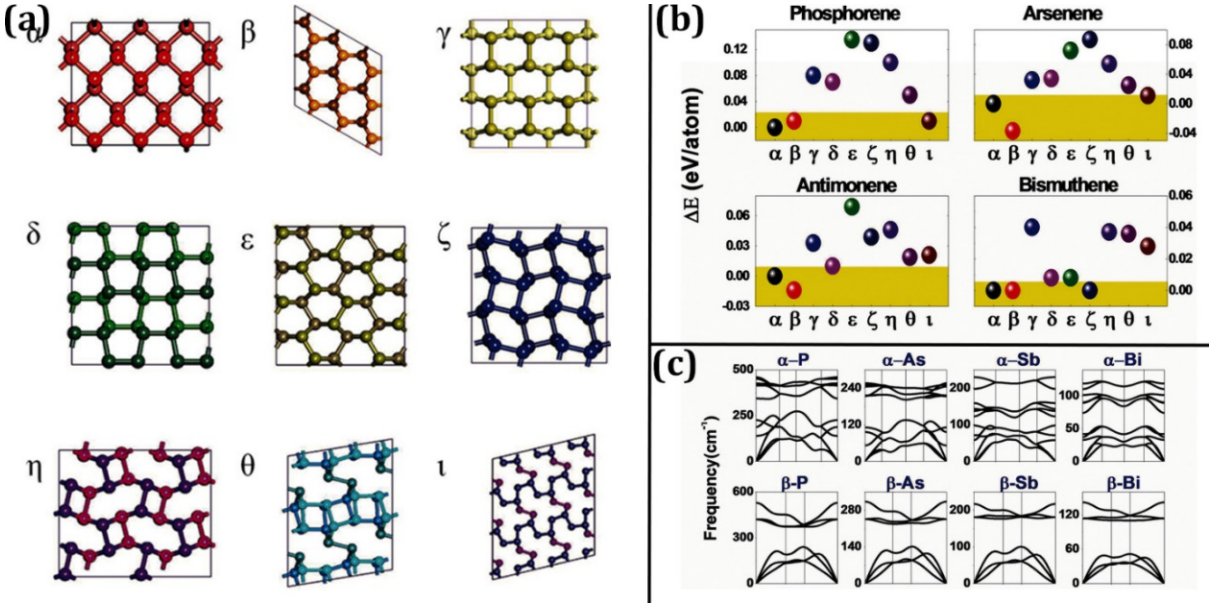

Figure 2.1: (a) Top views of the relaxed Group 15 monolayer allotropes with five typical honeycomb structures (α, β, γ, δ, ε) and four non-honeycomb structures (ζ, η, θ, ι). (b) Calculated average binding energies of all Group 15 monolayer allotropes, which show energetic stability for α and β phases of Group 15 monolayers. b) Phonon band dispersions of all Group 15 monolayers, which exhibit thermodynamic stability (adapted from ref: *5*)

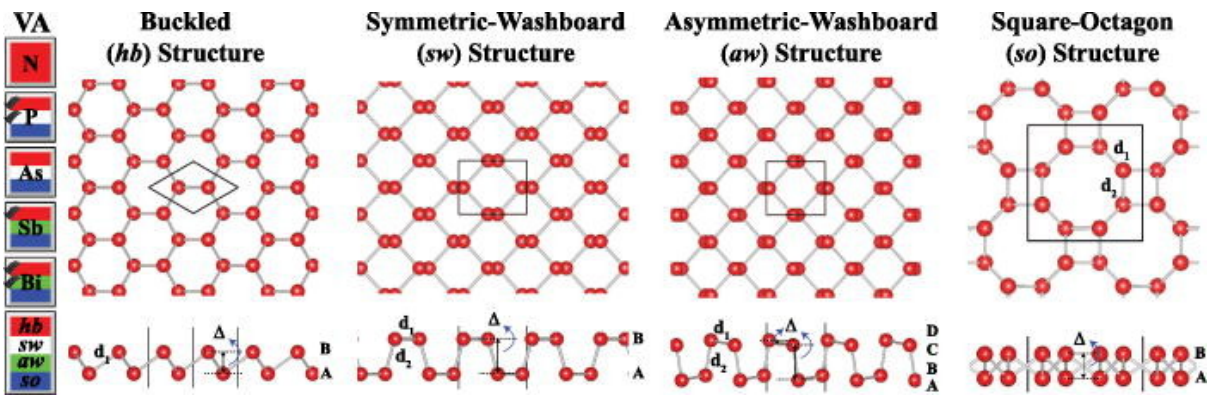

Figure 2.2: Stability analysis of group-VA elements that can form stable, 2D monolayer of hb-, sw- or aw-, and so-structures. Monolayers which are already synthesized are marked. The right panels display the top and side views of the optimized atomic structures. 2D hexagonal and rectangular unit cells are delineated (adapted from ref: 9)

The following sections will now summarize the current state of the art in terms of synthesis, properties and applications of two of the members of the pnictogen family in

Die approbierte gedruckte Originalversion dieser Dissertation ist an der TU Wien Bibliothek verfügbar.
The approved original version of this doctoral thesis is available in print at TU Wien Bibliothek.
TU Bibliothek Your knowledge hub WIEN

their low dimensional forms: antimonene and bismuthene, which constitutes the subject of investigation in this thesis.

2.3 Antimonene

Antimonene has emerged as a promising 2D material since its discovery in 2015[14] because of its unique opto-electronic properties. Theoretical and experimental studies parameterized its notable semiconducting properties including including low thermal conductivity, tunable bandgap, superior optical response and high carrier mobility as well as its electrochemical and catalytic properties for its suitability in various application regimes[6,15,16]. Unlike for its fellow family member phosphorene, good structural stability was predicted for antimonene which further led to its increased attention.

2.3.1 Structure

Bulk antimony exists in three allotropic forms in normal conditions: Gray, black, and explosive antimony. Among them, the most stable form is the Gray Sb with rhombohedral structure and typical semi-metallic features in its layered bulk structure. This bulk rhombohedral phase undergoes a thickness dependent transition in its electronic properties where its 22-layer film behaves as a topological insulator, 8-layer film exhibits quantum spin Hall (QSH) effect and thicknesses under three layers show semiconducting nature[17]. As already mentioned in section 2.2, antimonene has been found to exist only in α- and β-phases. Figure 2.3 shows the optimized structures for α- and β-allotropes of antimony having nonplanar structures as per prior studies. The calculated lattice parameters of both the phases are a = 4.74 Å and b = 4.36 Å, and the corresponding Sb–Sb bond length being 2.95 and 2.87 Å for α-Sb; while for β-Sb monolayer, $a = b$ = 4.07 Å with Sb–Sb bond length to be 2.84 Å[10]. The β-Sb monolayer has a buckling height of 1.67 Å[18].

Die approbierte gedruckte Originalversion dieser Dissertation ist an der TU Wien Bibliothek verfügbar.
The approved original version of this doctoral thesis is available in print at TU Wien Bibliothek.
TU Bibliothek Your knowledge hub WIEN

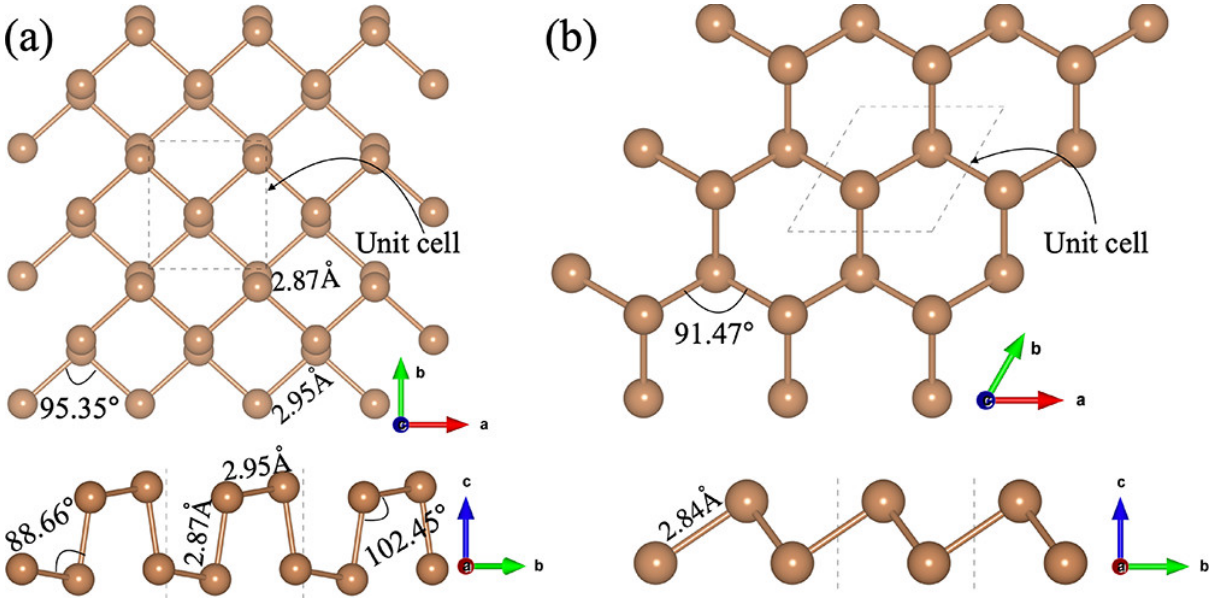

Figure 2.3: Top and side views of (a) α-Sb and (b) β-Sb structure (adapted from ref: 19)

2.3.2 Properties

Stability: In addition to the evaluated stability of the α and β allotropes of Sb at room temperature via phonon dispersion calculations as shown in Figure 2.1[5], finite temperature ab-initio, molecular dynamics simulations revealed that both α and β allotropes of antimonene remain stable at 1000 K for 2 ps[18]. Prior studies reported higher cohesive energy of α-phase than β-phase[9] with α-phase having the highest cohesive energy among all the other allotropes. Annealing few-layered antimonene at 210 °C revealed its oxidation behavior confirmed by band gap of ~ 1 eV measured by UPS which were further supported by Density Functional Theory (DFT) in one prior study[20]. Remarkable ambient oxidation stability was highlighted by the preserved antimony vibrational modes in the Raman spectra over a period of a month by a former work[21].

Mechanical: Antimonene in its layered β-allotropic form has been studied to possess an in-plane stiffness of around 41 J m^{-2}, which is comparable to that of silicene (monolayer of Si)[18]. Calculated Youngs modulus and shear modulus of 31 J m^{-2} and 13 J m^{-2} reveal good mechanical properties of β-antimonene[22].

Die approbierte gedruckte Originalversion dieser Dissertation ist an der TU Wien Bibliothek verfügbar.
The approved original version of this doctoral thesis is available in print at TU Wien Bibliothek.

Thermal: Earlier work[23] recorded the highest thermoelectric performance of β-antimonene among all the other allotropes of antimonene, having a figure of merit (ZT) of 2.15 at room temperature which could be enhanced under the tensile strain. The thermal conductivity of β-allotrope was found to deteriorate under the effect of certain chemical functionalization processes such as full hydrogenation or halogenation[24]. In addition to this chemical modification, size and nature of edges were also found to have an impact on the thermal conductivity of α and β allotropes of antimonene[25].

Optical: Earlier theoretical study[14] reported an opening of band gap of 2.28 eV in antimonene of one layer thickness, which was subsequently modified by several other studies[10,18,26] by considering different potentials and taking spin-orbit coupling into account thereby reporting much lesser band gap values of 0.76 and 1.55 eV. Consistently all these studies reported the nature of band gap to be indirect, which restricted the applicability of antimonene for certain applications like solar cells. Lately, the possibility of transforming the nature of band gap from indirect to direct under the effect of up to 12 % biaxial strain[14] was discovered where the transition from indirect to direct band gap happened at about 3.8 % strain. Along this direction, a recent study[27] demonstrated the insensitivity of the strain along zig-zag direction towards tuning the nature of band gap. Only the strain in the armchair direction was found to activate this indirect to direct band gap transition via a band switching mechanism. Surface charged dopants have also been studied to enhance the optical absorption of antimonene in lower light energy regions[28]. Particularly, absorption of α-Sb was studied to range from visible to UV region[29].

Electronic: Antimonene has higher carrier mobilities (150 / 510 $cm^2 V^{-1} s^{-1}$ for electron / hole) than arsenene (21 / 66 $cm^2 V^{-1} s^{-1}$) owing to stronger electron-phonon interaction. Moreover it was found that more phonons possess stronger interaction with electrons in conduction band than those at valence band[30]. Akin to the change of nature of band gap of antimonene on the application of biaxial strain as outlined previously, application of strain was also found to be effective in modulating the electronic structure and effective mass of carriers, particularly in the case of α-antimonene, where applying ~8% strain

Die approbierte gedruckte Originalversion dieser Dissertation ist an der TU Wien Bibliothek verfügbar.
The approved original version of this doctoral thesis is available in print at TU Wien Bibliothek.
TU WIEN Bibliothek Your knowledge hub

along the arm-chair direction was found to enhance the carrier mobility up to 4×10^5 cm^2 V^{-1} s^{-1} quite close to that of graphene[31].

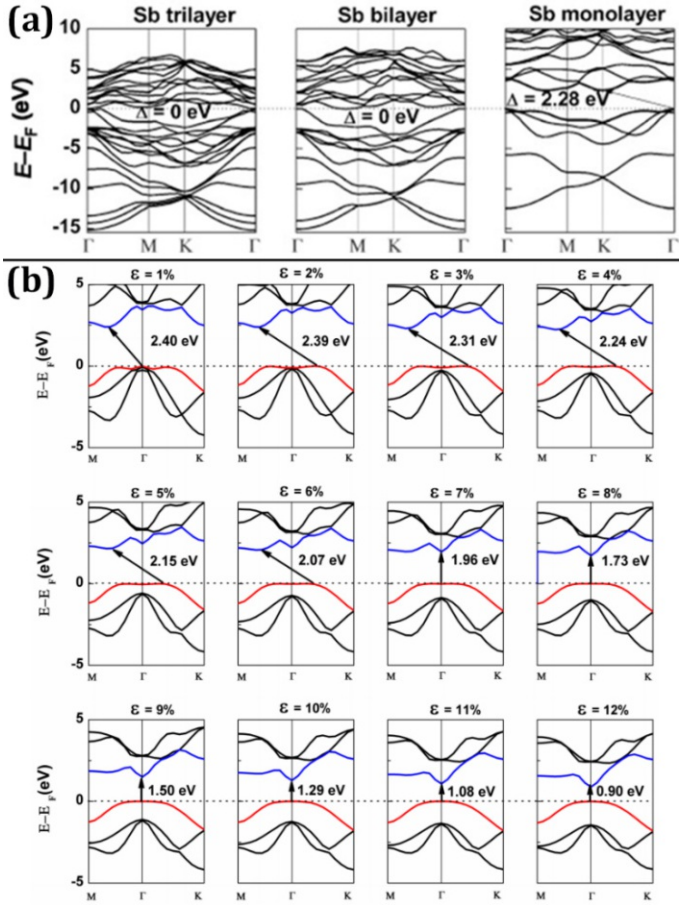

Figure 2.4: (a) Electronic band structures of antimonene trilayer, bilayer and monolayer (calculated at the HSE06 level of theory). (b) Electronic band structures of the monolayered antimonene (Sb) under biaxial strain calculated at theHSE06 level. The horizontal dash lines indicate the Fermi level (adapted from ref: 14)

Electrochemical: First principle calculations[32] show high specific capacity and small diffusion barriers towards Na absorption for antimonene exhibiting its ability to enable fast ionic diffusion over its surface. This has been fruitfully exploited in designing anodes based on antimonene for lithium and sodium ion batteries[33]. Antimony in its elementary form has always been a promising battery anode material because of its high theoretical capacity (C = 660 mAh g^{-1}) upon its complete lithiation and for exhibiting fast inter-layer ionic transport[34]. Nanosculpting antimony to dimensions up to 20 nm has been studied to exhibit not only stable operation with higher current densities along with faster

Die approbierte gedruckte Originalversion dieser Dissertation ist an der TU Wien Bibliothek verfügbar.
The approved original version of this doctoral thesis is available in print at TU Wien Bibliothek.
TU Bibliothek Your knowledge hub WIEN

kinetics but also showed higher rate capabilities at higher current rates[33]. In a yet another study[35] exploring antimonene for supercapacitor applications, antimonene demonstrated remarkable capacitance of 1578 F g^{-1} with high current density of 14 A g^{-1} making net energy and power densities to reach competitive values of 20mWh kg^{-1} and 4.8 kW kg^{-1} respectively.

Catalytic: Based on its strong interaction with light and excellent semiconducting properties, antimonene has also been studied for photocatalysis. First principle calculations[36] demonstrated that antimonene exhibits photocatalytic properties irrespective of the pH conditions, but is dependent on the length of the armchair edge. Moreover, 2D engineering of bulk Sb to antimonene has been found to make it an active 2D electro-catalyst for formate formation upon CO_2 reduction on account of exposure of large number of catalytically active edge sites[37].

2.4 Bismuthene

Currently, Bismuth is the heaviest element in its elemental 2D form of bismuthene among all the group VA single layer materials. Unlike graphene which behaves as a conductor, bismuthene is a topological insulator at room temperature [38] and hence is novel and superior since most topological insulators operate at cryogenic temperatures. The electronic properties of bismuthene can be altered from semi-metallic to semi-conducting / metallic based on the interplay between the thickness and stacking of sheets much similar to its fellow pnictogen member Sb, as already described above. The room temperature display of topological insulation property also broadens the scope of applicability of bismuthene in wide domains ranging from nanoelectronics, spintronics, saturable absorbers, quantum computing etc[39]. Quantum confinement effects in nanostructures of bismuth give rise to several interesting properties like superconductivity[40], semimetal to semiconductor transition[41,42], large magnetoresistance[43,44], high thermoelectric efficiency[45] etc.

Die approbierte gedruckte Originalversion dieser Dissertation ist an der TU Wien Bibliothek verfügbar.
The approved original version of this doctoral thesis is available in print at TU Wien Bibliothek.
TU Bibliothek Your knowledge hub WIEN

2.4.1 Structure

Bismuth has rhombohedral (gray arsenic type) crystal structure with space group D^5_{3d} (R-3m) and corresponding point group D_{3d} (-3m). Bulk bismuth is ABC stacking of bismuthene layers along $[001]_{Hex}$ direction. It is also referred to as A7 crystallographic structure or the blue phosphorus structure. Note that the direction referred to here is in hexagonal notation. The bonds of the trivalent bismuth atoms are directed to the three nearest neighbors and since there is only weak bonding between the layers, Bi single crystals cleave in the $(001)_{Hex}$ plane[46]. Bismuthene has experimentally been realized in three different allotropic forms as shown in Figure 2.5 out of the 9 predicted as described before. Out of these, two are the α- and β-phases having A17 black phosphorus and A7 blue phosphorus structures respectively. The third allotrope depicted in Figure 2.5 (c) is the recently realized puckered single layer of bismuthene with rectangular symmetry similar to that of α-Bi[47] denoted as M-Bi. Important to note is that α-phase is the same rhombohedral phase when viewed along [2-21] zone axis. Following translations from rhombohedral notations to hexagonal notations will help remove any ambiguities:

$$(111)_{Rh} = (003)_{Hex} \perp [001]_{Hex} \rightarrow \beta\text{-Sb/Bi} = \text{hb Sb/Bi}$$

$$(110)_{Rh} = (012)_{Hex} \perp [2\text{-}21]_{Hex} \rightarrow \alpha\text{-Sb/Bi} = \text{aw Sb/Bi}$$

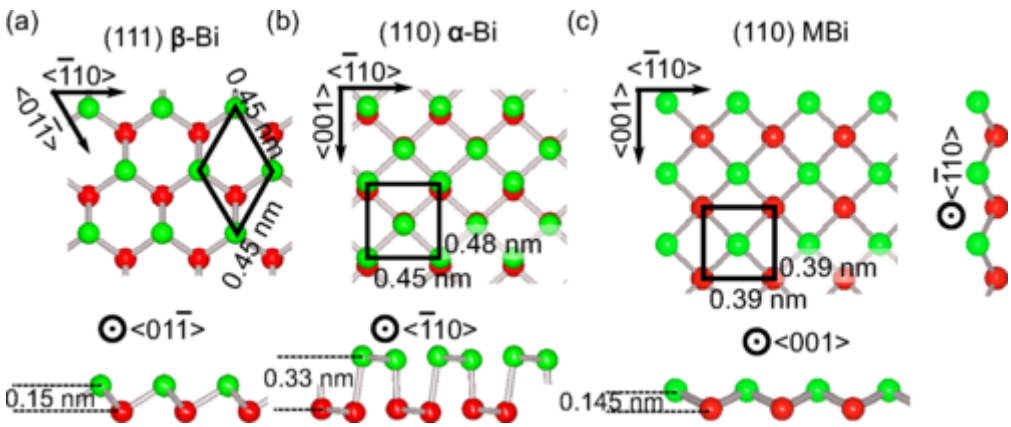

Figure 2.5: Crystallographic structure of bismuth allotropes: (a) β-Bi [hexagonal, (111) structure], (b) α-Bi [(110) paired layer structure with rectangular unit cell], and (c) monolayer bismuth (MBi)—the new single layer rectangular structure reported. Crystallographic directions, unit cells, and interlayer distances are marked in each case (adapted from ref: 47). The directions given here are in rhombohedral notations.

Die approbierte gedruckte Originalversion dieser Dissertation ist an der TU Wien Bibliothek verfügbar.
The approved original version of this doctoral thesis is available in print at TU Wien Bibliothek.
TU Bibliothek Your knowledge hub WIEN

Where ( ) denote planes (h k l) and [ ] denote directions [u v w]. It is however reported that A17 structure or the α-phase can only exist in paired layer form since the second layer is required to bind it together providing them even layer stability[48]. The lattice constants of the free-standing monolayer of β-Bi is a = 4.5 Å whereas for the α- phase is a = 4.5 Å and b = 4.8 Å. The approximate thickness of a monolayer of β-Bi is 1.5 Å and that of α-Bi is 3.3 Å[49]. As compared to the fellow pnictogen Sb, Bi is more isotropic and less layered in structure[50].

2.4.2 Properties

Stability: While β-allotrope is the most stable and energetically favorable allotrope of bismuthene, it can readily transform into metastable planar structures[51]. Additionally, studies synthesizing bismuthene via vapor growth methods have found α-Bi to transform into the bulk β-Bi above critical thickness of 4 layers at room temperature. This critical thickness of transformation was found to increase with substrate temperature. Even layer stability of the α-Bi as mentioned before makes it grow laterally flat[48]. Molecular dynamics calculations suggested that both β-Bi and α-Bi structures sustain to thermal excitations; however, irreversible distortions start to occur above 700 K[52]. The effects of oxygen and water environmental molecules on the structural stability of bismuthene was outlined using first-principles calculations where strong acceptor role and the low splitting energy barrier (~0.60 eV) of oxygen on bismuthene suggested the high possibility of formation of bismuthene oxides at elevated temperatures on its surface. Nevertheless, similar to that of antimonene, the stability of bismuthene under ambient environment was maintained due to donor role of water to the oxidized bismuthene surface as found by one of the earlier studies[39].

Mechanical: The reported Young's moduli of bismuthene along the armchair and zigzag directions are ~26.2 N m^{-1} and ~25.46 N m^{-1}, respectively[53,54] whereas fracture stress and fracture strain are ~4.21 N m^{-1} and ~19.50% along the armchair direction and ~4.22 N m^{-1} and ~25.5% along the zigzag directions respectively. Increasing temperature was found to cause the failure at lower fracture stress and strain. Overall, zigzag direction was

Die approbierte gedruckte Originalversion dieser Dissertation ist an der TU Wien Bibliothek verfügbar.
The approved original version of this doctoral thesis is available in print at TU Wien Bibliothek.
TU Bibliothek Your knowledge hub WIEN

found to be more resilient to fracture and less vulnerable to temperature change than the armchair direction. In addition to the temperature-based studies, increasing vacancy defects were equally found to impact and deteriorate the mechanical properties of the β-bismuthene[54]. Earlier studies outlined the values of in-plane stiffness for single layer bismuthene and found it to be smaller when compared with those of graphene (330 N m^{-1}), h-BN (240 N m^{-1}), silicene (65 N m^{-1}), and MoS2 (138 N m^{-1}), all having single-layer honeycomb structure[52].

Thermal: Thermoelectric performance of monolayer β-Bi was predicted to be much better than its bulk counterpart owing to larger power factors and lower thermal conductivity of monolayer β-Bi. Similar to β-Sb, the β-Bi structure also has a high thermoelectric efficiency[55]. The figure of merit (*ZT)* value for monolayer bismuthene can be optimized to as high as 2.4 at 300 K (higher than the bulk Bi, which is 1.44[56]) by doping and could be further improved to maximum of 4.1 at 500 K[55]. In line with these observations, thermal conductivity was found to decrease with increasing temperature and vacancy concentrations in a former study where the predicted thermal conductivity of ~1.3 W m^{-1} K^{-1} at 300 K (which is considerably lower than other analogous 2D honeycombs) could be engineered to ~0.75 W m^{-1} K^{-1} by removing only ~1% bismuth atom from the domain. This renders β-bismuthene a promising material for high-performance thermoelectric operations[54].

Electronic: The monolayer of bismuthene is characterized by an indirect band gap of 0.56 eV as computed via first principle calculations by prior studies[57] on account of strong spin orbit coupling effect due to its heavy mass. However, the nature of the band gap of monolayer of bismuthene can be tuned from indirect to direct by either stacking another bismuthene monolayer atop or by the application of in-layer biaxial strain[58]. Another study[57] found the band gaps to be unaffected by up to ±6% strains and perpendicular electric fields up to 0.8 eV $Å^{-1}$, indicating the robustness of electronic properties of bismuthene against possible strain or interfacial charge transfer. However, band gap closes for compressive strain beyond 7% transforming the nature of monolayer bismuthene from semiconductor to semi-metal as shown in Figure 2.6.

Die approbierte gedruckte Originalversion dieser Dissertation ist an der TU Wien Bibliothek verfügbar.
The approved original version of this doctoral thesis is available in print at TU Wien Bibliothek.
TU Bibliothek Your knowledge hub WIEN

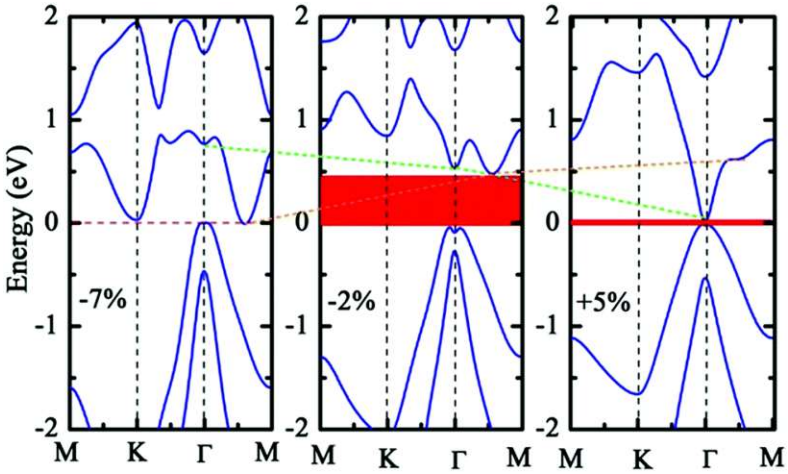

Figure 2.6: Calculated band structure of monolayer bismuthene under −7%, −2% and +5% strains (adapted from ref: 58)

Electrochemical: Layered structure with large interlayer spacing, eco-friendly nature, long mean free path, relatively low working potential and high volumetric capacity of 3800 mA h L^{-1} impart great potential to bismuth for its use an anode material in batteries[59]. The interlayer spacing in bismuth along the c-direction is 3.979 Å, which remarkably facilitates the diffusion of lithium (1.52 Å) and sodium (2.04 Å) ions[60] and even potassium ions. Not only its bulk but also in its 2D form of bismuthene, the layered structure facilitates the diffusion of ions penetration of electrolyte and buffering the volumetric variations further boost its anodic performance[59]. Prior studies via in situ microscopic as well as theoretical studies found large anisotropic volume expansions of ~ 142 % during sodiation in bulk bismuth which was mitigated by the use of 2D bismuthene with large aspect ratio[61]. Former studies found bismuthene to deliver an extraordinary charge–discharge capacity of 201 mA h g^{-1} at the current density of 20 A g^{-1} for more than 2500 cycles without any obvious decay and achieve a capacity of 423 mA h g^{-1} at the current density of 2.5 A g^{-1} realizing excellent rate-capability and long-term cycling stability in potassium ion batteries as also shown in Figure 2.7[59].

Catalytic: Close positioning of Bi to traditional formate-producing metals in the periodic table (e.g: Pb, Tl, Sn, Hg) suggested its possible activity for CO_2 reduction to formate, where its less toxic and environment benign nature than many of its neighbors proved to

Die approbierte gedruckte Originalversion dieser Dissertation ist an der TU Wien Bibliothek verfügbar.
The approved original version of this doctoral thesis is available in print at TU Wien Bibliothek.

be advantageous in further exploring its catalytic potential[62]. Interestingly, bismuthene monolayers have been studied to show the capability of selectively reducing CO_2 to HCOOH only with high Faradaic efficiency of ~99%, high durability (>75 h) and low onset overpotential of <90 mV[63]. This high performance out-beats many other studied electrocatalysts[64] for formate production. Importantly, α-Bi was found to show comparatively lower activity towards CO_2 reduction than β-Bi because of compressive strain[63]. The large amount of exposed active edge sites and high conductivity in bismuthene are responsible for its high intrinsic catalytic activity. The reduction activity was found to be more pronounced at the edge sites rather than the facet sites via first principle calculations[65].

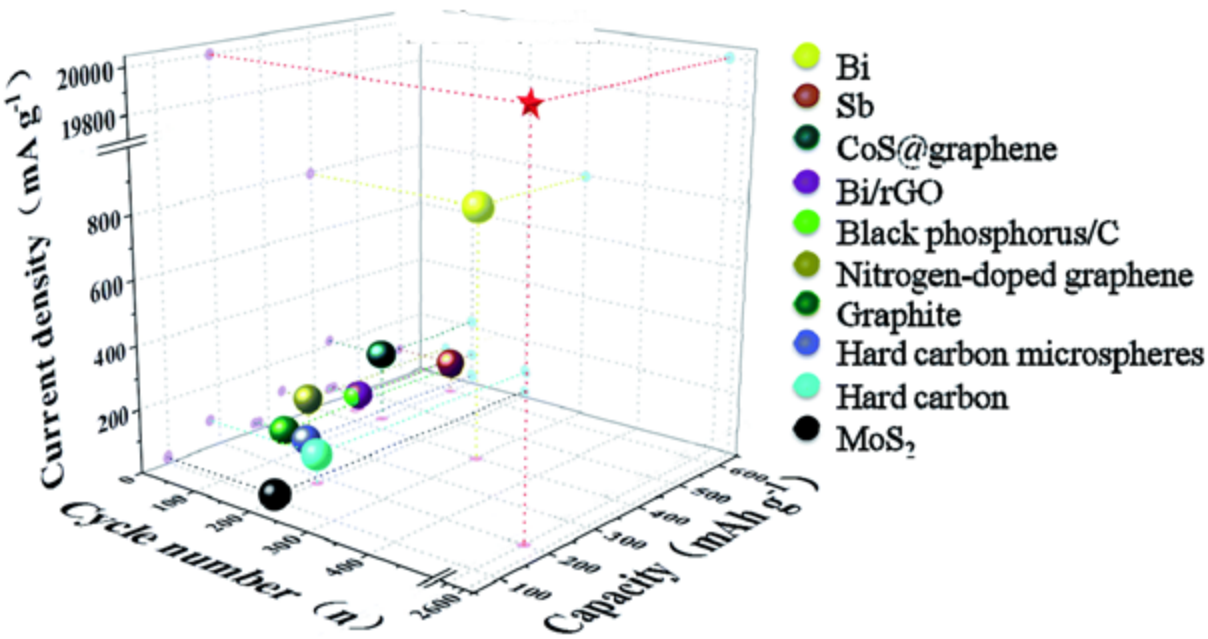

Figure 2.7: A comparison of cycling performance with as-reported anodes for potassium ion batteries (adapted from ref: 59). The star mark is an indicator for bismuthene.

2.5 Synthesis of antimonene and bismuthene

This section describes the state-of-the-art in the physical vapor deposition assisted process of thermal evaporation of antimony and bismuth as well as the wet chemical approach of liquid phase exfoliation. Due to the vast available literature, for the case of

Die approbierte gedruckte Originalversion dieser Dissertation ist an der TU Wien Bibliothek verfügbar.
The approved original version of this doctoral thesis is available in print at TU Wien Bibliothek.
TU Bibliothek Your knowledge hub WIEN

thermal evaporation, only key insights from the antimony and bismuth deposition on graphene/ highly ordered pyrolytic graphite-based substrates will be presented to enable catch the similarities and dissimilarities with the here explored Sb/Bi-graphene based heterostructures. For the case of LPE, prior studies involving only sonication and centrifugation assisted exfoliation of pure metal precursors have been presented to assist projecting the findings of this thesis in a relatable background.

2.5.1 Thermal Evaporation

Earliest studies regarding the vapor assisted synthesis of antimonene and bismuthene date back to as early as 1970s where the deposition was carried out in an ultra-high vacuum chamber with a base pressure of around 10^{-10} mbar, equipped with a quartz crystal microbalance for precise monitoring of the growth / thickness deposition and a thermocouple for monitoring the source temperature. High purity precursor powders/ crystals (~99.9998% or 6N grade) were mounted on a tungsten boat and resistively heated controlled by a thermocouple. A prior step of degassing of the substrates was adopted before carrying out the deposition to ensure the removal of contaminants[66–68]. For the type of substrates employed , while highly ordered pyrolytic graphite (HOPG) was the preferred choice, the growth characteristics of antimonene and bismuthene were also studied on other substrates like MoS_2[69], Si(111)[48]. The surface inertness of these materials as substrates provides the feasibility of fabricating the nano-crystallites of various elements / alloys. Synthesis of antimony and bismuth in low dimensional form via vapor assisted route of thermal evaporation reveals a huge difference in their growth dynamics and deposits characteristics as discussed below.

Antimony deposition on HOPG, MoS_2 etc. at room temperature yielded separated 3D spherical islands mostly nucleated at the steps of the substrate employed. A small fraction of 2D and 1D structures were also found to be present during room temperature deposition. Apparently, 3D morphology was completely transformed to mainly 2D and 1D deposits during deposition at substrates placed at temperatures ≥ 100 °C as can be

Die approbierte gedruckte Originalversion dieser Dissertation ist an der TU Wien Bibliothek verfügbar.
The approved original version of this doctoral thesis is available in print at TU Wien Bibliothek.
TU Bibliothek Your knowledge hub WIEN

seen in Figure 2.8 (B). Along with the substrate temperature, the flux rate was also found to govern the lateral sizes of the deposits as can be seen in Figure 2.8 (A). The synthesis of 2D and 1D crystallites of Sb at higher substrate temperature was done at an expense of loss of amount of deposited antimony as prior studies[66,67,70] observed significant amount of desorption of antimony from surface placed at temperatures ≥ 220 °C due to the decrease in sticking coefficient of antimony. The formation of 3D spherical/ fractal islands of antimony has been studied to occur via condensation (physisorption) of antimony vapors (consisting of Sb_4 flux)[71,72] on a relatively colder substrate (referring to room temperature depositions) while during depositions at higher temperatures, the antimony flux in its Sb_4 form dissociates to Sb_2 and Sb_1 (both being chemisorbed) leading to the formation of 2D and 1D structures of antimony. In the same direction, it has also been suggested that the crystallization of the antimony deposits is also thickness dependent as shown in Figure 2.8 (C), along with being substrate temperature dependent. These all constitute few of the several other observations found in this study as well and have been well described in Chapter 4 with respect to graphene as a novel substrate. However, the existing anomalies in the accurate assignment of the 1D structures of antimony calls out for a more detailed analysis which is one of the major foundations of the research presented in this thesis. Several prior studies[73] have notably regarded the hexagonal ordered structure of the 2D Sb to be α-Sb $(111)_{Rh}$, while square symmetry observed in 1D nanorods of Sb was often indexed to as simple cubic antimony[74]. This inconsistency has been very well resolved in this study by presenting a clear structural and crystallographic annotations for the obtained different structures of antimony on monolayer graphene in Chapter 4.

Similar experiments were performed to obtain bismuthene via thermal evaporation on HOPG[75], mica[76], silicon nitride[77], Si (111)[48], Si (001)[78], graphene[79,80] etc. Bismuth deposits follow similar fashion as that of antimony where the step edges of the HOPG act as nucleation sites for the growth of Bi nanostructures as outlined by several prior studies[75,81–83] but in terms of morphology of the deposits, they exhibit significant variation from the antimony. For the deposition of bismuth at room temperature, the morphology ranges from rod-shaped morphology to star shaped morphology depending on the pre-treatment procedure of the HOPG before the actual deposition[75,83]. Both the

Die approbierte gedruckte Originalversion dieser Dissertation ist an der TU Wien Bibliothek verfügbar.
The approved original version of this doctoral thesis is available in print at TU Wien Bibliothek.
TU Bibliothek Your knowledge hub WIEN

morphologies expand laterally with increasing deposited thickness as well as the flux and eventually form compact structures as shown in Figure 2.9(A) and (B). The room temperature (RT) deposits exhibited high degree of crystallinity and have also been observed to show some epitaxy relations with respect to HOPG and graphene. The Bi structures were found to grow with Bi $(012)_{Hex}$ plane parallel to the substrate thereby showing the preferred epitaxial relations existing in the Bi-HOPG systems to be $Bi(012)_{Hex}$ || $HOPG(001)_{Hex}$ and in the case of Bi-graphene systems to be $Bi(012)_{Hex}$ || $graphene(001)_{Hex}$ as outlined by prior work[80] and also outlined in Figure 2.9(C). As already discussed in section 2.4.2, the films at smaller thickness have $(012)_{Hex}$ orientation which undergoes a transition to $(001)_{Hex}$ orientation at higher thicknesses.

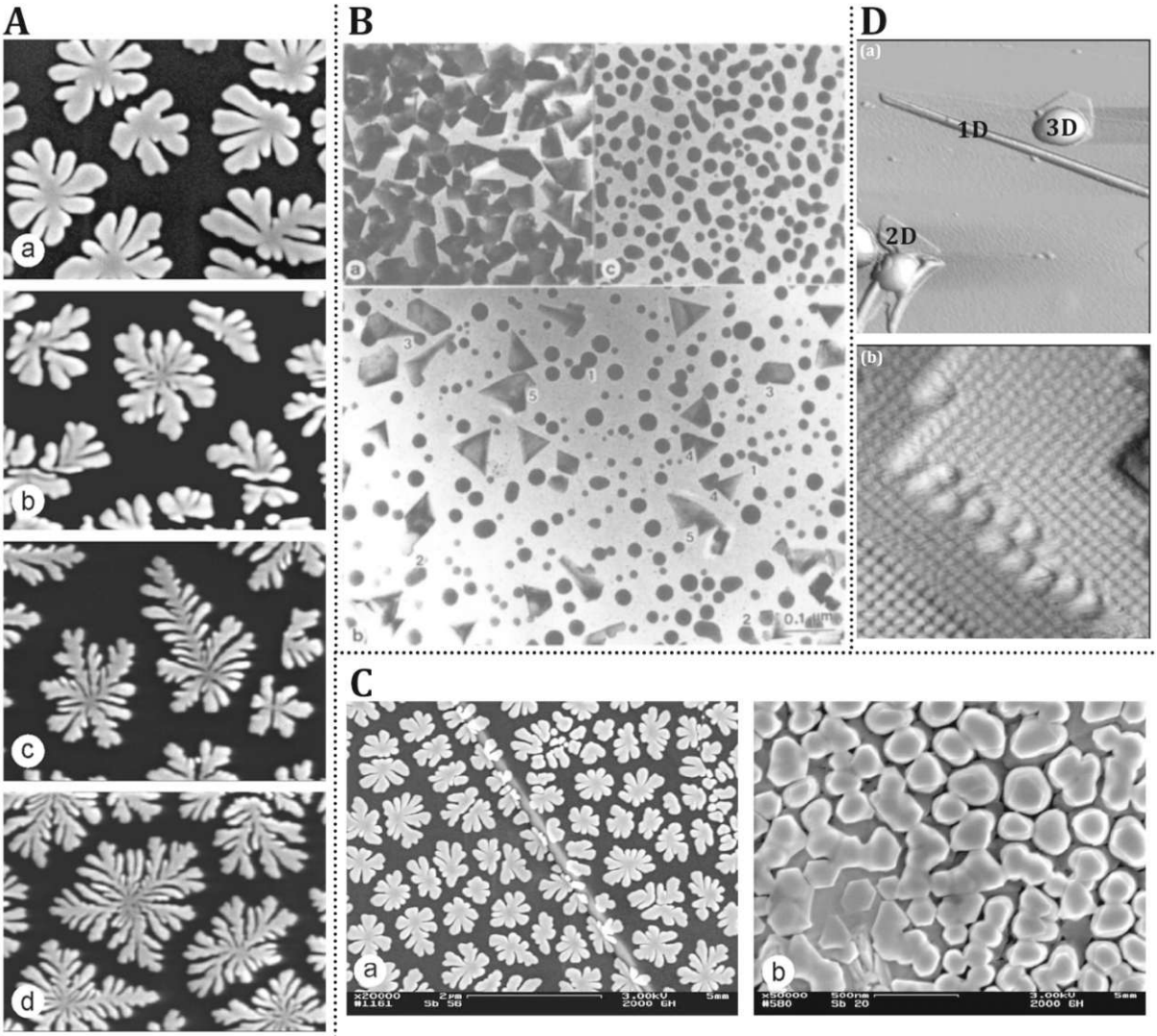

Figure 2.8: (A) SEM images (2.2 µm x 1.6 µm) of the evolution of the surface morphology after deposition of 40 ML antimony at deposition rates of (a) 1.0 Å s^{-1}, (b) 2.0 Å s^{-1}, (c) 10 Å s^{-1}, and (d) 20 Å s^{-1} (adapted from ref: 84). (B) crystalline (a), amorphous + crystalline (b)amorphous (c) Sb deposits obtained at heated (a, b) and room temperature (c) deposition of Sb (adapted from ref:

Die approbierte gedruckte Originalversion dieser Dissertation ist an der TU Wien Bibliothek verfügbar.
The approved original version of this doctoral thesis is available in print at TU Wien Bibliothek.
TU Bibliothek Your knowledge hub WIEN

85). (C) SEM images of antimony deposited on HOPG (0001) (a) 40 monolayer thickness of Sb with deposition rate of 1.0 Å s^{-1}, (b) 200 monolayer thickness of Sb with deposition rate of 1.0 Å s^{-1} (adapted from ref: 86). (D) (a) 3D-view STM image after 3.9 monolayer Sb deposition on HOPG with a flux of 4 Å min^{-1} at room temperature. Scan size: $(1000\ nm)^2$, (b) small-area (9 nm × 9 nm) image taken on the top region of a 1D structure (adapted from ref: 73)

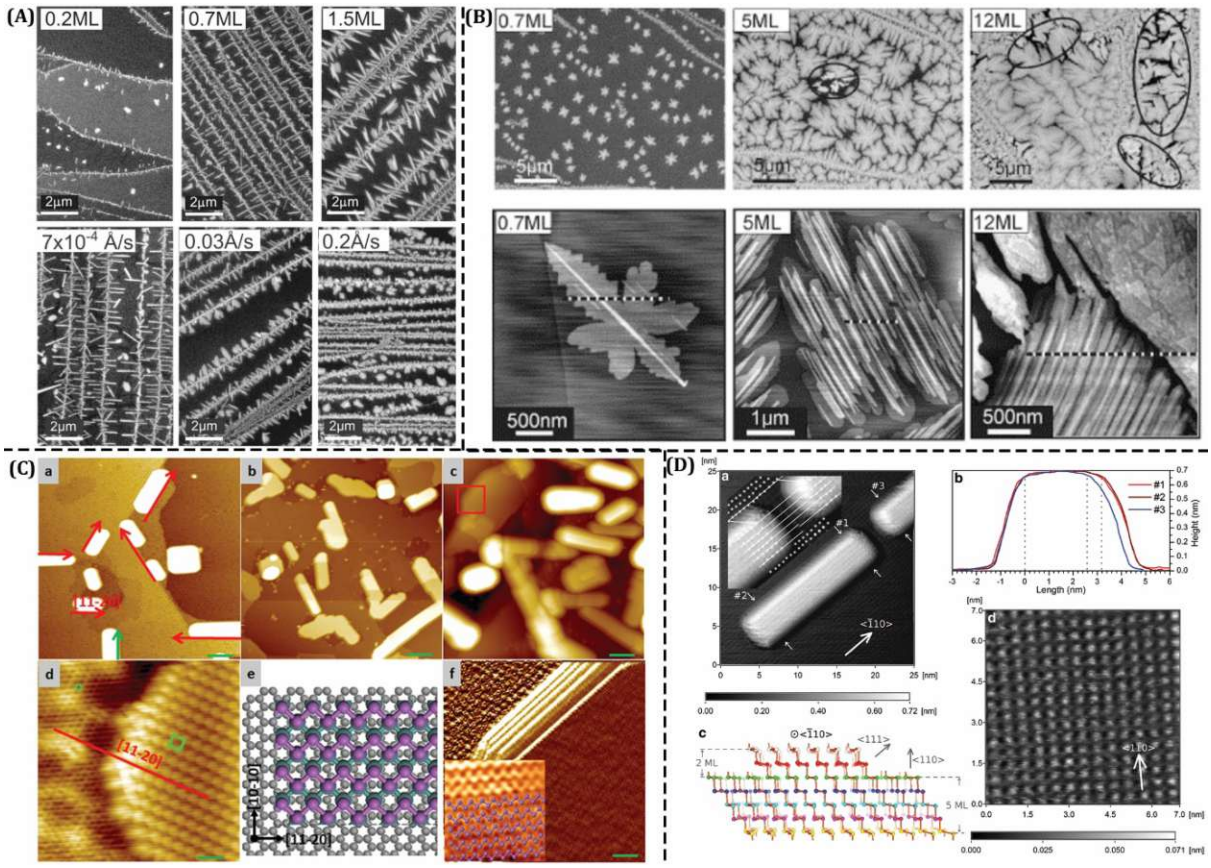

Figure 2.9: (A) SEM images of the evolution of step-edge morphology as a function of increasing coverage (flux ~ 0.005 Å s^{-1}) and as a function of increasing flux (adapted from ref: [75]). (B) SEM images of bismuth films for the coverage range of 0.7–100 ML (flux = 0.03 Å s^{-1}) (adapted from ref: 83). (C) STM images of Bi on monolayer EG. (a–c) Large scale images (scale bar = 12, 20, and 25 nm, respectively) of Bi at coverage of 0.5 monolayer (ML), 1.0 ML, and 2.0 ML. The red arrows in panel a direct to graphene <11-20>$_{Rh}$, the green one to <10-10>$_{Rh}$. (d) High-resolution image (scale bar =0.8 nm) shows the atomic structures of Bi and graphene. The red line highlights Bi <11-20>$_{Rh}$ || graphene <11-20>$_{Rh}$. The green hexagon and rectangle highlight one honeycomb of graphene and one unit cell of Bi film. (e) Proposed model of ultrathin Bi on graphene. (f) Zoomed-in STM image (scale bar = 5 nm) from the red square in panel c. The inset (4 nm × 4 nm) shows the atomic zigzag structure of $Bi(01\text{-}12)_{Hex}$ with Bi atoms overlaid (adapted from ref: 80). (D) Atomic resolution images recorded on two different 5 ML thick islands: (a) 25 × 25 nm 3D top view and (d) 7 × 7 nm. In the top–left inset in (a) magnification of two stripes (which are 2 ML higher than the 5 ML base) is shown. (b) The cross-section profiles recorded in two places on the thicker stripe (marked with light and dark red arrows and with #1 and #2 respectively) and thinner one (marked with blue arrow and #3). (c) Model for 2 ML stripe on top of 5 ML base. White arrows in (a) and (d) indicate the direction (adapted from ref: 87).

Our work here for the first time also compare these prior results on supported graphene with truly free-standing, unsupported graphene to capture intrinsic effects only.

Die approbierte gedruckte Originalversion dieser Dissertation ist an der TU Wien Bibliothek verfügbar.
The approved original version of this doctoral thesis is available in print at TU Wien Bibliothek.
TU Bibliothek Your knowledge hub WIEN

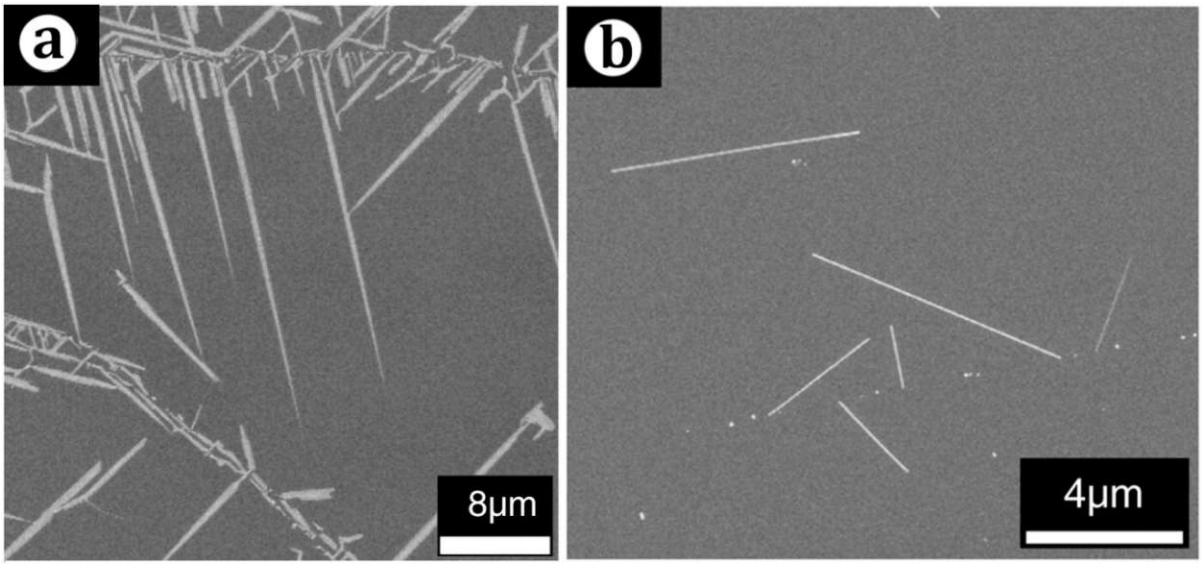

Figure 2.10: SEM images from 5 ML samples grown at flux of 0.018 Å s^{-1} at temperatures of (a) 373 K and (b) 421 K (adapted from ref: 82)

Bismuth, alike antimony, also suffers from the low sticking probability at higher temperatures and therefore bismuth deposition at higher temperature leads to relatively less amount of Bi deposits on the substrates. Prior studies[82] dealing with deposition of bismuth at higher substrate temperatures have reported growth of 1D structures from step edges of HOPG with a very low density of terrace nucleated islands as shown in Figure 2.10. However, the range of substrate temperature utilized in those studies were very narrow ranging from room temperature to around 150 °C. Such narrow temperature ranges make it impossible to exacerbate the effects of the substrate temperature on the morphology of the Bi deposits and hence present an overall different picture as compared to studies[77] performed on other inert substrates but on a wider temperature range where melting of Bi deposits was observed during deposition of Bi at higher substrate temperatures eventually leading to spherical particle like morphology. However, with increasing deposition thickness the bismuth deposits were found to expand laterally even at higher temperature deposition much in concord to the room temperature deposition.

2.5.2 Liquid phase exfoliation (LPE)

The wet chemical approach for the synthesis of layered materials via liquid phase exfoliation has recently gained remarkable attention due to its several advantages over

Die approbierte gedruckte Originalversion dieser Dissertation ist an der TU Wien Bibliothek verfügbar.
The approved original version of this doctoral thesis is available in print at TU Wien Bibliothek.
TU Bibliothek Your knowledge hub WIEN

other synthesis techniques like mechanical exfoliation and chemical vapor deposition (CVD) particularly, its cost-effective nature and high-yield[88] of the exfoliated layered products. Additionally, the insensitivity of the process to air and water and potential to be scaled up to produce larger amounts of exfoliated materials further enables the formation of hybrid films with enhanced properties[89] through this technique. The process essentially introduces the layered materials to ultrasonic waves in the solvent of choice with a selection criterion based on similarity between solvent's surface energy to that of layered material. These sonic waves result in generation of the cavitation bubbles which burst to release energy sufficient to break the layered materials to produce exfoliated materials[90].

In this context, use of LPE technique to obtain stable suspension of few-layered antimonene sheets in an isopropanol : water (4:1) mixture without the use of any surfactants was demonstrated by Gibaja et al[91]. Several other solvents namely: ethanol, acetone, isopropanol, chloroform, water etc. were also tested for their performance towards exfoliating antimony, all of them however did not show any promising results. Several techniques like Raman spectroscopy, Atomic Force Microscopy (AFM), Transmission Electron Microscopy (TEM) were particularly utilized for demonstrating the few-layered nature of the exfoliated materials and could potentially be used to decipher their oxidative susceptibility as well, given the difference in the signature Raman modes and electron diffractions of antimony and its oxide as outlined in Figure 2.11. Other optical techniques like UV-Vis absorption spectroscopy and Photoluminescence (PL) spectroscopy have also been utilized for understanding the nature and properties of exfoliated materials, especially the semiconducting ones like MoO_3[92], MoS_2[93] etc. These techniques, however are not very effective in providing a direct measure of the thinness of the exfoliated antimonene and bismuthene because of their semi-metallic nature even in few-layered form as already described in section 2.3 and 2.4. While Gibaja et al.[91] used relatively shorter sonication time of 40 mins, another study[94] employed typical sonication times up to 30 h for obtaining much thinner and laterally large antimonene sheets by exfoliating antimony in isopropanol with a concentration of sodium hydroxide. This process although yielded better quality of antimonene sheets, but because of relatively longer sonication times employed, the process was time consuming.

Die approbierte gedruckte Originalversion dieser Dissertation ist an der TU Wien Bibliothek verfügbar.
The approved original version of this doctoral thesis is available in print at TU Wien Bibliothek.
TU Bibliothek Your knowledge hub WIEN

This bottleneck was overcome by a simple pre-treatment step of the antimony bulk precursors introduced by Martínez-Periñán et al.[35], which involved ball-milling of the antimony crystals for 180 min at 3000 rpm before 40 min sonication in isopropanol : water (4 : 1) mixture, resulting in a 10 times higher yield of antimonene. The process was thus often referred to as modified LPE. Following this approach, Wang et al.[95] explored butanol-2 to be the suitable solvent for exfoliating antimonene based on contact angle and wettability measurements. The studies further suggested grinding of the antimony crystals in the mortar provides shear force along the surface in a controlled manner as compared to ball milling and mechanical exfoliation via kitchen blenders[50] thereby facilitating the exfoliation of antimony into laterally large and thin sheets as shown in Figure 2.11.

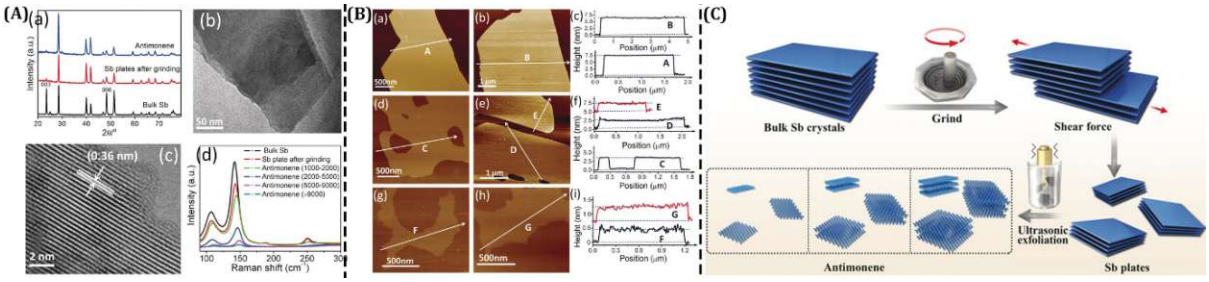

Figure 2.11: (A) (a)X-ray diffraction (XRD) patterns of bulk Sb crystals, Sb plates after grinding, and the resulting antimonene. (b) TEM and (c) high-resolution TEM (HRTEM) images of obtained antimonene. d) Raman spectra of bulk Sb crystals, Sb plates after grinding, and antimonene obtained at different centrifugation speeds. (B) AFM images and corresponding height profiles of antimonene with tunable layer thickness obtained at different centrifugation speeds by spin-coating onto mica film. (a–c) 1000–2000 rpm; (d–f) 2000–5000 rpm; (g–i) 5000–9000 rpm. (C) schematic of adopted LPE procedure to exfoliate antimony (adapted from ref: 95).

Liquid phase exfoliation of bismuth followed a similar route as adopted for the exfoliation of antimony. In the prior studies[96–98], bulk bismuth was firstly grinded in the solvent of choice (mostly ethanol and isopropanol) . This slurry of grinded bismuth + solvent was then diluted with extra solvent to make a concentration of about 4 g L^{-1} and was then subjected to very long sonication times of around 15 h followed by one step centrifugation at around 5000 – 7000 rpm for 20 min. A bit different from the antimony, for the exfoliation of bismuth, particularly the use of ice bath was stressed upon during the sonication which is apparent from the very long sonication times employed leading to localized heating of the solution as well as of the sonic bath/ sonic tip as well. In terms

Die approbierte gedruckte Originalversion dieser Dissertation ist an der TU Wien Bibliothek verfügbar.
The approved original version of this doctoral thesis is available in print at TU Wien Bibliothek.
TU Bibliothek Your knowledge hub WIEN

of performance of various solvents in exfoliating bismuth: ethanol[97,98], isopropanol[96] and N-methyl-2-pyrrolidone (NMP)[99] were found to outperform other tested solvents and yielded thin bismuthene sheets with higher aspect ratios. The quality of the exfoliated bismuth sheets was confirmed with the help of TEM, X-ray diffraction (XRD), AFM and Raman spectroscopy as shown in Figure 2.12. Notably, a recent study[100] synthesized large aspect ratio bismuthene sheets employing bulk bismuth powder with spherical particle like morphology as the precursor without employing the grinding step but employing relatively shorter sonication times of ~ 50 min. The details of this study along with an analogy with our adopted methodology for the liquid phase exfoliation of bismuth has been described in detail in Chapter 6.

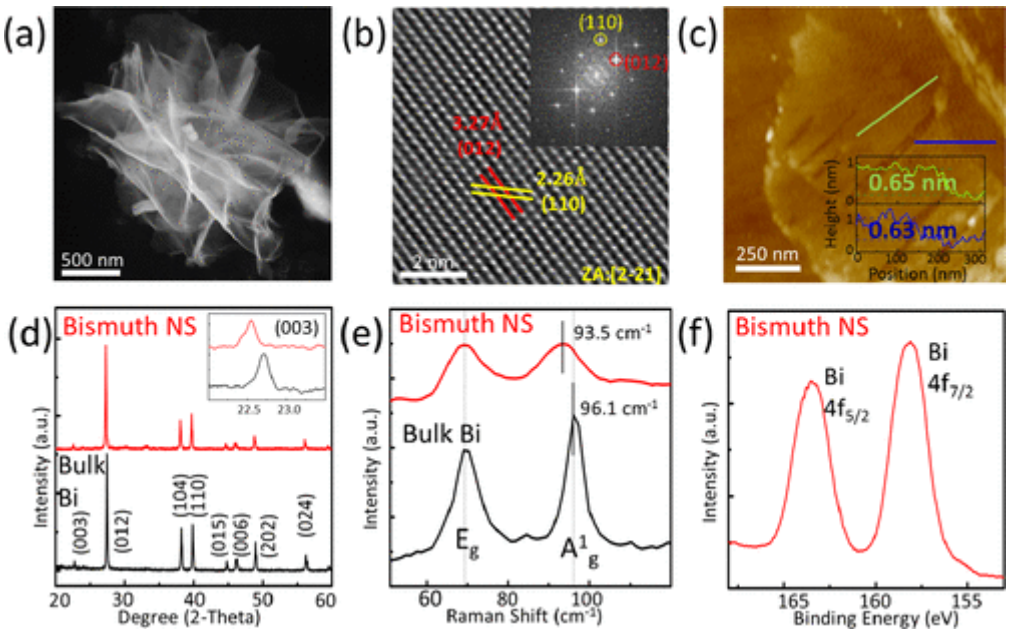

Figure 2.12: Characterization of ultrathin bismuth nanosheets. (a) SEM image of ultrathin bismuth nanosheets. (b) HRTEM image of ultrathin bismuth nanosheets with the lattice fringes of (012) and (110) planes, upper inset is FFT. (c) AFM image of as-obtained ultrathin bismuth nanosheets and the corresponding height profiles. (d) XRD patterns, (003) peak upper inset, and (e) Raman spectra of bulk Bi crystals and bismuth nanosheets. (f) XPS of bismuth nanosheets (adapted from ref: 101).

"An important outcome of the prior LPE studies was the interplay between sonication conditions like ultrasonic power and duration, solvent selection criterion, centrifugation conditions like speed, number of repetitions and duration in governing the size and yield of the exfoliated materials. This overall constitutes a huge parameter space to explore and thus renders the optimization of a standard LPE process to be highly material selective."

Die approbierte gedruckte Originalversion dieser Dissertation ist an der TU Wien Bibliothek verfügbar.
The approved original version of this doctoral thesis is available in print at TU Wien Bibliothek.
TU Bibliothek Your knowledge hub WIEN

2.6 Photocatalytic Water splitting

Photocatalytic water splitting[102], or as it is often called "artificial photosynthesis" is a technique of splitting water into gaseous form of its two constitutional elements $H_2 \uparrow$ and $O_2 \uparrow$ respectively via mimicking the natural process of photosynthesis. While in the conventional process of photosynthesis, sunlight is utilized by plants to synthesize nutrients from water and CO_2, akin to this, a typical photocatalytic water splitting experiment utilizes a photocatalyst provided with an artificial source of light (photon energy) to break H_2O into $H_2 \uparrow$ and $O_2 \uparrow$ respectively. A co-catalyst is sometimes may be needed to drive this reaction smoothly; depending upon the catalytic properties of the photocatalyst used and on the range of wavelength used for excitation. This form of water splitting has long been studied to be the most promising technology to produce hydrogen energy directly from renewable sources like water and solar energy[103–106]. This further implies that successful cost-effective development of this technology could be an answer to the current as well as future major energy and environmental problems with particular emphasis on minimizing our reliance on depletable fossil fuels and CO_2 generation. Since its first demonstration back in 1972 by Fujishima and Honda[102], the field of photocatalytic water splitting has made tremendous progress but mostly under ultra-violet (UV) excitation as there remain multiple challenges to be resolved for driving the process under visible light. Some of them include: finding new single-phase materials, strategies for decorating photosensitizer absorbing visible light on UV-active photocatalysts, band gap tuning etc. [103]

The photochemistry of the water splitting process deals with the absorption of photons in the form of incident light by the photocatalyst. For this reason, the photocatalysts are generally required to be semiconductor materials with band gap (Eg) value that facilitates the capturing of the photons ($h\nu$) by the electrons at the lowest energy state (ground state) implying $h\nu \geq Eg$. As a result of this photon capture, the ground state electrons break away from their electronic shells and make a transition to the higher vacant electron shells and thus creating photoexcited electrons (e^-) at conduction band (CB) and holes (h^+) at valence band (VB). These photogenerated charges are then

Die approbierte gedruckte Originalversion dieser Dissertation ist an der TU Wien Bibliothek verfügbar.
The approved original version of this doctoral thesis is available in print at TU Wien Bibliothek.
TU WIEN Bibliothek Your knowledge hub

transported to the surface of the photocatalyst. This makes large surface area to be an optimum structural constraint for the photocatalyst structure which could help facilitate the charge separation and prevent their recombination. Once transported to the surface of the photocatalyst, these charges interact with the water adsorbed on the surface of the photocatalyst thereby steering the redox reaction of dissociating H_2O into $H_2\uparrow$ and $O_2\uparrow$[107].

Concisely, the process of photocatalytic water splitting involves four prime chronological steps: photocatalyst absorbing photons → excitation of ground state electrons → generation of e^- - h^+ pairs (excitons) → redox reaction between photogenerated charges and water. The thermodynamic feasibility favors the spontaneous recombination of the generated charge carriers and poses a major impediment thereby severely limiting the efficiency of the overall process. This further imposes stringent prerequisite of a minimal band gap of of 1.23 eV to be possessed by the photocatalyst to ensure the feasibility of water splitting[107]. To further achieve higher H_2 production, a complementary strategy is the use of electron donor sacrificial reagents[108] which effectively consume holes and prevent the recombination of photoinduced electrons and holes on the photocatalyst's surface. Some commonly used sacrificial reagents are methanol, triethanolamine, lactic acid etc[109]. Band gaps along with band edge positions of selected semiconductor photocatalysts have been shown in Figure 2.13.

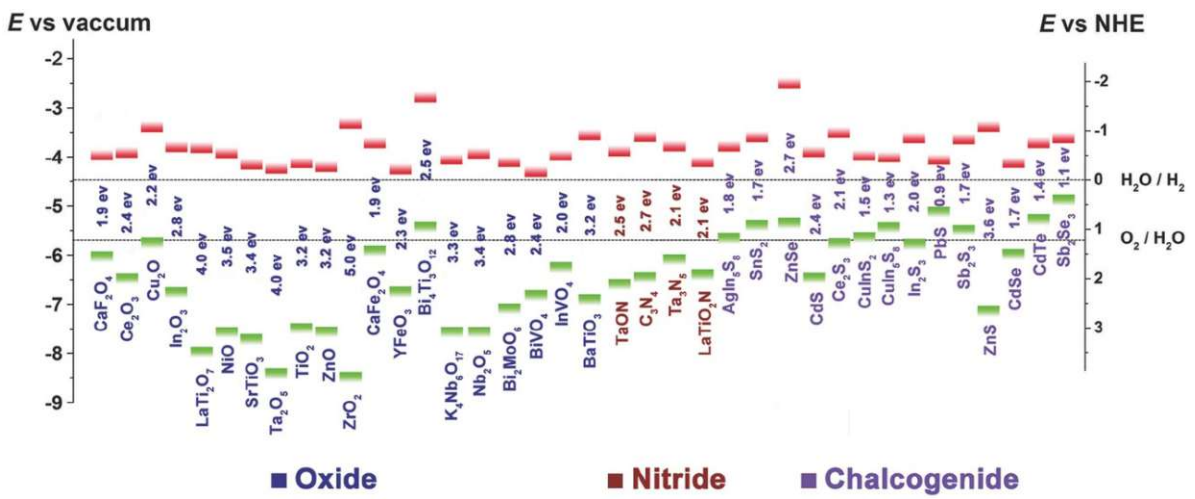

Figure 2.13: Bandgaps and band-edge positions with respect to the vacuum level and NHE for selected semiconductors. The horizontal red lines represent the conduction-band edges. The

Die approbierte gedruckte Originalversion dieser Dissertation ist an der TU Wien Bibliothek verfügbar.
The approved original version of this doctoral thesis is available in print at TU Wien Bibliothek.
TU Bibliothek Your knowledge hub WIEN

horizontal green lines represent the valence-band edges. The two dashed lines indicate the water redox reaction potentials (adapted from ref: 110)

Alongside it has also been well-acknowledged that the process of photocatalytic water splitting does not lead to the production of any concomitant hazardous byproducts. A general mechanistic process of water splitting can be summed up by following equations:

$$\text{Photocatalyst} \xrightarrow{h\nu} h^+ + e^- \quad (1)$$

$$4\,h^+ + 2H_2O \longrightarrow O_2\uparrow + 4H^+ \quad (2)$$

$$4e^- + 4H^+ \longrightarrow 2H_2\uparrow \quad (3)$$

$$2H_2O \xrightarrow{h\nu} O_2\uparrow + 2H_2\uparrow,\ (\Delta E° = -1.23eV) \quad (4)$$

The absorption of photons by the catalyst leads to the generation of excitons as shown by equation 1. The nucleophilic nature of water molecule due to two lone pair electrons on the O atom stimulates its oxidation with h^+ leading to the generation of oxygen gas and H^+ (equation 2). Finally, these dissociated H+ ions are reduced by the photogenerated electrons to release the hydrogen gas (Equation 3). The net equation of the overall photocatalytic water splitting process is given by Equation 4.

The scenario however changes on the introduction of the sacrificial reagent. As per its role of electron donor or hole scavenger, the h^+ is now no more available to cause the oxidation of water to generate O_2, instead methanol gets oxidized to formic acid and water gets reduced to generate the hydrogen gas. The same has been summed up in the equations below[111]:

$$\text{Photocatalyst} \xrightarrow{h\nu} h^+ + e^- \quad (1)$$

$$H_2O + h^+ \longrightarrow {}^{\bullet}OH + H^+ \quad (2)$$

$$CH_3OH + {}^{\bullet}OH \longrightarrow {}^{\bullet}CH_2OH + H_2O \quad (3)$$

$${}^{\bullet}CH_2OH \longrightarrow HCHO + H^+ + e^- \quad (4)$$

$$2H^+ + 2e^- \longrightarrow H_2\uparrow \quad (5)$$

Die approbierte gedruckte Originalversion dieser Dissertation ist an der TU Wien Bibliothek verfügbar.
The approved original version of this doctoral thesis is available in print at TU Wien Bibliothek.
TU Bibliothek Your knowledge hub WIEN

$$HCHO + H_2O \longrightarrow HCOOH + H_2\uparrow \quad (6)$$

$$HCOOH \longrightarrow CO_2\uparrow + H_2\uparrow \quad (7)$$

$$CH_3OH + H_2O \longrightarrow CO_2\uparrow + 3H_2\uparrow \quad (8)$$

The absorption of photons by the photocatalyst leads to the generation of excitons as shown by equation 1. The holes oxidize the H_2O to form the $^{\bullet}OH$ radicals (equation 2). These $^{\bullet}OH$ radicals oxidize the methanol to formic acid as shown by equation 3, 4 and 6. While the electrons reduce the H^+ ions to form the hydrogen gas (equation 5). The formic acid then dissociates into carbon dioxide and hydrogen gas as shown in equation 7. The net equation of the overall photocatalytic water splitting process under the influence of the sacrificial regent is given by Equation 8[111]. Please however note that the set of equations and hence the mechanism will differ in case a different sacrificial reagent is employed.

Current approaches for the successful realization of the water splitting systems can be broadly classified into two principle approaches. Where the first approach deals with the single photocatalyst (may be functionalized with co-catalyst) with a sufficiently narrow band gap and good stability against photo-corrosion. Due to the stringent pre-requisites, the number of reliable, reproducible photocatalysts suitable for one-step water splitting is limited[112,113]. The other approach is inspired by the natural process of photosynthesis and is also referred to as "Z-scheme". In this approach two different photocatalysts[114] are used, utilizing a two-step excitation mechanism. The advantages of using two different photocatalysts over a single photocatalyst includes the possibility of utilization of wider solar spectrum which reduces the change in Gibbs free energy required to drive each photocatalyst further facilitating the separate evolution of H_2 and O_2. Prior studies have observed good O_2 evolution utilizing two different photocatalysts WO_3 and $BiVO_4$ with a redox mediator[115,116]. However, the studies are not limited to these two systems, many other combinations of two different photocatalysts have been explored by earlier works[117] where improving charge transfer has often been presented as a major obstacle in the successful performance of these two mixed photocatalysts. Figure 2.14 shows the mechanistic model of current successful photocatalytic water splitting systems based on the two approaches described above.

Die approbierte gedruckte Originalversion dieser Dissertation ist an der TU Wien Bibliothek verfügbar.
The approved original version of this doctoral thesis is available in print at TU Wien Bibliothek.
TU Bibliothek WIEN Your knowledge hub

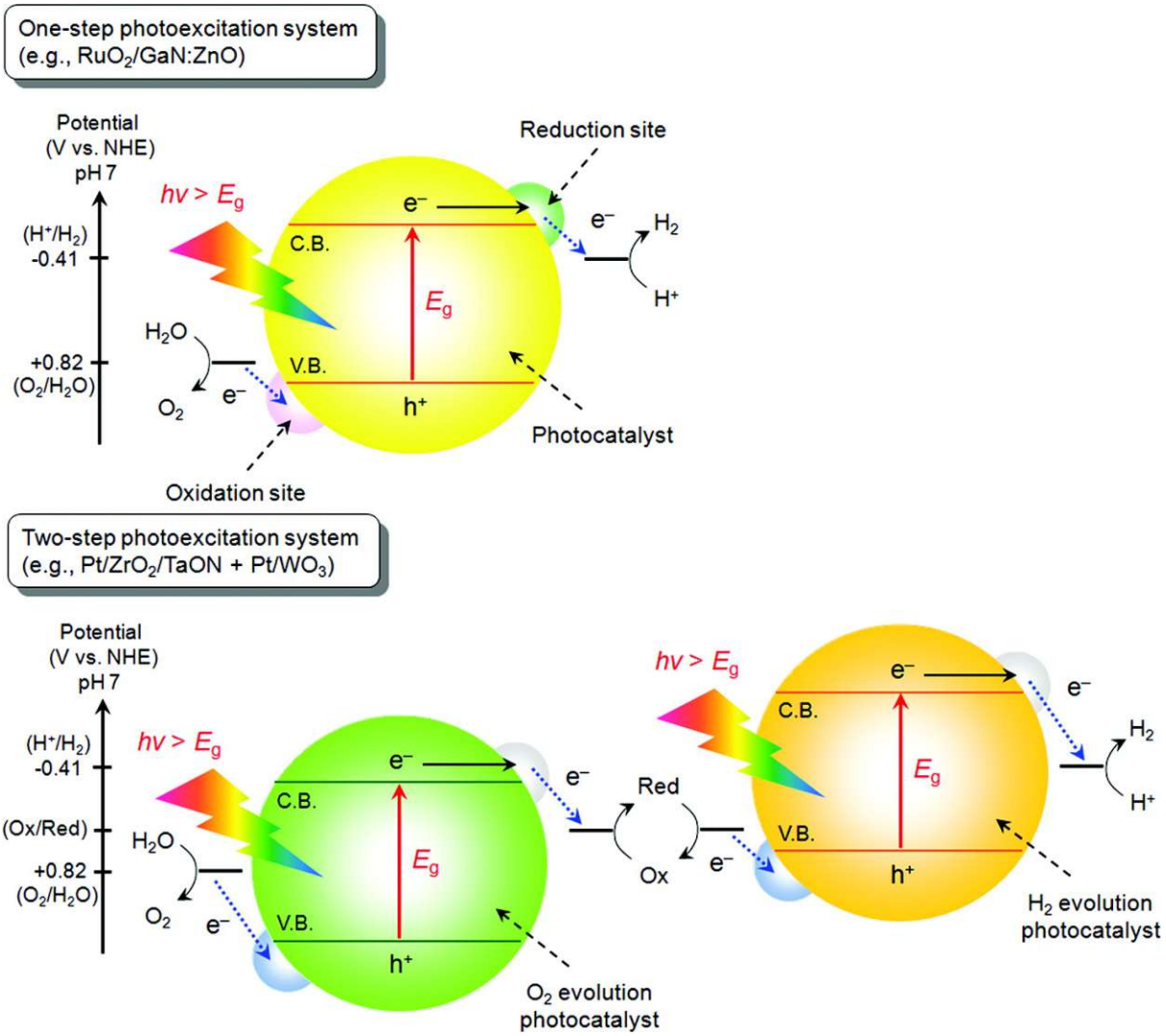

Figure 2.14: Schematic energy diagrams of photocatalytic water splitting by one-step and two-step photoexcitation systems. C.B.→ conduction band, V.B. → valence band, E_g → band gap (adapted from ref: 118)

2.7 Antimonene and Bismuthene as photocatalysts

Two-dimensional materials hold promising potential as photocatalysts owing to their several interesting and catalytic-suitable properties namely: large surface area, good mechanical strength, better optical and electrical performance compared to the bulk type photocatalysts[6]. Their high surface to volume ratios enables better charge separation and the high-density surface-active sites promote active reactions on the photocatalysts surface. Their superior mechanical properties provide durability, good thermal conductivity facilitates the dissipation of heat generated during exothermic reactions, combined with their thickness dependent tunable opto-electronic properties reflect on

Die approbierte gedruckte Originalversion dieser Dissertation ist an der TU Wien Bibliothek verfügbar.
The approved original version of this doctoral thesis is available in print at TU Wien Bibliothek.
TU Bibliothek Your knowledge hub WIEN

their capabilities as a potential photocatalyst[119,120]. In order to tackle the crucial problem of short life time of photogenerated charges, 2D materials are now being more considered because of their ability to separate the electrons and holes effectively[121]. This all comes well complemented by their economically viable synthesis which could help replace currently used noble metal co-catalysts like platinum, palladium, gold etc. which are expensive and have limited reserve[120].

In that context, bismuthene nanosheets have been positively evaluated for their enhanced hydrogen evolution activity both theoretically and experimentally in prior studies[122,123], where the recorded higher catalytic activity was attributed to sufficient exposure of the active sites in 2D layered morphology of bismuthene and short charge diffusion distances, both leading to enhanced hydrogen adsorption on the catalyst surface. Bismuthene under long term hydrogen evolution tests demonstrated excellent durability and efficient catalytic activity, all indicating towards prosperous implications of bismuthene in the domain of catalytic hydrogen evolution reaction applications. Along with bismuthene, several other ternary compounds of bismuth in their 2D form have also been studied for their optimal response towards photocatalytic hydrogen evolution reaction[124,125].

2.8 Conclusion

Given the numerous fascinating properties of antimonene and bismuthene as already outlined in section 2.3.2 and section 2.4.2, these materials tend to dominate the current field of research on 2D materials for their various promising prospective applications in the field of energy and electronics. The field however critical hinges on several platforms, such as:

- Lack of clear distinct structural identification of the different low-dimensional forms of these materials via various top-down and bottom up approaches.
- While most of the studies have focused on the successful synthesis of antimonene and bismuthene, only very few of those studies have provided comprehensible

Die approbierte gedruckte Originalversion dieser Dissertation ist an der TU Wien Bibliothek verfügbar.
The approved original version of this doctoral thesis is available in print at TU Wien Bibliothek.
TU Bibliothek Your knowledge hub WIEN

details on the scalability of the adopted technique. The here adopted technique hold the promise of intrinsic scalability with limited control as compared to other techniques like molecular beam epitaxy (MBE).

- For the field of catalysis, antimonene and bismuthene have been immensely studied by prior works, but for the specific field of photocatalytic hydrogen evolution reaction via water splitting, the studies are rather scarce in number.

These bottlenecks form the major basis / motivation for the research on antimonene and bismuthene presented in this thesis. Clear and distinct crystallographic structural evaluation of the synthesized low dimensional antimonene and bismuthene has been presented in parallel to outlining their several other interesting but seldom reported oxidation resilience property and structure-property correlations etc. The applicability of the adopted synthesis techniques has been also been presented on the merits of its scalability. And finally, the photocatalytic hydrogen evolution performance of these pnictogens has been presented thereby filling some major gaps in the synthesis, characterization and applications of two-dimensional pnictogens and based heterostructures.

2.9 References

1. Novoselov, K. S. *et al.* Electric Field Effect in Atomically Thin Carbon Films. *Science* **306**, 666–669 (2004).
2. Liu, Y. *et al.* Van der Waals heterostructures and devices. *Nat Rev Mater* **1**, 1–17 (2016).
3. Chhowalla, M. *et al.* The chemistry of two-dimensional layered transition metal dichalcogenide nanosheets. *Nature Chem* **5**, 263–275 (2013).
4. Zhou, D. *et al.* Epitaxial Growth of Main Group Monoelemental 2D Materials. *Advanced Functional Materials* **31**, 2006997 (2021).
5. Zhang, S. *et al.* Semiconducting Group 15 Monolayers: A Broad Range of Band Gaps and High Carrier Mobilities. *Angew. Chem. Int. Ed.* **55**, 1666–1669 (2016).
6. Yu, X. *et al.* Emerging 2D pnictogens for catalytic applications: status and challenges. *Journal of Materials Chemistry A* **8**, 12887–12927 (2020).
7. Roy, P. K., Luxa, J. & Sofer, Z. Emerging pnictogen-based 2D semiconductors: sensing and electronic devices. *Nanoscale* **12**, 10430–10446 (2020).
8. Zhou, W. *et al.* Two-Dimensional Pnictogen for Field-Effect Transistors. *Research* vol. 2019 https://spj.sciencemag.org/journals/research/2019/1046329/ (2019) .

Die approbierte gedruckte Originalversion dieser Dissertation ist an der TU Wien Bibliothek verfügbar.
The approved original version of this doctoral thesis is available in print at TU Wien Bibliothek.
TU Bibliothek Your knowledge hub WIEN

9. Ersan, F. *et al.* Two-dimensional pnictogens: A review of recent progresses and future research directions. *Applied Physics Reviews* **6**, 021308 (2019).
10. Wang, G., Pandey, R. & Karna, S. P. Atomically thin group-V elemental films: theoretical investigations of antimonene allotropes. *ACS Applied Materials & Interfaces* **7**, 11490–11496 (2015).
11. Kamal, C. & Ezawa, M. Arsenene: Two-dimensional buckled and puckered honeycomb arsenic systems. *Phys. Rev. B* **91**, 085423 (2015).
12. Zhu, Z. & Tománek, D. Semiconducting Layered Blue Phosphorus: A Computational Study. *Phys. Rev. Lett.* **112**, 176802 (2014).
13. Wu, M., Fu, H., Zhou, L., Yao, K. & Zeng, X. C. Nine New Phosphorene Polymorphs with Non-Honeycomb Structures: A Much Extended Family. *Nano Lett.* **15**, 3557–3562 (2015).
14. Zhang, S., Yan, Z., Li, Y., Chen, Z. & Zeng, H. Atomically Thin Arsenene and Antimonene: Semimetal–Semiconductor and Indirect–Direct Band-Gap Transitions. *Angew. Chem. Int. Ed.* **54**, 3112–3115 (2015).
15. Wang, X. *et al.* Two-dimensional semiconducting antimonene in nanophotonic applications – A review. *Chemical Engineering Journal* **406**, 126876 (2021).
16. Yu, S., Kim, S.-O., Kim, H.-S. & Choi, W. Computational screening of anode materials for potassium-ion batteries. *International Journal of Energy Research* **43**, 7646–7654 (2019).
17. Zhang, P., Liu, Z., Duan, W., Liu, F. & Wu, J. Topological and electronic transitions in a Sb(111) nanofilm: The interplay between quantum confinement and surface effect. *Phys. Rev. B* **85**, 201410 (2012).
18. Aktürk, O. Ü., Özçelik, V. O. & Ciraci, S. Single-layer crystalline phases of antimony: Antimonenes. *Phys. Rev. B* **91**, 235446 (2015).
19. Singh, D. *et al.* Antimonene Allotropes α- and β-Phases as Promising Anchoring Materials for Lithium–Sulfur Batteries. *Energy Fuels* **35**, 9001–9009 (2021).
20. Assebban, M. *et al.* Unveiling the oxidation behavior of liquid-phase exfoliated antimony nanosheets. *2D Mater.* **7**, 025039 (2020).
21. Ji, J. *et al.* Two-dimensional antimonene single crystals grown by van der Waals epitaxy. *Nature Communications* **7**, 13352 (2016).
22. Peng, B. *et al.* The conflicting role of buckled structure in phonon transport of 2D group-IV and group-V materials. *Nanoscale* **9**, 7397–7407 (2017).
23. Chen, K.-X. *et al.* Excellent Thermoelectric Performance Predicted in Two-Dimensional Buckled Antimonene: A First-Principles Study. *J. Phys. Chem. C* **121**, 13035–13042 (2017).
24. Zhang, T., Qi, Y.-Y., Chen, X.-R. & Cai, L.-C. Predicted low thermal conductivities in antimony films and the role of chemical functionalization. *Phys. Chem. Chem. Phys.* **18**, 30061–30067 (2016).
25. Gupta, S. K., Sonvane, Y., Wang, G. & Pandey, R. Size and edge roughness effects on thermal conductivity of pristine antimonene allotropes. *Chemical Physics Letters* **641**, 169–172 (2015).
26. Liu, Y. *et al.* Band Structure, Band Offsets, and Intrinsic Defect Properties of Few-Layer Arsenic and Antimony. *J. Phys. Chem. C* **124**, 7441–7448 (2020).
27. Kripalani, D. R., Kistanov, A. A., Cai, Y., Xue, M. & Zhou, K. Strain engineering of antimonene by a first-principles study: Mechanical and electronic properties. *Phys. Rev. B* **98**, 085410 (2018).
28. Xia, F. *et al.* Tuning the Electronic and Optical Properties of Monolayers As, Sb, and Bi via Surface Charge Transfer Doping. *J. Phys. Chem. C* **121**, 19530–19537 (2017).

Die approbierte gedruckte Originalversion dieser Dissertation ist an der TU Wien Bibliothek verfügbar.
The approved original version of this doctoral thesis is available in print at TU Wien Bibliothek.
TU Bibliothek Your knowledge hub WIEN

29. Xu, Y. *et al.* First-principle calculations of optical properties of monolayer arsenene and antimonene allotropes. *Annalen der Physik* **529**, 1600152 (2017).
30. Wang, Y. *et al.* Many-body Effect, Carrier Mobility, and Device Performance of Hexagonal Arsenene and Antimonene. *Chem. Mater.* **29**, 2191–2201 (2017).
31. Wu, Y. *et al.* Ultrahigh carrier mobilities and high thermoelectric performance at room temperature optimized by strain-engineering to two-dimensional aw-antimonene. *Nano Energy* **63**, 103870 (2019).
32. Sengupta, A. & Frauenheim, T. Lithium and sodium adsorption properties of monolayer antimonene. *Materials Today Energy* **5**, 347–354 (2017).
33. He, M., Kravchyk, K., Walter, M. & Kovalenko, M. V. Monodisperse Antimony Nanocrystals for High-Rate Li-ion and Na-ion Battery Anodes: Nano versus Bulk. *Nano Lett.* **14**, 1255–1262 (2014).
34. Hayner, C. M., Zhao, X. & Kung, H. H. Materials for Rechargeable Lithium-Ion Batteries. *Annu. Rev. Chem. Biomol. Eng.* **3**, 445–471 (2012).
35. Martínez-Periñán, E. *et al.* Antimonene: A Novel 2D Nanomaterial for Supercapacitor Applications. *Adv. Energy Mater.* n/a-n/a doi:10.1002/aenm.201702606.
36. Kokabi, A. & Touski, S. B. Electronic and photocatalytic properties of Antimonene nanosheets. *Physica E: Low-dimensional Systems and Nanostructures* **124**, 114336 (2020).
37. Li, F. *et al.* Unlocking the Electrocatalytic Activity of Antimony for CO2 Reduction by Two-Dimensional Engineering of the Bulk Material. *Angewandte Chemie International Edition* **56**, 14718–14722 (2017).
38. Reis, F. *et al.* Bismuthene on a SiC substrate: A candidate for a high-temperature quantum spin Hall material. *Science* **357**, 287–290 (2017).
39. A. Kistanov, A., Kh. Khadiullin, S., Zhou, K., V. Dmitriev, S. & A. Korznikova, E. Environmental stability of bismuthene: oxidation mechanism and structural stability of 2D pnictogens. *Journal of Materials Chemistry C* **7**, 9195–9202 (2019).
40. Weitzel, B. & Micklitz, H. Superconductivity in granular systems built from well-defined rhombohedral Bi-clusters: Evidence for Bi-surface superconductivity. *Physical Review Letters* **66**, 385–388 (1991).
41. Zhang, Z., Sun, X., Dresselhaus, M. S., Ying, J. Y. & Heremans, J. P. Magnetotransport investigations of ultrafine single-crystalline bismuth nanowire arrays. *Appl. Phys. Lett.* **73**, 1589–1591 (1998).
42. Heremans, J. *et al.* Bismuth nanowire arrays: Synthesis and galvanomagnetic properties. *Phys. Rev. B* **61**, 2921–2930 (2000).
43. Liu, K., Chien, C. L. & Searson, P. C. Finite-size effects in bismuth nanowires. *Phys. Rev. B* **58**, R14681–R14684 (1998).
44. Cho, S. *et al.* Large magnetoresistance in postannealed Bi thin films. 4.
45. Lin, Y.-M., Sun, X. & Dresselhaus1, 2, M. S. Theoretical investigation of thermoelectric transport properties of cylindrical Bi nanowires. *Phys. Rev. B* **62**, 4610–4623 (2000).
46. Ofitserov, A. V. & Edel'man, V. S. Investigation of the spectrum of surface states in bismuth by scanning tunneling spectroscopy. *Journal of Experimental and Theoretical Physics* **93**, 642–648 (2001).
47. Kowalczyk, P. J. *et al.* Single atomic layer allotrope of bismuth with rectangular symmetry. *Physical Review B* **96**, (2017).
48. Nagao, T. *et al.* Nanofilm Allotrope and Phase Transformation of Ultrathin Bi Film on Si(111)-7x7. *Phys. Rev. Lett.* **93**, 105501 (2004).
49. Gonze, X., Michenaud, J.-P. & Vigneron, J.-P. First-principles study of As, Sb, and Bi electronic properties. *Phys. Rev. B* **41**, 11827–11836 (1990).

Die approbierte gedruckte Originalversion dieser Dissertation ist an der TU Wien Bibliothek verfügbar.
The approved original version of this doctoral thesis is available in print at TU Wien Bibliothek.
TU Bibliothek Your knowledge hub WIEN

50. Gusmão, R., Sofer, Z., Bouša, D. & Pumera, M. Pnictogen (As, Sb, Bi) Nanosheets for Electrochemical Applications Are Produced by Shear Exfoliation Using Kitchen Blenders. *Angew. Chem. Int. Ed.* **56**, 14417–14422 (2017).
51. Huang, Z.-Q. *et al.* Nontrivial topological electronic structures in a single Bi(111) bilayer on different substrates: A first-principles study. *Phys. Rev. B* **88**, 165301 (2013).
52. Aktürk, E., Aktürk, O. Ü. & Ciraci, S. Single and bilayer bismuthene: Stability at high temperature and mechanical and electronic properties. *Physical Review B* **94**, (2016).
53. Aghdasi, P., Ansari, R., Rouhi, S. & Goli, M. On the elastic and plastic properties of the bismuthene adsorbed by H, F, Cl and Br atoms. *Superlattices and Microstructures* **135**, 106242 (2019).
54. Chowdhury, E. H., Rahman, M. H., Bose, P., Jayan, R. & Islam, M. M. Atomic-scale analysis of the physical strength and phonon transport mechanisms of monolayer β-bismuthene. *Phys. Chem. Chem. Phys.* **22**, 28238–28255 (2020).
55. Cheng, L. *et al.* Thermoelectric Properties of a Monolayer Bismuth. *The Journal of Physical Chemistry C* **118**, 904–910 (2014).
56. Thonhauser, T., Scheidemantel, T. J. & Sofo, J. O. Improved thermoelectric devices using bismuth alloys. *Appl. Phys. Lett.* **85**, 588–590 (2004).
57. Chen, L., Wang, Z. F. & Liu, F. Robustness of two-dimensional topological insulator states in bilayer bismuth against strain and electrical field. *Phys. Rev. B* **87**, 235420 (2013).
58. Liu, M.-Y. *et al.* Strain and electric field tunable electronic structure of buckled bismuthene. *RSC Advances* **7**, 39546–39555 (2017).
59. Shen, C. *et al.* Bismuthene from sonoelectrochemistry as a superior anode for potassium-ion batteries. *Journal of Materials Chemistry A* **8**, 453–460 (2020).
60. Komaba, S. *et al.* Electrochemical Na Insertion and Solid Electrolyte Interphase for Hard-Carbon Electrodes and Application to Na-Ion Batteries. *Advanced Functional Materials* **21**, 3859–3867 (2011).
61. Zhou, J. *et al.* Few-Layer Bismuthene with Anisotropic Expansion for High-Areal-Capacity Sodium-Ion Batteries. *Advanced Materials* **31**, 1807874 (2019).
62. Han, N. *et al.* Ultrathin bismuth nanosheets from in situ topotactic transformation for selective electrocatalytic CO 2 reduction to formate. *Nature Communications* **9**, 1320 (2018).
63. Yang, F. *et al.* Bismuthene for highly efficient carbon dioxide electroreduction reaction. *Nat Commun* **11**, 1088 (2020).
64. Lei, F. *et al.* Metallic tin quantum sheets confined in graphene toward high-efficiency carbon dioxide electroreduction. *Nat Commun* **7**, 12697 (2016).
65. Zhang, W. *et al.* Liquid-phase exfoliated ultrathin Bi nanosheets: Uncovering the origins of enhanced electrocatalytic CO2 reduction on two-dimensional metal nanostructure. *Nano Energy* **53**, 808–816 (2018).
66. Xiao, W., Yan, Z., Kushvaha, S. S., Xu, M. & Wang, X.-S. DIFFERENT GROWTH BEHAVIOR OF Ge, Al AND Sb ON GRAPHITE. *Surf. Rev. Lett.* **13**, 287–296 (2006).
67. Yan, Z., Kushvaha, S. S., Xiao, W. & Wang, X.-S. Different-dimensional structures of antimony formed selectively on graphite. *Appl. Phys. A* **88**, 299–307 (2007).
68. Bernhardt, T. M., Stegemann, B., Kaiser, B. & Rademann, K. Crystalline Structures of Sb4 Molecules in Antimony Thin Films. *Angewandte Chemie International Edition* **42**, 199–202 (2003).

Die approbierte gedruckte Originalversion dieser Dissertation ist an der TU Wien Bibliothek verfügbar.
The approved original version of this doctoral thesis is available in print at TU Wien Bibliothek.
TU Bibliothek Your knowledge hub WIEN

69. Märkl, T. *et al.* Engineering multiple topological phases in nanoscale Van der Waals heterostructures: realisation of α -antimonene. *2D Mater.* **5**, 011002 (2018).
70. Scott, S. A. & Brown, S. A. Three-dimensional growth characteristics of antimony aggregates on graphite. *Eur. Phys. J. D* **39**, 433–438 (2006).
71. Rouillard, Y., Lambert, B., Toudic, Y., Baudet, M. & Gauneau, M. On the use of dimeric antimony in molecular beam epitaxy. *Journal of Crystal Growth* **156**, 30–38 (1995).
72. Brewer, P. D., Chow, D. H. & Miles, R. H. Atomic antimony for molecular beam epitaxy of high quality III–V semiconductor alloys. *Journal of Vacuum Science & Technology B: Microelectronics and Nanometer Structures Processing, Measurement, and Phenomena* **14**, 2335–2338 (1996).
73. Kushvaha, S. S., Yan, Z., Xiao, W. & Wang, X.-S. Surface morphology of crystalline antimony islands on graphite at room temperature. *J. Phys.: Condens. Matter* **18**, 3425 (2006).
74. Kolobyanina, T. N., Kabalkina, S. S., Vereshchagin, L. F. & Fedina, L. V. Investigation of the crystal structure of antimony at high pressures. *SOV PHYS JETP* **28**, 88–90 (1969).
75. Scott, S. A., Kral, M. V. & Brown, S. A. Growth of oriented Bi nanorods at graphite step-edges. *Phys. Rev. B* **72**, 205423 (2005).
76. Wang, H., Jing, J., Mallik, R. R., Chu, H. T. & Henriksen, P. N. Crystallographic structure and defects in epitaxial bismuth films grown on mica. *Journal of Crystal Growth* **130**, 571–577 (1993).
77. Olson, E. A., Efremov, M. Yu., Zhang, M., Zhang, Z. & Allen, L. H. Size-dependent melting of Bi nanoparticles. *Journal of Applied Physics* **97**, 034304 (2005).
78. Marcano, N. *et al.* Structural and magnetotransport properties of Bi thin films grown by thermal evaporation. *Journal of Magnetism and Magnetic Materials* **322**, 1460–1463 (2010).
79. Shen, K. *et al.* Epitaxial Growth of Free-Standing Bismuth Film on Graphene Embedded with Nontrivial Properties. *ACS Appl. Electron. Mater.* **1**, 1817–1824 (2019).
80. Huang, H. *et al.* Scanning Tunneling Microscope and Photoemission Spectroscopy Investigations of Bismuth on Epitaxial Graphene on SiC(0001). *The Journal of Physical Chemistry C* **118**, 24995–24999 (2014).
81. Song, F., Wells, J. W., Jiang, Z., Saxegaard, M. & Wahlström, E. Low-Temperature Growth of Bismuth Thin Films with (111) Facet on Highly Oriented Pyrolytic Graphite. *ACS Applied Materials & Interfaces* **7**, 8525–8532 (2015).
82. McCarthy, D. N., Robertson, D., Kowalczyk, P. J. & Brown, S. A. The effects of annealing and growth temperature on the morphologies of Bi nanostructures on HOPG. *Surface Science* **604**, 1273–1282 (2010).
83. Scott, S. A., Kral, M. V. & Brown, S. A. A crystallographic orientation transition and early stage growth characteristics of thin Bi films on HOPG. *Surface Science* **587**, 175–184 (2005).
84. Stegemann, B., Ritter, C., Kaiser, B. & Rademann, K. Crystallization of Antimony Nanoparticles: Pattern Formation and Fractal Growth. *J. Phys. Chem. B* **108**, 14292–14297 (2004).
85. Isshiki, T., Nishio, K., Saijo, H. & Shiojiri, M. Growth and crystallographic, surface and defect structures of antimony particles deposited in a high-resolution transmission electron microscope. *Thin Solid Films* **237**, 155–159 (1994).

Die approbierte gedruckte Originalversion dieser Dissertation ist an der TU Wien Bibliothek verfügbar.
The approved original version of this doctoral thesis is available in print at TU Wien Bibliothek.
TU WIEN Bibliothek Your knowledge hub

86. Kaiser, B., Stegemann, B., Kaukel, H. & Rademann, K. Instabilities and pattern formation during the self-organized growth of nanoparticles on graphite. *Surface Science* **496**, L18–L22 (2002).
87. Kowalczyk, P. J. *et al.* STM and XPS investigations of bismuth islands on HOPG. *Surface Science* **605**, 659–667 (2011).
88. Huo, C., Yan, Z., Song, X. & Zeng, H. 2D materials via liquid exfoliation: a review on fabrication and applications. *Science Bulletin* **60**, 1994–2008 (2015).
89. Coleman, J. N. *et al.* Two-Dimensional Nanosheets Produced by Liquid Exfoliation of Layered Materials. *Science* **331**, 568–571 (2011).
90. Nicolosi, V., Chhowalla, M., Kanatzidis, M. G., Strano, M. S. & Coleman, J. N. Liquid Exfoliation of Layered Materials. *Science* **340**, (2013).
91. Gibaja, C. *et al. Few-Layer Antimonene by Liquid-Phase Exfoliation*. (2016). doi:10.1002/ange.201609591.
92. Hanlon, D. *et al.* Production of Molybdenum Trioxide Nanosheets by Liquid Exfoliation and Their Application in High-Performance Supercapacitors. *Chem. Mater.* **26**, 1751–1763 (2014).
93. Bang, G. S. *et al.* Effective Liquid-Phase Exfoliation and Sodium Ion Battery Application of MoS2 Nanosheets. *ACS Appl. Mater. Interfaces* **6**, 7084–7089 (2014).
94. Gu, J. *et al.* Liquid-Phase Exfoliated Metallic Antimony Nanosheets toward High Volumetric Sodium Storage. *Adv. Energy Mater.* **7**, n/a-n/a (2017).
95. Wang, X. *et al.* Bandgap-Tunable Preparation of Smooth and Large Two-Dimensional Antimonene. *Angewandte Chemie International Edition* **57**, 8668–8673 (2018).
96. Lu, L. *et al.* Few-layer Bismuthene: Sonochemical Exfoliation, Nonlinear Optics and Applications for Ultrafast Photonics with Enhanced Stability. *Laser & Photonics Reviews* **12**, 1700221 (2018).
97. Lu, L. *et al.* All-Optical Switching of Two Continuous Waves in Few Layer Bismuthene Based on Spatial Cross-Phase Modulation. *ACS Photonics* **4**, 2852–2861 (2017).
98. Guo, B. *et al.* Sub-200 fs soliton mode-locked fiber laser based on bismuthene saturable absorber. *Optics Express* **26**, 22750 (2018).
99. Huang, H. *et al.* Two-dimensional bismuth nanosheets as prospective photo-detector with tunable optoelectronic performance. *Nanotechnology* **29**, 235201 (2018).
100. Beladi-Mousavi, S. M., Ying, Y., Plutnar, J. & Pumera, M. Bismuthene Metallurgy: Transformation of Bismuth Particles to Ultrahigh-Aspect-Ratio 2D Microsheets. *Small* **16**, 2002037 (2020).
101. Huang, Y. *et al.* Ultrathin Bismuth Nanosheets for Stable Na-Ion Batteries: Clarification of Structure and Phase Transition by in Situ Observation. *Nano Lett.* **19**, 1118–1123 (2019).
102. Fujishima, A. & Honda, K. Electrochemical Photolysis of Water at a Semiconductor Electrode. *Nature* **238**, 37–38 (1972).
103. Lee, J. S. Photocatalytic Water Splitting Under Visible Light with Particulate Semiconductor Catalysts. *Catal Surv Asia* **9**, 217–227 (2005).
104. Kudo, A. & Miseki, Y. Heterogeneous photocatalyst materials for water splitting. *Chem. Soc. Rev.* **38**, 253–278 (2008).
105. Osterloh, F. E. Inorganic Materials as Catalysts for Photochemical Splitting of Water. *Chem. Mater.* **20**, 35–54 (2008).
106. Maeda, K. & Domen, K. New Non-Oxide Photocatalysts Designed for Overall Water Splitting under Visible Light. *J. Phys. Chem. C* **111**, 7851–7861 (2007).

Die approbierte gedruckte Originalversion dieser Dissertation ist an der TU Wien Bibliothek verfügbar.
The approved original version of this doctoral thesis is available in print at TU Wien Bibliothek.
TU Bibliothek Your knowledge hub WIEN

107. Ng, K. H., Lai, S. Y., Cheng, C. K., Cheng, Y. W. & Chong, C. C. Photocatalytic water splitting for solving energy crisis: Myth, Fact or Busted? *Chemical Engineering Journal* **417**, 128847 (2021).
108. Wang, M., Shen, S., Li, L., Tang, Z. & Yang, J. Effects of sacrificial reagents on photocatalytic hydrogen evolution over different photocatalysts. *J Mater Sci* **52**, 5155–5164 (2017).
109. Chen, X. & Mao, S. S. Titanium Dioxide Nanomaterials: Synthesis, Properties, Modifications, and Applications. *Chem. Rev.* **107**, 2891–2959 (2007).
110. Lu, Q., Yu, Y., Ma, Q., Chen, B. & Zhang, H. 2D Transition-Metal-Dichalcogenide-Nanosheet-Based Composites for Photocatalytic and Electrocatalytic Hydrogen Evolution Reactions. *Advanced Materials* **28**, 1917–1933 (2016).
111. Kumaravel, V. *et al.* Photocatalytic Hydrogen Production: Role of Sacrificial Reagents on the Activity of Oxide, Carbon, and Sulfide Catalysts. *Catalysts* **9**, 276 (2019).
112. Maeda, K. *et al.* GaN:ZnO Solid Solution as a Photocatalyst for Visible-Light-Driven Overall Water Splitting. *J. Am. Chem. Soc.* **127**, 8286–8287 (2005).
113. Lee, Y. *et al.* Zinc Germanium Oxynitride as a Photocatalyst for Overall Water Splitting under Visible Light. *J. Phys. Chem. C* **111**, 1042–1048 (2007).
114. Bard, A. J. Photoelectrochemistry and heterogeneous photo-catalysis at semiconductors. *Journal of Photochemistry* **10**, 59–75 (1979).
115. Sayama, K., Mukasa, K., Abe, R., Abe, Y. & Arakawa, H. Stoichiometric water splitting into H2 and O2 using a mixture of two different photocatalysts and an IO3−/I− shuttle redox mediator under visible light irradiation. *Chem. Commun.* 2416–2417 (2001) doi:10.1039/B107673F.
116. Kato, H., Hori, M., Konta, R., Shimodaira, Y. & Kudo, A. Construction of Z-scheme Type Heterogeneous Photocatalysis Systems for Water Splitting into H_2 and O_2 under Visible Light Irradiation. *Chem. Lett.* **33**, 1348–1349 (2004).
117. Sasaki, Y., Nemoto, H., Saito, K. & Kudo, A. Solar Water Splitting Using Powdered Photocatalysts Driven by Z-Schematic Interparticle Electron Transfer without an Electron Mediator. *J. Phys. Chem. C* **113**, 17536–17542 (2009).
118. Maeda, K. & Domen, K. Photocatalytic Water Splitting: Recent Progress and Future Challenges. *J. Phys. Chem. Lett.* **1**, 2655–2661 (2010).
119. Deng, D. *et al.* Catalysis with two-dimensional materials and their heterostructures. *Nature Nanotech* **11**, 218–230 (2016).
120. Deng, J., Deng, D. & Bao, X. Robust Catalysis on 2D Materials Encapsulating Metals: Concept, Application, and Perspective. *Advanced Materials* **29**, 1606967 (2017).
121. Ren, K., Wang, K., Cheng, Y., Tang, W. & Zhang, G. Two-dimensional heterostructures for photocatalytic water splitting: a review of recent progress. *Nano Futures* **4**, 032006 (2020).
122. Duan, C. *et al.* Two-dimensional Bi nanosheets as an enhanced electrocatalyst for hydrogen evolution reaction. *J Sol-Gel Sci Technol* **99**, 132–139 (2021).
123. Pillai, S. B., Dabhi, S. D. & Jha, P. K. Hydrogen evolution reaction and electronic structure calculation of two dimensional bismuth and its alloys. *International Journal of Hydrogen Energy* **43**, 21649–21654 (2018).
124. Zhao, A. *et al.* Emerging members of two-dimensional materials: bismuth-based ternary compounds. *2D Mater.* **8**, 012004 (2020).
125. Selvamani, T., Raj, B. G. S., Anandan, S., Wu, J. J. & Ashokkumar, M. Synthesis of morphology-controlled bismutite for selective applications. *Phys. Chem. Chem. Phys.* **18**, 7768–7779 (2016).

Die approbierte gedruckte Originalversion dieser Dissertation ist an der TU Wien Bibliothek verfügbar.
The approved original version of this doctoral thesis is available in print at TU Wien Bibliothek.
TU Bibliothek Your knowledge hub WIEN

Chapter 3

Experimental Techniques

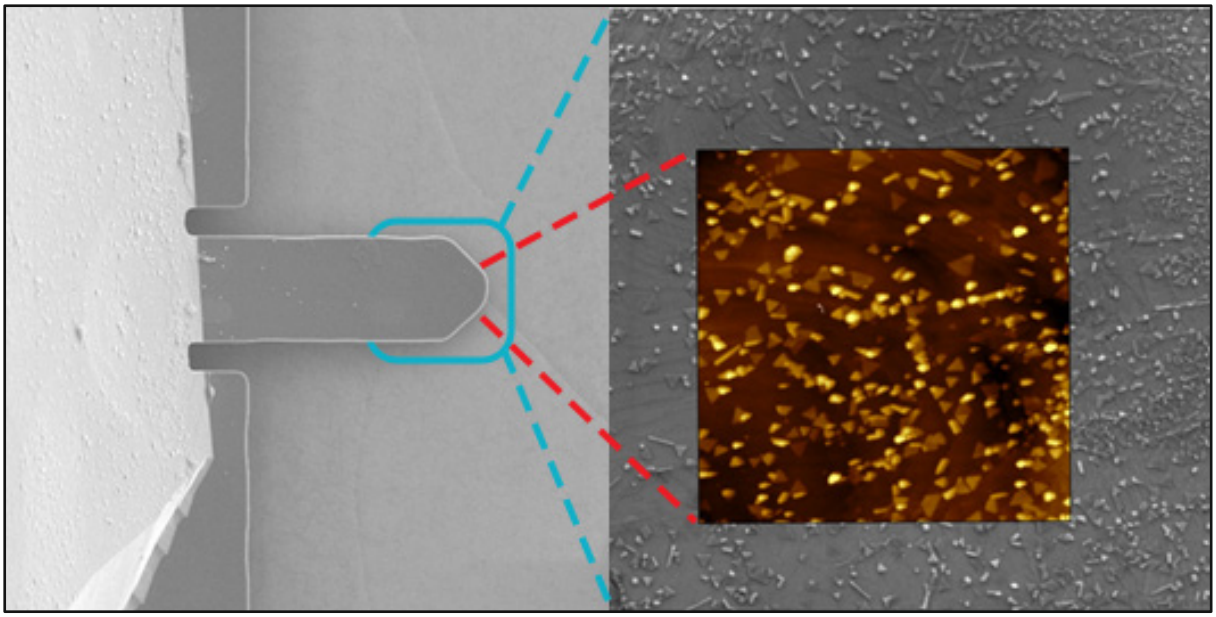

Die approbierte gedruckte Originalversion dieser Dissertation ist an der TU Wien Bibliothek verfügbar.
TU Bibliothek, Die approbierte gedruckte Originalversion dieser Dissertation ist an der TU Wien Bibliothek verfügbar.
WIEN Vien Vourknowledge hub

Chapter Preview

Chapter 3 *sheds light on the fundamentals and working principles of the various instruments employed for the synthesis and characterization of the model systems explored in this thesis.*

A distinctive outline has been provided as to how particular technique was utilized to gain wealth of information on the material's structure, property and could even assist establishing a structure-property correlation.

The figure caption for chapter 3 is the image of the correlative AFM-SEM measurements performed on the few-layered antimonene-graphene heterostructures.

Die approbierte gedruckte Originalversion dieser Dissertation ist an der TU Wien Bibliothek verfügbar.
The approved original version of this doctoral thesis is available in print at TU Wien Bibliothek.
TU Bibliothek Your knowledge hub WIEN

3. Experimental Techniques

3.1 General Sample preparation

Two different procedures were adopted for the synthesis of few-layered pnictogens (particularly, antimonene and bismuthene), namely physical vapor deposition (PVD) technique of thermal evaporation and wet-chemical approach of liquid phase exfoliation (LPE). For the part of the studies dealing with the PVD of Sb and Bi, primarily two types of substrates were employed: (a) Chemical vapor deposition (CVD) (960 °C in $CH_4/H_2/Ar$ at ~12 mbar) grown polycrystalline (grain size tens of µm)[1] monolayer graphene films remaining on their 25 µm thick Cu foil catalysts and (b) CVD graphene films suspended as freestanding monolayer membranes over the regular hole arrays in an amorphous carbon film of a Transmission electron microscope (TEM) grid {Quantifoil (QF TEM)} i.e. no Cu underneath[2]. The same has been schematically explained in Figure 3.1. For studies regarding deposition on graphene-free reference, also Cu foils without graphene were prepared as substrates by annealing Cu foils at 960 °C in 12 mbar H_2 without CH_4. All the samples were handled and stored in ambient atmosphere between *ex-situ* graphene, antimonene and bismuthene deposition / preparation steps and measurements in aberration-corrected Scanning Transmission Electron Microscopy (STEM) and TEM, resulting in adventitious hydrocarbon contaminations on the graphene membranes as discussed in detail in Chapter 4 and 5, which were however typical and relevant for scalable 2D heterostructure processing[3].

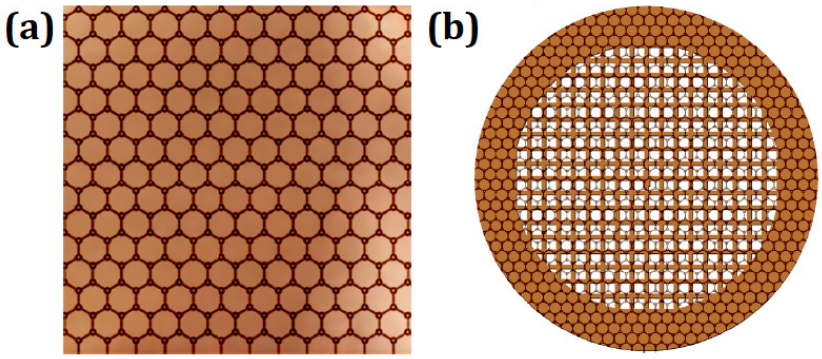

Figure 3.1: Schematic drawings (not to scale) showing the different substrates employed for the PVD of Sb and Bi (a) shows the typical Cu foil catalyst having monolayer graphene grown via CVD (b) shows the transferred monolayer graphene on the Quantifoil TEM grids

Die approbierte gedruckte Originalversion dieser Dissertation ist an der TU Wien Bibliothek verfügbar.
The approved original version of this doctoral thesis is available in print at TU Wien Bibliothek.
TU Bibliothek Your knowledge hub WIEN

Figure 3.2 outlines the quality of the monolayer graphene (MLG) samples supported on the copper catalyst foils as well as suspended on the QF TEM grids. The high-quality of the monolayer graphene on both the substrates has been well concorded with the Raman spectroscopy showing very low intensity of D bands at 1350 cm^{-1} compared to intense G and 2D bands at ~ 1560 cm^{-1} and ~ 2700 cm^{-1} respectively. All lying in line with the standard monolayer graphene characterization via Raman spectroscopy as per prior reported studies[4]. In addition to the Raman spectrum acquired on the QF TEM grids, Annular Dark Field (ADF) images of the suspended MLG captured in aberration-corrected STEM also suggested the high quality of graphene utilized as a substrate for the PVD of Sb and Bi.

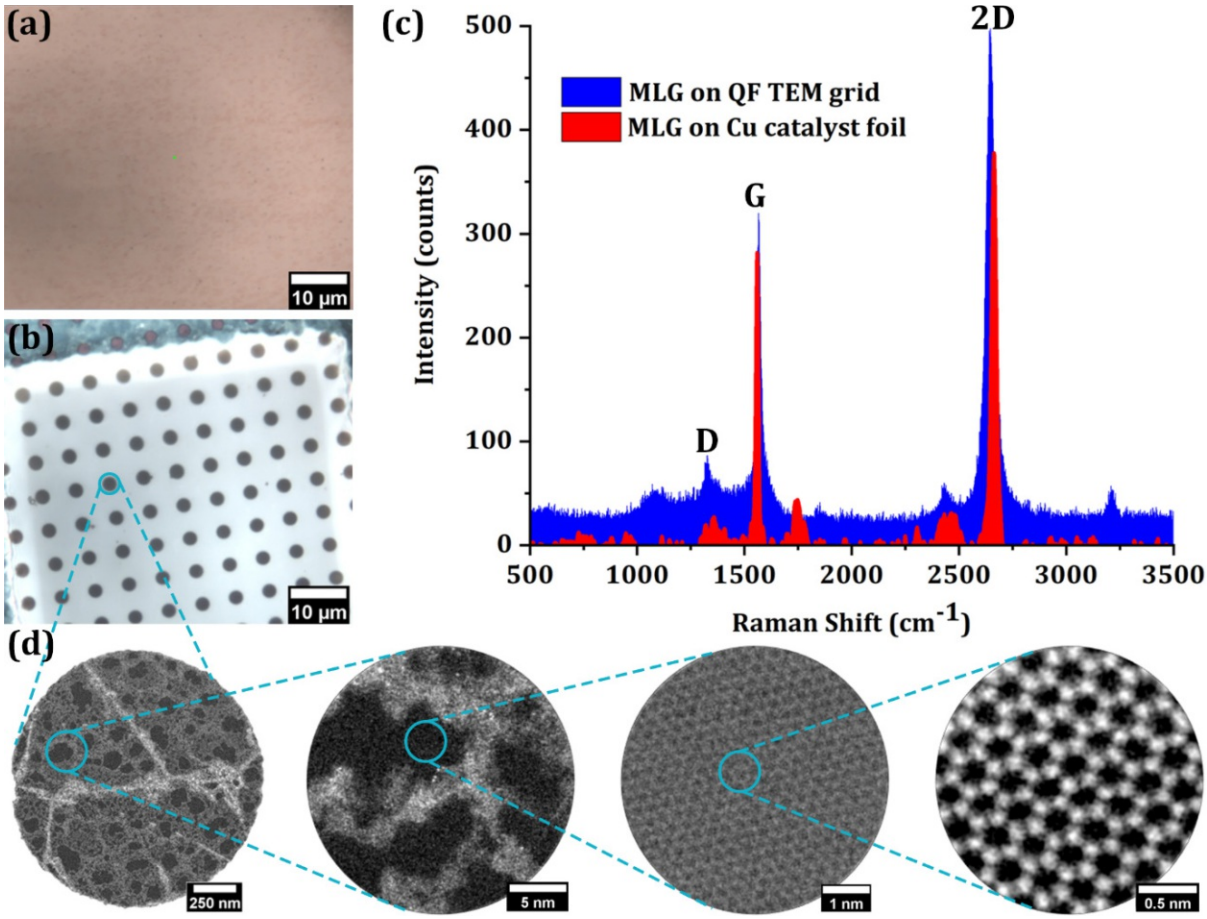

Figure 3.2: Optical image of the (a) Cu tape with CVD grown MLG, (b) QF TEM grids with MLG. (c) Raman spectrum acquired on (a) and (b). (d) shows a series of ADF images acquired in aberration-corrected STEM in increasing magnification to resolve the high quality MLG on the QF TEM grids.

For the part of this thesis dealing with the liquid phase exfoliation (LPE)[5] studies, the solvents (namely: Water (H_2O), methanol (MeOH), isopropanol (IPA), ethanol (EtOH) and

Die approbierte gedruckte Originalversion dieser Dissertation ist an der TU Wien Bibliothek verfügbar.
The approved original version of this doctoral thesis is available in print at TU Wien Bibliothek.

H_2O:IPA (4:1) mixture) with exfoliated flakes/nano-sheets (or the final suspension) were drop-casted onto single-crystalline Si(100) wafers with pre-grown 90nm of SiO_2 and the solvent was then allowed to evaporate at room temperature. These Si wafers with the drop-casted exfoliated flakes/ nano-sheets were then readily utilized for the Scanning Electron Microcopy (SEM), Atomic force Microscopy (AFM), X-Ray Diffraction (XRD), X-Ray Photoelectron spectroscopy (XPS), Photoluminescence (PL) and Raman measurements. For the Transmission Electron Microscopic (TEM) measurements, {including bright-field (BF-TEM), Selected Area Electron Diffraction (SAED) and Energy Dispersive X-Ray spectroscopy (EDS)} the exfoliated solutions were drop-casted on the lacey carbon TEM grids.

"Substrates employed for the PVD of Sb and Bi included monolayer graphene supported on its Cu catalyst foils and suspended on Quantifoil TEM grids. Raman and ADF images indicated the high quality of monolayer graphene employed as a substrate. For LPE, samples were drop-casted on Si wafers and lacey carbon TEM grids"

3.2 Deposition/ Growth Methods

3.2.1 Physical Vapor Deposition

Physical Vapor Deposition (PVD) of antimony and bismuth on monolayer graphene-based substrates (QF TEM grids as well as Cu tapes with CVD grown monolayer Graphene) employed a commercial thermal evaporation system (MANTIS deposition system QUBE series, see Figure 3.3) with a base pressure of 4×10^{-5} mbar. For PVD, Sb powder (Goodfellow, 99.999% purity, maximum particle size 150 µm) and Bi powder (Goodfellow, 99.999% purity, maximum particle size 150 µm) (see Figure 3.6) were loaded into a Tungsten boat, which was heated resistively to sublime the Sb and Bi powders. Phase diagrams of W and Sb[6] as well as Bi and W[7] were cross-checked to ensure that no undesired intermetallics were formed during evaporation under the implemented experimental conditions. Samples were loaded upside down over the evaporation source and were placed behind a manual shutter. The sample table was

Die approbierte gedruckte Originalversion dieser Dissertation ist an der TU Wien Bibliothek verfügbar.
The approved original version of this doctoral thesis is available in print at TU Wien Bibliothek.
TU Bibliothek Your knowledge hub WIEN

electrically heated to a desired substrate temperature, where primarily three set of temperatures namely: RT (i.e. non-heated), 150 °C and 250 °C were employed in this study. The Sb and Bi evaporation flux and thus their nominally deposited thickness was monitored *in-situ* using a non-heated Quartz Crystal Microbalance (QMB).

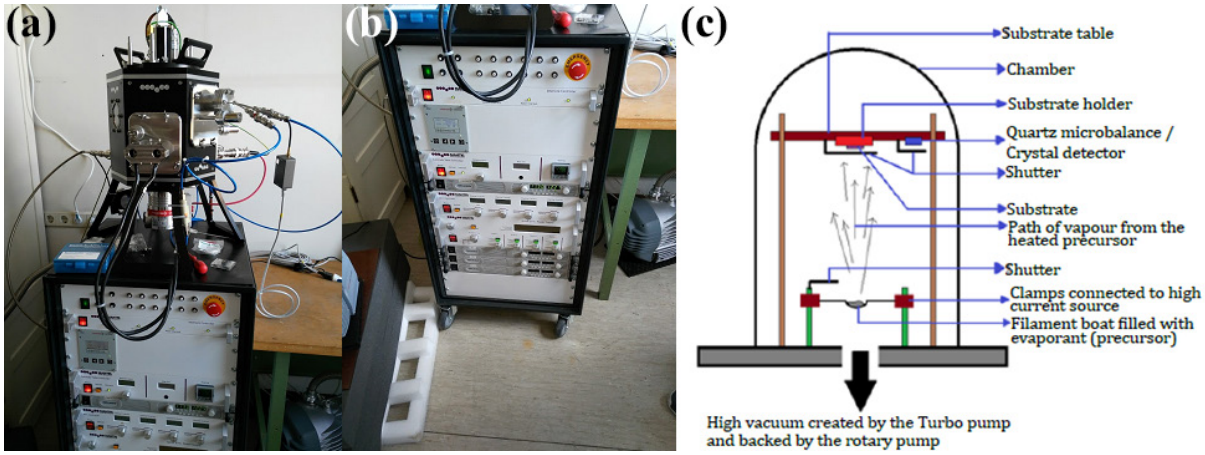

Figure 3.3: The MANTIS deposition system (QUBE series) employed for the PVD of Sb and Bi. (a) chamber and (b) the user control module placed below the deposition chamber. The schematic of the thermal evaporation (c) with all the labelled components.

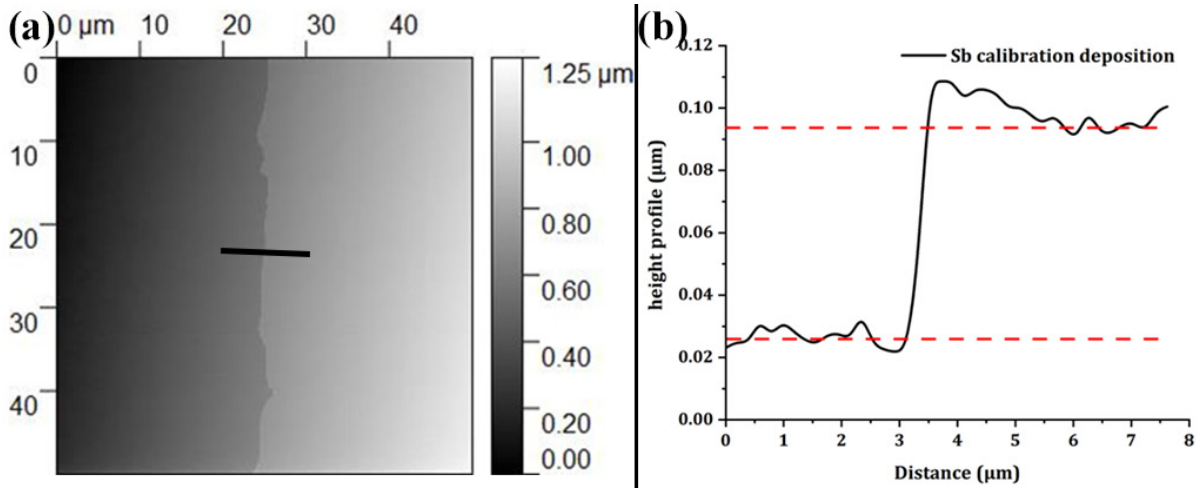

Figure 3.4: (a) The AFM image of the 70nm Sb deposited on Si wafer (with pre-grown 90nm SiO_2). (b) height profile measured across the edge of the deposited Sb film showing the obtained thickness of the Sb film measured via AFM to be same as the thickness displayed by the QMB during *in-situ* deposition of Sb on the Si wafer. This provided a tooling factor of 1 for Sb deposition thickness monitoring via quartz crystal microbalance implying that the thickness displayed during the PVD of Sb is actually the thickness of the Sb deposits but this generally holds true for the depositions at room temperature. See chapter 4 and 5 for more details.

The nominal Sb and Bi thickness QMB measurement was calibrated by evaporation of selected Sb and Bi films over partially masked Si wafers ("thickness monitors") at room

Die approbierte gedruckte Originalversion dieser Dissertation ist an der TU Wien Bibliothek verfügbar.
The approved original version of this doctoral thesis is available in print at TU Wien Bibliothek.
TU Bibliothek Your knowledge hub WIEN

temperature to measure Sb and Bi film thickness over film edges by AFM. Note that the nominal thicknesses quoted for the Sb and Bi throughout this thesis refers to the measured thickness values obtained from the non-heated QMB and from the Si wafer calibration depositions at RT. A typical calibration study for the Sb PVD has been presented in Figure 3.4, where the AFM data has been presented for the 70 nm Sb which was test deposited for the calibration studies on the partially masked wafer. The edge of the Sb film deposited can be clearly seen in the AFM image in Figure 3.4. The thickness of the deposited film via AFM measurements was found to be exactly same as the thickness monitored via QMB during the Sb PVD.

As will be discussed in detail later in Chapters 4 and 5, where in-depth studies on the exploration of the parameter space of Sb and Bi PVD on monolayer graphene (supported on Cu tapes as well as suspended on QF TEM grids) have been provided, actual retained thicknesses of Sb and Bi on the substrate (monolayer graphene) could strongly vary as a function of increasing substrate temperature and also on type of direct support underneath the substrate via desorption effects.

3.2.2 Liquid Phase Exfoliation

For the liquid phase exfoliation of Bi, a one-step Sonication + Centrifugation assisted recipe was implemented. The sonication of Bi powder (Goodfellow, 99.999% purity, maximum particle size of 150 µm) (Figure 3.6) employed a commercial ultra-sonic bath system (SONOREX DIGITEC DT255 H-RC ultrasonic bath manufactured by BANDELIN Electronic GmbH & Co. KG) with an operating ultrasonic frequency of 35 kHz and ultrasonic nominal power of 160 W. Five different solvents were tested for their efficacy towards sonication of bismuth powder, namely: Water (H_2O), methanol (MeOH), isopropanol (IPA), ethanol (EtOH) and IPA:H_2O (4:1) mixture. All the five chemicals used were technical grade and were used without any further processing. Sonication was carried out for 15hrs. Centrifugation was carried out at a commercial laboratory centrifuge (Model 1-6P, manufactured by SIGMA laborzentrifugen GmbH) at the maximum speed of 5630 rpm for 20 mins. Handheld digital thermometer [Model HH11B series, single input, Type-K (Chromium-Alum) thermocouple with an accuracy of ± (0.1%

Die approbierte gedruckte Originalversion dieser Dissertation ist an der TU Wien Bibliothek verfügbar.
The approved original version of this doctoral thesis is available in print at TU Wien Bibliothek.
TU Bibliothek WIEN Your knowledge hub

reading + 1 °C) manufactured by OMEGA Engineering GmbH] was employed for the regular monitoring of the temperature to carry out the sonication process strictly within the permissible limits of the temperature range required.

Liquid phase exfoliation of bismuth was carried out at two different environments: at room temperature and at ice-cold temperature (to note here is that the temperatures (RT and ICE) could only be maintained for the process of sonication) to investigate the effect of temperature in addition to the effect of the sonication process. The room temperature sonication was carried out at temperatures maintained strictly between 22 °C to 26 °C, whereas during the ice sonication procedure, the temperature was strictly maintained between 0.1 °C to 2.2 °C. The temperature was regularly monitored with the help of a digital thermometer. The initial starting concentration was chosen to be 4 mg mL^{-1}, where 60 mg of 5N grade Bi Powder was dispersed in 15 mL of 5 different solvents namely: water (H_2O), methanol (MeOH), isopropanol (IPA), ethanol (EtOH) and IPA:H_2O (4:1).

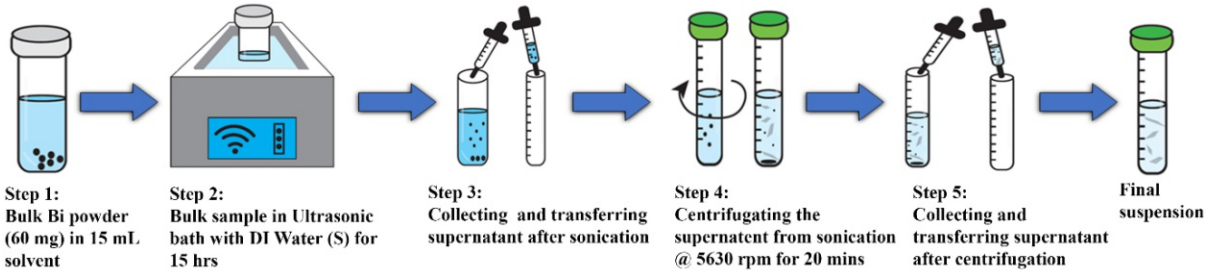

Figure 3.5: Schematic diagram of the synthesis methodology including ultrasonication and centrifugation steps.

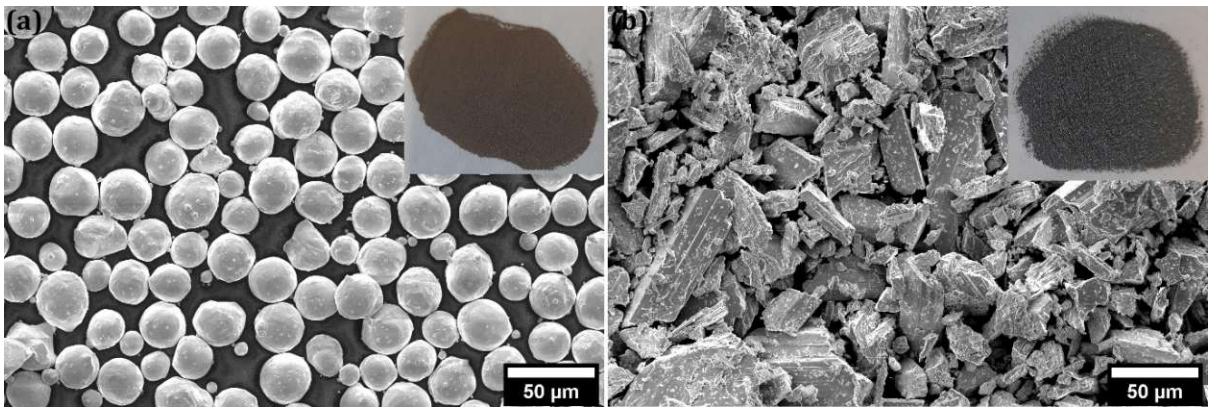

Figure 3.6: The initial starting bulk materials for the PVD as well as LPE deposition / growth schemes. (a) bulk Bi powder (b) bulk Sb powder. The inset shows the optical appearance of the respective bulk powders.

Die approbierte gedruckte Originalversion dieser Dissertation ist an der TU Wien Bibliothek verfügbar.
The approved original version of this doctoral thesis is available in print at TU Wien Bibliothek.
TU Bibliothek Your knowledge hub WIEN

Sonication process was carried out for 15 hrs. After the process of sonication, the supernatant was immediately and carefully collected and transferred to the fresh centrifuge tubes without disturbing the sediment. From the initial 15 mL volume of the solution used for the sonication, an approximate volume of 10 mL was safely collected for the next step of centrifugation. Centrifugation was only done once since the second centrifugation step was found to considerably damage the samples in terms of flake size and distribution as discussed in detail in chapter 6. After the centrifugation, again the supernatant was immediately and carefully separated without disturbing the sediment and transferred to a separate tube. From the initial 10 mL volume of the sonicated sample used for centrifugation, approximately 7.5 mL volume of supernatant was safely recovered after centrifugation. It was this volume of the supernatant (after sonication and centrifugation) that was further utilized for testing its potential towards photocatalysis and is referred to as exfoliated flake/nano-sheets. The schematic of the overall exfoliation process is described in Figure 3.5

"PVD technique of thermal evaporation was employed for the growth of few layered antimonene and bismuthene on monolayer graphene supported on polycrystalline Cu catalyst tapes and suspended on Quantifoil TEM grids. Wet chemical route of liquid phase exfoliation was employed to obtain thin flakes/nano-sheets of bismutite. The efficacy of five different solvents (Water (H_2O), methanol (MeOH), isopropanol (IPA), ethanol (EtOH) and H_2O:IPA (4:1) mixture) in LPE was tested."

3.3 Characterization Tools

3.3.1 Transmission Electron Microscopy

The bright field and dark field imaging, diffraction measurements and associated spectroscopic measurements involving energy dispersive X-ray spectroscopy (EDS) and Electron Energy Loss Spectroscopy (EELS) were performed on FEI TECNAI F20 transmission electron microscope, a facility at USTEM, TU Wien, Vienna. The qualitative and quantitative elemental analysis was done with the help of EDS with EDAX Apollo

Die approbierte gedruckte Originalversion dieser Dissertation ist an der TU Wien Bibliothek verfügbar.
The approved original version of this doctoral thesis is available in print at TU Wien Bibliothek.
TU Bibliothek WIEN Your knowledge hub

XLTW SDD system equipped at the FEI TECNAI F20, which is a window less version of a Peltier cooled silicon drift detector for enhanced performance towards lighter elements. The spectroscopic measurements involving EELS were carried out using GIF Tridiem post column energy filter equipped at FEI TECNAI F20. Bright/ dark field images (tilted and non-tilted) as well as diffraction patterns (tilted and non-tilted) were captured with the help of GATAN Rio16, a bottom mount CMOS camera attached on the FEI TECNAI F20 TEM. For all the measurements including imaging, diffraction and spectroscopy, the TEM was operated at 60 kV, since imaging under the electrons with energy ≥ 80 keV has been found to induce structural changes in pristine graphene, including also its point defects, grain boundaries and dislocations via the phenomenon of beam induced knock-on damage as already highlighted by prior studies[8–11]. Visualizing the Fourier Transform (FT) patterns on the high-resolution images as well as the basic processing of the images in terms of additional contrast/ brightness adjustment, scaling etc. was carried out with the help of ImageJ[12] and Gatan™ DigitalMicrograph[13] software packages wherever required, for all the microscopic images obtained via TEM, scanning electron microscope (SEM) and (S)TEM.

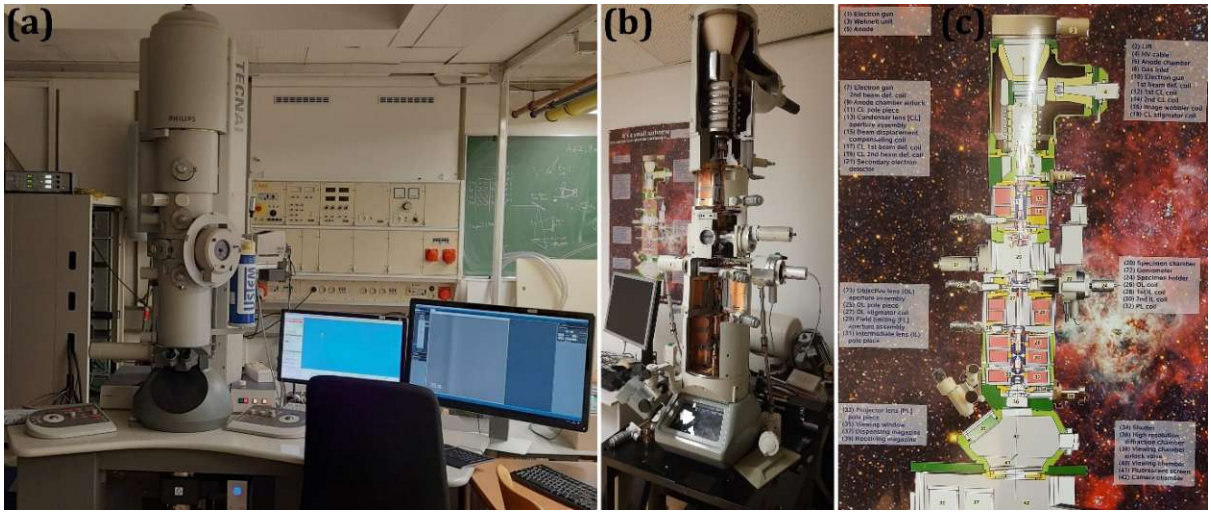

Figure 3.7: (a)FEI TECNAI F20 transmission electron microscope facility at USTEM, TU Wien utilized for all the imaging (BF, DF and diffraction) and spectroscopic studies (EELS).(b) Cross sectionally cut TEM. (c) All the components of TEM (labelled). (courtesy: USTEM, TU Wien, Vienna.)

The basic working principle of a transmission electron microscope[14] is the same as that of a light or an optical microscope except the fact that in a light microscope we use light for imaging the sample, on the other hand in an electron microscope (whether

Die approbierte gedruckte Originalversion dieser Dissertation ist an der TU Wien Bibliothek verfügbar.
The approved original version of this doctoral thesis is available in print at TU Wien Bibliothek.
TU Bibliothek Your knowledge hub WIEN

Transmission, Scanning or (Scanning) Transmission), electron beam is used to image material of interest. Since the light microscope primarily uses the visible light which has a fixed range of wavelength (and hence fixed energy), the resolution of a light microscope is limited and low whereas in an electron microscope the possibility of accelerating the electrons to variable energy offers the advantage of providing atomic-scale resolution, given the fact that the wavelength of electrons is much smaller than light.

The TECNAI F20 FEG-TEM employed had a Schottky-type electron gun with tungsten tip (cathode) emitter. The electrons ejected from the emitter are then focused by a set of electromagnetic lenses which are Cu windings having current running through them. The current carrying Cu windings create a magnetic field and thereby enabling the functionality of the whole entity as an electromagnetic lens. Several sets of lenses focus the electrons to be parallel to the optic axis which is then passed through the sample. An important pre-requisite for the samples to be successfully investigated in a TEM is that they have to be thin enough to be electron beam transparent. The TEM's are high vacuum devices where the sample sits inside the vacuum column having typical pressures in the range of 10^{-7} mbar to maximize the mean free path of the electrons. This is further complemented by a cold trap (cooled by liquid nitrogen) to trap the residual gases or any contaminants. The beam after passing through the sample picks up the image and this image is further magnified by a set of projector lenses sitting below the sample. The image of the sample is made observable when the electron beam hits the fluorescent screen. This screen is also a junction between the column and the camera. The screen has to be lifted so that the image of the sample can reach the camera for the final image of the specimen to be recorded/acquired. The TEM also houses a set of apertures namely condenser aperture, objective aperture and SAED aperture whose roles are to adjust the intensity of the electron beam, adjusting the contrast of the image and for recording the diffraction patterns respectively[14].

Figure 3.7 shows the image of the FEI TECNAI F20 (a) employed for all the TEM studies reported in this thesis. A picture of the cross-sectionally cut TEM (b) is attached with all the components labelled (c) to provide a better understanding of the insides of a transmission electron microscope in general. Both the instruments in the Figure 3.7 including the labelling chart are the facility at USTEM, TU Wien, Vienna.

Die approbierte gedruckte Originalversion dieser Dissertation ist an der TU Wien Bibliothek verfügbar.
The approved original version of this doctoral thesis is available in print at TU Wien Bibliothek.
TU Bibliothek Your knowledge hub WIEN

"FEI TECNAI F20 TEM was mainly utilized for all the BF images presented in this thesis (including high-resolution images). TEM was extensively utilized for the evaluation of the epitaxial relationships in Sb/graphene and Bi/graphene systems via Fourier transform (FT) on high resolution TEM images as well as via diffraction patterns. Fourier transform of high- resolution images and diffraction patterns were used for the phase analysis."

3.3.2 Scanning Electron Microscopy

The SEM utilized for all the respective studies presented in this thesis was FEI Quanta 250 FEG, a facility at USTEM, TU Wien, Vienna. The SEM was primarily utilized for the imaging as well as for energy dispersive x-ray spectroscopic studies for compositional analysis. EDAX studies were carried out via EDAX SDD Octane Elite 55 detector with Si_3N_4 window. The Everhart-Thornley secondary electron detector employed in the SEM provided the images of the sample. An acceleration voltage of 10 kV was employed for imaging conditions while the choice of the acceleration voltage for the EDS was made as per the elements to be identified.

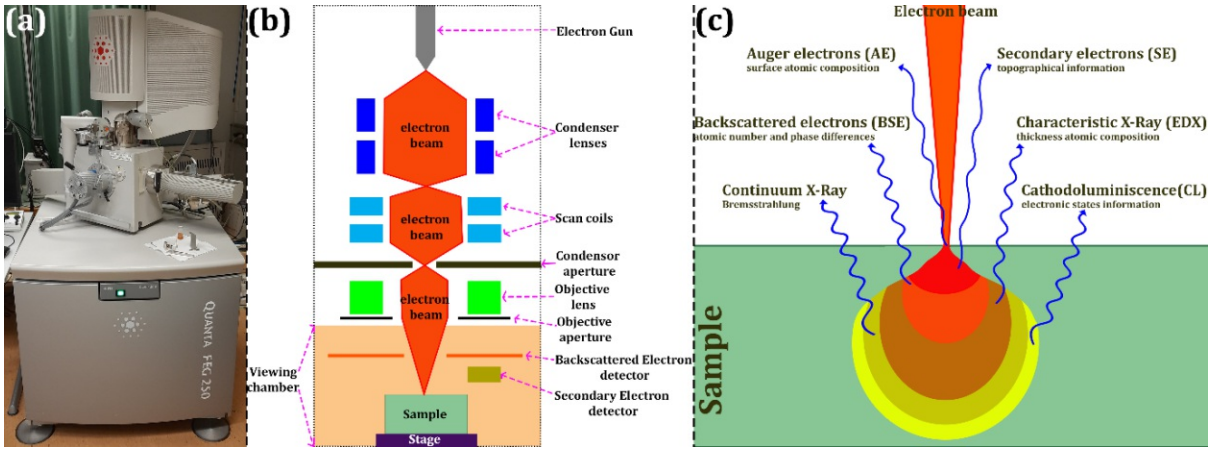

Figure 3.8: Picture of (a)FEI Quanta 250 FEG scanning electron microscope facility at USTEM, TU Wien utilized for the secondary electron imaging as well as EDS studies. The schematic of SEM showing the labelled components of an SEM (b) and (c) shows the interaction of electron beam with the sample.

Figure 3.8 shows the picture of the SEM (a) utilized for any SEM-related study reported in this work along with the schematic showing different parts of an SEM (b) and the

Die approbierte gedruckte Originalversion dieser Dissertation ist an der TU Wien Bibliothek verfügbar.
The approved original version of this doctoral thesis is available in print at TU Wien Bibliothek.
TU Bibliothek Your knowledge hub WIEN

electron beam-sample interaction (c). What differentiates an SEM from TEM is the mode of operation[15]. While for TEM, an electron transparent sample was the pre-requisite, there is no such thickness-based restrictions on the samples to be investigated under an SEM. This makes the microscope structure completely different for a SEM as compared to the TEM especially for the part after the sample. Since the electron beam does not passes through the sample the SEM is only limited only till the sample chamber starting from the electron gun in terms of its design. The electron beam is focused onto the sample surface with the help of electromagnetic lenses (akin to that in a TEM). Now another set of lenses (along with scan coils) direct the electron beam from side to side in order to scan the sample (these lenses are analogues to the projector lens which magnify the image in a TEM). On account of interaction of the electron beam with the sample, secondary electrons are produced. These electrons are the electrons from the sample spurred by the incident electron of the beam. These secondary electrons are collected by the secondary electron detector which are then translated to the image giving information about the topology of the sample. The sample here is also kept in vacuum with pressure values ~ 10^{-6} mbar to maximize the electron mean free path and reduce the scattering of electrons from the ambient gases in the sample chamber[15].

3.3.3 Energy Dispersive X-ray Spectroscopy

As already described in Figure 3.8c, regarding the interaction of the electron beam with the sample, characteristic X-rays are also generated among the different emissions produced. These X-rays are produced when an inner electron in the atom of the specimen is knocked off from its shell by the electron beam. This vacancy of the inner electron is ultimately filled by the electron from the outer shell. This transition from outer higher energy shell to inner lower energy shell results in release of energy (the energy difference) in the form of X-rays, which are called as characteristic X-rays. The energy of these X-rays is unique to the transition and specific element and hence can provide information on the elemental composition of the sample under investigation.

The EDS detector comprises a crystal (Si) which absorbs the incoming X-rays (a collimator helps in capturing X-rays only from the illuminated area of the sample), these

Die approbierte gedruckte Originalversion dieser Dissertation ist an der TU Wien Bibliothek verfügbar.
The approved original version of this doctoral thesis is available in print at TU Wien Bibliothek.
TU Bibliothek Your knowledge hub WIEN

absorbed X-rays are then converted into charge which is further converted into voltage signal by a preamplifier. These voltage signals are then passed onto a pulse processor which after measuring the voltage signals passes them to an analyzer subunit for the display of the data. EDS can help in quantitative as well as qualitative elemental analysis of the samples[14]. A typical EDX spectrum has been shown in Figure 3.9.

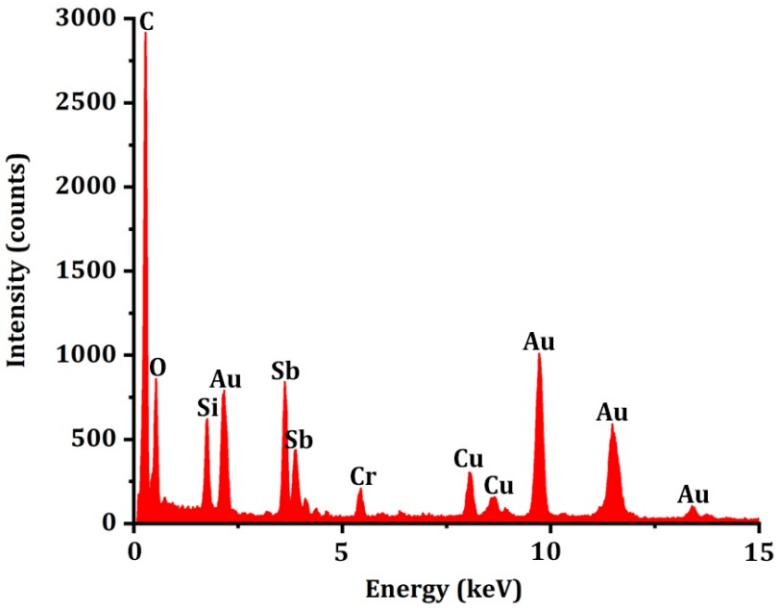

Figure 3.9: A typical EDX spectrum

"FEI Quanta 250 FEG SEM was mainly utilized for secondary electron imaging as well as for energy dispersive x-ray spectroscopic studies on the samples. Correlative AFM-SEM studies were carried out in a different SEM (FEI Quanta 600F SEM) by installing a GETec AFSEM module inside the specimen chamber"

3.3.4 Raman Spectroscopy

All the Raman spectroscopic measurements presented in this thesis were carried out using HORIBA LabRAM 800HR Raman Spectrometer, a facility under the research group of Process Analytics at Institute of Chemical Technologies and Analytics, TU Wien, Vienna (see Figure 3.10). Every Raman measurement carried out employed a green laser having wavelength of 532 nm and power ~ 54.25 mW. Complete care was taken to use the laser intensity sufficient enough to provide good signal to noise ratio without causing any

Die approbierte gedruckte Originalversion dieser Dissertation ist an der TU Wien Bibliothek verfügbar.
The approved original version of this doctoral thesis is available in print at TU Wien Bibliothek.
TU Bibliothek Your knowledge hub WIEN

visible damage to the samples. Choice of the type of filter (notch or edge) and therefore the spacer was made depending on the position of the Raman active modes of the sample under investigation and the same has been described in chapters 4-6. An objective lens of 100x was employed to focus the light onto the sample as well as to collect the scattered light. Generally, a diffraction grating of 1800/mm was used to obtain well resolved Raman modes from the sample in the spectrum.

Figure 3.10: HORIBA LabRAM 800 HR dispersive Raman microscope (facility at Institute of Chemical Technologies and Analytics (research group of process analytics), TU Wien, Vienna) utilized for the Raman spectroscopic studies on all the samples investigated in this thesis.

Any spectroscopy, in general, refers to the study of the interaction of electromagnetic radiation with matter. While there are many diverse types of spectroscopic techniques devoted for studying various particular phenomena, the name of the spectroscopic technique is generally after the part of the electromagnetic radiation spectrum used or the typical exploited interaction phenomena. Raman spectroscopy[16] is a vibrational spectroscopic technique which is based on the inelastic scattering of the light upon interaction with the matter. While the majority of the incident photons are scattered elastically (following the principle of conservation of energy and momentum i.e. the scattered photon has the same energy or wavelength as the incident photon, a phenomenon called as Rayleigh scattering) upon interacting with the matter (specimen),

Die approbierte gedruckte Originalversion dieser Dissertation ist an der TU Wien Bibliothek verfügbar.
The approved original version of this doctoral thesis is available in print at TU Wien Bibliothek.
TU Bibliothek Your knowledge hub WIEN

a small fraction of the incident photons is inelastically scattered (approximately ~ 1 in 10^6) which also makes Raman scattering a very weak process. It is these inelastically scattered photons which provide a wealth of information sufficient enough to chemically fingerprint the sample (matter) under investigation[16,17].

The inelastic scattering occurs via two ways: anti-Stokes scattering (when the scattered photon has higher energy or lower wavelength than the incident photon) and Stokes scattering (when the scattered photon has lower energy or higher wavelength than the incident photon).

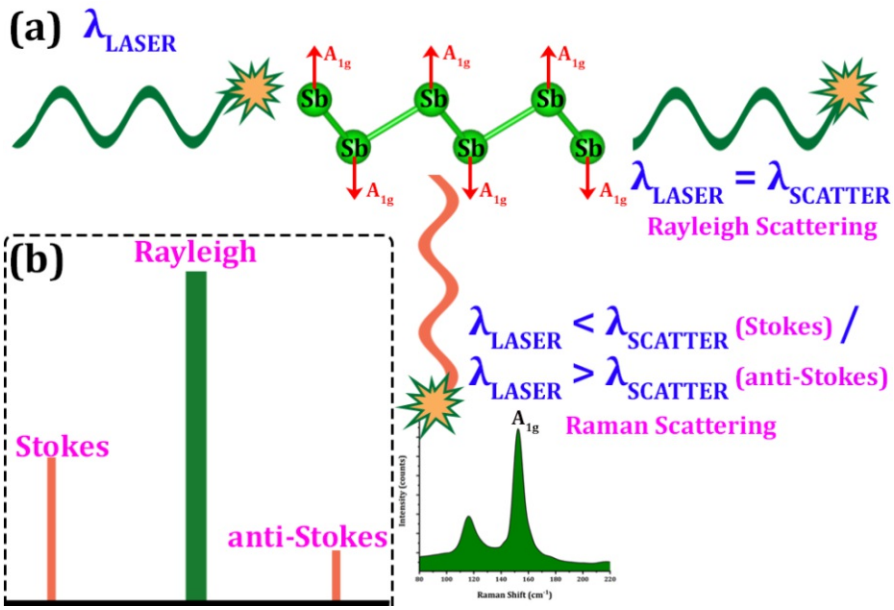

Figure 3.11: (a) A pictorial representation of the principle of the Raman spectroscopy depicted by incident laser light on the antimony atoms exhibiting A_{1g} mode of vibration (b) representation of the relative intensities of the elastic and inelastic scattering. (image not subject to scale)

This decrease or increase in energy of the scattered photon is related to the vibrational energy spacing in the ground electronic state of the molecule and therefore the wavenumber of the Stokes and anti-Stokes lines are a direct measure of the vibrational energies of the molecule in sample under investigation[16]. Both the anti-Stokes as well as the Stokes lines are equi-spaced from the central Rayleigh line due to the gain or loss of one vibrational quantum of energy in either case[18]. But since the intensity of the anti-Stokes line is much less as compared to the Stokes line only the more intense Stokes lines are measured in the Raman spectrum as also the case with measurements reported in this thesis.

Die approbierte gedruckte Originalversion dieser Dissertation ist an der TU Wien Bibliothek verfügbar.
The approved original version of this doctoral thesis is available in print at TU Wien Bibliothek.
TU Bibliothek Your knowledge hub WIEN

A brief pictorial representation of the working principle of the Raman spectroscopy with antimony as sample showing one of its vibrational modes (A_{1g})[19] in its monolayer form has been presented in Figure 3.11.

"Raman spectroscopic measurements were mainly carried out for chemical finger printing of the initial bulk as well as few layered samples. Another objective behind the Raman studies was to help distinguish metallic pnictogens from their oxides (if any) and to deduce the nature of oxides (whether superficial or bulk). For all the Raman measurements presented in this thesis, HORIBA LabRAM 800 HR dispersive Raman microscope was employed"

3.3.5 Electron Energy Loss Spectroscopy

Electron Energy Loss Spectroscopy or EELS[20] is a yet another analytical spectroscopy associated with a TEM. It is also used for the qualitative and quantitative compositional analysis in addition to identifying the allotropes, studying oxidation, chemical fingerprinting etc.[21] The compositional sensitivity of EELS spans from Helium to Uranium which is much higher than other techniques like EDS, XPS, Auger electron spectroscopy. In a TEM, the electron beam passing through the sample primarily emerges out in three possible ways:

1. as a direct un-scattered beam (which is used for capturing the bright field images).
2. as an elastically scattered beam (used for recording the diffraction pattern) and,
3. as an inelastically scattered beam, where the electrons in the beam encounter the change in the energy and momentum on account of their interaction with the sample. It is this change in energy (loss or gain) which provides a wealth of information about the samples[22].

A typical EELS spectrometer system, as shown in Figure 3.12a, consists of a magnetic prism in which a uniform magnetic field of around 0.01T is generated by the carefully designed pole pieces (the curved surfaces). The inelastically scattered electrons enter the spectrometer, where the magnetic field of the magnetic prism disperses them according

Die approbierte gedruckte Originalversion dieser Dissertation ist an der TU Wien Bibliothek verfügbar.
The approved original version of this doctoral thesis is available in print at TU Wien Bibliothek.
TU Bibliothek Your knowledge hub WIEN

to their kinetic energy, much analogous to the splitting of white light into VIBGYOR by a glass prism. An important consideration regarding the EELS measurement is to have thinnest sample possible to avoid background effect due to scattering in thick samples[20].

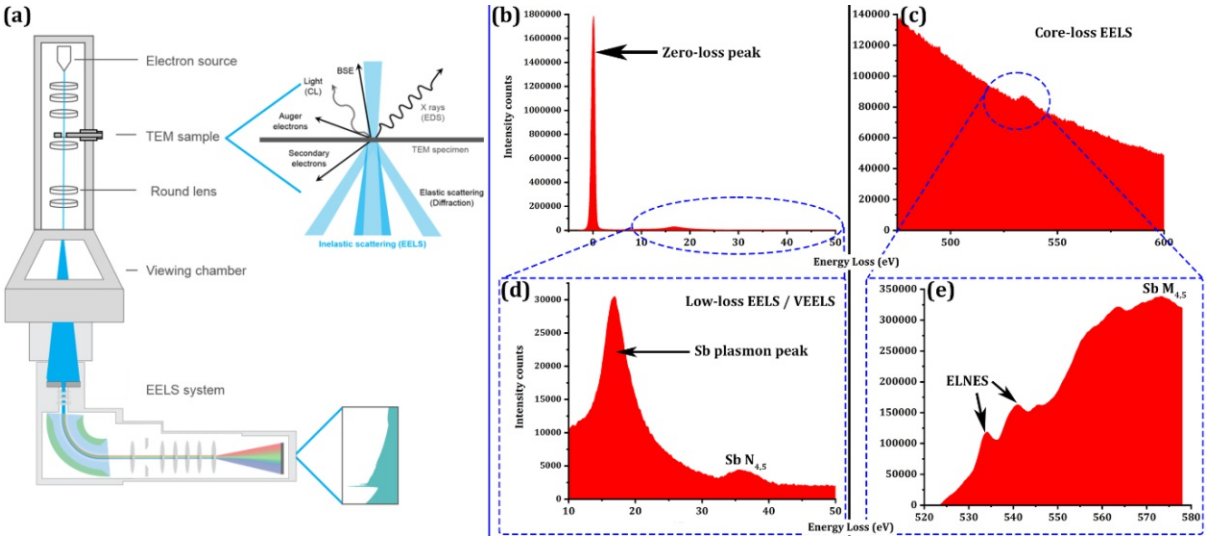

Figure 3.12: (a) EELS Instrumentation typically incorporated in a TEM which is also the case with the TEM (FEI TECNAI F20 TEM) employed for the imaging and EELS spectroscopic measurements here. ((a) is adopted from ref: 23). Different parts of a typical EELS spectrum recorded on the antimony nanostructures in one of our model systems has been presented in (b-e), where (b) shows the highly intense zero loss peak constituted by direct un-scattered electrons. (d) is a magnified version of the region next to the zero-loss peak also known as the low loss region where Sb plasmon peak and low energy Sb N-edge can be seen. (c) represents the core loss region with huge background and a little hump has been resolved in (e) after the background subtraction to clearly visualize the Sb M-edge along with the ELNES features present in the corresponding ionization edge.

EELS is the analysis of the energy distribution of the electrons that have interacted with the specimen inelastically. These in-elastic collisions tell us a tremendous amount of information about the electronic structure of the specimen atoms, which in turn reveals the details of the nature of the atoms, their bonding and the nearest neighbor distributions, their dielectric response etc. Figure 3.12b,c shows a typical EELS spectrum, which can be categorized into three principal regions of the spectrum, giving us different information about the specimen:

1. The zero-loss peak, comprising of elastically scattered electrons, defines the energy resolution and is essential in calibrating the spectrum.
2. The low loss region up to an energy loss of 50 eV contains electrons which have interacted with the weakly bound outer shell electrons of the atoms in the

Die approbierte gedruckte Originalversion dieser Dissertation ist an der TU Wien Bibliothek verfügbar.
The approved original version of this doctoral thesis is available in print at TU Wien Bibliothek.
TU Bibliothek Your knowledge hub WIEN

specimen. This part of the spectrum contains information about the electronic properties of the specimen.

3. The core-loss region comprises of electrons that interact with the more tightly bound inner-shell or the core electrons. This part of the spectrum therefore contains the characteristic information of the atoms in the specimen.

The excitation of atomic inner shells facilitates the study of unoccupied conduction states in the sample. This excitation requires an amount of energy which is a function of specific electron shell of a specific atom and hence is uniquely determined. These distinctive signals in the core-loss region are therefore known as "atomic ionization edges". Named by the initial state, the atomic ionization edges are used for the elemental fingerprinting[24]. During the process of ionization, after providing sufficient energy to electrons to escape nucleus attraction some electrons might move to higher empty energy levels instead of escaping completely. Energy distribution due to influence of its neighbors on an atom govern these unfilled energy levels. This is reflected by the intensity fluctuations in ionization edge are termed ELNES (Energy Loss Near Edge Structures, as shown in Figure 3.12e) which can give information on bonding state of ionized atom[25]. For the studies concluded in this thesis, EELS applicability was two-fold:

1. For outlining the presence of superficial surface oxidation in the case of antimonene/graphene heterostructures, where simultaneous help of core-loss as well as low-loss spectrum was taken to show the good oxidation stability of antimonene/graphene heterostructures. (see chapter 4 for details)
2. For delineating the associated property change during in-situ crystallization of Bi nanoparticles on graphene. Real time VEELS was performed. (see chapter 5 for details.)

"EELS studies helped disentangling superficial surface oxidation in the case of antimonene on graphene, thus outlining their good oxidation resilience towards environmental oxidation. For this both low-loss as well as core-loss regions of the EELS spectrum were investigated. In a yet another study involving in-situ crystallization of the bismuthene nanostructures on graphene, EELS experiments helped in suggesting a

Die approbierte gedruckte Originalversion dieser Dissertation ist an der TU Wien Bibliothek verfügbar.
The approved original version of this doctoral thesis is available in print at TU Wien Bibliothek.
TU WIEN Bibliothek Your knowledge hub

possible structure-property correlation occurring during crystallization phenomena. For this real time EELS measurements were performed"

3.3.6 Photocatalytic Hydrogen Evolution Reaction

For a typical photocatalytic HER experiment, 7.5 mg of the photo-catalyst (TiO_2) was first dispersed into 15 mL DIW and was then subjected to 3 min sonication. After sonication, the reaction mixture was transferred to the custom-made flow reactor (see Figure: 3.13) under constant stirring. To this reaction mixture 15 mL of the exfoliated solutions were mixed. To note here is that since most of the solvents used for the exfoliation were alcohols, the whole suspension (exfoliated flakes /nano-sheets in solvents) was utilized for the role of sacrificial agent (alcohol) as well as for the co-catalyst (exfoliated flakes /nano-sheets). For the case of the exfoliated flakes /nano-sheets in DIW, the 7.5 mg of photo-catalyst was dispersed in 15 mL HPLC-grade methanol and the solution of exfoliated flakes /nano-sheets in DIW was used as it is. This suspension of photo-catalyst solution and solution of exfoliated flakes /nano-sheets (total volume 30 mL) was then purged with Ar flow to eliminate the dissolved oxygen and also to ensure the proper mixing of the two different solutions of the photo-catalyst and the co-catalyst. Afterwards, the reactor was closed.

During light irradiation, the reactant solution was kept under constant stirring at speed of 250 rpm under a constant Ar (argon 5.0) flow of 30 mL / min controlled by a mass flow controller (Q-flow 140 series, MCC-Instruments) carrying all the gases from the reactor to the gas detector after passing through $CaCl_2$ trap (model WT 20.5 N, SUN-Control-Analytik GmbH) to avoid water impurities entering the X-stream gas analyzer. Hydrogen generation was detected online and in-stream using Emerson gas analyzer equipped with a TCD (thermal conductivity detector). The light source used was a 4 W output power LED (SOLIS-365C by THORLABS, Inc.), which can provide irradiation with a nominal wavelength of 365 nm. The reactors were placed in a black box to avoid the environmental influences.

Die approbierte gedruckte Originalversion dieser Dissertation ist an der TU Wien Bibliothek verfügbar.
The approved original version of this doctoral thesis is available in print at TU Wien Bibliothek.
TU Bibliothek Your knowledge hub WIEN

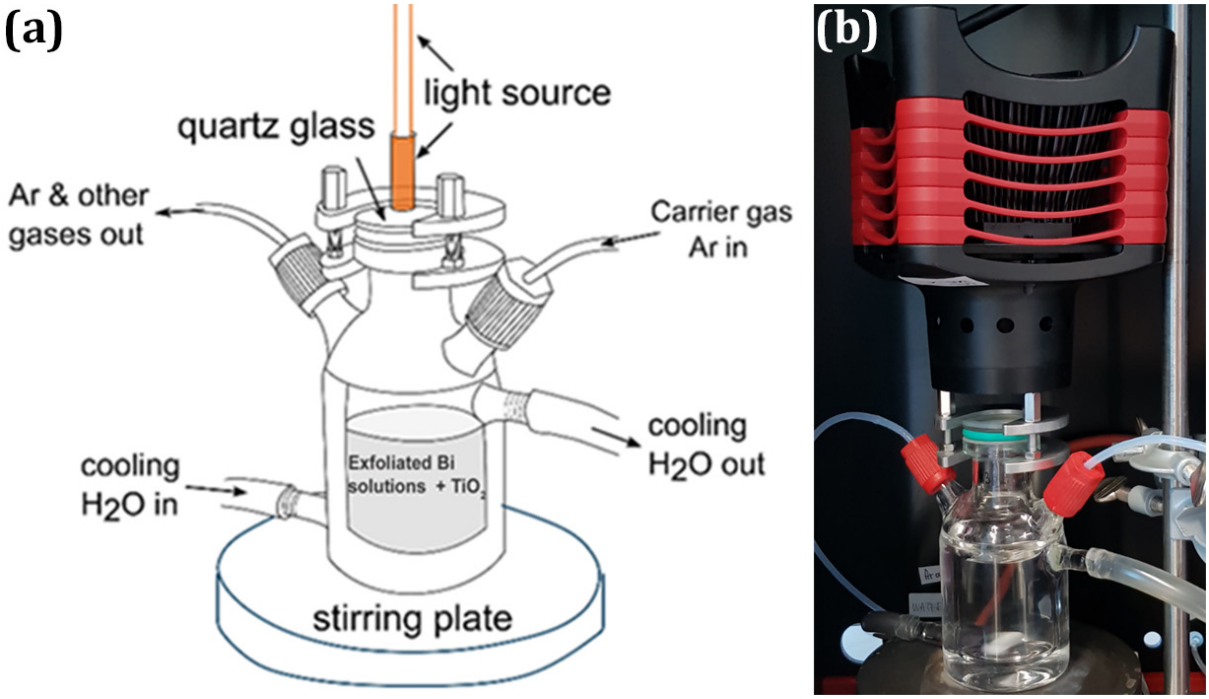

Figure 3.13: (a) Drawing scheme of the reactor utilized for evaluating the photocatalytic performance of the liquid phase exfoliated Bi solutions in response to hydrogen evolution via water splitting (adapted from ref: 26) (b) actual reaction setup

The light source, SOLIS LED (λ = 365 nm) was directed via cable and made to irradiate from the top of the reactor. The top cap of the reactor was made of quartz. The total volume of the reactor is about 100 mL, a typical volume of 30 mL reactant solution (15 mL of the exfoliated solution + 15 mL of TiO_2 (7.5 mg) solution in solvent (DIW / MeOH)) was placed inside. The measurements were repeated once to ensure the repeatability of the overall process.

The samples which showed positive response towards photocatalysis were further subjected to TEM characterization in their suspension form to investigate the immobilization mechanisms of the co-catalyst over the photo-catalyst to account for the observed HER. A scheme of the overall photocatalytic experiment assembly has been shown in Figure 3.14.

Die approbierte gedruckte Originalversion dieser Dissertation ist an der TU Wien Bibliothek verfügbar.
The approved original version of this doctoral thesis is available in print at TU Wien Bibliothek.
TU Bibliothek Your knowledge hub WIEN

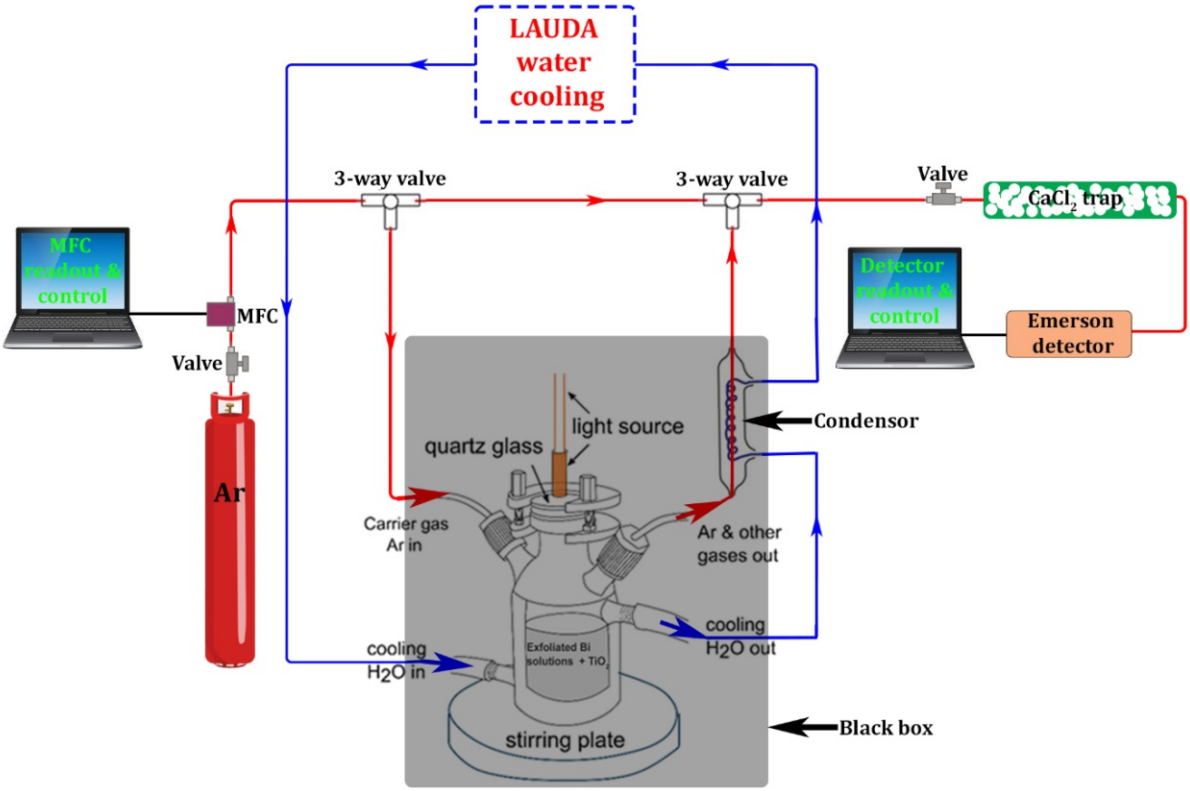

Figure 3.14: Schematic illustration of the overall experiment setup for carrying out the photocatalytic water splitting reactions.

"Photocatalytic experiments were performed by mixing the exfoliated solutions obtained via LPE of Bi with TiO_2 and were carried out in a flow reactor. TiO_2 was employed as photocatalyst and exfoliated flakes / nano-sheets were utilized as co-catalyst. This was principally performed to show the advantageous application prospects of the exfoliated flakes/ nano-sheets in the catalysis domain. Their positive response towards photocatalysis provides an extra-edge to the exfoliated flakes/ nano-sheets in addition to their ultra-large and thin lateral sizes obtained by the adopted LPE protocol"

3.3.7 Scanning Transmission Electron Microscopy

The Scanning Transmission Electron Microscope or (S)TEM differs from the traditional Transmission Electron Microscope (TEM) in its way of addressing the sample. While a conventional TEM exploits a near-parallel electron beam which passes though the

Die approbierte gedruckte Originalversion dieser Dissertation ist an der TU Wien Bibliothek verfügbar.
The approved original version of this doctoral thesis is available in print at TU Wien Bibliothek.
TU Bibliothek Your knowledge hub WIEN

sample. In STEM, a convergent fine focused beam is deployed which is scanned across the specimen surface in raster fashion providing unprecedented insights about the specimen at the atomic scale. Probe of atomic dimension is the key to high resolution STEM which is principally governed by the electron optics of the microscope[27]. The diameter of the probe determines the resolution of the scanned image. Additionally, the incorporation of aberration correctors have significantly improved the performance of STEMs[28] by improving depth of focus and signal-to-noise ratio in annular dark field (ADF) images[29].

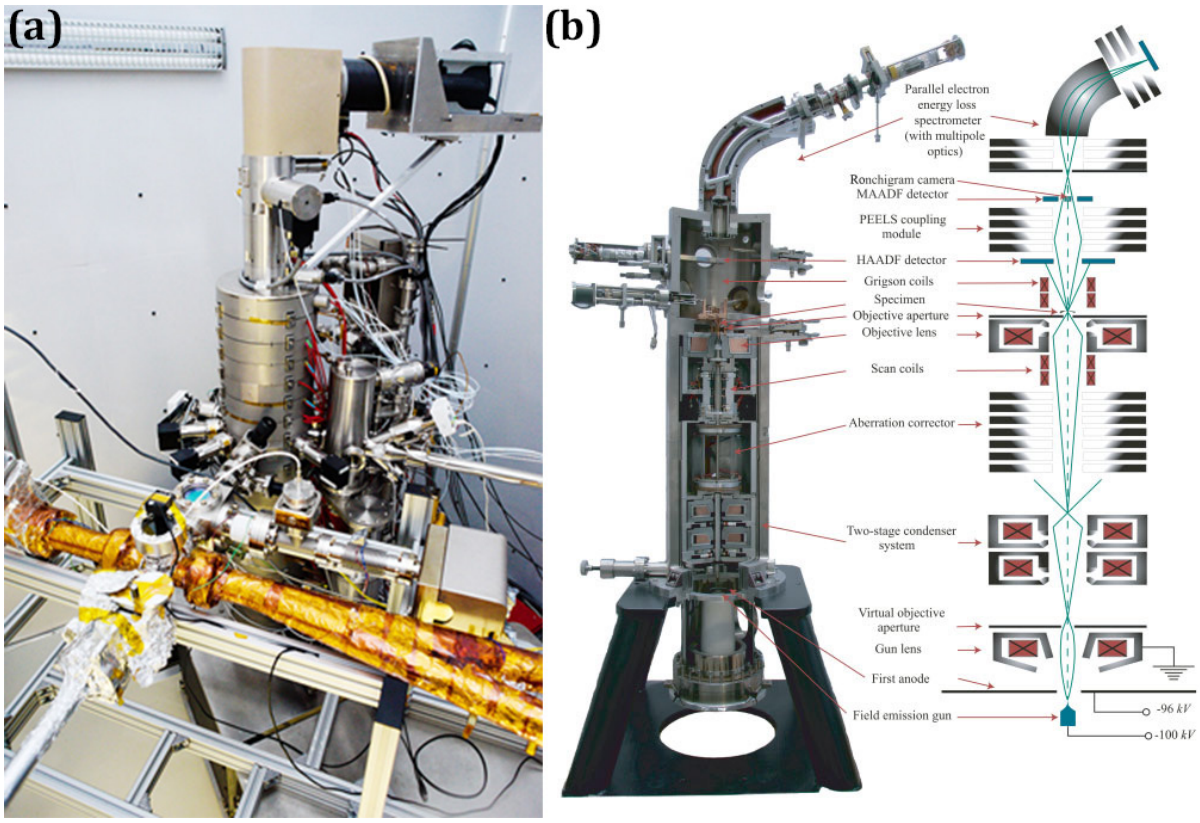

Figure 3.15: (a) Aberration-corrected NION UltraSTEM 100 (a facility at Division of physics of nanostructured materials, faculty of physics, University of Vienna, Vienna), utilized for capturing all the ADF images presented in this thesis. (b) shows the cross-sectional view of a STEM with all its components labelled (adapted from ref: 30)

All the HAADF (High Angle Annular Dark-Field) images were acquired in NION UltraSTEM 100, a facility at Division of physics of nanostructured materials, faculty of physics, University of Vienna, Vienna. The design of aberration-corrected STEM varies significantly from a conventional TEM. As described in section 3.3.1, in a TEM the electron gun (or source of electron) is mounted on the top, whereas in the NION STEM, the electron gun is mounted at the bottom and the sample is placed at the top as can be seen

Die approbierte gedruckte Originalversion dieser Dissertation ist an der TU Wien Bibliothek verfügbar.
The approved original version of this doctoral thesis is available in print at TU Wien Bibliothek.
TU Bibliothek Your knowledge hub WIEN

from Figure 3.15. The electron beam from the gun is then steered up by a pair of deflectors and continues with three round condenser lenses, a quadrupole–octupole C_3/C_5 corrector, a quadrupole triplet called quadrupole lens module (QLM) for coupling the corrector electron-optically to the OL, a lower OL winding module, sample stage/OL polepiece module, an upper OL winding module, four round projector lenses, and a detector column that includes several detectors and other devices: a high-angle annular dark-field (HAADF) detector, a pneumatically controlled beam stop that can be inserted when recording diffraction patterns, medium angle annular dark-field (MAADF) detector, bright field (BF) detector, a quadrupole/octupole module called quadrupole–octupole coupling module (QOCM) for optimized coupling of inelastically scattered electrons into an electron energy loss spectrometer, a 1k×1k fast read-out CCD camera for Ronchigram, diffraction pattern and image read out, an EELS entrance aperture and finally an electron energy-loss spectrometer[28].

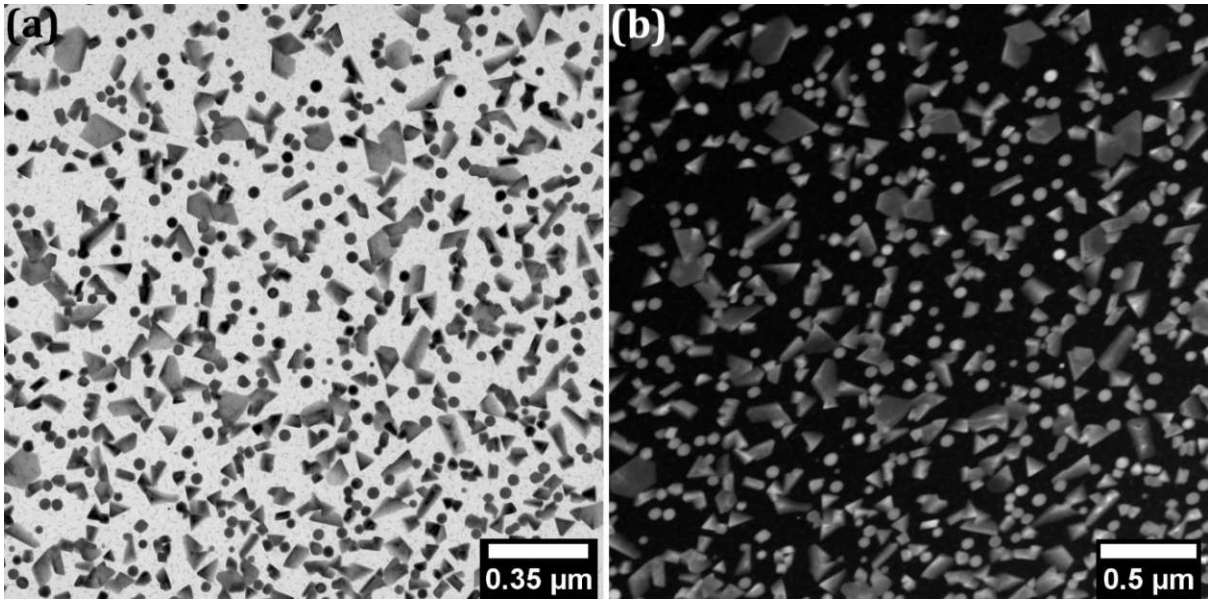

Figure 3.16: (a) BF image and corresponding (b) DF image of 10 nm Sb deposited on monolayer graphene suspended on quanti-foil TEM grids at 150 °C captured on FEI TECNAI F20 TEM.

While a BF detector employed at TEM includes the transmitted beam thereby making the holes appears bright, a DF detector excludes the transmitted beam and therefore holes (or vacuum) appears dark in a dark-field image, the same has been illustrated in Figure 3.16. In STEM, annular dark field (ADF) detectors are employed which surround the transmitted beam for collecting the scattered electrons. The inner angle of the ADF can

Die approbierte gedruckte Originalversion dieser Dissertation ist an der TU Wien Bibliothek verfügbar.
The approved original version of this doctoral thesis is available in print at TU Wien Bibliothek.
TU Bibliothek Your knowledge hub WIEN

be adjusted via post-specimen lenses to enhance the efficiency to collect scattered electrons. At higher collection angles (HAADF), it offers an atomic number (Z) dependence of the image contrast (often referred to as Z-contrast imaging)[31]. To note is that the high angle of the detector signifies values in several of tens of mrad (typically 60-200 mrad), which is generally the angle at which all diffraction spots of significant intensity values will be excluded. Electrons scattered at higher angles are though relatively few in number, are strongly dependent on the atomic number "Z" and insensitive to the structure and orientation of the specimen[30]. The variation in the HAADF intensity as a function of the atomic number is given by the relation: $\boldsymbol{I} \propto \boldsymbol{Z}^{x}$, where x lies between 1.5 and 2 but a typical value of 1.7 has been often quoted for most experimental setups[32].

A custom-built enclosure for maximum thermal stability and low magnetic fields ensured the consistency and reproducibility of the results by the instrument. NION UltraSTEM 100, an aberration-corrected state-of-the-art scanning transmission electron microscope with ultra-high vacuum conditions (~ 10^{-8} mbar, ensuring minimal additional hydrocarbon adsorption from residual gas during imaging) at the sample having minimum probe size of 1.0 Å was operated at an acceleration voltage of 60 kV with a beam current of ~30 pA and a convergence semi-angle of 80-200 mrad[28] for obtaining all the HAADF images presented in this thesis. The NION UltraSTEM can be operated at acceleration voltages ranging from 20-100 kV, the choice of using 60 kV for imaging purposes was made for the purpose of consistency in all the electron microscopic data presented in this thesis since the TEM was operated at 60 kV (as described in section 3.3.1) in addition to the fact that operation at 60 kV reduces the radiation damage to the low-Z element (like B, C, N, O) containing specimens. For imaging light elements like carbon, ADF detectors with detector half angles ranging from ~ 60-200 mrad were employed on account of their recognized suitability[33]. The microscope houses a high-brightness cold field emission electron gun (CFEG)[28]. As a basic protocol for removing the adsorbed thin water films from the samples, the samples were annealed at 150 °C in ~10^{-5} mbar for ~8 h prior to being loaded into STEM. The same samples were checked at FEI TECNAI F20 before loading them into the STEM and this pre-processing step for the STEM was found to have no effect on the representative state of the samples.

Die approbierte gedruckte Originalversion dieser Dissertation ist an der TU Wien Bibliothek verfügbar.
The approved original version of this doctoral thesis is available in print at TU Wien Bibliothek.
TU Bibliothek Your knowledge hub WIEN

"ADF (HAADF and MAADF) images of antimonene and bismuthene deposited on graphene were captures in STEM to assist in elucidating the rotational vdW epitaxial relationships in both the model systems. Identifying and highlighting all the salient planes and directions was only possible with the help of atomically-resolved ADF captured in STEM. Atomically-resolved ADF images also helped in the phase analysis of the deposited antimonene and bismuthene structures on graphene in both top plan view as well as cross-sectional view configurations. STEM was operated at 60 kV to complement the TEM data which was also operated at 60 kV"

3.4 Miscellaneous: Contributions

All experimental preparations, characterizations and data analysis was done by the author himself with the following exceptions: All the CVD grown MLG on Cu tape samples utilized for the Sb and Bi PVD were prepared by the author with the help of Dr. Kenan Elibol with partial help from Dr. Kimmo Mustonen (Physics of Nanostructured Materials, Faculty of Physics, University of Vienna) at University of Vienna, Vienna. The correlative AFM-SEM measurements were performed by Dr. Stefan Hummel (Physics of Nanostructured Materials, Faculty of Physics, University of Vienna) at GETec Microscopy, Vienna via GETec AFSEM module installed in a FEI Quanta 600F SEM. All the AFM data presented in this thesis on the various samples have been kindly provided by Dr. Kenan Elibol (Physics of Nanostructured Materials, Faculty of Physics, University of Vienna, Vienna) on NT MDT NTEGRA Spectra in tapping mode and Maximilian Winzely (Institute of Chemical Technologies and Analytics, Faculty of Technical Chemistry, TU Wien, Vienna) on Brucker Nanoscope 8 multimode scanning probe microscope in tapping mode. Cross-sectional FIB sample preparation was done by Dr. Gerlinde Habler (Department of Lithospheric Research, University of Vienna, Vienna) on FEI Quanta 3D FEG. The real-time EELS data during *in-situ* crystallization of Bi nanoparticles on Graphene and the VEELS + core-loss EELS data on antimonene/graphene heterostructures was acquired and analyzed by the author with the assistance of Dr. Michael Stöger-Pollach (University Service Facility for Transmission Electron Microscopy, TU Wien, Vienna) on FEI TECNAI F20. PL measurements were kindly

Die approbierte gedruckte Originalversion dieser Dissertation ist an der TU Wien Bibliothek verfügbar.
The approved original version of this doctoral thesis is available in print at TU Wien Bibliothek.
TU Bibliothek Your knowledge hub WIEN

provided by Alexander Goetz and Dr. Sarah M. Skoff (Research unit of Applied Quantum Physics, Institute of Atomic and Sub-atomic Physics, TU Wien, Vienna) using a custom-built confocal microscope with a 50 x Mitutoyo objective (NA= 0.55) and an Andor Technology Shamrock SR-303i spectrometer. The excitation laser was a 532 nm extended cavity diode laser with typical powers of 10 μW at the target. XPS measurements (including the data processing and fitting) were generously performed by Dr. Markus Sauer and Dr. Annette Foelske (Analytical Instrumentation Center, TU Wien, Vienna) employing a custom-built SPECS XPS-spectrometer equipped with a monochromatic Al-Kα X-ray source (μFocus 350, spot size: 400 μm, power: 100 W) and a hemispherical WAL-150 analyzer (Acceptance angle 60°). The overview and detailed spectra were recorded with pass-energies of 100 eV and 30 eV, and energy resolutions of 1.0 eV and 0.1 eV, respectively and were analyzed using transmission corrections (as per manufacturer's specifications), Tougaard backgrounds, and sensitivity parameters after Scofield within CASA XPS software, and charge correction was applied so the binding energy value of adventitious carbon from surface contamination was shifted to 285 eV. Deconvolution of XPS signals was carried out using symmetric Gaussian-Lorentzian peaks (GL(30)) and Levenberg-Marquardt least-square peak fitting. Some XRD measurements were provided by Jakob Rath and Shaghayegh Naghdi (Institute of Materials Chemistry, TU Wien, Vienna) using a PANalytical X'Pert Pro multi-purpose diffractometer (MPD, CuKα, Bragg-Brentano geometry), a facility at X-Ray Center, TU Wien, Vienna. Ms. Nicole Rosza contributed to the LPE related studies in the form of her bachelor thesis which was co-supervised by the author.

3.5 References

1. Kidambi, P. R. *et al.* The Parameter Space of Graphene Chemical Vapor Deposition on Polycrystalline Cu. *J. Phys. Chem. C* **116**, 22492–22501 (2012).
2. Regan, W. *et al.* A direct transfer of layer-area graphene. *Appl. Phys. Lett.* **96**, 113102 (2010).
3. Pantelic, R. S., Meyer, J. C., Kaiser, U. & Stahlberg, H. The application of graphene as a sample support in transmission electron microscopy. *Solid State Commun.* **152**, 1375–1382 (2012).
4. Ferrari, A. C. *et al.* Raman Spectrum of Graphene and Graphene Layers. *Phys. Rev. Lett.* **97**, 187401 (2006).

Die approbierte gedruckte Originalversion dieser Dissertation ist an der TU Wien Bibliothek verfügbar.
The approved original version of this doctoral thesis is available in print at TU Wien Bibliothek.
TU Bibliothek Your knowledge hub WIEN

5. Nicolosi, V., Chhowalla, M., Kanatzidis, M. G., Strano, M. S. & Coleman, J. N. Liquid Exfoliation of Layered Materials. *Science* **340**, (2013).
6. Predel, B. Sb-W (Antimony-Tungsten). in *Pu-Re – Zn-Zr* (ed. Madelung, O.) vol. 5 J 1–1 (Springer-Verlag, 1998).
7. Predel, B. Bi-W (Bismuth-Tungsten). in *B-Ba – C-Zr* (ed. Madelung, O.) vol. 5b 1–1 (Springer-Verlag, 1992).
8. Meyer, J. C. *et al.* Direct Imaging of Lattice Atoms and Topological Defects in Graphene Membranes. *Nano Lett.* **8**, 3582–3586 (2008).
9. Robertson, A. W. *et al.* Structural Reconstruction of the Graphene Monovacancy. *ACS Nano* **7**, 4495–4502 (2013).
10. Kurasch, S. *et al.* Atom-by-Atom Observation of Grain Boundary Migration in Graphene. *Nano Lett.* **12**, 3168–3173 (2012).
11. Warner, J. H. *et al.* Dislocation-Driven Deformations in Graphene. *Science* **337**, 209–212 (2012).
12. Abramoff, M., Magalhães, P. & Ram, S. J. Image Processing with ImageJ. *Biophotonics Int.* **11**, 36–42 (2003).
13. Schaffer, B. Digital Micrograph. *Transm. Electron Microsc.* 167–196 (2016) doi:10.1007/978-3-319-26651-0_6.
14. Williams, D. B. & Carter, C. B. *Transmission Electron Microscopy: A Textbook for Materials Science*. (Springer US, 2009). doi:10.1007/978-0-387-76501-3.
15. Goodhew, P. J. & Humphreys, J. *Electron Microscopy and Analysis*. (CRC Press, 2000).
16. Raman, C. V. & Krishnan, K. S. A New Type of Secondary Radiation. *Nature* **121**, 501–502 (1928).
17. Das, R. S. & Agrawal, Y. K. Raman spectroscopy: Recent advancements, techniques and applications. *Vib. Spectrosc.* **57**, 163–176 (2011).
18. John, N. & George, S. Chapter 5 - Raman Spectroscopy. in *Spectroscopic Methods for Nanomaterials Characterization* (eds. Thomas, S., Thomas, R., Zachariah, A. K. & Mishra, R. K.) 95–127 (Elsevier, 2017). doi:10.1016/B978-0-323-46140-5.00005-4.
19. Gibaja, C. *et al. Few-Layer Antimonene by Liquid-Phase Exfoliation*. (2016). doi:10.1002/ange.201609591.
20. Egerton, R. F. & Malac, M. EELS in the TEM. *J. Electron Spectrosc. Relat. Phenom.* **143**, 43–50 (2005).
21. Keast, V. J. Application of EELS in Materials Science. *Mater. Charact.* **73**, 1–7 (2012).
22. Egerton, R. F. *Electron Energy-Loss Spectroscopy in the Electron Microscope*. (Springer Science & Business Media, 2011).
23. What is EELS? *EELS.info* https://eels.info/about/overview (2015).
24. Brydson, R. *Electron Energy Loss Spectroscopy*. (Garland Science, 2020).
25. Keast, V. J., Scott, A. J., Brydson, R., Williams, D. B. & Bruley, J. Electron energy-loss near-edge structure – a tool for the investigation of electronic structure on the nanometre scale. *J. Microsc.* **203**, 135–175 (2001).
26. Wang, J. *et al.* Ti-based MOFs: New insights on the impact of ligand composition and hole scavengers on stability, charge separation and photocatalytic hydrogen evolution. *Appl. Catal. B Environ.* **283**, 119626 (2021).
27. Browning, N. D. *et al.* SCANNING TRANSMISSION ELECTRON MICROSCOPY: AN EXPERIMENTAL TOOL FOR ATOMIC SCALE INTERFACE SCIENCE. *Scanning Transm. Electron Microsc.* 26.
28. Krivanek, O. L. *et al.* An electron microscope for the aberration-corrected era. *Ultramicroscopy* **108**, 179–195 (2008).

Die approbierte gedruckte Originalversion dieser Dissertation ist an der TU Wien Bibliothek verfügbar.
The approved original version of this doctoral thesis is available in print at TU Wien Bibliothek.
TU Bibliothek Your knowledge hub WIEN

29. *Scanning Transmission Electron Microscopy: Imaging and Analysis*. (Springer-Verlag, 2011). doi:10.1007/978-1-4419-7200-2.
30. Brydson, R. Aberration-Corrected Analytical Transmission Electron Microscopy | Wiley. *Wiley.com* https://www.wiley.com/en-us/Aberration+Corrected+Analytical+Transmission+Electron+Microscopy-p-9781119979906.
31. Pennycook, S. J. *et al.* Scanning Transmission Electron Microscopy for Nanostructure Characterization. in *Scanning Microscopy for Nanotechnology: Techniques and Applications* (eds. Zhou, W. & Wang, Z. L.) 152–191 (Springer, 2007). doi:10.1007/978-0-387-39620-0_6.
32. Krivanek, O. L. *et al.* Atom-by-atom structural and chemical analysis by annular dark-field electron microscopy. *Nature* **464**, 571–574 (2010).
33. Krivanek, O. L. *et al.* Gentle STEM of Single Atoms: Low keV Imaging and Analysis at Ultimate Detection Limits. in *Low Voltage Electron Microscopy* 119–161 (John Wiley & Sons, Ltd, 2012). doi:10.1002/9781118498514.ch6.

Die approbierte gedruckte Originalversion dieser Dissertation ist an der TU Wien Bibliothek verfügbar.
The approved original version of this doctoral thesis is available in print at TU Wien Bibliothek.
TU Bibliothek Your knowledge hub WIEN

Chapter 4:

Antimonene/Graphene Heterostructures

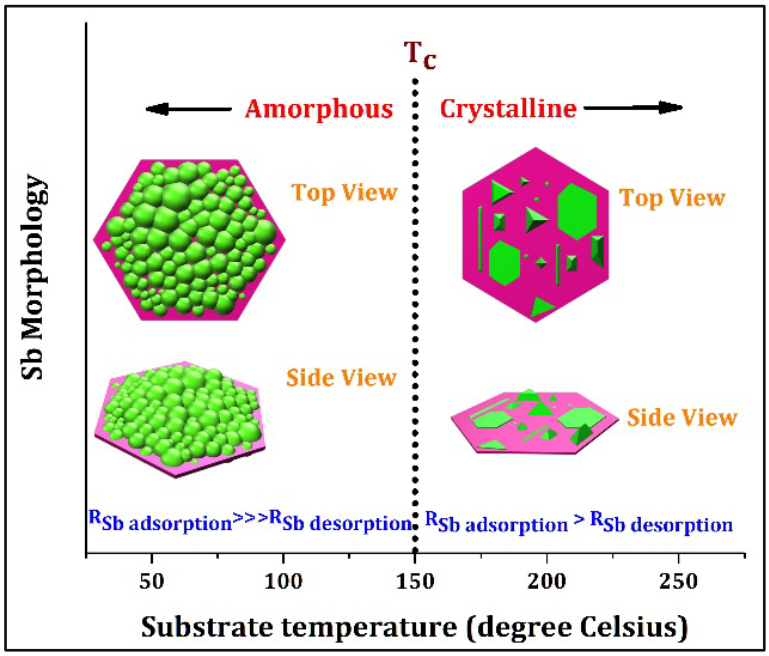

Die approbierte gedruckte Originalversion dieser Dissertation ist an der TU Wien Bibliothek verfügbar.
Your source for knowledge.
TU Bibliothek
WIEN Vien vourknowledge hub

Chapter Preview

Chapter 4 *provides a holistic assessment of two-dimensional antimony grown on monolayer graphene via a physical vapor deposition technique of thermal evaporation employing high resolution electron microscopy and associated analytical spectroscopic techniques.*

Two-dimensional (2D) antimony (Sb, "antimonene") recently attracted interest due to peculiar electronic properties and suitability as anode material in batteries. Sb however exhibits a large polymorphic/allotropic structural diversity, which is also influenced by the Sb's support. Thus, understanding Sb heterostructure formation is key in 2D Sb integration. Particularly 2D Sb/graphene interfaces are highly important in electronics and batteries. Few-layered 2D Sb/graphene heterostructures are thus studied here by atomic-resolution (scanning) transmission electron microscopy. Co-existence of two Sb morphologies was found: First was a 2D morphology of layered β-Sb with β-Sb (001) || graphene (001) texture. Second were one dimensional (1D) Sb nanowires which could be matched to β-Sb with β-Sb [2-21] ⊥ graphene (001) and were also closely related to thermodynamically non-preferred cubic Sb (001) || graphene (001). Importantly, both Sb morphologies showed rotational van-der-Waals epitaxy with graphene and were resilient against environmental bulk oxidation, although superficial surface Sb-oxide formation merits consideration, including epitaxial Sb_2O_3 *(111) / β-Sb (001) heterostructures. Exact Sb growth behavior depended on processing and substrate properties including, notably, the support underneath the graphene. This introduced the substrate underneath a direct 2D support as a key parameter in 2D Sb heterostructure formation. The study provides insights into the rich phase and epitaxy landscape in 2D Sb and 2D Sb/graphene heterostructures. The figure caption for chapter 4 is a schematic representation of the growth morphology evolution of Sb (green) on monolayer graphene (pink) as a function of substrate temperature.*

The contents of this chapter have been published as ***T. Gupta et al. Resolving few-layer antimonene/graphene heterostructures. Npj 2D Mater. Appl. 5, 53 (2021)***

Die approbierte gedruckte Originalversion dieser Dissertation ist an der TU Wien Bibliothek verfügbar.
The approved original version of this doctoral thesis is available in print at TU Wien Bibliothek.
TU Bibliothek Your knowledge hub WIEN

4. Antimonene/Graphene Heterostructures

4.1 Introduction

Among the two-dimensional (2D) pnictogens (i.e., group 15/VA elements, incl. P, As, Sb and Bi)[1–4] particularly mono- and few-layered 2D Sb ("antimonene") has recently attracted increasing research interest[5,6]. Firstly, this is due to 2D Sb's peculiar electronic properties towards novel 2D electronics incl. layer-dependent (semi-)metal-to-semiconductor transition[7,8] high carrier mobilities[9], strain-tunable indirect-to-direct band gap transition[7,8], and the possibility of two- and three-dimensional topological insulator behavior for mono[10]- and few-layered[5] 2D Sb, respectively. Secondly, the recent high interest equally resulted from 2D Sb's high suitability for sustainable energy and catalysis applications, incl. as an anode material in next-generation Li- and Na-ion batteries[11–21] as well as in (electro-)catalysis[22–24], supercapacitors[25], charge extraction in photovoltaics[26], and thermoelectrics[27].

Sb however shows a large polymorphic/allotropic structural diversity. This includes several layered, potential 2D forms[8,28–31] such as in particular the thermodynamically most stable, rhombohedral, buckled honeycomb-structured β-Sb (A7, R-3m, 166)[22,23,30–44] and the metastable orthorhombic, puckered "washboard"-structured α-Sb (A17, cmca, 64)[31,45,46]. Additionally several non-layered metastable allotropes at high pressure and in thin film form have been reported incl. simple cubic, body-centered-cubic, face-centered-cubic and hexagonally-close-packed Sb[47–56]. Most of these phases are related via small atomic rearrangements[31,54,56], and some even have been suggested to show thickness dependent phase transitions in nanostructures[31]. This polymorphicity calls for close control over Sb's structure in any potential synthesis scenario for the various desired application fields. The structure of Sb deposits is however not only determined by kinetic growth process conditions but is also intimately linked to the Sb deposits' support, an effect which is exacerbated for ultrathin 2D Sb. Therefore, understanding Sb heterostructure formation is key for controllable 2D Sb growth. This is true not only for Sb's use in 2D electronics, where typically laterally large, defect-free 2D Sb films are

Die approbierte gedruckte Originalversion dieser Dissertation ist an der TU Wien Bibliothek verfügbar.
The approved original version of this doctoral thesis is available in print at TU Wien Bibliothek.
TU WIEN Bibliothek Your knowledge hub

desired[33], but also for Sb's use in catalysis and energy applications, where often nano-sized 2D Sb deposits with a large number of edges are preferred[22,23].

Among the various possible Sb heterostructures[5], in particular 2D Sb/graphene interfaces were of prime importance for two reasons: First, in the context of catalysis and energy applications, Sb/carbon hybrids were emerging as a highly useful materials combination, e.g. in batteries[11–20], electrocatalysis[22,23] and supercapacitors[25]. 2D Sb/graphene heterostructures can readily approximate such Sb/carbon hybrids in order to understand their as-of-yet little elucidated interface properties. Second, in the context of 2D electronics, recent work suggested that device contacts formed by 2D Sb/graphene heterostructures could be technologically advantageous towards tuning contact resistances[57,58]. The structural properties and formation mechanisms of Sb heterostructures incl. 2D Sb/graphene, remain however largely underexplored, in particular at the atomically resolved level. To address this, an atomic-scale (scanning) transmission electron microscopy ((S)TEM) investigation into the properties of a few-layered 2D Sb/graphene heterostructure model system was undertaken and was found to readily emulate Sb/carbon heterostructures manufactured by vapor phase techniques for electronics[38,48,50,51] and also as synthesized by wet chemistry routes for energy applications[12,14,15,19,20]. The approach presented here thereby facilitates direct assessment of interfacing and epitaxial effects in 2D Sb/carbon heterostructures, with graphene also acting as an ideal support[59] for the employed atomic resolution (S)TEM techniques[60].

In the synthesized 2D Sb/graphene heterostructures, the co-existence of a 2D growth morphology of layered β-Sb(001)||graphene(001) phase and texture as well as of a one dimensional (1D) Sb growth morphology was revealed. The latter 1D morphology can be matched to β-Sb with β-Sb[2-21]⊥graphene(001) texture but also to a non-layered, thermodynamically non-preferred cubic Sb(001)||graphene(001). Importantly, both Sb morphologies showed preferred relative crystallographic (mis-)orientations with respect to the supporting graphene monolayer lattice, indicating that rotational van-der-Waals (vdW) epitaxy can readily exist in 2D Sb/graphene heterostructures. Both Sb morphologies were found to be well resilient against environmental oxidation in ambient atmosphere although superficial surface oxidation is shown to be important to consider,

Die approbierte gedruckte Originalversion dieser Dissertation ist an der TU Wien Bibliothek verfügbar.
The approved original version of this doctoral thesis is available in print at TU Wien Bibliothek.
TU Bibliothek WIEN Your knowledge hub

particularly due to here suggested formation of epitaxial Sb_2O_3(111)/β-Sb(001) heterostructures as top layer. Exact Sb growth results were also found to be sensitive on employed processing techniques and substrate properties incl., notably, the nature of the support underneath the direct graphene support. This work thereby provides fundamental insights into the rich phase and epitaxy relations in 2D Sb and 2D Sb/graphene heterostructures.

4.2 Experimental Procedure

4.2.1 Growth of 2D Sb on graphene

PVD of Sb employed a commercial thermal evaporation system as already described in chapter 3 including the types of substrates employed. Phase diagrams[61] of W and Sb were cross-checked to ensure that no undesired intermetallics were formed during evaporation. As will be discussed later in the exploration of the parameter space of Sb PVD, actual retained Sb thicknesses can strongly reduce as a function of increasing substrate temperature and also type of substrate type via desorption effects.

"Thermal evaporation of 10nm nominal thickness of Sb on monolayer graphene supported on Cu tapes and suspended on Quantifoil TEM grids at RT, 150 °C and 250 °C"

4.2.2 Phase and epitaxy analysis of Sb deposits

Phase analysis of (S)TEM data employed primarily FT/SAED pattern simulation using Highscore Plus/Pdf4+ software (ICDD Pdf4+ 2020 RDB: Software version: 4.20.0.1. Database version: 4.2001.)[62] for manual matching of measured and simulated FT/SAED patterns. Additionally, also automated phase identification of measured FT/SAED data was performed using JEMS software. Structure visualization was done by Vesta[63] software. In particular the following structural database entries were found to best fit the

Die approbierte gedruckte Originalversion dieser Dissertation ist an der TU Wien Bibliothek verfügbar.
The approved original version of this doctoral thesis is available in print at TU Wien Bibliothek.
TU Bibliothek Your knowledge hub WIEN

measured FT and SAED (Pdf4+ code/Inorganic Crystal Structure Database ICSD collection code/literature reference): β-Sb: 04-14-2871/55402/ref. [64]; simple cubic Sb: 04-3213-3319/651499/ref. 47; Sb_2O_3: 00-042-1466/1944/ref. [65]. Notably, additional 45 other Sb and 61 other Sb-oxide entries from the ICDD Pdf4+ database were checked which consistently gave worse matches to experimental data.

Note that β-Sb (A7, R-3m, 166) is often described in literature with hexagonal axis (as here) but also with rhombohedral axis[33,38,51]. Therefore, numerical (hkl) and [uvw] values need consideration of selected hexagonal or rhombohedral axis system, when comparing between reports. Likewise, within the hexagonal axis system some literature uses a *a,b* base vector inner angle of 120 ° (as here) while other literature uses *a,b* base vector inner angle of 60°[31,33,38,51]. Again, therefore comparison of numerical (hkl) and [uvw] values must consider the selected axis system. To avoid ambiguity the here used axis are typically plotted alongside the atomic models throughout. The average equivalent feature sizes for the Sb deposits from their base areas (computed by ImageJ[66]) in SEM and AFM data were calculated as follows: Due to the different asymmetries between the characteristic base shapes for 2D triangular/hexagonal β-Sb(001) and 1D rod-like β-Sb[2-21]/cubic Sb(001) a characteristic feature size assuming a square base shape for both phases and defining the side length of this square was recalculated as the equivalent features size.

4.3 Results and Discussion

4.3.1 Morphology and Structure

In Figure 4.1 the morphology and structure of the few-layer Sb on graphene model system is characterized, which was prepared by physical vapor deposition (PVD) of Sb onto chemical vapor deposited (CVD) monolayer graphene. Optimized Sb deposition conditions towards high Sb crystallinity were first focused upon, with the wider parameter space of the Sb PVD on graphene being discussed later. The nominal 10 nm thick Sb deposits were thermally evaporated onto monolayered CVD graphene films[67,68].

Die approbierte gedruckte Originalversion dieser Dissertation ist an der TU Wien Bibliothek verfügbar.
The approved original version of this doctoral thesis is available in print at TU Wien Bibliothek.
TU Bibliothek WIEN Your knowledge hub

During Sb PVD (base pressure ~10^{-5} mbar), the graphene substrates were held at room temperature (RT) and also at controlled temperatures of 150 °C and 250 °C. The graphene either remained on its Cu CVD catalyst foils[67,68] during Sb PVD (Figure 4.1a,b, Figure 4.5) or was additionally also transferred prior to Sb PVD to be suspended as a freestanding monolayer membrane across holey TEM grids[69] ((i.e. no Cu foils underneath, Figure 4.1c-g, Figures 4.9-4.12). Nominal deposited Sb thickness was measured via a co-exposed (non-heated) quartz crystal microbalance (QMB). After Sb deposition, samples were stored in ambient air.

The scanning electron microscopy (SEM) image of the 250 °C deposition in Figure 4.1a reveals that under the optimized PVD conditions, the Sb deposits on the graphene formed isolated islands with two distinctly different base shapes: First were flat 2D Sb deposits with (truncated) hexagonal or (truncated) triangular base shapes. Second were rod-like 1D Sb deposits with rectangular bases. Lateral extents of all Sb deposits were in the range of tens to hundreds of nm. While such lateral sizes were small for device fabrication in 2D electronics, they were well compatible with the requirements for 2D Sb catalysis and energy applications[22]. Importantly, such feature sizes also provided a convenient Sb/graphene heterostructure model system for elucidation of Sb phases and interfacing by high resolution (S)TEM. Notably, as shown in Figure 4.1a, the edges of both the triangular-/hexagonal-shaped and the rod-shaped Sb deposits showed a high degree of visually apparent directional alignment amongst each phase type, respectively. This was the first indication of potential epitaxy effects between the Sb deposits and their graphene support, which has been examined later.

The Raman spectrum corresponding to the 250 °C deposition in Figure 4.1b displays primarily two peaks at low wavenumbers that are characteristic for elemental Sb (117 cm^{-1}; 154 cm^{-1}). These peaks were best matched with E_g and A_{1g} modes of few layer β-Sb, respectively, but were also potentially consistent with α-Sb and/or pressure-induced phases of Sb[8,31,33,46,54]. To note is that thicker Sb deposits may be overrepresented in Raman intensity[42,43]. Significant volume Sb-oxide formation can be excluded based on the Raman data as the signal intensity at wavenumbers corresponding to Sb-oxides was comparatively weak (e.g. for thermodynamically most stable Sb_2O_3 expected at ~190 cm^{-1} and 250 cm^{-1})[70]. The minor peak at ~215 cm^{-1} was related to minor Cu-oxide formation

Die approbierte gedruckte Originalversion dieser Dissertation ist an der TU Wien Bibliothek verfügbar.
The approved original version of this doctoral thesis is available in print at TU Wien Bibliothek.
TU Bibliothek WIEN Your knowledge hub

on bare regions of the Cu support during ambient air storage[71,72]. Raman peaks characteristic for graphene (G at 1593 cm^{-1}; and 2D at 2701 cm^{-1}) were also found in Figure 4.1b, consistent with the high-quality CVD graphene used as substrate[67,68]. The absence of a significant defect-related D-peak at ~1350 cm^{-1} confirmed that the CVD graphene support was not degraded during Sb PVD. Thereby the Raman data also confirmed that no covalent Sb-carbon bond formation had occurred and that the 2D Sb/graphene interfaces were of vdW-type[38], consistent with theoretical predictions[8,57,58].

To assess the crystallographic structure of the Sb deposits in a localized fashion, aberration-corrected, atomically-resolved and element-specific STEM (Nion UltraSTEM 100 at 60 kV electron acceleration voltage) in annular dark field (ADF)[60] mode was employed in Figure 4.1c-g to image individual Sb deposits at high resolution in top plan view. Corresponding ADF STEM and bright-field (BF) TEM data from focused-ion-beam (FIB) cross-sections in Figure 4.5 provided a complementary side view of the Sb deposits. Figures 4.3 and 4.4 provide atomic models and Fourier transform (FT)/selected area electron diffraction (SAED) simulations of all identified phases. It was also noted that under STEM imaging conditions no electron beam induced phase transitions or materials modifications to the Sb deposits were observed.

The first group of interest was the flat Sb deposits from Figure 4.1a with (truncated) hexagonal (Figure 4.1c) or triangular base shape (Figure 4.1d). The phase identification for these structures was straightforward: At atomic resolution and view from top, all flat hexagonal/triangular deposits showed a six-fold symmetric appearance that was best indexed via the FT of their atomic resolution images to rhombohedral β-Sb viewed along the [001] zone axis (Figure 4.1h) i.e. with the basal (001) layers of the layered 2D β-Sb parallel to the graphene(001) substrate (i.e. β-Sb[001]⊥graphene(001) = β-Sb(001)||graphene(001)). This phase identification to β-Sb(001) was also fully corroborated by the corresponding side view of a triangular/hexagonal deposits in Figure 4.5b-d, which clearly resolved the layered nature of the β-Sb(001) when viewed along the [110] zone axis, with the β-Sb(001) planes parallel to the graphene(001) substrate. Delineating projected edge directions correspond to [100], [010] and [110] in the top view STEM images for both hexagonal and triangular β-Sb (Figure 4.1c, d). Hexagonal and triangular deposits typically appeared flat in STEM images, indicating

Die approbierte gedruckte Originalversion dieser Dissertation ist an der TU Wien Bibliothek verfügbar.
The approved original version of this doctoral thesis is available in print at TU Wien Bibliothek.
TU Bibliothek WIEN Your knowledge hub

(001) top surfaces. The observation of 2D β-Sb(001)||graphene(001) was in line with prior literature[31–39].

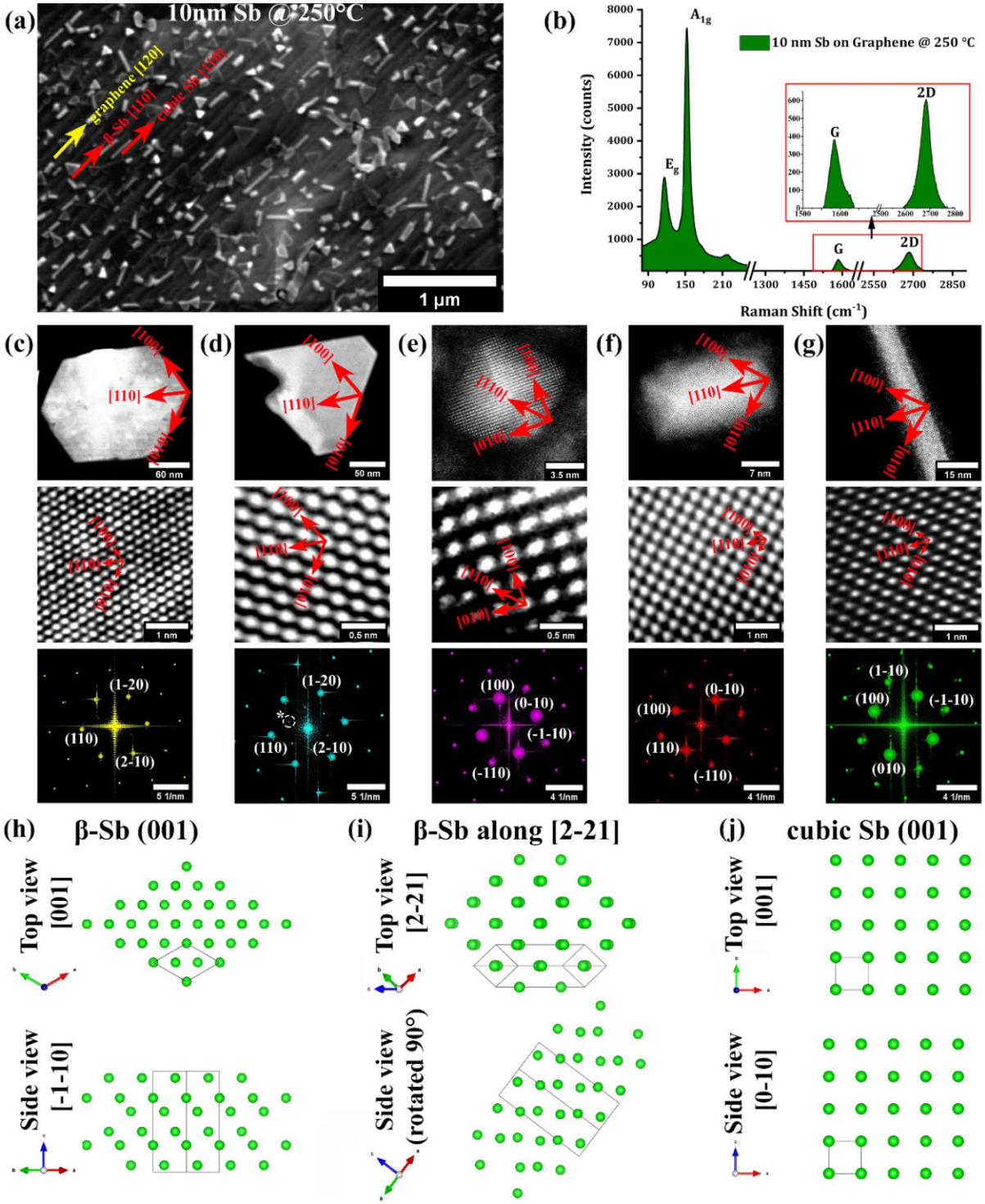

Figure 4.1: (a) SEM image and (b) Raman spectrum of 10 nm Sb deposited at 250 °C onto Cu-supported CVD graphene. Salient lattice directions in the graphene and the Sb are labelled in (a). (c-g) ADF STEM images of individual particles of 10 nm Sb deposited at 150 °C and 250 °C onto suspended monolayer graphene, showing overview (top) and atomic resolution images (middle) and corresponding FTs (bottom). The FTs are indexed to β-Sb(001) viewed along [001] zone axis (c,d) and cubic Sb(001) viewed along [001] zone axis (e,f,g), respectively. Corresponding salient

Die approbierte gedruckte Originalversion dieser Dissertation ist an der TU Wien Bibliothek verfügbar.
The approved original version of this doctoral thesis is available in print at TU Wien Bibliothek.
TU Bibliothek Your knowledge hub WIEN

crystallographic directions are superimposed over the ADF images. The six-fold symmetric "*"-indexed reflection set in (d) is ascribed cubic Sb_2O_3 viewed along the [111] zone axis and corresponds to Sb_2O_3 (2-20) reflection family, as described later. False-color coded ADF STEM images of overview and atomic resolution images can be found in Fig. 4.2. (h-j) Atomic models of β-Sb(001), β-Sb[2-21] and cubic Sb(001), respectively. For further information on atomic models and FT simulations see Figures 4.3 and 4.4.

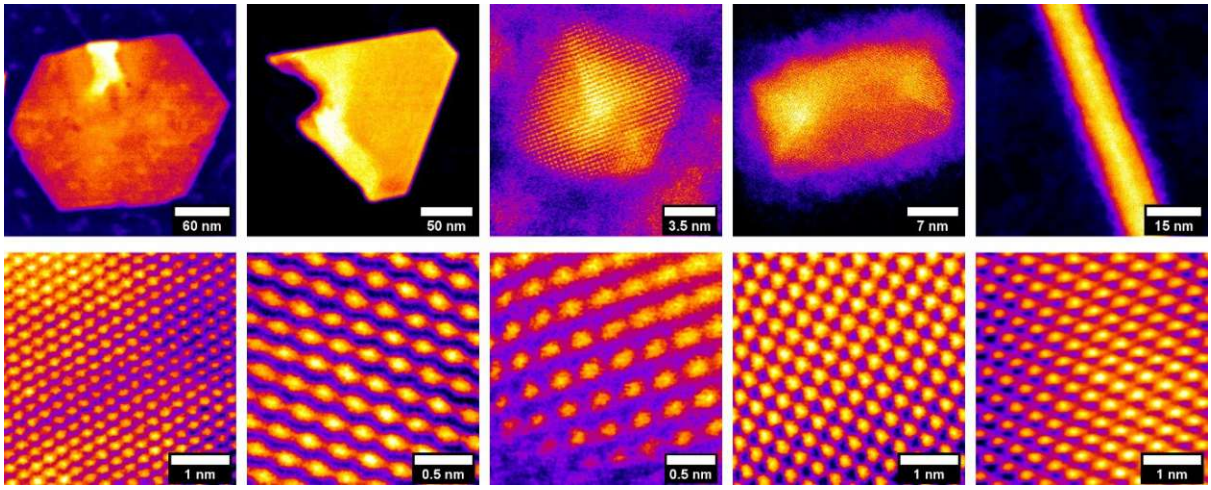

Figure 4.2: False-color coded ADF STEM images of individual particles of 10 nm Sb deposited at 150 °C and 250 °C onto suspended monolayer graphene, showing overview (top) and atomic resolution images (bottom), corresponding to the ADF STEM data plotted in grey-scale in Figure 4.1c-g.

The second group of interest were the rod-like 1D Sb deposits with rectangular bases (Figure 4.1e-g). In top view at atomic resolution, these structures always showed a FT with four-fold symmetry. Their phase identification was less straight forward: On the one hand, the STEM data agreed with β-Sb when viewed along the [2-21] zone axis i.e. at a texture of β-Sb[2-21]⊥graphene(001). Notably, β-Sb with [2-21] zone axis perpendicular to support does not have a defined low (hkl) value interface plane parallel to the support when viewed from the side, but only slightly inclined base planes (Figure 4.1i; an approximation for an interface plane would be β-Sb(10 -10 23)). β-Sb[2-21] is closely related to AA-stacked α-Sb multilayers via a small shear deformation[31]. Lately, a thickness-dependent crossover from α-Sb to β-Sb[2-21] was suggested to occur in 1D Sb deposits[31]. On the other hand, the fourfold symmetry STEM images of the 1D rod-like Sb deposits also matched well with a thermodynamically non-preferred simple cubic, non-layered Sb polymorph viewed along its [001] zone axis (Figure 4.1j) i.e. cubic Sb[001]⊥graphene(001) = cubic Sb(001)||graphene(001)[47,50]. Cubic Sb polymorphs are related to rhombohedral β-Sb via a unidirectional deformation[54–56]. While the existence of cubic Sb in bulk form has been a longstanding matter of debate in literature[52–56], cubic

Die approbierte gedruckte Originalversion dieser Dissertation ist an der TU Wien Bibliothek verfügbar.
The approved original version of this doctoral thesis is available in print at TU Wien Bibliothek.
TU Bibliothek Your knowledge hub WIEN

Sb was typically associated with high pressure conditions but has also been reported to occur in Sb thin films, presumably formed via substrate-induced stress[47–56].

Structurally β-Sb[2-21] (and AA α-Sb multilayers) and cubic Sb(001) structures were all closely related and might gradually transition into each other[31,54–56]. This made their differentiation difficult and partly ambiguous. This was also underlined by, e.g., the cross-sectional TEM of a rod-like Sb deposit in Figure 4.5d which showed lattice planes with a principal spacing of ~0.3 nm. These were consistent with β-Sb[2-21] as well as cubic Sb(001) viewed from the side (Figure 4.1i,j). Therefore for the remainder of this chapter, the 1D Sb morphology has been referred to as "β-Sb[2-21]/cubic Sb(001)" phase and texture, suggesting that the 1D rods being compatible with both β-Sb[2-21]⊥graphene(001) and cubic Sb(001)||graphene(001).For determination of β-Sb[2-21]/cubic Sb(001) in-plane epitaxial relations to graphene support, delineating projected edge directions and similar discussion later, the cubic Sb unit cell and associated (hkl) plane and [uvw] direction notation was predominantly used since this conveniently simplified the description of the crystallographic system compared to the inclined plane β-Sb[2-21] description. Delineating projected edge directions in the top view STEM images were cubic Sb [110] for the rods (Figure 4.1e-g). Consequently, the rods long axis was cubic Sb [110] direction.

Figure 4.1e-g and Figure 4.5e show that the 1D morphology did not have a flat top surface but rather very strong faceting to a pyramidal shape over a square (Figure 4.1e) or rectangular (Figure 4.1f,g) base. To best reproduce the observed angles in Figure 4.1e-g and Figure 4.5d the delineating faceted surfaces have to be of (223) family in cubic Sb notation (see Figure 4.7). Alternatively, also (111) family facets could provide a reasonable match. 1D Sb morphologies with four-fold atomic symmetries that co-exist with 2D β-Sb(001) had been observed in earlier work on Sb/graphite[50,51] and also recent work on Sb/graphene[31], albeit other recent work under very similar conditions for Sb/graphene heterostructures did not observe 1D nanostructure growth[38]. Notably, one recent paper[73] ascribed 1D Sb nanostructures to β-Sb(001), albeit without providing direct crystalline structure confirmation for their assignment.

Die approbierte gedruckte Originalversion dieser Dissertation ist an der TU Wien Bibliothek verfügbar.
The approved original version of this doctoral thesis is available in print at TU Wien Bibliothek.
TU Bibliothek Your knowledge hub WIEN

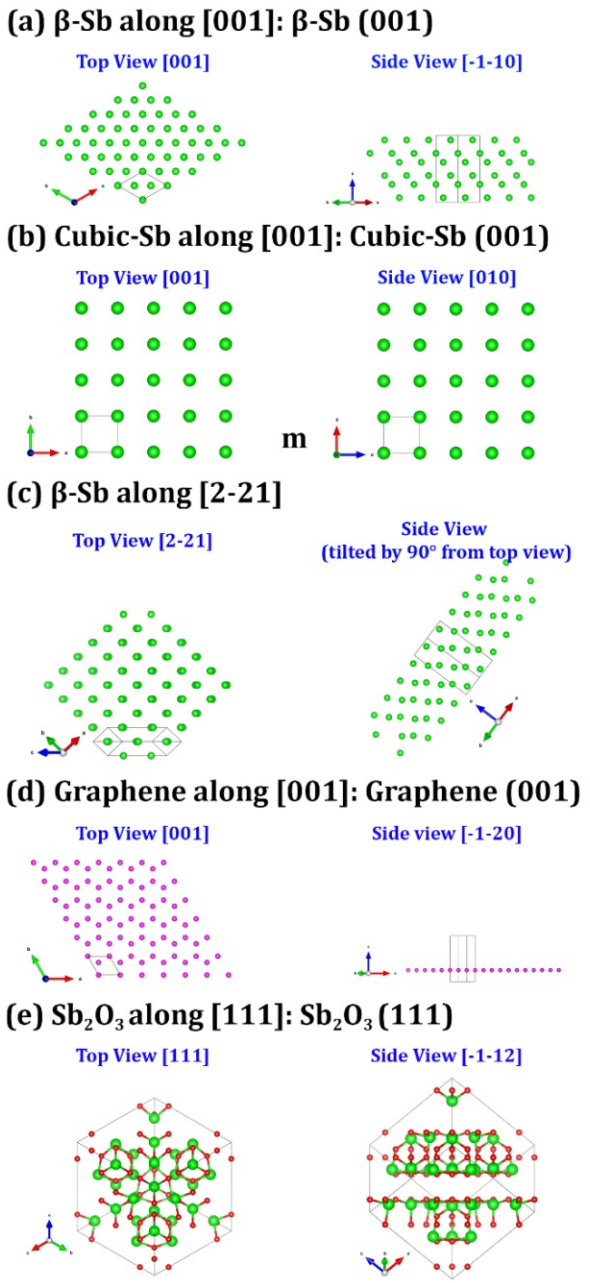

Figure 4.3: Atomic models in (left) "top/plan view" (as in "normal" ADF STEM and BF TEM of Sb deposits on graphene) and (right) "side" view (as in cross-sectional ADF STEM and BF TEM data) for (a) β-Sb(001), (b) cubic Sb(001), (c) β-Sb[2-21], (d) graphene(001) and (e) cubic Sb_2O_3(111). Unit cells and axes are plotted for all phases. The zone axis for all views are indicated. Note that β-Sb with [2-21] zone axis perpendicular to support does not have a defined low (hkl) value interface plane parallel to the support when viewed from the side, but only slightly inclined base planes (c). An approximation for an interface plane is β-Sb(10 -10 23). For corresponding simulated SAED/FT patterns see Figure 4.4

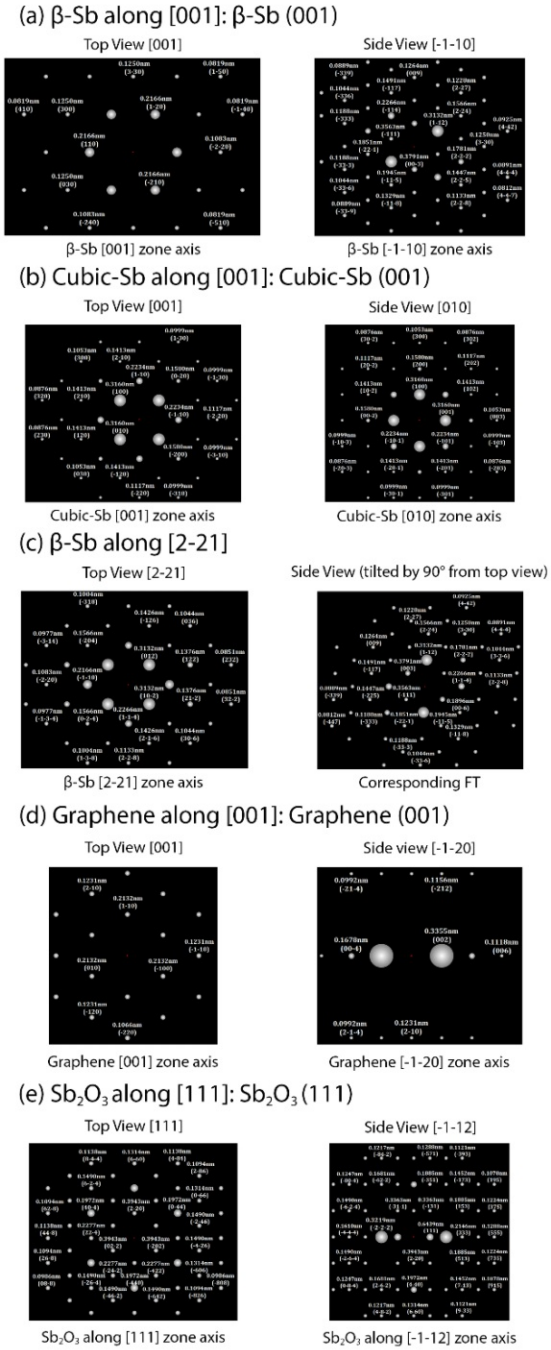

Figure 4.4: Simulated SAED/FT patterns corresponding to the atomic models in Figure 4.3 from (left) "top/plan view" (as in "normal" ADF STEM and BF TEM of Sb deposits on graphene) and (right) "side" view (as in cross-sectional ADF STEM and BF TEM data) for (a) β-Sb(001), (b) cubic Sb(001), (c) β-Sb[2-21], (d) graphene(001) and (e) cubic Sb_2O_3(111). Note that atomic models in Figure 4.3 and simulated SAED/FT patterns here are not rotation corrected and therefore may include arbitrary rotations around the zone axis with respect to each other.

Die approbierte gedruckte Originalversion dieser Dissertation ist an der TU Wien Bibliothek verfügbar.
The approved original version of this doctoral thesis is available in print at TU Wien Bibliothek.
TU Bibliothek Your knowledge hub WIEN

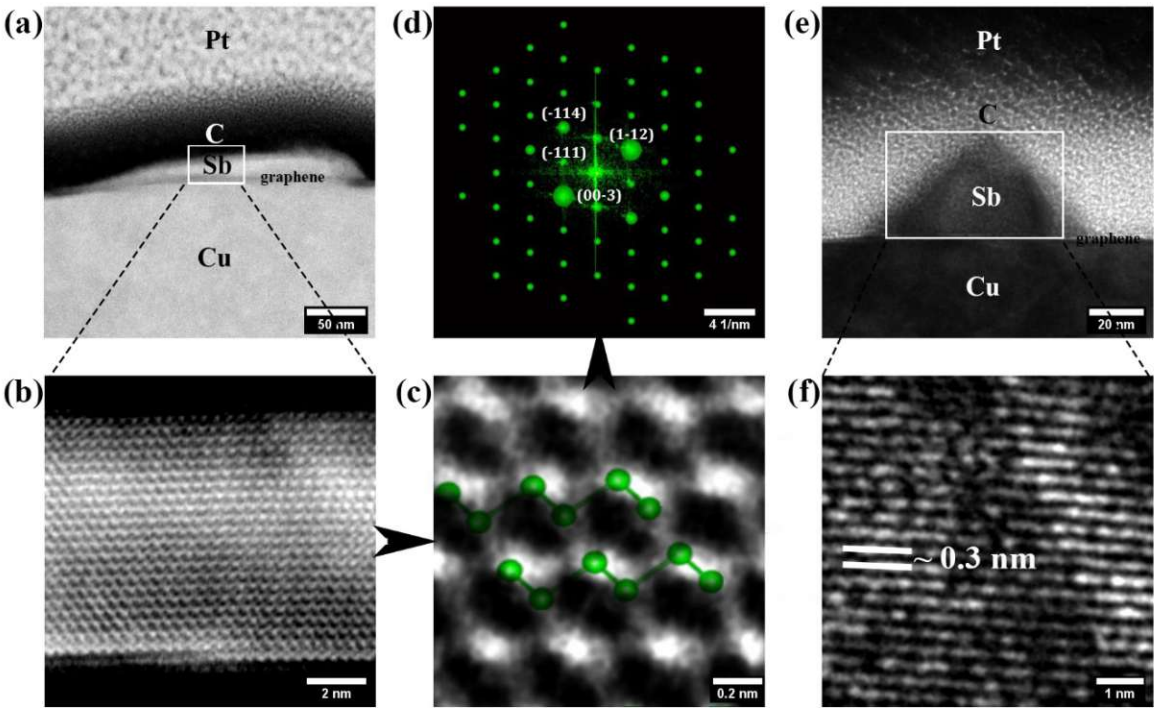

Figure 4.5: Cross-sectional STEM/TEM of 10 nm Sb deposited onto Cu-supported graphene: (a-c) show ADF STEM of a β-Sb(001) deposit in overview (a), intermediate (b) and high resolution (c). (d) shows the FT of (c) indexed to β-Sb(001) viewed along the [110] zone axis. In (c) a schematic of the β-Sb(001) layers is superimposed as illustration. (e,f) shows BF-TEM of a β-Sb[2-21]/cubic Sb(001) deposit in overview (e) and at high resolution (f).

The morphology-structure relation of triangular/hexagonal base shape corresponding to layered 2D β-Sb(001) and rectangular rod base shape corresponding to β-Sb[2-21]/cubic Sb(001) was confirmed via >60 atomic resolution STEM, lattice resolution TEM and SAED observations. Thereby assuring that the crystallographic phase of a deposit could be safely assigned via its macroscopic base shape as observed in lower magnification SEM or atomic force microscopy (AFM) data[51].

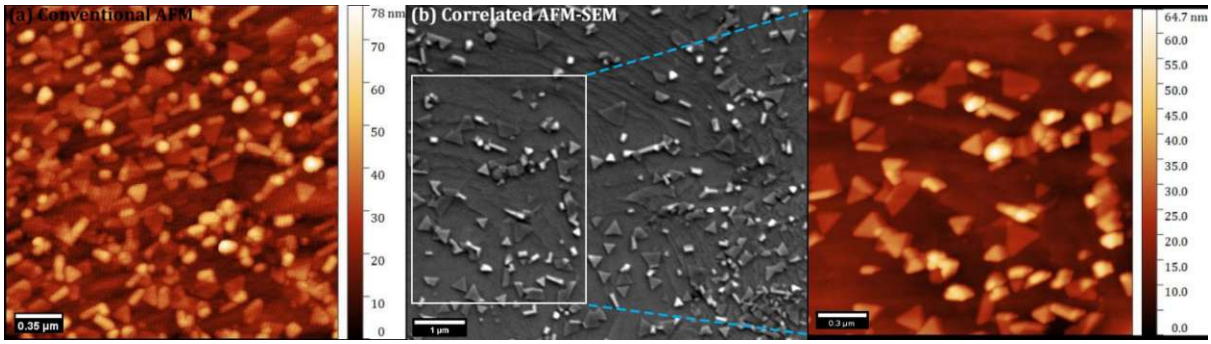

Figure 4.6: (Left) Conventional AFM of 10 nm Sb deposits on Cu-supported graphene from 250 °C depositions. (Middle and right) Correlated SEM (middle) and AFM (right) from the same sample, measured by a GETec AFSEM[74].

Die approbierte gedruckte Originalversion dieser Dissertation ist an der TU Wien Bibliothek verfügbar.
The approved original version of this doctoral thesis is available in print at TU Wien Bibliothek.
TU WIEN Bibliothek Your knowledge hub

Following this approach, AFM data (taken via conventional AFM as well as via correlated AFM-SEM, GETec AFSEM[74], see Figure 4.6) indicated for depositions at 250 °C, for the layered 2D β-Sb(001) deposits, a minimum thickness of 4.7 nm (equivalent to ~12 layers[8,29,42], i.e. few-layer antimonene) and an average thickness (± standard deviation) of 21±14 nm. The 1D rod-like β-Sb[2-21]/cubic Sb(001) deposits were relatively thicker, with a minimum thickness of 10 nm and an average thickness of 31±10 nm. To estimate the relative abundance of 2D β-Sb(001) and 1D β-Sb[2-21]/cubic Sb(001) in the deposits, both domain number counts and average equivalent feature sizes for each phase were computed from SEM and AFM images for the 250 °C depositions. Via this analysis, a lower number fraction of 2D β-Sb(001) domains (40±1 count-%) compared to β-Sb[2-21]/cubic Sb(001) (60±1 count-%) was found. These 2D β-Sb(001) domains grew to however cover a relatively larger area (60±5 area-% for 2D β-Sb(001) vs. 40±5 area-% for β-Sb[2-21]/cubic Sb(001)). The observation that the 2D β-Sb(001) islands grew to larger lateral sizes was also reflected in a larger maximum and average equivalent feature size for the 2D β-Sb(001) (maximum: 260 nm; average: 113±95 nm) compared to the β-Sb[2-21]/cubic Sb(001) (maximum: 130 nm; average: 72±54 nm).

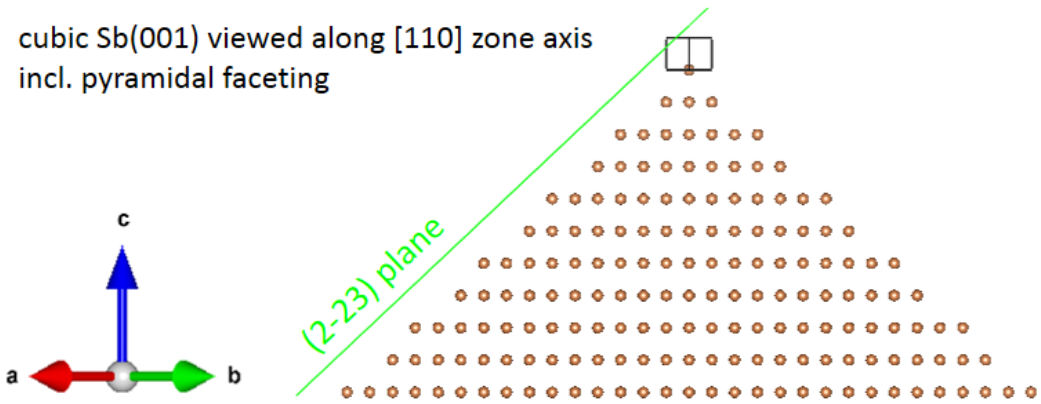

Figure 4.7: Atomic model of cubic Sb(001) viewed along the [110] zone (i.e. in side view corresponding to Figure 4.5e), showing that pyramidal faceting matches with (2-23) plane family delineating surface planes matches the measured angles in Figure 4.5e. Consistently, top view projections of the (2-23) faceting matches the top view images in Figure 4.1e-g.

Comparing the findings here with prior literature, the overall morphology and size of the Sb domains on carbon substrates were consistent not only with vacuum-based vapor deposition techniques as usually used in electronics[38,48,50,51] (akin to the here adopted PVD synthesis) but also with several wet-chemistry synthesis routes (incl. using

Die approbierte gedruckte Originalversion dieser Dissertation ist an der TU Wien Bibliothek verfügbar.
The approved original version of this doctoral thesis is available in print at TU Wien Bibliothek.
TU Bibliothek Your knowledge hub WIEN

$SbCl_3$[12,14,19,20] and ball-milled and annealed Sb/carbon mixtures[15]) as usually used in energy materials synthesis. This highlights that the here investigated 2D Sb/graphene heterostructure model system is relevant to a wide range of synthesis conditions and electronics and energy-related applications of Sb on carbon.

In terms of application potential, trigonally deformed Sb (like simple cubic Sb) has recently been predicted to feature superior thermoelectrical performance over β-Sb[56]. Given that monolayered 2D β-Sb has been predicted to surpass all other pristine 2D materials in terms of thermoelectric performance[27], future studies on band structure and electronic properties of the here observed β-Sb[2-21]/cubic Sb(001) deposits merit consideration.

"Simultaneous existence of natural rhombohedral (β-(001)) phase in 2D morphology and cubic / β-[2-21]- phase in 1D morphology was found in few layered antimonene structures deposited on monolayer graphene"

4.3.2 Van-der-Waals Epitaxy

So far it has been shown that in the grown 2D Sb/graphene heterostructures, Sb deposits were comprised of two co-existing morphologies, namely few-layer 2D β-Sb(001) and 1D nanorods β-Sb[2-21]/cubic Sb(001). Importantly, for both these Sb morphologies Figure 4.1a indicated a high degree of directional alignment of their respective domain edges on the monolayer graphene support. Given the vdW nature of the Sb/graphene interface (Figure 4.1b), three mechanisms could contribute to such alignment: First is direct rotational vdW epitaxy between the growing Sb and its graphene support directly underneath[75]. For 2D β-Sb(001) direct epitaxial relationships with various substrates have been reported incl., e.g., WSe_2[39], tellurides[32,36], mica[33] and Ge[35]. Particularly, for β-Sb(001) on graphene prior work has given a mixed picture: Earlier work[38] reported rotational vdW epitaxy for β-Sb/graphene via indirect measurements, while other work observed no such epitaxy[31,44,50,51]. For the 1D nanorod β-Sb[2-21]/cubic Sb(001), epitaxial effects have to date not been reported[31,51]. Therefore, the question if direct vdW epitaxy is prevalent in the Sb/graphene system remains open. Secondly however,

Die approbierte gedruckte Originalversion dieser Dissertation ist an der TU Wien Bibliothek verfügbar.
The approved original version of this doctoral thesis is available in print at TU Wien Bibliothek.
TU Bibliothek Your knowledge hub WIEN

complicating elucidation of this question, also recently reported "remote" epitaxy needs consideration in which epitaxy is impressed "remotely" between a deposit and its underlying substrate through an intermediate 2D layer[76]. In the present work, this would involve interactions between Sb and the underlying Cu catalyst foils impressed through the graphene monolayer[38]. Notably, in this scenario the graphene could also be required to act as a diffusion barrier to prevent chemical reactions between Sb and Cu[77,78], thus actually actively facilitating the remote epitaxy. Third, in contrast to the atomic-scale epitaxy, the third possibility involves macroscopic corrugations on the support (e.g. Cu surface steps) that result in alignment via preferred heterogeneous nucleation sites (e.g. at steps) and diffusion directing effects[79].

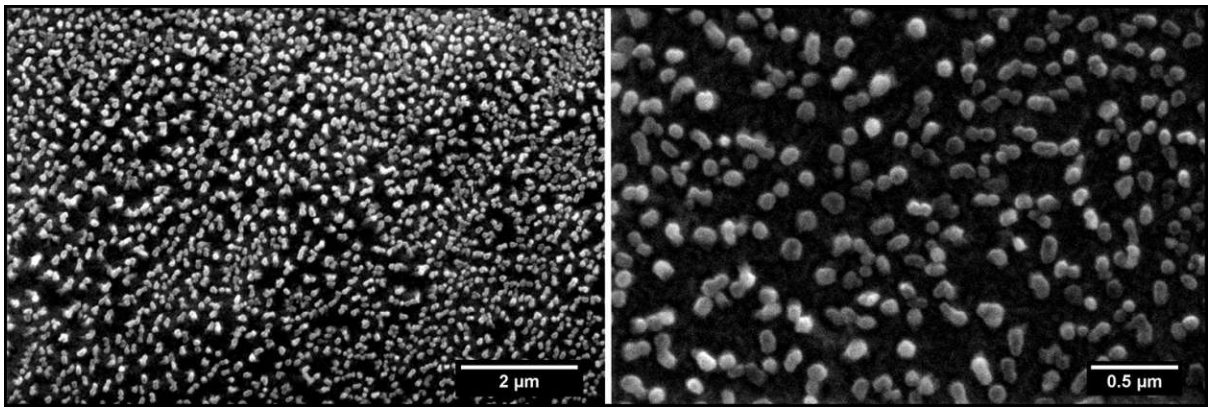

Figure 4.8: SEM of 10 nm Sb deposition at 250 °C onto bare Cu foils (i.e. without graphene). Cu foils have been annealed prior to Sb deposition at 960 °C in H_2/Ar (but without CH_4 exposure) to obtain a similar Cu grain structure as for the Cu foils after graphene CVD. Notably the Sb deposits on the bare Cu foils do not show the typical hexagonal/triangular and nanorod shapes seen on the Cu-supported graphene, indicating that the monolayer graphene drastically changes Sb growth behavior.

From SEM data as in Figure 4.1a alone, these three possible causes of the observed Sb alignments were hard to disentangle: First, direct vdW epitaxy would be readily compatible with the observed lateral length scales of alignment in Figure 4.1a as the lateral size of CVD graphene domains was in the tens of µm range[67,68,80].Therefore the field of view in Figure 4.1a represents most likely only one single-crystalline graphene domain which could facilitate rotational alignment over the entire field of view. Second however, graphene-mediated remote epitaxy between Sb and Cu is also conceivable for Figure 4.1a, since the Cu grain sizes in Cu foils after graphene CVD were in the mm range[67,68]. Notably, no Cu grain boundary was visible in Figure 4.1a[68], thus confirming a single Cu orientation across the field of view in Figure 4.1a. However, as shown in Figure

Die approbierte gedruckte Originalversion dieser Dissertation ist an der TU Wien Bibliothek verfügbar.
The approved original version of this doctoral thesis is available in print at TU Wien Bibliothek.
TU Bibliothek Your knowledge hub WIEN

4.8, direct deposition of Sb on Cu (i.e. without graphene in between) did not show any indications of epitaxial order in the Sb deposits under the adopted conditions[77]. Nevertheless, a graphene-mediated remote epitaxy mechanism between Sb and Cu[38] cannot be excluded based on Figure 4.1a. The third possibility, i.e. surface corrugations on the Cu support, could also direct the Sb deposits, although not resolvable in Figure 4.1a.

To disentangle these three possible influences, the relative orientation of Sb depositions at 150 °C and 250 °C directly onto suspended monolayer graphene membranes, i.e. without Cu foil underneath was investigated in Figure 4.9. In doing so, any possible indirect influence of Cu underneath the graphene on the Sb alignment (i.e. "remote" epitaxy and an influence from Cu surface corrugations) were excluded. In particular, the STEM-derived orientation (via FT analysis) of the lattice of the Sb deposits was correlated with the underlying graphene lattice orientation measured adjacent to the Sb deposit within a few nm distance[80] for multiple Sb deposits of both morphologies (β-Sb(001): Figure 4.9a-g; cubic Sb(001): Figure 4.9i-n; β-Sb[2-21]: Figure 4.10). Via plotting histograms of the relative rotational (mis)orientations of the graphene [120] direction ("armchair direction") and prominent orientations in the two respective Sb lattices (β-Sb [110]: Figure 4.9g; cubic Sb [110]: Figure 4.9n; β-Sb[2-21]: Figure 4.10) clear peaks in the (mis)orientation distributions for both Sb phases were found.

This unambiguously suggested direct epitaxy effects to be present between the graphene and both Sb phases. In particular 2D β-Sb showed a preferred misorientation of ~0° between the graphene [120] and the β-Sb [110] in-plane directions (i.e. β-Sb [110]||graphene[120]), as shown in the model in Figure 4.9e. Additionally, a secondary, less prominently preferred misorientation appeared at an offset of ~30° for β-Sb [110] and graphene [120] in Figure 4.9e. For cubic Sb, a single preferred misorientation of ~0° between the graphene [120] and cubic Sb [110] directions (i.e. cubic Sb[110]||graphene[120]) was found, as depicted in the model in Figure 4.9l. Notably, since the long axis direction of the cubic Sb rods is [110] (Figure 4.1), this implied that the rods' long axes were aligned along the graphene [120] direction. Notably, this preferential alignment might be intertwined with symmetry breaking of the cubic Sb(001) toward anisotropic rod formation.

Die approbierte gedruckte Originalversion dieser Dissertation ist an der TU Wien Bibliothek verfügbar.
The approved original version of this doctoral thesis is available in print at TU Wien Bibliothek.
TU Bibliothek Your knowledge hub WIEN

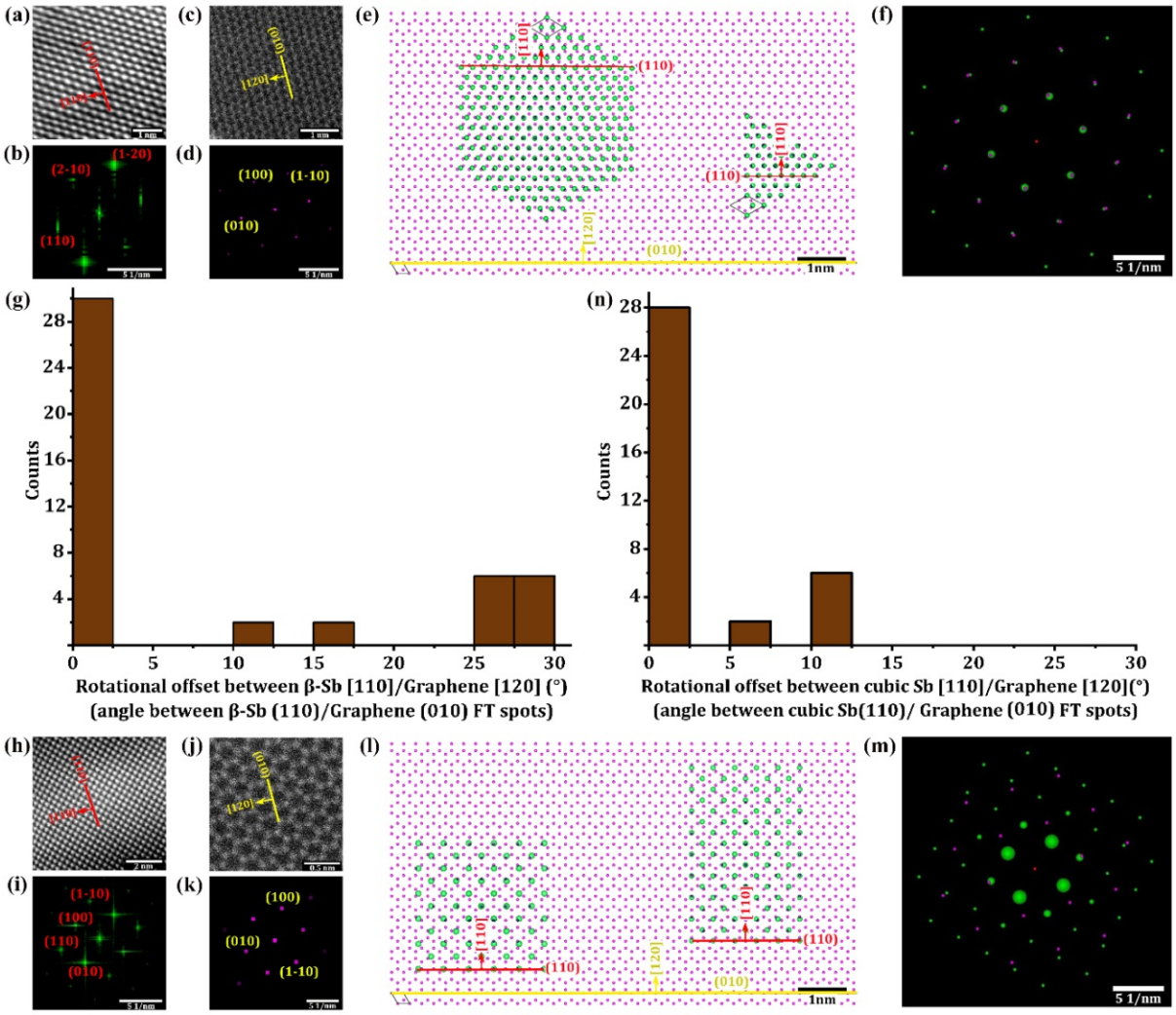

Figure 4.9: (a) Atomic resolution ADF STEM and (b) corresponding FT of a β-Sb(001) particle on suspended graphene. (c) ADF STEM and (d) FT of the graphene(001) lattice just adjacent to the particle in (a). The FTs are indexed to their corresponding phases and in the ADF images salient planes and directions are highlighted. (e) Atomic models showing in-plane vdW epitaxial relations derived from the data in (a-d), suggesting β-Sb(001)||graphene(001)/β-Sb[110]||graphene[120] i.e. angle between β-Sb[110] and graphene[120] = 0 °. (f) shows the overlay of simulated FTs corresponding to the models in (e). (g) Histogram of multiple measurements similar to (a-f) showing a distribution of(mis)rotation angles between β-Sb[110] and graphene[120] which peaks at 0°, confirming the suggested in-plane vdW epitaxy relation depicted in (e) to be preferred. (h-n) Corresponding measurements for cubic(001) deposits on suspended graphene, yielding a preferred cubic Sb(001)||graphene(001)/cubic Sb[110]||graphene[120] in-plane vdW epitaxy relation. For epitaxial relations in β-Sb[2-21] notation see Figure 4.10. Note that direction vector lengths in (a,c,e,h,j,l) are not to scale but enlarged for readability.

To cross-check these STEM-derived rotational vdW epitaxy relations via the SEM data in Figure 4.1a, the salient directions were labelled by colored arrows in Figure 4.1a: The long axis of the cubic Sb rods was first assigned to cubic Sb [110] based on Figure 4.1e-g (red arrow). Based on cubic Sb[110]||Graphene[120], this direction then coincided with graphene [120] direction (brown arrow). Thereby it became apparent that for most of

Die approbierte gedruckte Originalversion dieser Dissertation ist an der TU Wien Bibliothek verfügbar.
The approved original version of this doctoral thesis is available in print at TU Wien Bibliothek.
TU Bibliothek Your knowledge hub WIEN

the β-Sb triangles in Figure 4.1a one triangle edge (red arrow) coincided with the graphene[120] direction. This was exactly as expected from the β-Sb [110]||graphene[120] relation and from the observation that one edge direction of the triangles was typically β-Sb [110], as inferred in Figure 4.1c,d. Consequently, STEM and SEM data consistently suggested direct Sb/graphene vdW epitaxy for both β-Sb and cubic Sb with the preferred overall relations β-Sb(001)||graphene(001) / β-Sb[110]||graphene[120] and cubic Sb(001)||graphene(001) / cubic Sb[110]||graphene[120], respectively. (For epitaxial relations in β-Sb[2-21] notation see Figure 4.10).

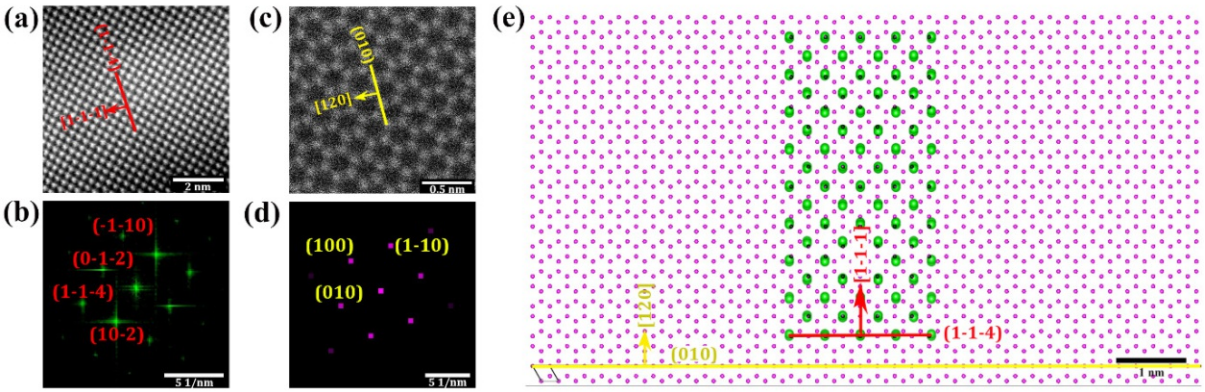

Figure 4.10: (a) Atomic resolution ADF STEM and (b) corresponding FT of a β-Sb[2-21]/cubic Sb(001) particle on suspended graphene. (c) ADF STEM and (d) FT of the graphene(001) lattice just adjacent to the particle in (a). (a-d) are replotted from Fig. 4.9(h-k), but are here annotated in the β-Sb[2-21] planes and directions system while in Fig. 4.9 the simpler cubic Sb(001) notation has been used. The FTs are indexed to their corresponding phases and in the ADF images salient planes and directions are highlighted using β-Sb[2-21] notation. (e) Atomic model showing in-plane vdW epitaxial relations between β-Sb[2-21] and graphene(001) derived from the data in (a-d) and the corresponding histogram in Fig. 4.9(n), suggesting that the epitaxial relation is reasonably described by β-Sb[2-21]⊥graphene(001)/β-Sb[1-1-1]||graphene[120]. It is emphasized however that the β-Sb[1-1-1] direction is (in side view) slightly inclined with respect to the supporting graphene plane, since no low (hkl) value interface plane in β-Sb[2-21]⊥graphene(001) exists (see Figure 4.3) and hence the relation β-Sb[1-1-1]||graphene[120] holds in top view but is only a very close approximation in side view.

Prior work had investigated possible epitaxy between Sb polymorphs and graphene (and graphite) with mixed results: Early work did not find evidence for epitaxy in β-Sb/graphite (but had only limited statistics measured)[51]. Also recent other studies did not observe epitaxy in β-Sb/graphene[31,44]. In contrast, another study of β-Sb and Cu-supported graphene suggested epitaxy for β-Sb/graphene to exist based on indirect measurements, identifying two preferred orientations of (in our notation) 0° and 30° offset between β-Sb [110] and graphene [120][38]. This was in good agreement with the

Die approbierte gedruckte Originalversion dieser Dissertation ist an der TU Wien Bibliothek verfügbar.
The approved original version of this doctoral thesis is available in print at TU Wien Bibliothek.
TU Bibliothek Your knowledge hub WIEN

findings in Figure 4.9g which were based on direct observations of the β-Sb/graphene interface. For β-Sb[2-21]/cubic Sb(001) on graphite no evidence for epitaxy has been reported prior[31,51]. In contrast, strong evidence also for rotational vdW epitaxy in the β-Sb[2-21]/cubic Sb(001)/graphene system was found. Combined, these observations show that vdW epitaxy could be enforced on 2D and 1D Sb deposits on graphene.

"Monolayer graphene was found to be a suitable substrate promoting the epitaxial growth of antimonene on it and the following epitaxial relationships were realized:

- *β-Sb(001)| |graphene(001) / β-Sb[110]| |graphene[120]*
- *Cubic Sb(001)| |graphene(001) / Cubic Sb [110]| |graphene[120]*
- *β-Sb[2-21]⊥graphene(001) / β-Sb[1-1-1]| |graphene[120]*

Importantly, epitaxy data reflected on the preferential alignment of cubic Sb rods long axis (cubic Sb [110] direction) along the graphene [120] direction (armchair direction)"

4.3.3 Oxidation Susceptibility

After having identified the nature of our Sb deposits and their relation to the graphene support, the oxidation susceptibility of Sb deposits was studied. Oxidation susceptibility is of significant importance in terms of processing and applications. Additionally, 2D Sb-oxides were beginning to attract research interest in their own right[70,81,82]. While Raman spectroscopy in Figure 4.1b did not suggest significant Sb-oxide presence in the samples, close inspection of the β-Sb(001) FT in Figure 4.1d revealed another, weaker intensity set of spots of six-fold symmetry at lower k-vectors (indexed "*" at ~0.4 nm) than the six-fold (110) β-Sb(001) spot family which was indexed in the FT. These weak inner spots might be identified with the presence of cubic Sb_2O_3 viewed along the [111] zone axis[70] (i.e. cubic Sb_2O_3(111), see Figure 4.3 and 4.4). This posed the question whether the β-Sb deposits were partly and/or superficially oxidized during sample storage in ambient air. Some prior work had reported stability of antimonene against oxidation in the ambient conditions[33,35,36,42,43,46,83] but other work had suggested thin antimony oxide present

Die approbierte gedruckte Originalversion dieser Dissertation ist an der TU Wien Bibliothek verfügbar.
The approved original version of this doctoral thesis is available in print at TU Wien Bibliothek.
TU Bibliothek Your knowledge hub WIEN

around Sb structures to be also prevalent[22,23,26,38,84–86] . Notably, for the β-Sb[2-21]/cubic Sb(001) deposits, no signs of additional crystalline oxides were found in (S)TEM or FT data.

To investigate possible oxidation effects for the Sb deposits in a localized fashion chemical identification via electron energy loss spectroscopy (EELS) was used. In EELS of Sb/Sb-oxide mixtures, compositional analysis based on the commonly used EELS core loss regions was however difficult since the core loss Sb $M_{4,5}$ edge at ~528 eV (which follows a delayed maxima fashion) was very close/partially overlapping the O K-edge at ~532 eV (see Figure 4.12)[87,88]. An alternative approach was investigating the valence EELS (VEELS) low loss region in which a sharp bulk plasmon peak at ~16.8 eV is related to metallic Sb[89], while the plasmon peak shifts for Sb-oxides to a distinctly higher energy of ~22eV[87]. For VEELS, however, also the graphene support (and, if present, amorphous carbon TEM grid membrane) had to be considered with plasmon signatures at ~27 eV[90].

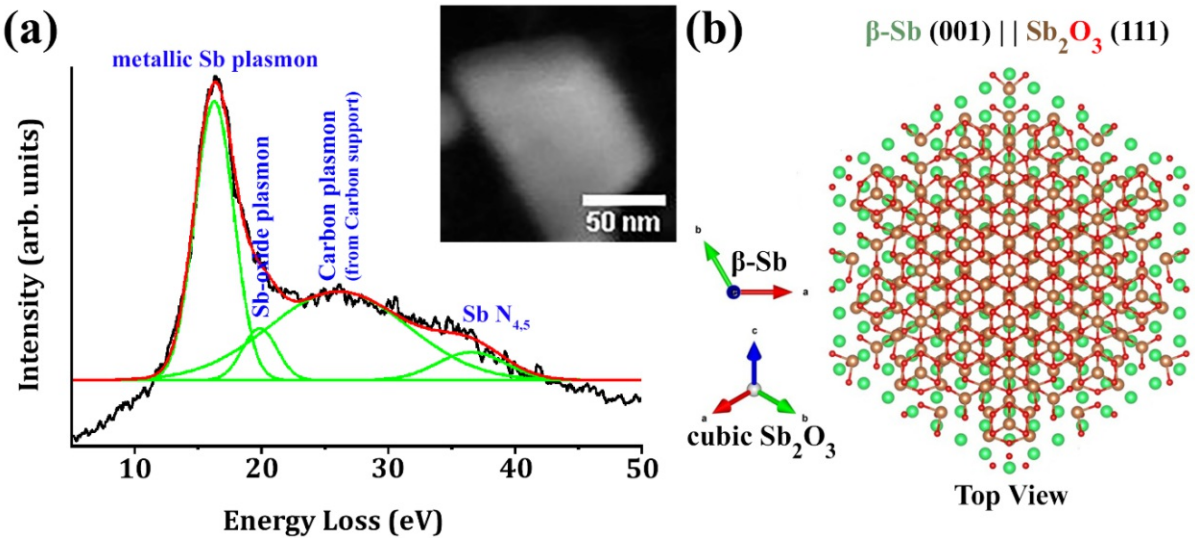

Figure 4.11: (a) VEELS spectrum of the β-Sb(001) crystal on suspended graphene (on amorphous carbon support) in the ADF STEM in the inset. The spectrum was acquired after ~8 months ambient air exposure of the sample. The VEELS data is fitted to the components labelled and described in the main text. Measurements on multiple β-Sb(001) and β-Sb[2-21]/cubic Sb(001) deposits showed similar results in terms of only low Sb-oxide plasmon signal. Note that the metallic Sb plasmon has the same energy for β-Sb(001) and β-Sb[2-21]/cubic Sb(001) in VEELS measurements[91]. (b) Atomic model of the suggested Sb_2O_3(111)||β-Sb(001) heterostructure that forms from ambient air exposure on β-Sb(001) crystals.

Die approbierte gedruckte Originalversion dieser Dissertation ist an der TU Wien Bibliothek verfügbar.
The approved original version of this doctoral thesis is available in print at TU Wien Bibliothek.
TU Bibliothek Your knowledge hub WIEN

In Figure 4.11(a), a typical VEELS spectrum acquired from a flat 2D β-Sb crystal (inset) is shown. Notably, this particular Sb deposit was characterized by VEELS after ~8 months of ambient air storage, thus allowing to probe long-term resilience against oxidation. A sharp metallic Sb VEELS peak was found to dominate the fitted VEELS spectrum with only a small contribution of the Sb-oxide component present even after the long-term air exposure. VEELS data for β-Sb[2-21]/cubic Sb(001) deposits showed similar results of only low Sb-oxide signal. The VEELS findings were thereby in agreement with the Raman data in Figure 4.1b that suggested metallic Sb to be dominant in our deposits. The VEELS results however suggested the possibility of a very thin superficial oxide layer (which might be below the detection limit for Raman). This further implied for the β-Sb(001) that the inner reflections (labelled "*") in the FT in Figure 4.1d may be indeed related to a very thin crystalline cubic Sb_2O_3(111) top layer on the elemental 2D β-Sb(001) crystal (where reflection "*" in Figure 4.1d corresponded to the (2-20) reflection in Sb_2O_3, see also Figures 4.3 and 4.4). This suggested the possibility of intrinsic Sb-oxide/Sb/graphene heterostructure formation from simple ambient air exposure.

In particular, whenever present, the six-fold Sb_2O_3 (2-20) reflection family consistently had a rotational misorientation of ~30° with the six-fold β-Sb (110) reflection family (as in Figure 4.1d). This indicated an epitaxial relation Sb_2O_3(111)||β-Sb(001)/Sb_2O_3[2-20]||β-Sb[110] for the Sb-oxide/Sb interface. See Figure 4.11(b) for an atomic model of the suggested Sb-oxide/Sb heterostructure (Sb-oxide/Sb/graphene). Unfortunately, the top regions in the β-Sb flakes in cross-section (S)TEM data were all not well enough resolved (due to Pt/C protection layers) to finally fully confirm the suggested presence of this ultrathin epitaxial Sb_2O_3 top layer. However, prior x-ray photoelectron spectroscopy measurements of 2D Sb oxidation found oxide stoichiometries consistent with the here suggested crystalline Sb_2O_3 phase[85], and that core loss EELS in Figure 4.12 also was best matched with Sb_2O_3 stoichiometry. No such crystalline overlayers were suggested from the data for the β-Sb[2-21]/cubic Sb(001), albeit a thin amorphous Sb-oxide overlayer was suggested to be also present based on the presence of the minor Sb-oxide signals in VEELS.

Die approbierte gedruckte Originalversion dieser Dissertation ist an der TU Wien Bibliothek verfügbar.
The approved original version of this doctoral thesis is available in print at TU Wien Bibliothek.
TU Bibliothek Your knowledge hub WIEN

Combined, the microscopic and spectroscopic data shows that while Sb deposits were overall well resilient against environmental bulk oxidation, the possibility of superficial oxidation in ambient air still required consideration, in particular since for β-Sb(001) deposits the formation of an epitaxial Sb_2O_3(111) oxide overlayer is inferred from the data.

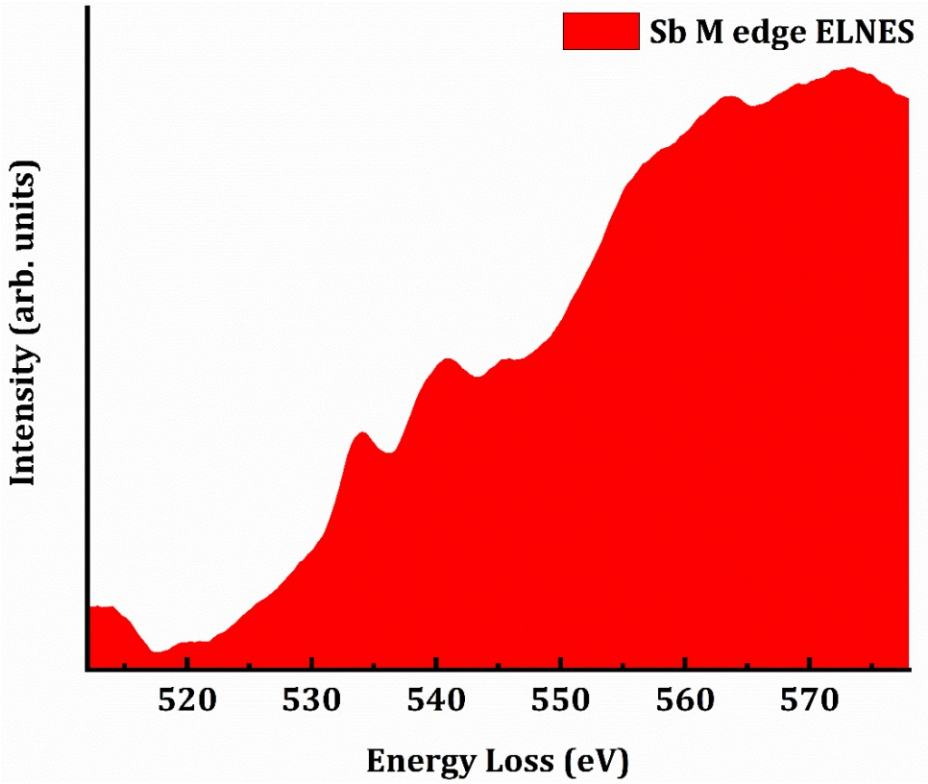

Figure 4.12: Core loss EELS spectrum of the Sb deposit corresponding to a Sb deposit on graphene as in Figure 4.11a. Based on this core-loss[87,88] EELS spectrum, the presence of some Sb-oxide is indicated (best matched Sb_2O_3) but it cannot be confirmed from this spectrum alone whether/how much metallic Sb remains (since metallic Sb/Sb-oxide quantification is not possible from core loss EELS due to overlap of respective spectral features, see also main text)[87,88].

"Combined studies via core-loss EELS + VEELS revealed the good resilience of few layered antimonene structures on monolayer graphene, where ELNES in the Sb $M_{4,5}$ edge (core-loss EELS) highlighted the presence of oxide, the intactness of the Sb plasmon peak in VEELS confirmed its superficial nature. Following this, an epitaxial relationship: Sb_2O_3(111) || β-Sb (001) / Sb_2O_3 [2-20] || β-Sb [110] for the Sb-oxide / Sb interface is suggested."

Die approbierte gedruckte Originalversion dieser Dissertation ist an der TU Wien Bibliothek verfügbar.
The approved original version of this doctoral thesis is available in print at TU Wien Bibliothek.
TU Bibliothek Your knowledge hub WIEN

4.3.4 Growth Parameter Space

Finally, the wider parameter space of Sb PVD was examined. Figure 4.13 compares Sb deposition results of nominally 10 nm Sb (regulated via a co-exposed (non-heated) quartz crystal microbalance) as a function of substrate temperature from RT to 250 °C onto CVD graphene-covered Cu foils (Figure 4.13a,c,e, SEM) as well as directly onto suspended graphene membranes (no Cu underneath, Figure 4.13b,d,f, TEM). Figure 4.13 shows that the Sb deposit morphology drastically changed between RT and elevated temperature (150 °C, 250 °C) depositions: For RT depositions (Figure 4.13a,b) merged (truncated) (semi-)spherical features dominated. High resolution STEM in Figure 4.14 shows that these RT-deposited (truncated) (semi-)spheres were amorphous. For 150 °C depositions (Figure 4.13c,d) the formerly described triangular/hexagonal shaped 2D β-Sb and rod-shaped cubic Sb crystals along with few (semi-)spherical Sb deposits were found. Among the 2D β-Sb deposits the hexagonal base shape was more prevalent. For 250 °C depositions (Figure 4.13e,f) practically only triangular/hexagonal shaped 2D β-Sb and rod-shaped cubic Sb were found, whereby now among the 2D β-Sb triangles dominate.

Notably, for neither 150 °C nor 250 °C evidence for an underlying continuous Sb layer on neither Cu-supported nor freestanding graphene, the former in contrast to prior literature[38] was found. Besides deposit morphology, also coverage and retained Sb amount of the nominally 10 nm Sb deposits was strongly influenced by substrate temperature during Sb deposition and, notably, also strongly dependent on substrate-type. In particular, Sb coverage and retained Sb amount strongly decreased with increasing substrate temperature. For RT depositions a homogeneous coverage close to 100 % was achieved on both Cu-supported and freestanding graphene in Figures 4.13a,b and for RT samples good agreement between nominal 10 nm thickness and AFM-calibrated average deposit thickness was found. In comparison, the coverage for 150 °C and 250 °C depositions decrease, whereby the coverage decrease with substrate temperature was even more prominent on the freestanding graphene (150 °C~40 %, 250 °C: <5 %) than on the Cu-supported graphene (150 °C: ~40%, 250 °C: ~20%). For Sb deposits with an average thickness of 21 ± 14 nm at 250 °C (see above) this equated to a

Die approbierte gedruckte Originalversion dieser Dissertation ist an der TU Wien Bibliothek verfügbar.
The approved original version of this doctoral thesis is available in print at TU Wien Bibliothek.
TU Bibliothek WIEN Your knowledge hub

reduction in Sb amount deposited from RT to 250 °C of ~50 % on Cu-supported graphene and of ~90 % on freestanding graphene, respectively. Notably, also the size of individual deposits of Cu was significantly larger than on the suspended graphene, best seen in the 250 °C depositions (Figure 4.13e,f).

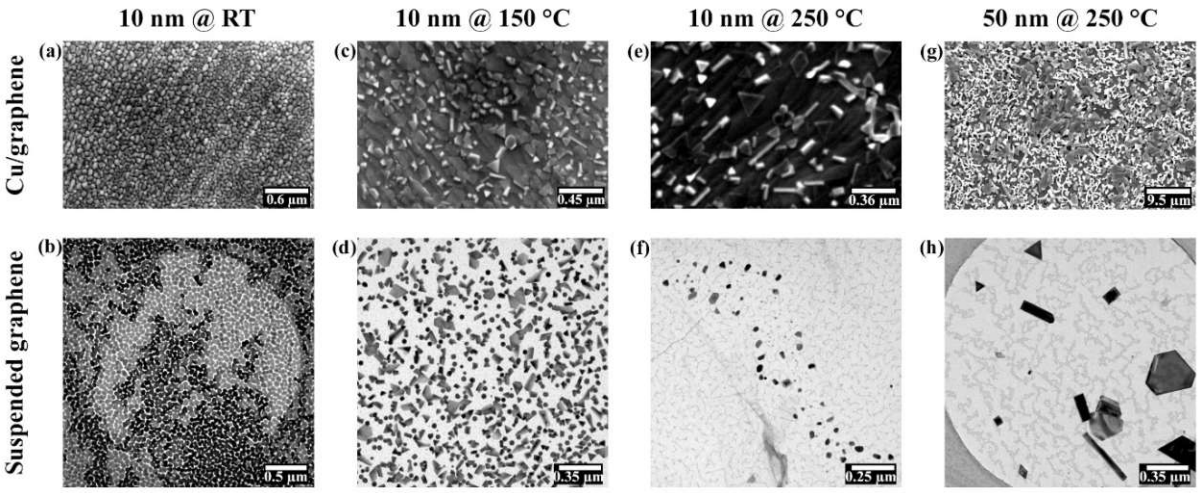

Figure 4.13: Sb deposits on Cu-supported graphene (SEM in a,c,e,g) and suspended graphene (BF TEM in b,d,f,h) deposited at nominal thicknesses of 10 nm at RT (a,b), 150 °C (c,d) and 250 °C (e,f) and 50 nm at 250 °C (g,h), respectively. (e) is replotted from Figure 4.1a.

Combined, this suggested a key influence of temperature dependent desorption processes on Sb nanostructure growth[35,37,47–51]. In particular, the balance of Sb adsorption flux ($F_{Sb,ad}$) from the evaporation source onto the graphene substrate and a substrate temperature-dependent Sb desorption flux from the graphene substrate into vacuum ($F_{Sb,de}(T)$) was key: The observed Sb morphologies implied that at RT $F_{Sb,ad} >> F_{Sb,de}(RT)$ resulting in strong deposition, while the low temperature hindered crystallization of the resulting Sb deposits (possibly via incomplete fragmentation of physisorbed Sb_4 species which were the preferred arriving Sb vapor species[51]). This led to the observed fully covering amorphous Sb deposits at RT. Increasing substrate temperature led to a strong increase in $F_{Sb,de}(150\text{-}250\ °C)$, reducing the net retained amount of Sb at higher substrate temperature. In turn the higher substrate temperatures facilitated crystallization of the retained Sb deposits (possibly via thermally activated fragmentation of surface-bound Sb species[51] and thus increased Sb re-arrangement).

Die approbierte gedruckte Originalversion dieser Dissertation ist an der TU Wien Bibliothek verfügbar.
The approved original version of this doctoral thesis is available in print at TU Wien Bibliothek.
TU Bibliothek Your knowledge hub WIEN

Thereby crystalline Sb deposits grew with an onset temperature of crystallization of ~150 °C. The observation that this temperature dependence was more pronounced on freestanding graphene membranes as compared to Cu-foil supported graphene, is suggested to be related either to intrinsic substrate effects whereby the Cu surface states underneath the graphene modify e.g. sticking coefficients to the Sb flux (akin to Cu supports modifying the surface properties of graphene in liquid wetting[92]) or to a different local temperature profile on Cu-foil supported graphene vs. suspended graphene membranes due to the macroscopic thickness 25 µm Cu foils. In the latter scenario, the Cu foil acted as an effective heat sink for the additional energy arriving with the incoming Sb flux $F_{Sb,ad}$ compared to the vacuum-suspended monolayer graphene membranes (and, if present, thin amorphous carbon support), thus resulting in a (slightly) lower actual local substrate temperatures on the Cu supported graphene.

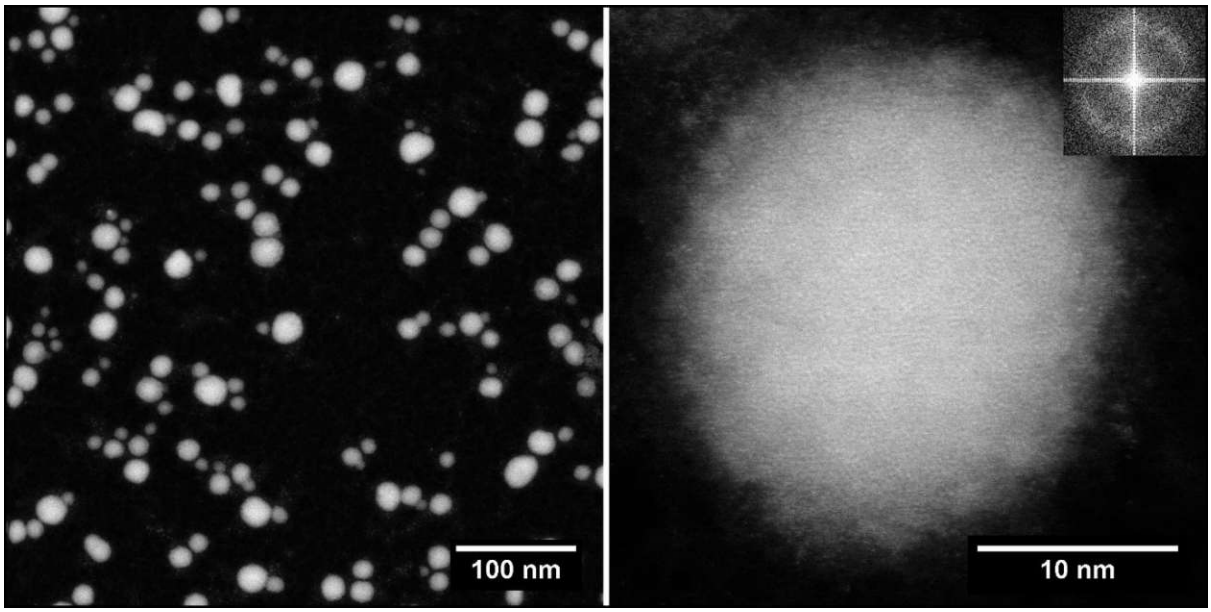

Figure 4.14: ADF STEM images of RT Sb depositions on suspended graphene at overview (left) and atomic resolution (right). The inset shows the FT to the atomic resolution image. Both visual appearance and FT confirmed that the RT deposited Sb on graphene is amorphous. The nominal thickness of the Sb deposits is ~1.6 nm, which was chosen in order to obtain individual particles for STEM imaging.

The here observed temperature dependence of Sb deposit morphology, crystallization onset and retained Sb amount was in good agreement with prior literature[35,37,47–51]. Beyond this, these results confirmed that not only the directly supporting growth

Die approbierte gedruckte Originalversion dieser Dissertation ist an der TU Wien Bibliothek verfügbar.
The approved original version of this doctoral thesis is available in print at TU Wien Bibliothek.
TU Bibliothek Your knowledge hub WIEN

substrate (here, monolayer graphene) but also the supporting material underneath (here, Cu vs. vacuum) could strongly influence Sb nanostructure growth results[38]. This is important to consider when designing Sb 2D/2D heterostructure stacks. Finally, in Figure 4.13g,h it is shown that the here derived understanding of the balance of adsorption, nucleation, desorption and "sub-support" can also be advantageously employed to engineer larger Sb deposits of high crystalline quality. Figure 4.13g,h shows deposition of nominally ~50 nm Sb at 250 °C on Cu-supported (Figure 4.13g) and freely suspended graphene (Figure 4.13h). On the Cu-supported graphene, increasing the deposited Sb amount led not only to laterally larger Sb domains but to the onset of undesired three-dimensional Sb overgrowth (Figure 4.13g). In contrast, the relatively higher desorption on the suspended graphene enabled a lower Sb nucleation density and consequently a desired larger lateral growth of remaining Sb crystallites (Figure 4.13h, since presumably desorption probability decreases with increasing deposit radius). Thereby by adjusting the substrate underneath the actual graphene support, a lateral size of >400 nm diagonal for β-Sb(001) and >500 nm long axis for β-Sb[2-21]/cubic Sb(001) deposits, respectively could be obtained. This was an improvement not only over the undesired three-dimensional Sb overgrowth from Cu/graphene supported 250 °C/50 nm but also an improvement of factor ~2 compared to the 250 °C/10 nm Cu/graphene-supported deposits. This introduced the substrate underneath the direct 2D support as an important parameter to consider in 2D Sb deposition.

"Temperature and substrate under monolayer graphene have been highlighted as an important parameter to consider for realization of 2D antimonene, while temperature of the substrate governs the crystallization and morphology of the deposited few-layered antimonene, direct support underneath substrate plays a vital role in promoting the large lateral growth for deposited 2D antimonene structures"

4.4 Conclusion

In summary, using high resolution STEM, the structural relations in 2D Sb/graphene heterostructures was elucidated which is presented as a model system for 2D Sb's use in

Die approbierte gedruckte Originalversion dieser Dissertation ist an der TU Wien Bibliothek verfügbar.
The approved original version of this doctoral thesis is available in print at TU Wien Bibliothek.
TU Bibliothek Your knowledge hub WIEN

electronics and energy applications. Two Sb morphologies were found to co-exist under optimized deposition conditions: Few-layer 2D β-Sb(001)||graphene(001) and 1D Sb which could be matched to both Sb[2-21]⊥graphene(001) and cubic Sb(001)||graphene(001). Notably, both morphologies exhibited direct in-plane rotational vdW epitaxy with the graphene support. Both morphologies were stable against ambient air oxidation even for prolonged storage, albeit superficial surface Sb-oxide formation was found. Notably, for β-Sb(001) growth of an epitaxial Sb_2O_3(111)||β-Sb(001) overlayer was suggested from the here presented data. While exact Sb growth results depend on growth parameters such as temperature, importantly also the nature of the support under the direct graphene support was found to have a key influence on Sb growth. Combined, these findings explored at high resolution the structural diversity in scalably fabricated 2D Sb and in 2D Sb/graphene heterostructures.

4.5 References

1. Pumera, M. & Sofer, Z. 2D Monoelemental Arsenene, Antimonene, and Bismuthene: Beyond Black Phosphorus. *Adv. Mater.* **29**, n/a-n/a (2017).
2. Zhang, S. *et al.* Recent progress in 2D group-VA semiconductors: from theory to experiment. *Chem. Soc. Rev.* (2017) doi:10.1039/C7CS00125H.
3. Ersan, F. *et al.* Two-dimensional pnictogens: A review of recent progresses and future research directions. *Applied Physics Reviews* **6**, 021308 (2019).
4. Zhao, A. *et al.* Review of 2D group VA material-based heterostructures. *J. Phys. D: Appl. Phys.* **53**, 293002 (2020).
5. Ares, P., Palacios, J. J., Abellán, G., Gómez-Herrero, J. & Zamora, F. Recent Progress on Antimonene: A New Bidimensional Material. *Adv. Mater.* **30**, n/a-n/a (2018).
6. Wang, X., Song, J. & Qu, J. Antimonene: From Experimental Preparation to Practical Application. *Angewandte Chemie International Edition* **58**, 1574–1584 (2019).
7. Zhang, S., Yan, Z., Li, Y., Chen, Z. & Zeng, H. Atomically Thin Arsenene and Antimonene: Semimetal–Semiconductor and Indirect–Direct Band-Gap Transitions. *Angew. Chem. Int. Ed.* **54**, 3112–3115 (2015).
8. Wang, G., Pandey, R. & Karna, S. P. Atomically thin group-V elemental films: theoretical investigations of antimonene allotropes. *ACS Applied Materials & Interfaces* **7**, 11490–11496 (2015).
9. Pizzi, G. *et al.* Performance of arsenene and antimonene double-gate MOSFETs from first principles. *Nature Communications* **7**, 12585 (2016).
10. Zhao, M., Zhang, X. & Li, L. Strain-driven band inversion and topological aspects in Antimonene. *Sci Rep* **5**, (2015).
11. Qian, J. *et al.* High capacity Na-storage and superior cyclability of nanocomposite Sb/C anode for Na-ion batteries. *Chem. Commun.* **48**, 7070–7072 (2012).

Die approbierte gedruckte Originalversion dieser Dissertation ist an der TU Wien Bibliothek verfügbar.
The approved original version of this doctoral thesis is available in print at TU Wien Bibliothek.
TU Bibliothek Your knowledge hub WIEN

12. Zhou, X. *et al.* Sb nanoparticles decorated N-rich carbon nanosheets as anode materials for sodium ion batteries with superior rate capability and long cycling stability. *Chem. Commun.* **50**, 12888–12891 (2014).
13. Hu, L. *et al.* A Chemically Coupled Antimony/Multilayer Graphene Hybrid as a High-Performance Anode for Sodium-Ion Batteries. *Chem. Mater.* **27**, 8138–8145 (2015).
14. Cheng, Y. *et al.* Nanostructured Carbon/Antimony Composites as Anode Materials for Lithium-Ion Batteries with Long Life. *Chemistry – An Asian Journal* **11**, 2173–2180 (2016).
15. Liu, X. *et al.* Enhancing the Anode Performance of Antimony through Nitrogen-Doped Car bon and Carbon Nanotubes. *J. Phys. Chem. C* **120**, 3214–3220 (2016).
16. Gu, J. *et al.* Liquid-Phase Exfoliated Metallic Antimony Nanosheets toward High Volumetric Sodium Storage. *Adv. Energy Mater.* **7**, n/a-n/a (2017).
17. Cui, C. *et al.* Antimony Nanorod Encapsulated in Cross-Linked Carbon for High-Performance Sodium Ion Battery Anodes. *Nano Lett.* **19**, 538–544 (2019).
18. Tian, W. *et al.* Few-Layer Antimonene: Anisotropic Expansion and Reversible Crystalline-Phase Evolution Enable Large-Capacity and Long-Life Na-Ion Batteries. *ACS Nano* **12**, 1887–1893 (2018).
19. Wang, H., Wu, X., Qi, X., Zhao, W. & Ju, Z. Sb nanoparticles encapsulated in 3D porous carbon as anode material for lithium-ion and potassium-ion batteries. *Materials Research Bulletin* **103**, 32–37 (2018).
20. Zhang, X. *et al.* Metallic Sb nanoparticles embedded in carbon nanosheets as anode material for lithium ion batteries with superior rate capability and long cycling stability. *Electrochimica Acta* **283**, 1689–1694 (2018).
21. Walter, M., Erni, R. & Kovalenko, M. V. Inexpensive Antimony Nanocrystals and Their Composites with Red Phosphorus as High-Performance Anode Materials for Na-ion Batteries. *Scientific Reports* **5**, 8418 (2015).
22. Li, F. *et al.* Unlocking the Electrocatalytic Activity of Antimony for CO2 Reduction by Two-Dimensional Engineering of the Bulk Material. *Angewandte Chemie International Edition* **56**, 14718–14722 (2017).
23. Gusmão, R., Sofer, Z., Bouša, D. & Pumera, M. Pnictogen (As, Sb, Bi) Nanosheets for Electrochemical Applications Are Produced by Shear Exfoliation Using Kitchen Blenders. *Angew. Chem. Int. Ed.* **56**, 14417–14422 (2017).
24. Yu, X. *et al.* Emerging 2D pnictogens for catalytic applications: status and challenges. *Journal of Materials Chemistry A* **8**, 12887–12927 (2020).
25. Martínez-Periñán, E. *et al.* Antimonene: A Novel 2D Nanomaterial for Supercapacitor Applications. *Adv. Energy Mater.* n/a-n/a doi:10.1002/aenm.201702606.
26. Wang, X. *et al.* Bandgap-Tunable Preparation of Smooth and Large Two-Dimensional Antimonene. *Angewandte Chemie International Edition* **57**, 8668–8673 (2018).
27. Chen, K.-X. *et al.* Excellent Thermoelectric Performance Predicted in Two-Dimensional Buckled Antimonene: A First-Principles Study. *J. Phys. Chem. C* **121**, 13035–13042 (2017).
28. Zhang, S. *et al.* Semiconducting Group 15 Monolayers: A Broad Range of Band Gaps and High Carrier Mobilities. *Angew. Chem. Int. Ed.* **55**, 1666–1669 (2016).
29. Aktürk, O. Ü., Özçelik, V. O. & Ciraci, S. Single-layer crystalline phases of antimony: Antimonenes. *Phys. Rev. B* **91**, 235446 (2015).
30. Hogan, C. *et al.* Temperature Driven Phase Transition at the Antimonene/Bi_2Se_3 van der Waals Heterostructure. *ACS Nano* **13**, 10481–10489 (2019).
31. Fortin-Deschênes, M. *et al.* Pnictogens Allotropy and Phase Transformation during van der Waals Growth. *Nano Lett.* **20**, 8258–8266 (2020).

Die approbierte gedruckte Originalversion dieser Dissertation ist an der TU Wien Bibliothek verfügbar.
The approved original version of this doctoral thesis is available in print at TU Wien Bibliothek.
TU Bibliothek WIEN Your knowledge hub

32. Lei, T. *et al.* Electronic structure of antimonene grown on Sb2Te3 (111) and Bi2Te3 substrates. *Journal of Applied Physics* **119**, 015302 (2016).
33. Ji, J. *et al.* Two-dimensional antimonene single crystals grown by van der Waals epitaxy. *Nature Communications* **7**, 13352 (2016).
34. Tsai, H.-S., Chen, C.-W., Hsiao, C.-H., Ouyang, H. & Liang, J.-H. The advent of multilayer antimonene nanoribbons with room temperature orange light emission. *Chem. Commun.* **52**, 8409–8412 (2016).
35. Fortin-Deschênes, M. *et al.* Synthesis of Antimonene on Germanium. *Nano Lett.* **17**, 4970–4975 (2017).
36. Wu, X. *et al.* Epitaxial Growth and Air-Stability of Monolayer Antimonene on PdTe2. *Advanced Materials* **29**, 1605407 (2017).
37. Chen, H.-A. *et al.* Single-Crystal Antimonene Films Prepared by Molecular Beam Epitaxy: Selective Growth and Contact Resistance Reduction of the 2D Material Heterostructure. *ACS Appl. Mater. Interfaces* **10**, 15058–15064 (2018).
38. Sun, X. *et al.* van der Waals Epitaxy of Antimony Islands, Sheets, and Thin Films on Single-Crystalline Graphene. *ACS Nano* (2018) doi:10.1021/acsnano.8b02374.
39. Liu, X. *et al.* High-performance asymmetric electrodes photodiode based on Sb/WSe2 heterostructure. *Nano Res.* **12**, 339–344 (2019).
40. Shao, Y. *et al.* Epitaxial Growth of Flat Antimonene Monolayer: A New Honeycomb Analogue of Graphene. *Nano Lett.* **18**, 2133–2139 (2018).
41. Mao, Y.-H. *et al.* Epitaxial growth of highly strained antimonene on Ag (111). *arXiv:1803.09865 [cond-mat]* (2018).
42. Ares, P. *et al.* Mechanical Isolation of Highly Stable Antimonene under Ambient Conditions. *Adv. Mater.* **28**, 6332–6336 (2016).
43. Gibaja, C. *et al. Few-Layer Antimonene by Liquid-Phase Exfoliation*. (2016). doi:10.1002/ange.201609591.
44. Fortin-Deschênes, M. *et al.* Dynamics of Antimonene–Graphene Van Der Waals Growth. *Advanced Materials* **31**, 1900569 (2019).
45. Märkl, T. *et al.* Engineering multiple topological phases in nanoscale Van der Waals heterostructures: realisation of α -antimonene. *2D Mater.* **5**, 011002 (2018).
46. Shi, Z.-Q. *et al.* Van der Waals Heteroepitaxial Growth of Monolayer Sb in a Puckered Honeycomb Structure. *Advanced Materials* **31**, 1806130 (2019).
47. Akhtar, D., Vankar, V. D., Goel, T. C. & Chopra, K. L. Metastable structures of liquid-quenched and vapour-quenched antimony films. *J Mater Sci* **14**, 988–994 (1979).
48. Isshiki, T., Nishio, K., Saijo, H. & Shiojiri, M. Growth and crystallographic, surface and defect structures of antimony particles deposited in a high-resolution transmission electron microscope. *Thin Solid Films* **237**, 155–159 (1994).
49. Bernhardt, T. M., Stegemann, B., Kaiser, B. & Rademann, K. Crystalline Structures of Sb4 Molecules in Antimony Thin Films. *Angewandte Chemie International Edition* **42**, 199–202 (2003).
50. Kushvaha, S. S., Yan, Z., Xiao, W. & Wang, X.-S. Surface morphology of crystalline antimony islands on graphite at room temperature. *J. Phys.: Condens. Matter* **18**, 3425 (2006).
51. Yan, Z., Kushvaha, S. S., Xiao, W. & Wang, X.-S. Different-dimensional structures of antimony formed selectively on graphite. *Appl. Phys. A* **88**, 299–307 (2007).
52. Kolobyanina, T. N., Kabalkina, S. S., Vereshchagin, L. F. & Fedina, L. V. Investigation of the crystal structure of antimony at high pressures. *SOV PHYS JETP* **28**, 88–90 (1969).
53. Chang, K. J. & Cohen, M. L. Rhombohedral phase stability of the group-VA elements. *Phys. Rev. B* **33**, 7371–7374 (1986).

Die approbierte gedruckte Originalversion dieser Dissertation ist an der TU Wien Bibliothek verfügbar.
The approved original version of this doctoral thesis is available in print at TU Wien Bibliothek.
TU Bibliothek Your knowledge hub WIEN

54. Wang, X., Kunc, K., Loa, I., Schwarz, U. & Syassen, K. Effect of pressure on the Raman modes of antimony. *Phys. Rev. B* **74**, 134305 (2006).
55. Zouhar, M. & Šob, M. *Ab initio* study of deformed As, Sb, and Bi with an application to thin films. *Phys. Rev. B* **94**, 184110 (2016).
56. Sun, L. *et al.* Band structure and thermoelectric performances of antimony under trigonal transformation. *Journal of Applied Physics* **125**, 145102 (2019).
57. Wang, Y. & Ding, Y. The electronic structures of group-V–group-IV hetero-bilayer structures: a first-principles study. *Phys. Chem. Chem. Phys.* **17**, 27769–27776 (2015).
58. Li, W., Wang, X. & Dai, X. Tunable Schottky contacts in the antimonene/graphene van der Waals heterostructures. *Solid State Communications* **254**, 37–41 (2017).
59. Pantelic, R. S., Meyer, J. C., Kaiser, U. & Stahlberg, H. The application of graphene as a sample support in transmission electron microscopy. *Solid State Communications* **152**, 1375–1382 (2012).
60. Krivanek, O. L. *et al.* Atom-by-atom structural and chemical analysis by annular dark-field electron microscopy. *Nature* **464**, 571–574 (2010).
61. Predel, B. Sb-W (Antimony-Tungsten). in *Pu-Re – Zn-Zr* (ed. Madelung, O.) vol. 5 J 1–1 (Springer-Verlag, 1998).
62. Gates-Rector, S. & Blanton, T. The Powder Diffraction File: a quality materials characterization database. *Powder Diffraction* **34**, 352–360 (2019).
63. Momma, K. & Izumi, F. VESTA: a three-dimensional visualization system for electronic and structural analysis. *J Appl Cryst* **41**, 653–658 (2008).
64. Mozharivskyj, Y., Pecharsky, A. O., Bud'ko, S. & Miller, G. J. A Promising Thermoelectric Material: Zn_4Sb_3 or $Zn_{6-\delta}Sb_5$. Its Composition, Structure, Stability, and Polymorphs. Structure and Stability of $Zn_{1-\delta}Sb$. *Chemistry of Materials* **16**, 1580–1589 (2004).
65. Svensson, C. Refinement of the crystal structure of cubic antimony trioxide, Sb2O3. *Acta Cryst B, Acta Cryst Sect B, Acta Crystallogr B, Acta Crystallogr Sect B, Acta Crystallogr B Struct Crystallogr Cryst Chem, Acta Crystallogr Sect B Struct Crystallogr Cryst Chem* **31**, 2016–2018 (1975).
66. Abramoff, M., Magalhães, P. & Ram, S. J. Image Processing with ImageJ. *Biophotonics International* **11**, 36–42 (2003).
67. Li, X. *et al.* Large-area synthesis of high-quality and uniform graphene films on copper foils. *Science* **324**, 1312–1314 (2009).
68. Kidambi, P. R. *et al.* Observing graphene grow: catalyst-graphene interactions during scalable graphene growth on polycrystalline copper. *Nano Lett* **13**, 4769–4778 (2013).
69. Regan, W. *et al.* A direct transfer of layer-area graphene. *Appl. Phys. Lett.* **96**, 113102 (2010).
70. Wu, Q. *et al.* Two-dimensional semiconducting and single-crystalline antimony trioxide directly-grown on monolayer graphene. *Chem. Commun.* **55**, 2473–2476 (2019).
71. Deng, Y., Handoko, A. D., Du, Y., Xi, S. & Yeo, B. S. *In Situ* Raman Spectroscopy of Copper and Copper Oxide Surfaces during Electrochemical Oxygen Evolution Reaction: Identification of Cu^{III} Oxides as Catalytically Active Species. *ACS Catal.* **6**, 2473–2481 (2016).
72. Kidambi, P. R. *et al.* The Parameter Space of Graphene Chemical Vapor Deposition on Polycrystalline Cu. *J. Phys. Chem. C* **116**, 22492–22501 (2012).
73. Rathore, J. & Mahapatra, S. Formation of antimonene nanoribbons by molecular beam epitaxy. *2D Mater.* **7**, 045003 (2020).

Die approbierte gedruckte Originalversion dieser Dissertation ist an der TU Wien Bibliothek verfügbar.
The approved original version of this doctoral thesis is available in print at TU Wien Bibliothek.
TU Bibliothek Your knowledge hub WIEN

74. Hummel, S. *et al.* Direct visualization of local deformations in suspended few-layer graphene membranes by coupled in situ atomic force and scanning electron microscopy. *Appl. Phys. Lett.* **118**, 103104 (2021).
75. Liu, Y., Huang, Y. & Duan, X. Van der Waals integration before and beyond two-dimensional materials. *Nature* **567**, 323–333 (2019).
76. Kim, Y. *et al.* Remote epitaxy through graphene enables two-dimensional material-based layer transfer. *Nature* **544**, 340–343 (2017).
77. Niu, T. *et al.* Modulating Epitaxial Atomic Structure of Antimonene through Interface Design. *Advanced Materials* **31**, 1902606 (2019).
78. Niu, T. *et al.* Large-Scale Synthesis of Strain-Tunable Semiconducting Antimonene on Copper Oxide. *Advanced Materials* **32**, 1906873 (2020).
79. *Materials Science of Thin Films*. (Elsevier, 2002). doi:10.1016/B978-0-12-524975-1.X5000-9.
80. Bayer, B. C. *et al.* Atomic-Scale *in Situ* Observations of Crystallization and Restructuring Processes in Two-Dimensional MoS_2 Films. *ACS Nano* **12**, 8758–8769 (2018).
81. Zhang, S. *et al.* Antimonene Oxides: Emerging Tunable Direct Bandgap Semiconductor and Novel Topological Insulator. *Nano Lett.* **17**, 3434–3440 (2017).
82. Wolff, S., Gillen, R., Assebban, M., Abellán, G. & Maultzsch, J. Two-Dimensional Antimony Oxide. *Phys. Rev. Lett.* **124**, 126101 (2020).
83. Wu, Q. & Song, Y. J. The environmental stability of large-size and single-crystalline antimony flakes grown by chemical vapor deposition on SiO2 substrates. *Chem. Commun.* **54**, 9671–9674 (2018).
84. Fuchs, G. *et al.* Electron irradiation effects in amorphous antimony thin films obtained by cluster-beam deposition. *Philosophical Magazine B* **63**, 715–725 (1991).
85. Assebban, M. *et al.* Unveiling the oxidation behavior of liquid-phase exfoliated antimony nanosheets. *2D Mater.* **7**, 025039 (2020).
86. Bat-Erdene, M. *et al.* Surface oxidized two-dimensional antimonene nanosheets for electrochemical ammonia synthesis under ambient conditions. *J. Mater. Chem. A* **8**, 4735–4739 (2020).
87. Sun, K., Liu, J. & Browning, N. D. Correlated Atomic Resolution Microscopy and Spectroscopy Studies of Sn(Sb)O2 Nanophase Catalysts. *Journal of Catalysis* **205**, 266–277 (2002).
88. Bouchet, D., Roy, E., Yu-Zhang, K. & Leprince-Wang, Y. *TEM and EELS studies of electrodeposited antimony nanowires*. vol. 30 (2005).
89. Wang, Y. W. *et al.* Antimony Nanowires Self-Assembled from Sb Nanoparticles. *J. Phys. Chem. B* **108**, 16723–16726 (2004).
90. Gass, M. H. *et al.* Free-standing graphene at atomic resolution. *Nature Nanotechnology* **3**, 676–681 (2008).
91. Singh, D., Gupta, S. K., Sonvane, Y. & Lukačević, I. Antimonene: a monolayer material for ultraviolet optical nanodevices. *J. Mater. Chem. C* **4**, 6386–6390 (2016).
92. Rafiee, J. *et al.* Wetting transparency of graphene. *Nature Materials* **11**, 217–222 (2012).

Die approbierte gedruckte Originalversion dieser Dissertation ist an der TU Wien Bibliothek verfügbar.
The approved original version of this doctoral thesis is available in print at TU Wien Bibliothek.
TU Bibliothek Your knowledge hub WIEN

Outcome:

Paper I:

"Resolving Few-Layer Antimonene/Graphene Heterostructures"

npj | 2D Materials and Applications www.nature.com/npj2dmaterials

ARTICLE OPEN Check for updates

Resolving few-layer antimonene/graphene heterostructures

Tushar Gupta[1], Kenan Elibol[2], Stefan Hummel[2,3], Michael Stöger-Pollach[4], Clemens Mangler[2], Gerlinde Habler[5], Jannik C. Meyer[2], Dominik Eder[1] ✉ and Bernhard C. Bayer[1,2] ✉

Two-dimensional (2D) antimony (Sb, "antimonene") is of interest in electronics and batteries. Sb however exhibits a large allotropic structural diversity, which is also influenced by its support. Thus, Sb heterostructure formation is key in 2D Sb integration. Particularly, 2D Sb/graphene interfaces are important. We thus study here few-layered 2D Sb/graphene heterostructures with atomic resolution (scanning) transmission electron microscopy. We find two Sb morphologies to coexist: first, a 2D morphology of layered β-Sb with β-Sb(001)||graphene(001) texture. Second, one-dimensional Sb nanowires which can be matched to β-Sb[2-21]⊥graphene(001) and are closely related to cubic Sb(001)||graphene(001). Importantly, both Sb morphologies show rotational van-der-Waals epitaxy with graphene. Both are resilient against oxidation, although superficial Sb-oxide formation merits consideration, including epitaxial Sb_2O_3(111)/β-Sb(001) heterostructures. Exact Sb growth behavior depends on processing and substrate properties including, notably, the support underneath the graphene. Our work elucidates the rich phase and epitaxy landscape in 2D Sb and 2D Sb/graphene heterostructures.

npj 2D Materials and Applications (2021)5:53 ; https://doi.org/10.1038/s41699-021-00230-3

Die approbierte gedruckte Originalversion dieser Dissertation ist an der TU Wien Bibliothek verfügbar.
The approved original version of this doctoral thesis is available in print at TU Wien Bibliothek.
TU Bibliothek Your knowledge hub WIEN

Chapter 5

Bismuthene/Graphene Heterostructures

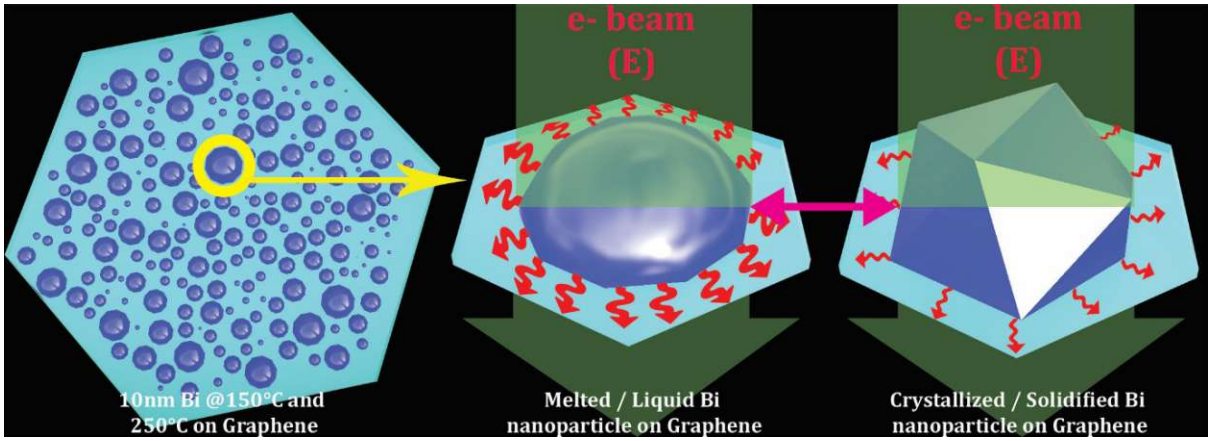

Die approbierte gedruckte Originalversion dieser Dissertation ist an der TU Wien Bibliothek verfügbar.
TU Bibliothek
WIEN Vourknowledge hub

Chapter Preview

Chapter 5 *expands the scope of studies performed on antimonene to its fellow pnictogen member bismuthene. The chapter helps unravel the different response of bismuthene as compared to antimonene when subjected to exactly similar processing conditions.*

Mixed-dimensional heterostructures of low-dimensional bismuth (Bi) with two-dimensional (2D) graphene are of interest in a variety of application fields ranging from nanoelectronics, next-generation batteries, (photo-)catalysis to plasmonics. The studies here explore the evolution of morphology and structure of low-dimensional Bi/graphene heterostructures by high-resolution (scanning) transmission electron microscopy ((S)TEM). To this end, low-dimensional Bi nanostructures were physical vapor deposited onto suspended monolayer graphene membranes. This facilitates intrinsic study of Bi/graphene interactions, in contrast to prior works that utilized Bi on itself supported graphene. Bi deposited onto room temperature graphene consisted grains formed by irregular shaped β-Bi crystals with β-Bi[001]⊥graphene(001) texture crystals and β-Bi nanorods with β-Bi[2-21]⊥graphene(001) texture. Importantly, both texture types show rotational van-der-Waals (vdW) epitaxy with the supporting graphene. The room temperature depositions grow via an initial amorphous β-Bi[2-21]-like state into a closed film of β-Bi structure. For higher graphene temperatures of 150 °C to 250 °C during deposition, formation of amorphous Bi nanoparticles at much reduced coverage due to Bi liquification, undercooling and reverse desorption at these temperatures was observed. While the room temperature deposited Bi films remain static under the electron beam in the (S)TEM, the amorphous Bi nanoparticles from higher temperature depositions exhibit electron beam induced in situ crystallisation in the TEM. In parallel to observing their structural evolution during this crystallisation, this study also probes the evolution of plasmonic features of Bi nanoparticles via (valence) electron energy loss spectroscopy ((V)EELS), thus suggesting a link between crystallisation state and Bi nanoparticle's surface plasmon energy. The figure caption for chapter 5 is a schematic representation of the electron beam induced crystallization of the Bi nanoparticles. ***The contents of this chapter are nearing to submission for publication.***

Die approbierte gedruckte Originalversion dieser Dissertation ist an der TU Wien Bibliothek verfügbar.
The approved original version of this doctoral thesis is available in print at TU Wien Bibliothek.
TU Bibliothek Your knowledge hub WIEN

5. Bismuthene/Graphene Heterostructures

5.1 Introduction

The allotropic wealth of low-dimensional pnictogens incl. antimony (Sb) and bismuth (Bi) has recently garnered tremendous attention.[1–5] This interest also includes mixed-dimensionality heterostructure formation, in which a low-dimensional (zero-, one- or two-dimensional (0D, 1D, 2D)) pnictogen is grown atop of a 2D material like graphene.[6–8] This study focuses on heterostructure formation of low-dimensional Bi on 2D graphene. Low-dimensional Bi is of high current interest due to its exotic electronic properties incl. readily emerging quantum size effects[9], topological insulation[10,11], large thermoelectric power[12,13], to its high suitability as anode material in next-generation batteries[14–18], due to its strong coupling with light as a plasmonic materials[19] and since also catalytically active as a potential material for (photo-)catalysis[20–22] and possibly even plasmon-driven catalysis[23,24].

All these Bi applications are intimately linked to the structure of the low-dimensional Bi, which is also intimately linked to the nature of the Bi's support, making heterostructure formation key in Bi applications. Among the various Bi heterostructure supports, graphene has been found to be of particular importance for applications: In 2D electronics, integration of 2D Bi ("bismuthene") with graphene has been found to eliminate metal induced gap states, thereby reducing Fermi-level pinning and enhancing the effective channel length because of weak van-der-Waals (vdW) interaction and thus mitigating contact resistances.[25] Also, Bi/graphene has been found useful in electrochemical sensing[26–28] applications. In energy applications, Bi/graphene heterostructures were found to be an optimum electrode material for next generation batteries[14–18,20,29–32] In catalysis, mixed-dimensionality Bi/graphene heterostructures have recently proven their photocatalytic activity under the excitation ranging from ultra-violet to infra-red with long term performance stability[20].

Die approbierte gedruckte Originalversion dieser Dissertation ist an der TU Wien Bibliothek verfügbar.
The approved original version of this doctoral thesis is available in print at TU Wien Bibliothek.
TU WIEN Bibliothek Your knowledge hub

Another key application field for Bi nanoparticles is plasmonics incl. demonstration of switchable localized optical resonances, paving the way toward possible applications in optical switches. Key to useful optical switching are plasmonic materials[19] that are (i) responsive to external stimuli and (ii) support optical resonances in the UV.[33,34] In particular, plasmonic nanostructures that exhibit phase transitions are found to be more suitable candidates for such switching applications.[35–38] Compared to conventional noble metal plasmonic structures[19], Bi nanoparticles can have external stimuli dependent phase transitions above room temperature incl. readily accessible melting/solidification[38] and show a contrast in dielectric function from UV to near IR range on account of the melting and solidification processes.[39] Ultrathin graphene may be a highly useful support materials for such plasmonic applications of nanostructured Bi[40]. In this context also, a further possible confluence of the plasmonic and photocatalysis applications of Bi on graphene is plasmonic catalysis, which is a currently emerging concept.[41,42] However, to date no dedicated work has been done on plasmonic properties of Bi nanoparticles on ultimately thin 2D graphene membranes.

In general, to date the exact structure relations in mixed-dimensionality Bi/graphene heterostructures often remain underexplored, in particular under dynamic conditions and at high resolution. Prior work has investigated mixed-dimensionality Bi/graphene heterostructures[43–45] but largely relied on ultra-high-vacuum (UHV) scanning tunnelling microscopy (STM) and also always had the Bi on graphene placed on an additional support which, depending on the strength of graphene-support interactions, can obscure the intrinsic Bi-graphene interactions.

In contrast, heterostructures formed from low-dimensional Bi from scalable physical vapour deposition (PVD) on truly *freestanding* monolayer graphene membranes are studied here. Hereby the graphene membranes act not only as 2D component in here fabricated heterostructures but also as an ideal substrate to make the low-dimensional Bi structure readily accessible to investigation by atomic-resolution (scanning) transmission electron microscopy ((S)TEM), due to graphene's low scattering background in (S)TEM.[46] This study thereby first maps out a parameter space of low-

Die approbierte gedruckte Originalversion dieser Dissertation ist an der TU Wien Bibliothek verfügbar.
The approved original version of this doctoral thesis is available in print at TU Wien Bibliothek.
TU Bibliothek Your knowledge hub WIEN

dimensional Bi morphology and structure on freestanding graphene with down to atomic resolution as function of archetypical Bi PVD conditions. This also includes investigation of vdW epitaxial effects between the Bi and the freestanding graphene in the heterostructures. Then, using the energy input of the electron beam in the (S)TEM as a proxy for *in situ* annealing,[8,47,48] the structural evolution of Bi/graphene heterostructures is probed. Notably, the plasmonic properties of the Bi nanoparticles as a function of their structural evolution by time-resolved *in situ* (valence) electron energy loss spectroscopy ((V)EELS) are also concurrently followed in this work.

5.2 Experimental Procedure

5.2.1 Growth of 2D Bi on graphene

PVD of Bi employed a commercial thermal evaporation system as already described in chapter 3 including the types of substrates employed. Phase diagrams[49] of W and Bi were cross-checked to ensure that no undesired intermetallics were formed during evaporation. As will be discussed later in the exploration of the parameter space of Bi PVD, actual retained Bi thicknesses can strongly reduce as a function of increasing substrate temperature via desorption effects.

"Thermal evaporation of 10nm nominal thickness of Bi on monolayer graphene suspended on Quantifoil transmission electron TEM grids and also on chemical vapor deposition (CVD) grown monolayer graphene supported on Cu tapes at RT, 150 °C and 250 °C"

5.2.2 Phase and epitaxy analysis of Bi deposits

Phase analysis of (S)TEM data employed primarily Fourier Transform (FT)/ Selected area electron diffraction (SAED) pattern simulation using Highscore Plus/Pdf4+ software

Die approbierte gedruckte Originalversion dieser Dissertation ist an der TU Wien Bibliothek verfügbar.
The approved original version of this doctoral thesis is available in print at TU Wien Bibliothek.
TU Bibliothek Your knowledge hub WIEN

(ICDD Pdf4+ 2021 RDB: Software version: 4.21.0.2. Database version: 4.2103.)[50] for manual matching of measured and simulated FT/SAED patterns. Structure visualization was done by Vesta[51] software. In particular the following structural database entries were found to best fit the measured FT and SAED (Pdf4+ code/literature reference): β-Bi (A7, rhombohedral, R-3m): 04-007-5315/ref. 52 ; graphene (graphite, hexagonal, P63/mmc): 00-056-0159/ref. 53. Figure 5.3 shows salient simulated FT/SAED patterns of β-Bi along [001] (β-Bi(001)) and [2-21] zone-axes and graphene [001] zone axis (graphene(001)) along with their atomic models in both top and side views. Please note that in this chapter, when describing β-Bi phase exclusively hexagonal labelling system has been adopted for β-Bi (hkl) plane and [uvw] direction notations. Equivalent rhombohedral labelling is also often used for β-Bi in literature for which a conversion table is available.[54]

5.3 Results and Discussion

5.3.1 Bi PVD Parameter Space

In Figure 5.1a,b,c, the morphology of Bi as a function of controlled graphene membrane substrate deposition temperature of RT, 150 °C and 250 °C for a fixed nominal Bi thickness of 10 nm is compared via bright field-transmission electron microscopic (BF-TEM) images. The RT deposition yields almost fully covering film-like deposits composed of predominantly pronounced, faceted grains (Figure 5.1a and Figure 5.2, areal coverage ~95 %). For the higher temperature depositions at 150 °C and 250 °C, the deposits change to small (projected diameter range ~3 nm to 20 nm), isolated non-faceted nanoparticles (Figure 5.1b,c). Concurrently, the amount of deposited Bi drastically decreased with increasing substrate temperature (to areal coverage ~11 % for 150 °C and ~0.4 % for 250 °C). Raman spectra of as deposited Bi depositions on graphene from RT, 150 °C, 250 °C depositions against the reference Raman spectrum of crystalline Bi bulk powder[55] is shown in Figure 5.1d. For bulk Bi powder two signature first order E_g and the A_{1g} Raman modes[56] of pure bismuth (β-Bi) at 68 cm^{-1} and 95 cm^{-1}, respectively were measured.[57–60] For the 10 nm Bi on graphene RT depositions, the E_g mode is

Die approbierte gedruckte Originalversion dieser Dissertation ist an der TU Wien Bibliothek verfügbar.
The approved original version of this doctoral thesis is available in print at TU Wien Bibliothek.
TU Bibliothek WIEN Your knowledge hub

observed at 72 cm^{-1} and A_{1g} mode at 94 cm^{-1}, respectively, also consistent with β-Bi structure. While E_g band undergoes a blue shift from bulk Bi powder to 10 nm RT Bi samples, the A_{1g} band for RT depositions shows a slight red shift. This is in accord with previous studies[57–59] suggesting thin layered nature of Bi deposits obtained during 10 nm Bi on graphene RT deposition. In the 150 °C and 250 °C samples, Raman peak intensities reduce below observable significant peaks. This points to low Raman signal due to the observed low coverage (Figure 5.1b,c) and/or an amorphous nature of the Bi deposits. The amorphous nature of the Bi at the 150 °C and 250 °C depositions will be confirmed by HRTEM below. Notably, Raman measurements in Figure 5.1d exclude formation of crystalline Bi-oxides from sample preparation or ambient air storage (in keeping with (S)TEM analysis below), as band corresponding to Bi-oxides at predominantly 128 cm^{-1}, 315 cm^{-1} and 461 cm^{-1} respectively[61–63] remain absent.

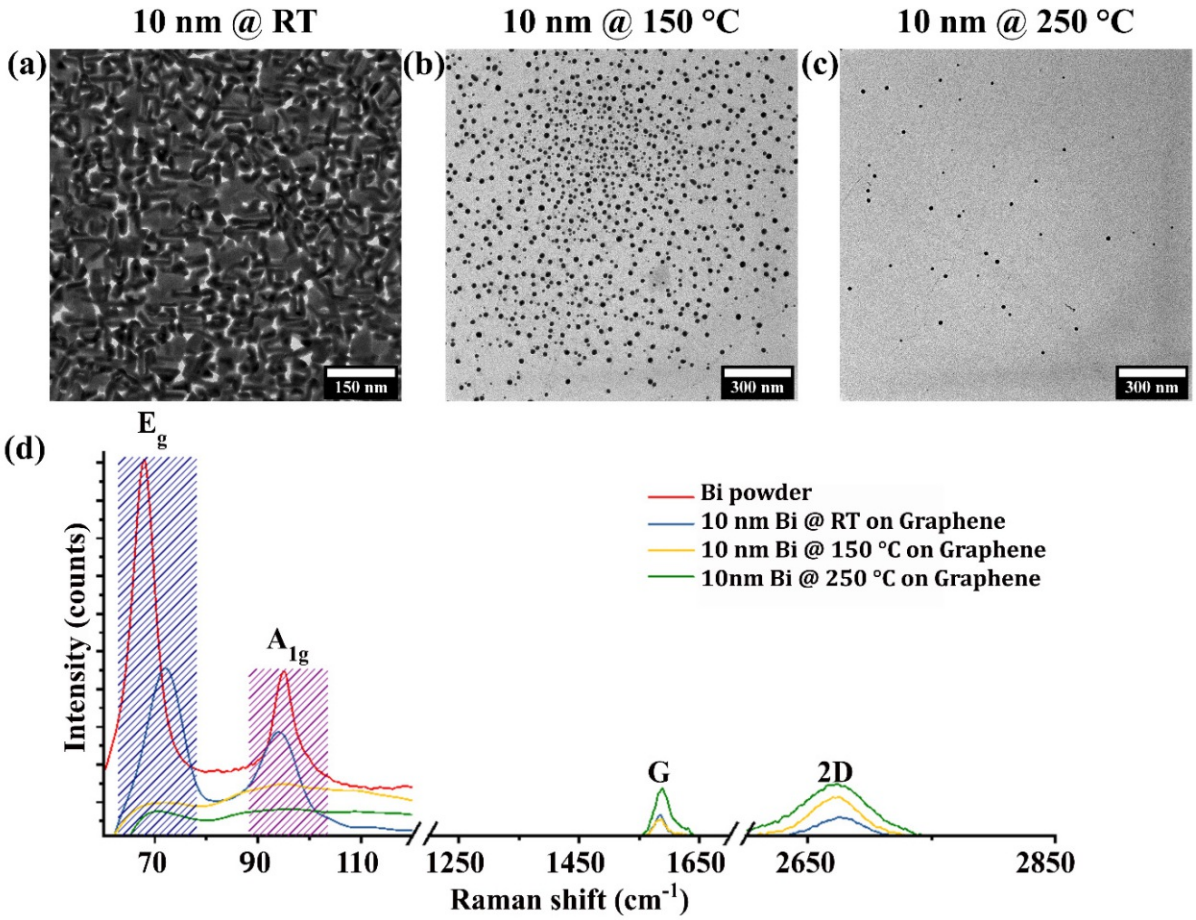

Figure 5.1: BF-TEM micrographs of nominally 10 nm Bi on freestanding monolayer CVD graphene membranes deposited at (a) RT, (b) 150 °C and (c) 250 °C substrate temperature. (d) Raman spectra measured on nominally 10 nm Bi on CVD graphene (remaining on Cu foil growth catalyst stack) deposited at RT, 150 °C and 250 °C and additionally, for reference, bulk Bi powder.

Die approbierte gedruckte Originalversion dieser Dissertation ist an der TU Wien Bibliothek verfügbar.
The approved original version of this doctoral thesis is available in print at TU Wien Bibliothek.
TU Bibliothek Your knowledge hub WIEN

Additional to the Bi features, graphene related G band at 1587 cm^{-1} and 2D band at 2674 cm^{-1} indicate the preserved high quality of the CVD graphene[64,65] substrate post deposition for all Bi deposition temperatures. Notably, no significant graphene-defect related D band intensity was observed at ~ 1350 cm^{-1} in any sample.[64,65] Observation of this Raman signature of high quality graphene after Bi deposition implies the presence of a vdW interaction at the Bi/graphene interface, i.e. absence of covalent Bi/graphene bonding.[5] Beyond Raman, the high quality of the graphene after Bi depositions is also evidenced by the clear SAED graphene reflections patterns for all deposition conditions presented below.[8] The observation of a vdW interface between Bi and graphene is consistent with previously reported density-functional-theory (DFT)[66] calculations and photoemission spectroscopic measurements.[67]

"Bi exhibits drastic change of morphology from film like deposits at RT to isolated spherical nanoparticle like morphology at 150 °C and 250 °C on graphene. This change of morphology is also accompanied by change in the areal coverage from ~ 95 % at RT to ~11 % at 150 °C and 0.4 % at 250 °C. This change of morphology with reduced areal coverage from RT to higher temperatures is because of low melting point of Bi."

5.3.2 RT Bi depositions

For the as deposited 10 nm Bi depositions at RT, films with three regions with different atomic arrangements were observed on the graphene supports, as observed via (S)TEM in Figure 5.2a,b. First are regions (example marked "1" in Figure 5.2a-c) showing well-crystallized six-fold symmetry of Bi atoms in projection (high resolution (S)TEM analysis in Figure 5.2c,d-f). This is assigned to thermodynamically most stable β-Bi allotrope (rhombohedral, R-3m, A7) with an out-of-plane texture of β-Bi[001] zone-axis perpendicular to graphene(001) (β-Bi[001]⊥graphene(001)), equivalent with β-Bi(001) plane parallel to graphene(001) (β-Bi(001)||graphene(001)).[68–70] Second are regions (example marked "2" in Figure 5.2a-c) with well crystallized four-fold symmetry of Bi atoms in projection (high resolution (S)TEM analysis in Figure 5.2c,g-i). This can be

Die approbierte gedruckte Originalversion dieser Dissertation ist an der TU Wien Bibliothek verfügbar.
The approved original version of this doctoral thesis is available in print at TU Wien Bibliothek.
TU Bibliothek Your knowledge hub WIEN

assigned to β-Bi with zone-axis β-Bi[2-21]⊥graphene(001) texture which shows a pseudo-cubic symmetry in projection. A very close terminating (but not perfectly parallel) plane for this texture is β-Bi(1-12), see Figure 5.3b. Since β-Bi(1-12) is equivalent to β-Bi(012), this orientation of β-Bi has in earlier literature often been referred to as β-Bi(012).[71] Notably, in projection this structure is similar to black-phosphorus alike A17 allotrope or α-Bi(001).[72–74] The two observed β-Bi textures will be referred to as β-Bi(001) and β-Bi[2-21], respectively, for the remainder of this chapter and of the thesis. Third are few regions (example marked "3" in Figure 5.2a,b) that show a predominantly amorphous structure. Close examination of these regions by FT, Figure 5.4) however reveals that these have also short range order consistent with the prime ~0.33 nm lattice distance found in β-Bi[2-21]. The amorphous regions are therefore assigned as less order predecessors ("amorphous β-Bi[2-21]-like") to the much more crystallized β-Bi[2-21] regions.

Beyond the β-Bi (001), β-Bi[2-21] and the few amorphous β-Bi[2-21]-like regions, no signs of other phases, e.g. Bi-oxides, have been detected by (S)TEM.[55] The absence of signs for further phases is in good keeping with the Raman data above. It was also noted that the RT depositions did not show any e-beam induced[8,47,48] structure or morphology changes under here employed imaging conditions but remained static also throughout extended imaging. See Figure 5.3 for simulated FT/ SAED patterns of β-Bi(001), β-Bi[2-21] and graphene(001) for reference against the experimental atomic-resolution data in Figure 5.2. In terms of morphology in Figure 5.2a-b, the six-fold symmetric β-Bi(001) and the amorphous β-Bi[2-21]-like regions are predominantly of irregular shape, while the four-fold symmetric β-Bi[2-21] are predominantly of one-dimensional rod-like shape. Figure 5.2b and Figure 5.4 however show that these β-Bi[2-21] rods do not terminate atomically perfectly and have several step edges in their terminal line projections. It was also noted that some rod-like appearing regions are also of six-fold symmetric β-Bi(001) structure. Readily visually apparent in Figure 5.1a and Figure 5.2a, is the preferred orientation of the long axes of rod-like deposits with respect to each other across the entire fields of view. Given that the graphene grains are μm-sized,[5,64] and thus the fields of view in Figure 5.1a and Figure 5.2a are likely single single-crystalline graphene grains, this apparent preferred orientation of Bi deposits could be indicative of rotational vdW

Die approbierte gedruckte Originalversion dieser Dissertation ist an der TU Wien Bibliothek verfügbar.
The approved original version of this doctoral thesis is available in print at TU Wien Bibliothek.
TU Bibliothek Your knowledge hub WIEN

epitaxy between the Bi and the graphene.[5,8,47] In Figure 5.5 this notion of possible vdW epitaxy is further explored.

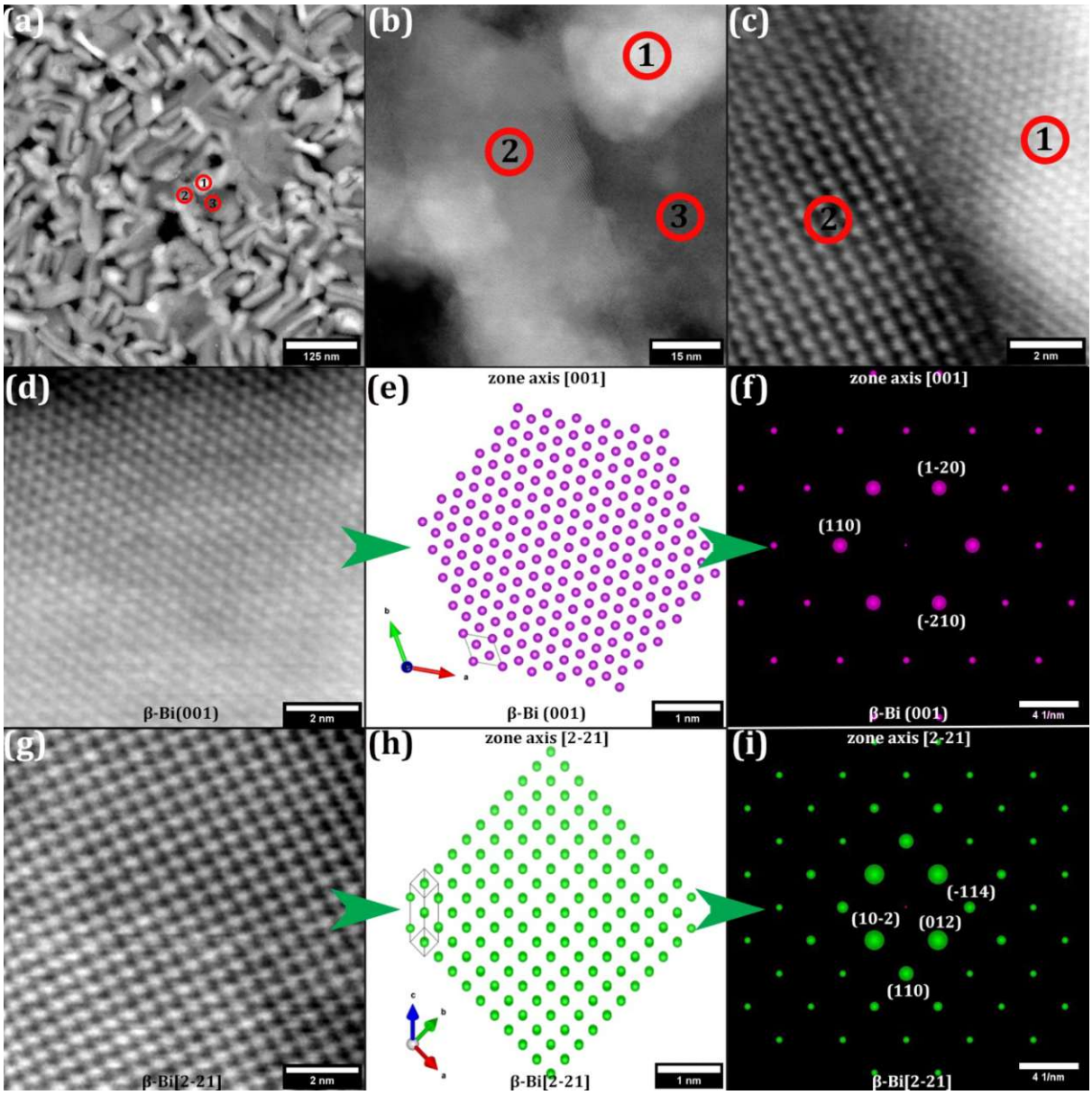

Figure 5.2: <u>RT Bi depositions (Texture)</u>: High-angle annular dark field (HAADF) (S)TEM images of 10 nm Bi films on graphene at RT outlining three different regions in overview (a,b) and at atomic resolution (c). d-f show atomically resolved (S)TEM image (d) atomic model (as in HAADF-(S)TEM) (e) and corresponding FT pattern (f) of β-Bi(001) marked as region 1 in a-c. The FT pattern is indexed to β-Bi(001) i.e. β-Bi viewed along [001] zone axis. g-i show atomically resolved (S)TEM image (g) atomic model (as in ADF-(S)TEM) (h) and corresponding FT pattern (i) of β-Bi[2-21] marked as region 2 in a-c. The FT pattern is indexed to β-Bi viewed along [2-21] zone axis. For further information on atomic models and FT simulations, see Figure 5.3. And for atomically resolved (S)TEM image and FT pattern of region 3 see Figure 5.4. The corresponding unit cells and zone axis for the atomic models has been indicated.

Die approbierte gedruckte Originalversion dieser Dissertation ist an der TU Wien Bibliothek verfügbar.
The approved original version of this doctoral thesis is available in print at TU Wien Bibliothek.
TU Bibliothek Your knowledge hub WIEN

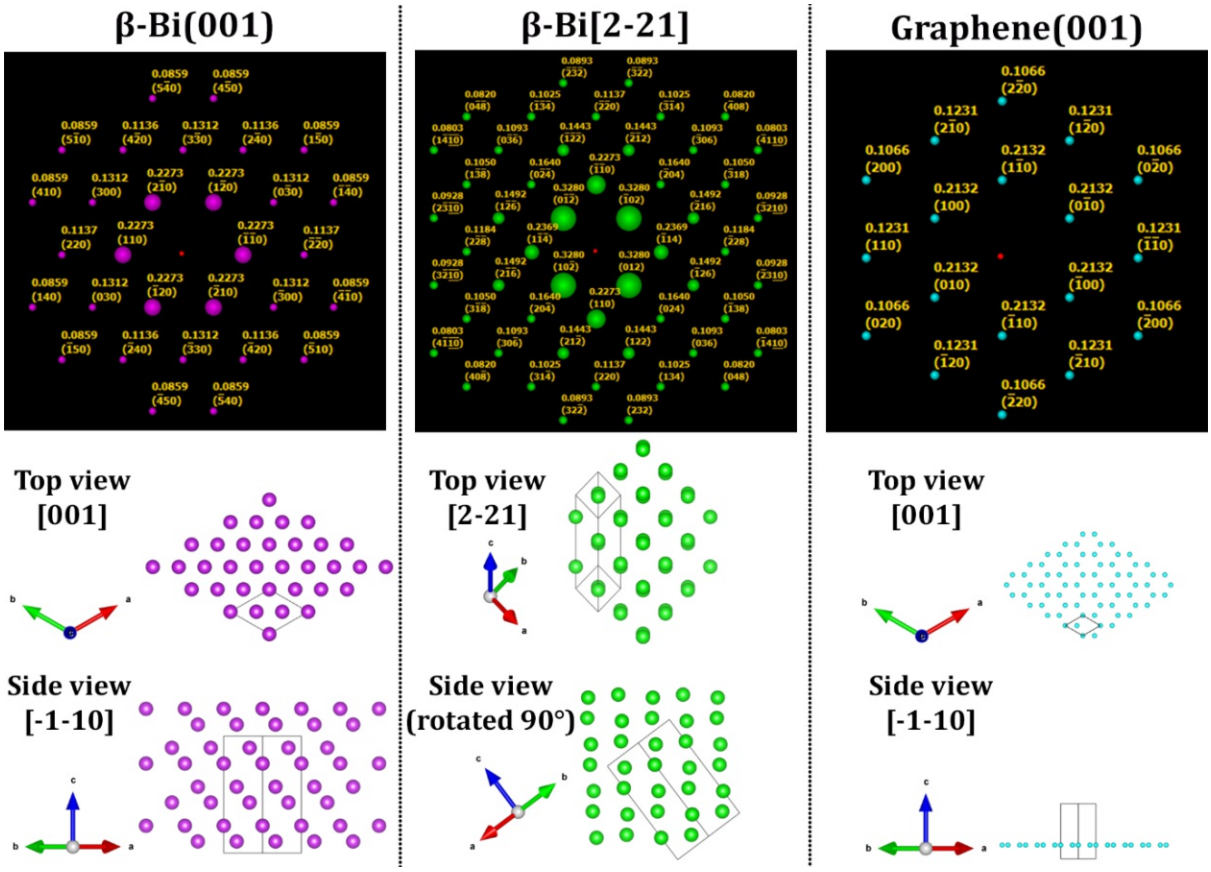

Figure 5.3: Simulated FT/SAED patterns (top) and corresponding atomic models in top/plan view (middle) and side view (below) of β-Bi(001), β-Bi[2-21] and graphene(001) respectively. The models in top view correspond to the atomic structure in ADF (S)TEM and BF TEM images of the Bi deposits on graphene. Unit cells and axes are also plotted and the zone axis for all views is indicated. Note that FT/SAED can have an arbitrary rotational offset with respect to the atomic top view sketches.

In particular, Figure 5.5a, inset plots a BF-TEM image of a 10 nm RT Bi film on graphene with its corresponding SAED pattern plotted in Figure 5.5a-d, left panels (in which the same SAED pattern is re-plotted four times in order to clearly illustrate the four different epitaxy assignments discussed in the following paragraphs). The highly sharp, six-fold SAED pattern for the graphene in Figure 5.5a-d (cyan indexing) indicates the excellent preservation of graphene structure upon Bi PVD. This corroborates formation of vdW interface between graphene and Bi, in full keeping with the Raman analysis above. Notably, the graphene-related SAED spots in Figure 5.5a-d (cyan indexing) are composed of only one single six-fold spot set. This confirms that in the field of view in Figure 5.5a, inset, only one individual, single single-crystalline graphene grain has been imaged. This readily allowed disentanglement of possible vdW epitaxial effects between the Bi deposits and the supporting single-crystalline graphene grain via SAED and BF-TEM.

Die approbierte gedruckte Originalversion dieser Dissertation ist an der TU Wien Bibliothek verfügbar.
The approved original version of this doctoral thesis is available in print at TU Wien Bibliothek.
TU Bibliothek Your knowledge hub WIEN

Indexing of the SAED in Figure 5.5a-d with respect to Bi indicates a phase mixture of β-Bi(001) (Figure 5.5a,b, magenta indexing) and β-Bi[2-21] (Figure 5.5c,d, green indexing) crystalline deposits, in keeping with (S)TEM data in Figure 5.1 (see also Figure 5.3 for reference of simulated SAED patterns). Importantly, Figure 5.5a-d shows that the reflections corresponding to β-Bi(001) (magenta indexing) and β-Bi[2-21] (green indexing) are not randomly arranged (forming rings) but have discrete intensity maxima at discrete rotation angles with respect to the six-fold graphene spots. This is a tell-tale sign of rotational vdW epitaxy between the graphene and the Bi deposits.[5,8]

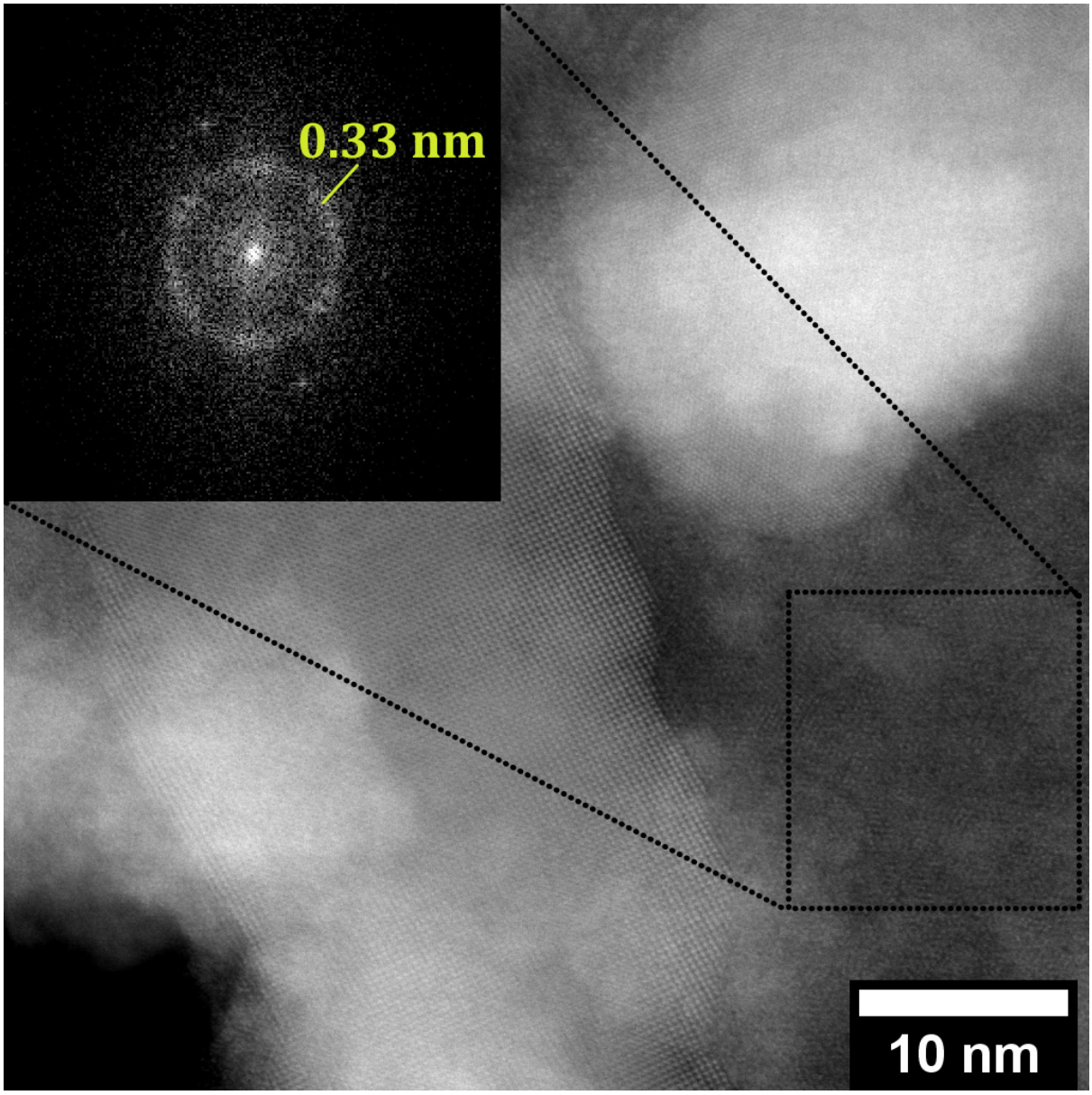

Figure 5.4: ADF (S)TEM images of 10 nm Bi films on graphene at RT outlining region 3 (as indexed in Fig. 2a,b) i.e. the amorphous β-Bi[2-21]. The FT pattern in the inset is recorded on the region 3

Die approbierte gedruckte Originalversion dieser Dissertation ist an der TU Wien Bibliothek verfügbar.
The approved original version of this doctoral thesis is available in print at TU Wien Bibliothek.
TU Bibliothek Your knowledge hub WIEN

(marked with dotted square). The ring in the FT pattern at d-spacing of 0.33 nm indicates the preferred orientation of this amorphous Bi phase to β-Bi[2-21].

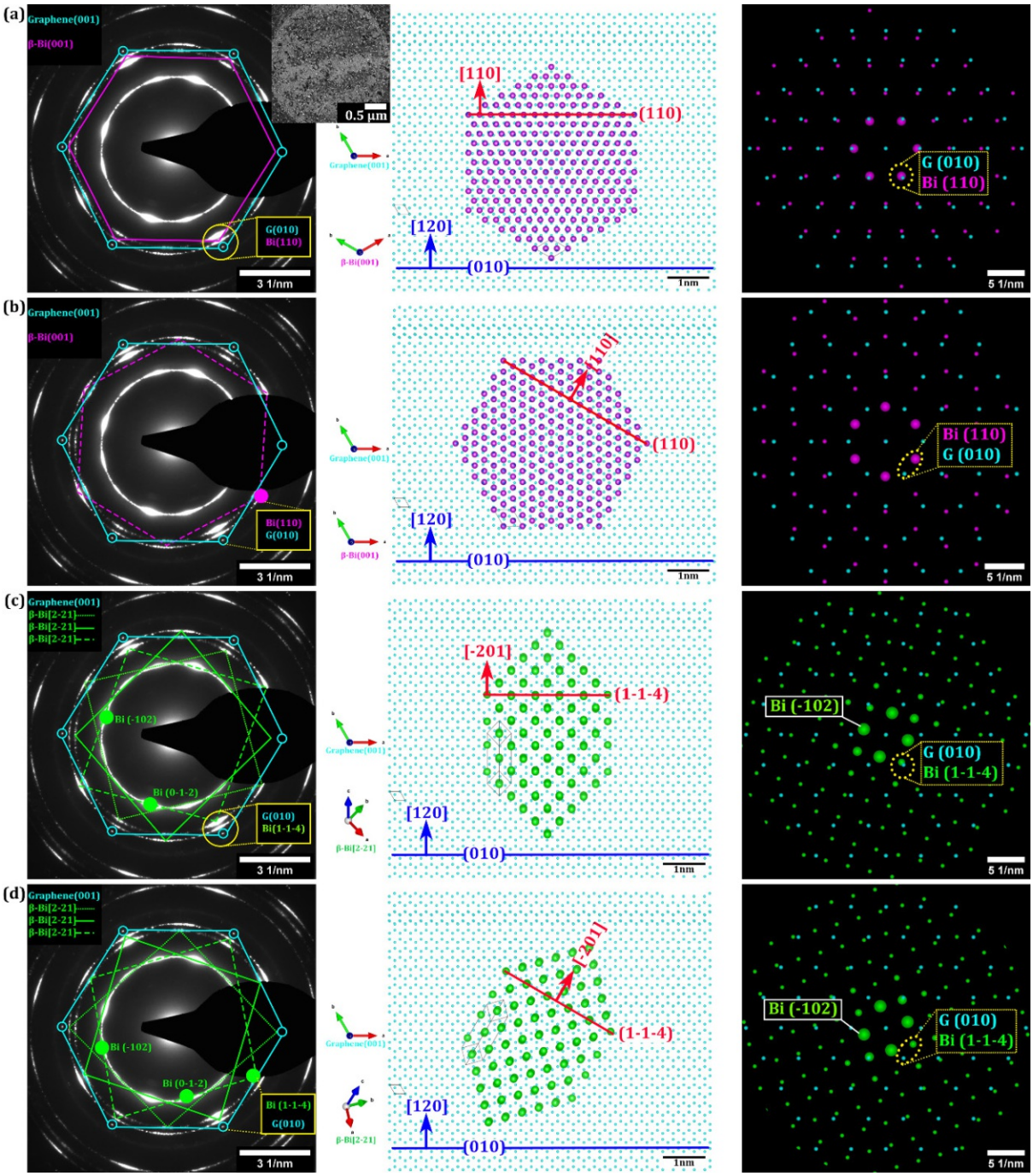

Figure 5.5: <u>RT Bi depositions (Epitaxy)</u>: (a-b) show β-Bi(001) and graphene indexed SAED patterns (left) atomic models showing in-plane vdW epitaxial relations derived from the corresponding marked features in the SAED patterns (middle) and overlay of simulated FTs corresponding to the atomic models and SAED (right) and suggest the presence of two concurrent epitaxial relations of β-Bi(001) with respect to graphene: β-Bi(001)||graphene(001) / β-Bi[110]||graphene[120] and β-Bi(001)||graphene(001) / β-Bi[110] ∠30° graphene[120]. The inset in (a) presents a BF-TEM image of the region on which the SAED data has been acquired. Similarly, (c-d) show β-Bi[2-21] and graphene indexed SAED patterns (left) atomic models showing in-plane vdW epitaxial relations derived from the corresponding marked features in the SAED patterns (middle) and overlay of

Die approbierte gedruckte Originalversion dieser Dissertation ist an der TU Wien Bibliothek verfügbar.
The approved original version of this doctoral thesis is available in print at TU Wien Bibliothek.
TU Bibliothek Your knowledge hub WIEN

simulated FTs corresponding to the atomic models and SAED (right) and suggest the presence of two concurrent epitaxial relations of β-Bi[2-21] with respect to graphene as well: β-Bi[2-21]⊥graphene(001) / β-Bi[-201]||graphene[120] and β-Bi[2-21]⊥ graphene(001) / β-Bi[-201] ∠30° graphene[120]. The colour coding is as follows: Magenta = β-Bi(001), Green = β-Bi[2-21], Cyan = graphene (001). All the four SAED patterns are same and were recorded on the region in inset. The magenta colored FT is indexed to β-Bi viewed along [001] zone axis. The green colored FT is indexed to β-Bi viewed along [2-21] zone axis and the cyan colored FT is indexed to graphene viewed along [001] zone axis. The unit cells and zone axis for the corresponding elements in the epitaxy atomic models has been indicated. It is to note that while referring to impressed epitaxial relations expressed for Bi on Graphene, the focus should be on the plane and the direction mentioned in the epitaxial relations and not on the morphology of the β-Bi(001) and β-Bi[2-21] phases (particularly in the atomic models). The morphology used is for the sake of convenience of representation of atomic models and might differ from the exact atomic edge structures of the two phases as already outlined above.

In particular, for β-Bi(001) a first preferred orientation of β-Bi(001)'s [110] direction with no rotational offset to graphene[120] (armchair) direction (β-Bi(001)||graphene(001) and β-Bi[110]||graphene[120]) was measured in Figure 5.5a. In Figure 5.5b, a second preferred orientation of β-Bi(001)'s [110] direction with 30° offset to graphene [120] (β-Bi(001)||graphene(001) and β-Bi[110] ∠30° graphene[120]) was also measured. For β-Bi[2-21] several equivalent sets of spots were measure in Figure 5.5a. It is to note that due to the respective six-fold symmetry of graphene this however translates to just two relative preferred β-Bi[2-21] crystal lattice orientation (incl. mirroring) with respect to the graphene lattice. First is in Figure 5.5c, β-Bi[2-21]'s [-201] with no rotational offset to graphene[120] (β-Bi[2-21]⊥graphene(001) and β-Bi[-201]||graphene[120]). Second is in Fig. 3d β-Bi[2-21]'s [-201] with 30° offset to graphene [120] (β-Bi[2-21]⊥graphene(001) and β-Bi [-201] ∠30° graphene[120]). Thereby this data clearly establishes rotational vdW epitaxy to exist in the Bi/graphene system for both β-Bi(001) and β-Bi[2-21], even in the case of non-supported, free-standing graphene.

Figure 5.6 expands this investigation to studying the evolution of Bi RT depositions as a function of deposited Bi amount by investigating varying nominal thicknesses from 2 nm to 20 nm. The highly sharp, six-fold SAED patterns for the graphene grains in Figure 5.6b,d,f,h again indicate the excellent preservation of graphene structure upon Bi PVD, again corroborating a vdW Bi/graphene interface. Notably, the graphene-related SAED spots in Figure 5.6b,d,f,h are all predominantly composed of only a single six-fold spot

Die approbierte gedruckte Originalversion dieser Dissertation ist an der TU Wien Bibliothek verfügbar.
The approved original version of this doctoral thesis is available in print at TU Wien Bibliothek.
TU Bibliothek Your knowledge hub WIEN

set, indicating that in each BF-TEM in Figure 5.6a,c,e,g only single single-crystalline graphene grains have been imaged.

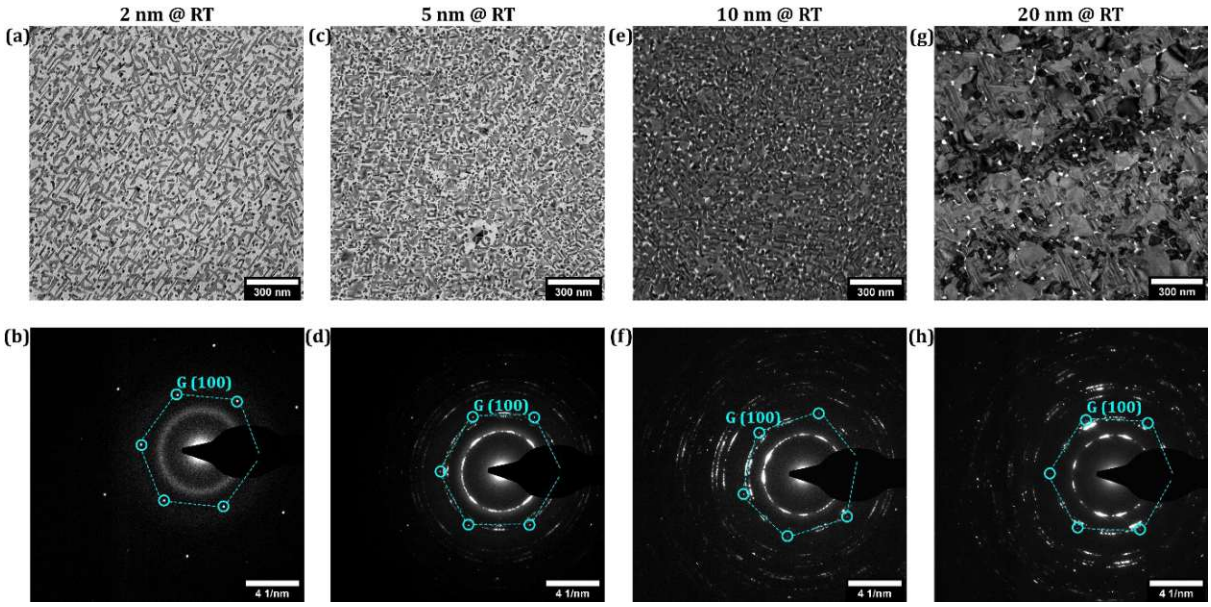

Figure 5.6: Bi RT growth parameter space: BF-TEM images and corresponding SAED patterns of Bi deposits of thicknesses 2nm (a,b), 5nm (c,d), 10nm (e,f) and 20nm (g,h) on suspended graphene. The preserved reflections from graphene underneath in the SAED patterns have been marked in cyan color and have been indexed to graphene(001) viewed along [001] zone axis.

For the initial 2 nm nominal thickness, Figure 5.6a shows that the Bi structures nucleate homogeneously over the entire monolayer graphene basal plane without forming a closed film yet (areal coverage ~54 %). Interestingly, the SAED in Figure 5.6b indicates that at this stage the Bi deposit is of amorphous nature. Closer inspection of the ring-like halo in Figure 5.6b at ~0.33 nm reveals that this is again consistent with amorphous β-Bi[2-21]-like structure similar to regions example marked "3" observed in 10nm RT depositions as shown in Figure 5.2a,b. Morphology indicates at this stage already coexisting rod-like shape and irregular shape of deposits. Notably, the rod-like deposits appear to have preferred orientation alignment over the field-of-view in Figure 5.6a. Interestingly, this is despite the amorphous nature of the deposits.

When increasing the Bi deposit thickness to 5 nm, in Figure 5.6c, the morphologies of features remain of the same nature as in 2nm deposits but they cover a higher fraction of

Die approbierte gedruckte Originalversion dieser Dissertation ist an der TU Wien Bibliothek verfügbar.
The approved original version of this doctoral thesis is available in print at TU Wien Bibliothek.
TU Bibliothek Your knowledge hub WIEN

the substrate, slowly closing towards a closed film (areal coverage ~73 %). Again, preferred orientations of the rod-like deposits are evident in the field of view in Figure 5.6c. Notably, the SAED in Figure 5.6d shows that at this stage the Bi film has crystallized. Indexing of the SAED in Figure 5.6d indicates a phase mixture of β-Bi(001) and β-Bi[2-21] with the same vdW epitaxy relations as discussed above.

Upon reaching 10 nm nominal thickness in Figure 5.6e, an almost fully covering film, akin to Figure 5.1a, Figure 5.2a and Figure 5.5a, inset is formed (areal coverage ~95 %). Consistent with the 5 nm deposition, the SAED in Figure 5.6f indicates the presence of both β-Bi(001) and β-Bi[2-21] phases on the graphene, and also exhibits the same rotational vdW epitaxial orientations, as described above.

Upon, reaching 20 nm nominal thickness in Figure 5.6g, the almost fully covering film (areal coverage ~99 %) has visually grown in overall thickness, evidenced by the lower intensity in the BF-TEM images. Notably, for the 20 nm film, somewhat larger fraction of irregular shaped Bi grains compared to a reduced number of (albeit longer) rod-like deposits was observed. Again, β-Bi(001) and β-Bi[2-21] are detected in SAED in Figure 5.6h with the same rotational vdW epitaxy relations as above. Based on above established morphology-structure relationship and the SAED in Figure 5.6h, the increased fraction of irregular shaped regions in Figure 5.6g points to larger fraction of β-Bi(001) in the 20 nm films compared to the thinner film.

While this work is the first report on Bi deposition on truly freestanding graphene, observations made here are now set in context with prior work on Bi deposition on supported graphene[43–45] and graphene's bulk analogue graphite.[72–80] Prior work has observed for RT-depositions mixed β-Bi(001)/β-Bi[2-21][45] and exclusive β-Bi[2-21][43,44] growth on supported graphene. For bulk graphite likewise β-Bi(001),[72,76] β-B[2-21][72–75,79] and mixed growth[72,78] has been reported for RT depositions. Morphologies of the β-Bi(001) and β-Bi[2-21] varied depending on study, but β-Bi(001) has been reported to exhibit (triangular) island[72] morphology, somewhat matching here observed irregular shapes, while β-Bi[2-21] was reported as rod-like[73–75], consistent with observations

Die approbierte gedruckte Originalversion dieser Dissertation ist an der TU Wien Bibliothek verfügbar.
The approved original version of this doctoral thesis is available in print at TU Wien Bibliothek.
TU Bibliothek WIEN Your knowledge hub

made in this work, and star-shaped.[72,73,75] For the planar freestanding monolayer, homogeneous nucleation on the graphene basal plane was observed. Due to the absence of step edges on the freestanding monolayer graphene films employed here, clearly no preferential nucleation at steps could be observed, as often seen in work on bulk graphite with ample step edges.[75–77] Prior work has not observed a third morphology of an amorphous β-Bi[2-21]-like deposit nature, as was found exclusively here in this study in the 2 nm depositions and in small fractions also in the consecutive higher nominal thickness depositions such as the 5nm and also 10 nm as shown in Figure 5.2b. Initial growth of Bi in amorphous form β-Bi[2-21]-like at ultralow thicknesses, which then undergoes crystallization upon increasing Bi thickness has not been reported for Bi before.[72] This new observation here may be related to the truly freestanding graphene support which is in contrast to all prior work on themselves supported or bulk supports. A transition from β-Bi[2-21] to β-Bi(001) i.e. higher β-Bi(001) fraction with increasing Bi deposit thickness has been prior reported, consistent with the 20 nm data. This subsequent transition of β-Bi[2-21] to β-Bi(001) is due to low thickness stability of β-Bi[2-21].[71,72]

Prior studies investigating the growth of Bi on similar adopted substrates like supported graphene on SiC[67,81], Highly ordered pyrolitic graphite (HOPG)[72,74,75,82,83] have observed identical epitaxial relations of the grown Bi structures with respect to graphene underneath. In a molecular beam epitaxy (MBE) based synthesis of Bi on supported graphene/SiC by Huang *et al.*[67], following epitaxial relations were established between Bi and SiC supported graphene: Bi(01-12)||graphene(0001) and Bi<11-20>||graphene<11-20>. Their Bi[1-120] direction corresponds to β-Bi[110] in terms of notation used here and graphene<11-20> corresponds to armchair direction which is denoted by graphene[120] in terms of notation used in this study and hence their relations fully overlap with here studied observations of β-Bi[2-21]⊥graphene(001) / β-Bi[-201] ∠30° graphene[120] as [2-21] zone axis is also ⊥ to β-Bi(01-12). To this end it is important to note that directions used in the prior works are in random rhombohedral/ hexagonal notations, either in (hkil) or (hkl) format, different to consistently used hexagonal notations in this study which are in (hkl) format throughout. However, the planes and directions in both notations were precisely checked to allow one-to-one comparison.

Die approbierte gedruckte Originalversion dieser Dissertation ist an der TU Wien Bibliothek verfügbar.
The approved original version of this doctoral thesis is available in print at TU Wien Bibliothek.
TU WIEN Bibliothek Your knowledge hub

Therefore, it is important to look into the atomic arrangement across the respective directions to have an accurate comparison of the crystallographic orientations. Similarly Song *et al.*[82], presented a 30° offset between the diffraction spots of Bi(111) (or β-Bi(001) in notation used here) and the HOPG substrate matching very well to here observed epitaxial relations: β-Bi(001)||graphene(001) / β-Bi[110] ∠30° graphene[120]. Interestingly, Hu *et al.*[81] observed the Bi<1-10>||graphene<11-20> epitaxial relation in Bi nanostructures grown on graphene / SiC via MBE, where graphene<11-20> is the armchair direction similar to graphene[120] used in this study and Bi<1-10> is the direction along the basal (001) plane of β-Bi(001) which will be equivalent to β-Bi[1-10] direction as per here used notation. This difference is believed to arise on the different stacking order of supported graphene on SiC step unlike the single-crystal monolayer suspended graphene employed here in this study.

On similar studies performed utilizing HOPG as substrate, Wang *et al.*[83] observed two different epitaxial relations: first a more predominant Bi[110]||graphene[120] which readily adheres to here observed epitaxial relation of β-Bi(001)||graphene(001) / β-Bi[110]||graphene[120]. They also observed a less predominant Bi[010]||graphene[010] which is also in line with here made observation of β-Bi(001)||graphene(001) / β-Bi[110] ∠30° graphene[120]. Scott *et al.*[75], while elucidating growth of Bi nanorods array on HOPG, found the preferential alignment of Bi<11-20>||HOPG<10-10> which in here followed notations will be β-Bi[110]||graphene[100] this is reflected from the observed epitaxy relation of β-Bi[2-21]⊥graphene(001) / β-Bi[-201]||graphene[120] in this work and the same relations has been obtained in their other studies[72] dealing with early stage growth characteristics of Bi films on HOPG. Studies dealing with origins of moiré patterns on Bi films grown on HOPG carried out by Kowalczyk *et al.*[74] suggested two different orientation of their grown Bi films on HOPG: Bi<-110>||HOPG <10-10> and Bi<-110>||HOPG<1-100> (where HOPG<10-10> and <1-100> denote the armchair[120] and zig-zag[100] direction in here followed notations respectively and Bi <1-10> corresponds to Bi[-201] in here used notation) which in here used notation will be β-Bi[-201]||graphene[120] and β-Bi[-201]||graphene[100]. These two relations are observed in here established relations of β-Bi[2-21]⊥ graphene(001) / β-Bi[-201]||graphene[120] and β-Bi[2-21]⊥graphene(001) / β-Bi[-201] ∠30° graphene[120] respectively. Thus,

Die approbierte gedruckte Originalversion dieser Dissertation ist an der TU Wien Bibliothek verfügbar.
The approved original version of this doctoral thesis is available in print at TU Wien Bibliothek.
TU Bibliothek WIEN Your knowledge hub

here observed relations of rotational vdW epitaxy for 10nm Bi with respect to graphene lie very well in line with prior studies on Bi on HOPG as well as Bi on supported graphene/SiC. This suggests that typical supports to a graphene layer do not change the intrinsically impressed epitaxial relationships for Bi deposits.

"10nm Bi RT deposits exhibit two different morphologies:

- *Rod shaped morphology with single crystalline β-Bi[2-21] texture.*
- *Irregular shaped regions with single crystalline β-Bi (001) texture.*
- *Irregular shaped regions with amorphous β-Bi[2-21] texture*

Both the single crystalline textures exhibited following distinct rotational vdW epitaxial relations with respect to graphene underneath:

- *β-Bi(001)||graphene(001) / β-Bi[110]||graphene[120] and β-Bi(001)||graphene(001) / β-Bi[110] ∠30° graphene[120]*
- *β-Bi[2-21]⊥graphene(001) / β-Bi[-201]||graphene[120] and β-Bi[2-21]⊥graphene(001) / β-Bi[-201] ∠30° graphene[120]"*

5.3.3 Higher substrate temperature Bi nanoparticles incl. e-beam driven dynamics

In contrast to the crystalline, film-like nature of the RT depositions with areal coverage of ~95 % for nominal 10 nm depositions, the nominal 10 nm depositions at 150 °C and 250 °C substrate temperature resulted in isolated Bi nanoparticles Figure 5.1b,c with sizes ranging from 3 to 20 nm and a much reduced areal coverage of ~11 % and 0.4 % at 150 °C and 250 °C, respectively. High resolution TEM shows that these nanoparticles are all amorphous in as deposited state (Figure 5.7a,b 00 min), showing a subtle substructure of discrete amorphous, adjacent islets comprising the individual particles. A thickness estimation based on HAADF (S)TEM intensity analysis,[8,84–86] places the average thickness of the 250 °C particles at ~6 nm. This translates to a loss of Bi amount between the RT depositions and the 250 °C of ~99 %. With a melting point of bulk Bi at ~270 °C,[87] the

Die approbierte gedruckte Originalversion dieser Dissertation ist an der TU Wien Bibliothek verfügbar.
The approved original version of this doctoral thesis is available in print at TU Wien Bibliothek.
TU Bibliothek Your knowledge hub WIEN

drastic morphology change as observed in Figure 5.1a-c in the Bi from RT to higher temperature depositions is related to nanosized melting point depression at the higher temperature depositions (to, e.g., ~160° C for 5 nm Bi particles)[88,89] and associated much increased, backward Bi desorption during deposition at higher substrate temperatures.[5] While the RT films are crystalline, the 150 °C and 250 °C are found to be amorphous. The amorphous structure results from quenching during cooling from the above-melting-point substrate temperature of 150 to 250 °C. Prior work has observed for annealing of RT-deposited Bi films or high temperature Bi deposition similar reduction of retained Bi[90–94] with few examples of retention of crystallinity at 150 °C albeit restructuring of morphology.[78]

In contrast to the static nature of the RT Bi depositions under the e-beam in (S)TEM, the Bi nanoparticles from the higher temperature 150 °C and 250 °C depositions show a great deal of atomic motions upon e-beam exposure in TEM under here employed conditions, as shown in Figure 5.7a,b (electron dose rate estimated to 2×10^{1} $e^{-}Å^{-2}s^{-1}$). In particular, the amorphous nature of the Bi nanoparticles from the higher temperature depositions changed *in situ* into fully crystallized structures with faceted morphology. It was found that the amorphous nanoparticles can readily evolve to nanoparticles with either β-Bi(001) (Figure 5.7a) or β-Bi[2-21] (Figure 5.7b) structure.

In the *in situ* measurements, it was found that the crystallization of the initial amorphous Bi nanoparticles proceeds via a two-step mechanism: In step 1, the crystallization begins with the formation of several irregular shaped isolated crystallized clusters within the amorphous islets of Bi nanoparticles (Figure 5.7a, 0-15 min; Figure 5.7b, 0-18 min). In step 2, these initially crystallized regions within the particles coalesce with each other and continue to rearrange, ultimately leading to gradual formation of a well faceted crystal (Figure 5.7a,b). The final crystalline Bi islet formed has a reduced projected area (and thereby higher density) as compared to the initial amorphous particles. Once crystallized, the Bi particle remain crystallized during further longer electron beam exposure, until electron beam induced damage[95] to the supporting graphene limits the stability of the entire heterostructure. It was found that some amorphous particles take

Die approbierte gedruckte Originalversion dieser Dissertation ist an der TU Wien Bibliothek verfügbar.
The approved original version of this doctoral thesis is available in print at TU Wien Bibliothek.
TU Bibliothek Your knowledge hub WIEN

as short[96,97] as ~ 3-4 min to completely crystallize under the employed conditions in this study.

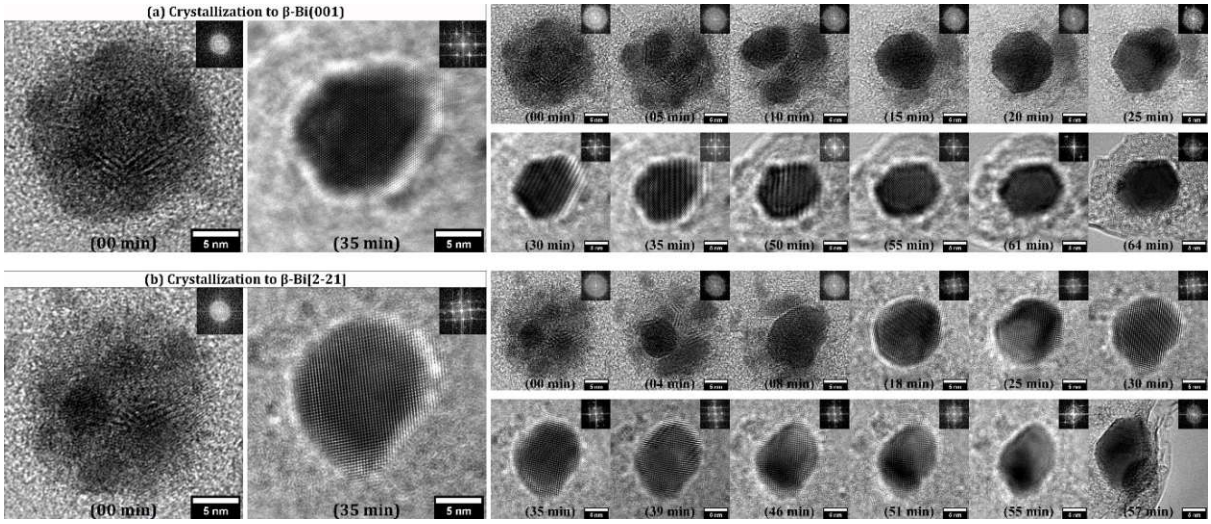

Figure 5.7: BF-TEM images of electron beam induced crystallization of amorphous Bi nanoparticles obtained from 150 °C deposition. (a) shows the crystallization of thicker (based on BF-TEM contrast) amorphous despoits to β-Bi(001) and (b) shows the crystallization of thinner (based on BF-TEM contrast) amorphous despoits to β-Bi[2-21]. The inset shows BF-TEM images of the structural reconstrucions acquired at an internval of 5 min till electron beam damaged the graphene.

Within the studied data, apparently thicker amorphous Bi islets (based on intensity in the BF-TEM images) show a preferential transition to β-Bi(001). In contrast, thinner amorphous Bi islets preferentially crystallize to β-Bi[2-21]. Overall more crystallisation events to β-Bi[2-21] (~40) than to β-Bi(001) (~9) were observed for the Bi nanoparticles obtained in 150 °C deposition. In addition to this, events of two isolated islets coalescing into each other and ultimately crystallizing to β-Bi(001) (Figure 5.8) were also observed. These observations are in line with the transition of preference from β-Bi[2-21] to β-Bi(001) at higher thicknesses,[71,72] akin as in the RT deposition samples.

With respect to rotational vdW epitaxy, it is to note that for the dataset of *in situ* crystallized nanoparticles, the relative orientation of Bi and graphene lattices can be compared via FT analysis post crystallisation, as exemplary shown for one β-Bi(001) particle in Figure 5.9a,b and for one β-Bi[2-21] particle in Figure 5.9d,e respectively.

Die approbierte gedruckte Originalversion dieser Dissertation ist an der TU Wien Bibliothek verfügbar.
The approved original version of this doctoral thesis is available in print at TU Wien Bibliothek.
TU WIEN Bibliothek Your knowledge hub

From the multiple (>45) crystallization sequences, a histogram of rotation values between Bi and graphene crystals is plotted (Figure 5.9c for β-Bi(001) and Figure 5.9f for β-Bi[2-21]). Consistent with the SAED analysis in Figure 5.5 above (which intrinsically averaged over multiple >>140 crystallites), also this statistical analysis of single particles shows strong signs of rotational vdW epitaxy for Bi/graphene. For β-Bi(001), a preferred orientation of β-Bi(001)'s [110] direction with no rotational offset to graphene [120] (armchair) direction (β-Bi(001)||graphene(001) and β-Bi [110]||graphene[120]) was found as shown in Figure 5.9c, akin to Figure 5.5a. For β-Bi[2-21], β-Bi[2-21]'s [-201] was found with no rotational offset to graphene [120] (β-Bi[2-21]⊥graphene(001) and β-Bi [-201]||graphene[120]) as shown in Figure 5.9f, akin to Figure 5.5c. The absence of 30° misorientations with respect to graphene [120] (as Figure 5.5b,d) for both β-Bi(001) and β-Bi[2-21] may be either related to the smaller number of observations than in the multi crystallite (>>140) averaging SAED in Figure 5.5 or indicates that the emergence of rotational vdW epitaxy in the Bi-graphene can also be kinetically limited.[8,47]

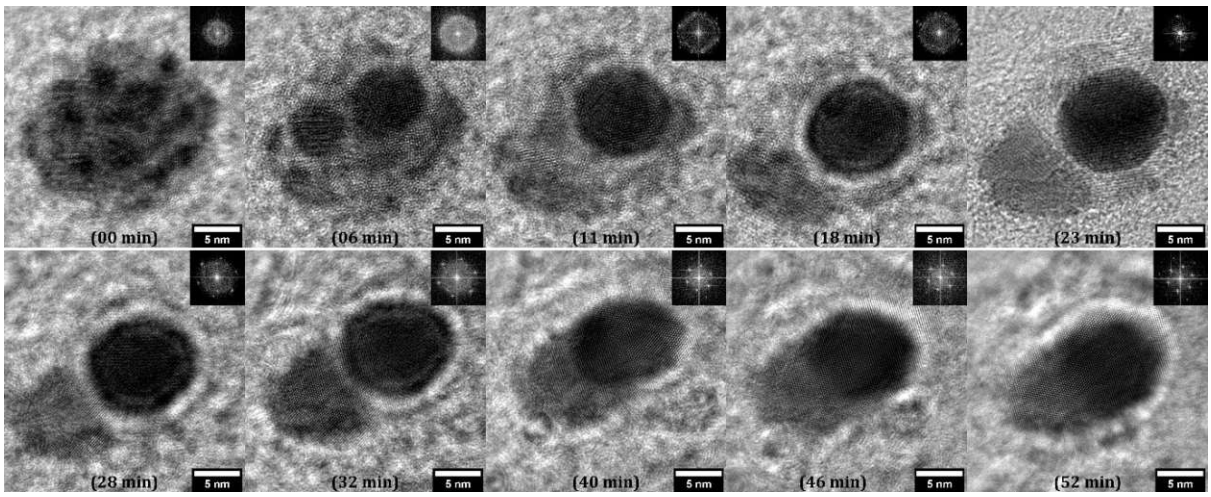

Figure 5.8: BF TEM image of the electron beam induced crystallization of Bi nanoparticles (from 10 nm Bi deposited on graphene at 150 °C) where two isolated β-Bi[2-21] crystallized nanoparticles were observed merging to β-Bi(001) crystallized nanoparticle suggesting the higher stability of β-Bi(001) with increasing thickness.

Electron beam exposure leading to amorphous/crystalline transitions in Bi nanoparticles has been prior reported unidirectionally[96,98] (as here) and also in a reversible manner.[97,99,100] It has been suggested to be related to heating/supercooling of the Bi particles via the energy delivered by the electron beam due to different thermal conductivities in

Die approbierte gedruckte Originalversion dieser Dissertation ist an der TU Wien Bibliothek verfügbar.
The approved original version of this doctoral thesis is available in print at TU Wien Bibliothek.
TU Bibliothek Your knowledge hub WIEN

crystalline/amorphous state of Bi,[97] which can lead to cyclic amorphization/crystallisation of particles. In this study, only forward amorphous to crystalline transitions was observed while cyclic crystallized ↔ amorphous state transitions were not observed. The reverse transformation of crystalline to amorphous state in Bi has thus far been attributed to continued heat input from the electron beam into the Bi which result in reaching the nanosize-related depressed melting point and thus liquification of the Bi crystallites under the beam[99].

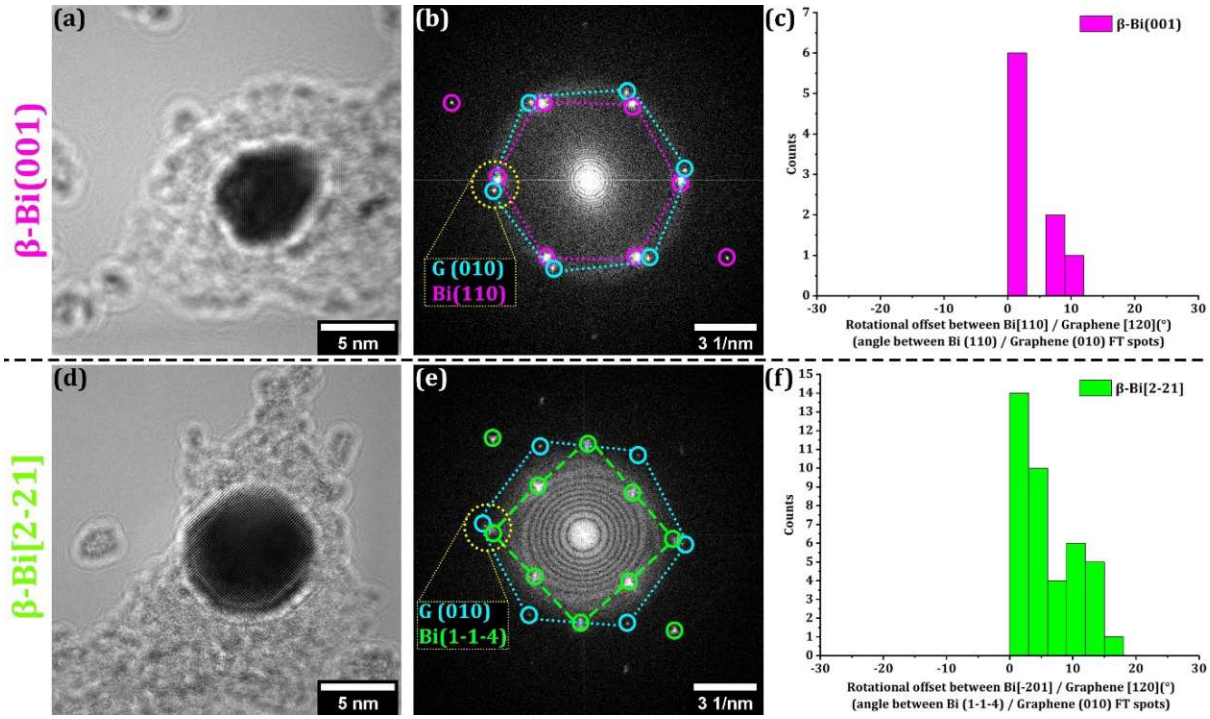

Figure 5.9: BF-TEM image (a) shows the electron beam crystallized β-Bi(001) particle (10 nm Bi at 150 °C) and the graphene support with corresponding FT pattern (b) from the BF-image showing β-Bi(001) (magenta) and graphene(001) (cyan) reflections indicating signs of the following rotational vdW epitaxy relation of β-Bi(001) with respect to graphene(001) underneath: β-Bi(001)||graphene(001) / β-Bi[110]||graphene[120], similar to what was observed for RT deposits in Figure 5.5. BF-TEM image (d) shows the electron beam crystallized β-Bi[2-21] particle (10 nm Bi at 150 °C) and the graphene support with corresponding FT pattern (e) from the BF-image showing β-Bi[2-21] (green) and graphene(001) (cyan) reflections indicating signs of the following rotational vdW epitaxy relation of β-Bi[2-21] with respect to graphene(001) underneath: β-Bi[2-21] ⊥ graphene(001) / β-Bi[110]||graphene[120], similar to what was observed for RT deposits in Figure 5.5. (c) and (f) show histogram of multiple measurements of misorientation angles between Bi[110] and graphene[120] in the crystallized β-Bi(001) and β-Bi[2-21] respectively with respect to graphene underneath, showing that most prevalent misorientations correspond to the cases in (a,b) and (d,e), in line with RT results in Figure 5.5.

The fact that this liquification behaviour for Bi crystallites was not observed in this study can be attributed to the efficient heat transfer away from the Bi because of the excellent

Die approbierte gedruckte Originalversion dieser Dissertation ist an der TU Wien Bibliothek verfügbar.
The approved original version of this doctoral thesis is available in print at TU Wien Bibliothek.
TU Bibliothek Your knowledge hub WIEN

heat conducting properties of the graphene membrane.[101] Thereby due to the graphene support, the threshold for the reverse liquification transition (before the graphene support loses structural integrity from beam damage for very prolonged e-beam exposures) was not reached. The observation of ~ 45 % area reduction upon complete crystallization of the amorphous Bi nanoparticles further overlaps with the initial liquid (amorphous) state to final solid (crystallized) state where compact structuring of the Bi atoms in their crystallized state leads to the reduction in area of the Bi nanoparticle.

Studies involving few-layer antimonene (2D Sb)/graphene heterostructures as already outlined in chapter 4,[5] will now be set in context to this work on Bi/graphene heterostructures. Notably, Sb (atomic number 51) is the pnictogen directly above Bi (atomic number 83) in group 15/VA in the periodic table. Key differences between Sb and Bi are the much higher melting temperature of Sb of ~630 °C compared to Bi of 270 °C,[102] as well as the more anisotropic, layered character of Sb compared to Bi.[103] A common observation in both Sb and Bi on graphene systems is the general co-existence of the two (001) and [2-21] textures in crystalline deposits. Also, both Sb/graphene and Bi/graphene systems show clear rotational vdW epitaxy. This shows that both pnictogens form structurally similar heterostructures with graphene. The higher melting temperature of Sb however translates to amorphous Sb growth at RT versus fully crystallized Bi growth at RT for the same nominal thickness. Likewise, the retained amount of Sb at higher deposition temperatures of up to 250 °C is much higher than the here observed drastic Bi loss. Also, the higher temperature Sb depositions readily retain crystallinity, unlike the here amorphized Bi nanoparticles at 150 °C and 250 °C. Combined, this clearly shows that processing windows to obtain similar pnictogen structure on graphene must differ in temperature and flux. A final difference between Sb and Bi was that, unlike in the Bi system where amorphous nanoparticles showed electron-beam induced crystallisation phenomena, in the Sb system all nanostructure remained static under the electron beam in the employed (S)TEM conditions. This can be again ascribed to the higher melting point of Sb compared to Bi.

Die approbierte gedruckte Originalversion dieser Dissertation ist an der TU Wien Bibliothek verfügbar.
The approved original version of this doctoral thesis is available in print at TU Wien Bibliothek.
TU Bibliothek Your knowledge hub WIEN

"Bi deposits obtained as nanoparticles on high temperature (150 °C and 250 °C) show electron beam driven restructuring mechanisms leading to their complete crystallization. Based on BF-TEM image intensity thinner deposits crystallize to β-Bi[2-21] texture and thicker deposits crystallize to β-Bi(001) texture. Both these crystallized textures of Bi also show following rotational vdW epitaxial relation with graphene:

- *β-Bi(001)||graphene(001) / β-Bi[110]||graphene[120]*
- *β-Bi[2-21]⊥graphene(001) / β-Bi[-201]||graphene[120]"*

5.3.4 Plasmon Shift during *in situ* Crystallization.

Finally, additionally to following the structural evolution of the 150 °C/250 °C deposited, initially amorphous Bi nanoparticles *in situ* under the electron beam in Figure 5.7 and Figure 5.8, the evolution of Bi nanoparticle plasmon signatures using time-resolved (V)EELS was also followed.[104] Recent advances in the instrumentation along with adapted mathematical methods have made the use of time resolved EELS in studying electron beam induced phase transformations quite feasible.[105,106] However, most of time resolved EELS studies remain concentrated to the core-loss spectra. Hardly any of the time resolved studies has focussed on the change in the low loss region (with special emphasis on the shift of the plasmonic modes) to account for the electron beam induced phase transitions. Given the key interest in plasmonic properties of Bi nanoparticles for optical switching and plasmon catalysis application and given the possible key influence of structure modifications to plasmonic signatures, such measurements would however be of high relevance.

In Figure 5.10a, a starting (V)EELS spectrum of an amorphous Bi particle on graphene (i.e. a Bi particle from 150 °C higher substrate temperature deposition) is plotted for which the EELS contribution of graphene has been subtracted as background i.e. Figure 5.10a shows only the Bi-related (V)EELS signal. A fit of the (V)EELS spectrum reveals three components, namely a predominant peak centred at ~19 eV, which is ascribed to

Die approbierte gedruckte Originalversion dieser Dissertation ist an der TU Wien Bibliothek verfügbar.
The approved original version of this doctoral thesis is available in print at TU Wien Bibliothek.
TU WIEN Bibliothek Your knowledge hub

the Bi volume plasmon,[107] a shoulder to this peak at ~10 eV, which is ascribed to the Bi surface plasmon,[107,108] and another peak at ~30 eV, which is related to the Bi $O_{4,5}$ edge.[107] These (V)EELS features are as expected for Bi nanostructures,[107,108] also further excluding formation of other phases such as Bi-oxides in line with Raman and (S)TEM data above.[108]

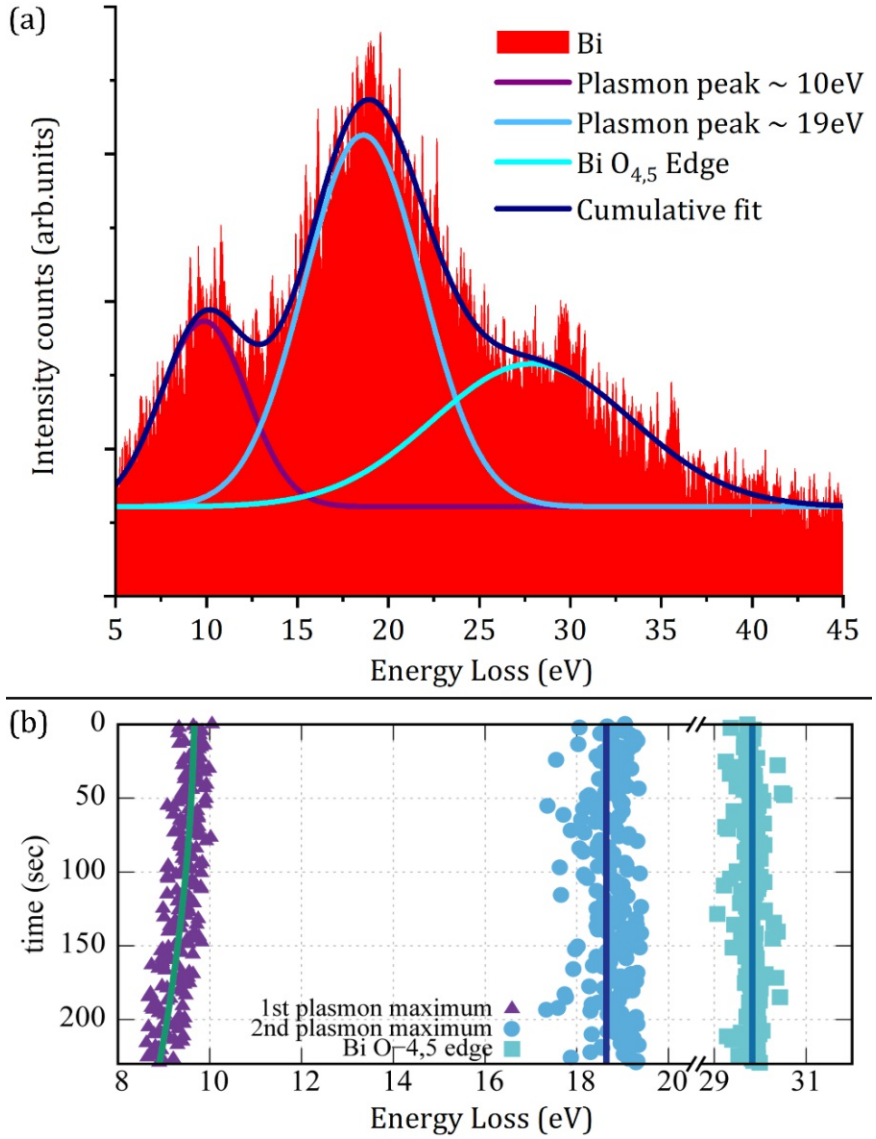

Figure 5.10: ***In situ*** **studies of Bi plasmon evolution during electron beam induced crystallization of Bi nanoparticles on graphene at 150 °C. (a) shows the low loss EELS spectra of Bi composed of three distinct features. Peak at ~ 10 eV corresponds to Bi surface plasmon, Peak at ~ 19 eV corresponds to Bi bulk/volume plasmon and peak at ~ 30 eV is the Bi $O_{4,5}$ edge. (b) shows the time resolved evolution of the three distinct features of the Bi low loss EELS spectra during electron beam driven crystallization. The Bi surface plasmon peak undergoes a shift from initial ~ 10 eV (amorphous state) to final ~ 8.6 eV (crystallized state) with no significant changes in the ~19 eV peak positions and the Bi $O_{4,5}$ edge.**

Die approbierte gedruckte Originalversion dieser Dissertation ist an der TU Wien Bibliothek verfügbar.
The approved original version of this doctoral thesis is available in print at TU Wien Bibliothek.
TU Bibliothek Your knowledge hub WIEN

In Figure 5.10b the change in the position of these three components with increasing exposure time to the e-beam, while the Bi nanoparticle transitions from amorphous to crystalline Bi, is plotted. Notably, while the volume plasmon peak at ~19 eV and Bi $O_{4,5}$ edge at ~30 eV do not change in energy, the surface plasmon shoulder at ~10 eV shifts with increasing e-beam exposure time to a lower energy down to ~8.6 eV. This suggests that the Bi surface plasmon is sensitive to the crystallinity of the Bi particles.

While some previous works[19,38,109–112] have described the change in Bi nanoparticle optical responses as a result of change in dielectric function, transmission and reflection changes during the melting and freezing of the Bi in different matrix, to the best knowledge of the state-of-art, no study on the effect of the crystallization process on the plasmonic modes of Bi has been reported to date. Since crystallisation can be enforced by external stimuli and has been shown to be cyclic reversible, this finding may point to the Bi surface plasmon as a potentially switchable plasmonic feature.

"During in-situ electron beam induced crystallization of the amorphous Bi nanoparticles, time-resolved (V)EELS studies were additionally performed which outlined the sensitivity of surface plasmon peak of Bi towards the structural reconstruction happening during electron beam induced crystallization. A shift from 10 eV in initial amorphous state to 8.6 eV to final crystallized state was observed in the surface plasmon peak in (V)EELS spectrum of Bi."

5.4 Conclusion

In summary, structure and morphology of low-dimensional Bi deposits on truly freestanding monolayer graphene membranes (i.e. removing any possible effect of an underlying substrate under itself supported graphene) was studied here. The high-resolution (S)TEM investigations of mixed-dimensional Bi/graphene heterostructures revealed the structure and morphology evolution of PVD Bi as a function of substrate

Die approbierte gedruckte Originalversion dieser Dissertation ist an der TU Wien Bibliothek verfügbar.
The approved original version of this doctoral thesis is available in print at TU Wien Bibliothek.
TU Bibliothek Your knowledge hub WIEN

temperature and deposition amount during deposition, where blanket like largely crystalline thin film morphology at RT conditions drastically transforms to isolated amorphous nanoparticles at higher temperatures. Nucleation of crystalline β-Bi at RT appears to be preceded by an intermediate amorphous state at ultralow thicknesses. Co-existence of two key β-Bi textures were observed in all crystalline depositions, both with clear rotational vdW epitaxy with the graphene support. For amorphous Bi particles an electron-beam induced *in situ* crystallization in the TEM is revealed and a link between crystallisation state and surface plasmon energy in Bi by concurrent (V)EELS measurements is also suggested. Combined, these findings elucidate the multi-faceted structural and morphological dynamics in mixed-dimensional Bi/graphene heterostructures at high resolution and for truly freestanding graphene.

5.5 References

1. Pumera, M. & Sofer, Z. 2D monoelemental arsenene, antimonene, and bismuthene: beyond black phosphorus. *Adv. Mater.* **29**, 1605299 (2017).
2. Zhang, S. *et al.* Recent progress in 2D group-VA semiconductors: from theory to experiment. *Chem. Soc. Rev.* **47**, 982–1021 (2018).
3. Ersan, F. *et al.* Two-dimensional pnictogens: A review of recent progresses and future research directions. *Appl. Phys. Rev.* **6**, 021308 (2019).
4. Zhao, A. *et al.* Review of 2D group VA material-based heterostructures. *J. Phys. Appl. Phys.* **53**, 293002 (2020).
5. Gupta, T. *et al.* Resolving few-layer antimonene/graphene heterostructures. *Npj 2D Mater. Appl.* **5**, 53 (2021).
6. Jariwala, D., Marks, T. J. & Hersam, M. C. Mixed-dimensional van der Waals heterostructures. *Nat. Mater.* **16**, 170 (2016).
7. Periwal, P. *et al.* Catalytically mediated epitaxy of 3D semiconductors on van der Waals substrates. *Appl. Phys. Rev.* **7**, 031402 (2020).
8. Elibol, K. *et al.* Process Pathway Controlled Evolution of Phase and Van-der-Waals Epitaxy in In/In2O3 on Graphene Heterostructures. *Adv. Funct. Mater.* **30**, 2003300 (2020).
9. Hoffman, C. A. *et al.* Semimetal-to-semiconductor transition in bismuth thin films. *Phys. Rev. B* **48**, 11431–11434 (1993).
10. Freitas, R. R. Q. *et al.* Topological Insulating Phases in Two-Dimensional Bismuth-Containing Single Layers Preserved by Hydrogenation. *J. Phys. Chem. C* **119**, 23599–23606 (2015).
11. Wang, X. *et al.* Topological phase stability and transformation of bismuthene. *EPL Europhys. Lett.* **119**, 27002 (2017).
12. Heremans, J. & Thrush, C. M. Thermoelectric power of bismuth nanowires. *Phys. Rev. B* **59**, 12579–12583 (1999).

Die approbierte gedruckte Originalversion dieser Dissertation ist an der TU Wien Bibliothek verfügbar.
The approved original version of this doctoral thesis is available in print at TU Wien Bibliothek.
TU Bibliothek Your knowledge hub WIEN

13. Cheng, L. *et al.* Thermoelectric Properties of a Monolayer Bismuth. *J. Phys. Chem. C* **118**, 904–910 (2014).
14. Zhao, Y. *et al.* In Situ Formation of Hierarchical Bismuth Nanodots/Graphene Nanoarchitectures for Ultrahigh-Rate and Durable Potassium-Ion Storage. *Small* **16**, 1905789 (2020).
15. Li, S., Yang, Y., Liu, L. & Zhao, Q. Electron transfer-induced catalytic enhancement over bismuth nanoparticles supported by N-doped graphene. *Chem. Eng. J.* **334**, 1691–1698 (2018).
16. Su, D., Dou, S. & Wang, G. Bismuth: A new anode for the Na-ion battery. *Nano Energy* **12**, 88–95 (2015).
17. Cheng, X., Li, D., Wu, Y., Xu, R. & Yu, Y. Bismuth nanospheres embedded in three-dimensional (3D) porous graphene frameworks as high performance anodes for sodium- and potassium-ion batteries. *J. Mater. Chem. A* **7**, 4913–4921 (2019).
18. Zhang, Y., Wang, Q., Wang, B., Mei, Y. & Lian, P. N-doped graphene/Bi nanocomposite with excellent electrochemical properties for lithium–ion batteries. *Ionics* **23**, 1407–1415 (2017).
19. Cuadrado, A., Toudert, J. & Serna, R. Polaritonic-to-Plasmonic Transition in Optically Resonant Bismuth Nanospheres for High-Contrast Switchable Ultraviolet Meta-Filters. *IEEE Photonics J.* **8**, 1–11 (2016).
20. Yan, L. *et al.* Elemental Bismuth–Graphene Heterostructures for Photocatalysis from Ultraviolet to Infrared Light. *ACS Catal.* **7**, 7043–7050 (2017).
21. Yang, F. *et al.* Bismuthene for highly efficient carbon dioxide electroreduction reaction. *Nat. Commun.* **11**, 1088 (2020).
22. Yu, X. *et al.* Emerging 2D pnictogens for catalytic applications: status and challenges. *J. Mater. Chem. A* **8**, 12887–12927 (2020).
23. Dong, F. *et al.* A semimetal bismuth element as a direct plasmonic photocatalyst. *Chem. Commun.* **50**, 10386–10389 (2014).
24. Zhou, Y. *et al.* Non-noble metal plasmonic photocatalysis in semimetal bismuth films for photocatalytic NO oxidation. *Phys. Chem. Chem. Phys.* **19**, 25610–25616 (2017).
25. Guo, Y. *et al.* Monolayer Bismuthene-Metal Contacts: A Theoretical Study. *ACS Appl. Mater. Interfaces* **9**, 23128–23140 (2017).
26. Lazanas, A. C., Tsirka, K., Paipetis, A. S. & Prodromidis, M. I. 2D bismuthene/graphene modified electrodes for the ultra-sensitive stripping voltammetric determination of lead and cadmium. *Electrochimica Acta* **336**, 135726 (2020).
27. Devasenathipathy, R., Mani, V. & Chen, S.-M. Highly selective amperometric sensor for the trace level detection of hydrazine at bismuth nanoparticles decorated graphene nanosheets modified electrode. *Talanta* **124**, 43–51 (2014).
28. Jeromiyas, N., Elaiyappillai, E., Kumar, A. S., Huang, S.-T. & Mani, V. Bismuth nanoparticles decorated graphenated carbon nanotubes modified screen-printed electrode for mercury detection. *J. Taiwan Inst. Chem. Eng.* **95**, 466–474 (2019).
29. Rao Penki, T., Valurouthu, G., Shivakumara, S., Anand Sethuraman, V. & Munichandraiah, N. In situ synthesis of bismuth (Bi)/reduced graphene oxide (RGO) nanocomposites as high-capacity anode materials for a Mg-ion battery. *New J. Chem.* **42**, 5996–6004 (2018).
30. Chen, J. *et al.* Intercalation of Bi nanoparticles into graphite results in an ultra-fast and ultra-stable anode material for sodium-ion batteries. *Energy Environ. Sci.* **11**, 1218–1225 (2018).
31. Zhong, Y. *et al.* Bi Nanoparticles Anchored in N-Doped Porous Carbon as Anode of High Energy Density Lithium Ion Battery. *Nano-Micro Lett.* **10**, 56 (2018).

Die approbierte gedruckte Originalversion dieser Dissertation ist an der TU Wien Bibliothek verfügbar.
The approved original version of this doctoral thesis is available in print at TU Wien Bibliothek.
TU Bibliothek WIEN Your knowledge hub

32. Yang, F. *et al.* Bismuth Nanoparticles Embedded in Carbon Spheres as Anode Materials for Sodium/Lithium-Ion Batteries. *Chem. – Eur. J.* **22**, 2333–2338 (2016).
33. Kooij, E. S., Ahmed, W., Zandvliet, H. J. W. & Poelsema, B. Localized Plasmons in Noble Metal Nanospheroids. *J. Phys. Chem. C* **115**, 10321–10332 (2011).
34. Toudert, J. *et al.* Using ion beams to tune the nanostructure and optical response of co-deposited Ag\hspace0.167em:\hspace0.167emBN thin films. *J. Phys. Appl. Phys.* **40**, 4614–4620 (2007).
35. MacDonald, K. F. & Zheludev, N. I. Active plasmonics: current status. *Laser Photonics Rev.* **4**, 562–567 (2010).
36. Soares, B. F., MacDonald, K. F., Fedotov, V. A. & Zheludev, N. I. Light-Induced Switching between Structural Forms with Different Optical Properties in a Single Gallium Nanoparticulate. *Nano Lett.* **5**, 2104–2107 (2005).
37. Blaber, M. G., Arnold, M. D. & Ford, M. J. A review of the optical properties of alloys and intermetallics for plasmonics. *J. Phys. Condens. Matter* **22**, 143201 (2010).
38. Jiménez de Castro, M., Cabello, F., Toudert, J., Serna, R. & Haro-Poniatowski, E. Potential of bismuth nanoparticles embedded in a glass matrix for spectral-selective thermo-optical devices. *Appl. Phys. Lett.* **105**, 113102 (2014).
39. Inagaki, T., Arakawa, E. T., Cahters, A. R. & Glastad, K. A. Optical properties of liquid Pb and Bi between 0.6 and 3.7 eV. *Phys. Rev. B* **25**, 6130–6138 (1982).
40. Chen, F., Yao, D. & Liu, Y. Graphene–metal hybrid plasmonic switch. *Appl. Phys. Express* **7**, 082202 (2014).
41. Linic, S., Aslam, U., Boerigter, C. & Morabito, M. Photochemical transformations on plasmonic metal nanoparticles. *Nat. Mater.* **14**, 567–576 (2015).
42. Kale, M. J., Avanesian, T. & Christopher, P. Direct Photocatalysis by Plasmonic Nanostructures. *ACS Catal.* **4**, 116–128 (2014).
43. Huang, H. *et al.* Scanning tunneling microscope and photoemission spectroscopy investigations of bismuth on epitaxial graphene on SiC (0001). *J. Phys. Chem. C* **118**, 24995–24999 (2014).
44. Hu, T. *et al.* Nanostructured Bi grown on epitaxial graphene/SiC. *J. Phys. Chem. Lett.* **9**, 5679–5684 (2018).
45. Shen, K. *et al.* Epitaxial Growth of Free-Standing Bismuth Film on Graphene Embedded with Nontrivial Properties. *ACS Appl. Electron. Mater.* **1**, 1817–1824 (2019).
46. Pantelic, R. S., Meyer, J. C., Kaiser, U. & Stahlberg, H. The application of graphene as a sample support in transmission electron microscopy. *Solid State Commun.* **152**, 1375–1382 (2012).
47. Bayer, B. C. *et al.* Atomic-Scale in Situ Observations of Crystallization and Restructuring Processes in Two-Dimensional MoS2 Films. *ACS Nano* **12**, 8758–8769 (2018).
48. Elibol, K. *et al.* Single Indium Atoms and Few-Atom Indium Clusters Anchored onto Graphene via Silicon Heteroatoms. *ACS Nano* (2021) doi:10.1021/acsnano.1c03535.
49. Predel, B. Bi-W (Bismuth-Tungsten). in *B-Ba – C-Zr* (ed. Madelung, O.) vol. 5b 1–1 (Springer-Verlag, 1992).
50. Gates-Rector, S. & Blanton, T. The Powder Diffraction File: a quality materials characterization database. *Powder Diffr.* **34**, 352–360 (2019).
51. Momma, K. & Izumi, F. VESTA: a three-dimensional visualization system for electronic and structural analysis. *J. Appl. Crystallogr.* **41**, 653–658 (2008).
52. Cucka, P. & Barrett, C. S. The crystal structure of Bi and of solid solutions of Pb, Sn, Sb and Te in Bi. *Acta Crystallogr.* **15**, 865–872 (1962).

Die approbierte gedruckte Originalversion dieser Dissertation ist an der TU Wien Bibliothek verfügbar.
The approved original version of this doctoral thesis is available in print at TU Wien Bibliothek.
TU Bibliothek Your knowledge hub WIEN

53. Howe, J. Y., Rawn, C. J., Jones, L. E. & Ow, H. Improved crystallographic data for graphite. *Powder Diffr.* **18**, 150–154 (2003).
54. Jona, F. Low-energy electron diffraction study of surfaces of antimony and bismuth. *Surf. Sci.* **8**, 57–76 (1967).
55. Gupta, T. *et al.* Sonochemical synthesis of large two-dimensional Bi2O2CO3 nanosheets for hydrogen evolution in photocatalytic water splitting. *ArXiv Prepr. ArXiv210509885* (2021).
56. Renucci, J. B., Richter, W., Cardona, M. & SchÖstherr, E. Resonance raman scattering in group Vb semimetals: As, Sb, and Bi. *Phys. Status Solidi B* **60**, 299–308 (1973).
57. Haro-Poniatowski, E. *et al.* Size effects investigated by Raman spectroscopy in Bi nanocrystals. *Phys. Rev. B* **60**, 10080–10085 (1999).
58. Mitch, M. G., Chase, S. J., Fortner, J., Yu, R. Q. & Lannin, J. S. Phase transition in ultrathin Bi films. *Phys. Rev. Lett.* **67**, 875–878 (1991).
59. Lannin, J. S. Finite size effects on the dynamics of amorphous and nanocrystalline materials. *J. Non-Cryst. Solids* **141**, 233–240 (1992).
60. Kumari, L., Lin, J.-H. & Ma, Y.-R. Laser oxidation and wide-band photoluminescence of thermal evaporated bismuth thin films. *J. Phys. Appl. Phys.* **41**, 025405 (2008).
61. Steele, J. A. & Lewis, R. A. In situ micro-Raman studies of laser-induced bismuth oxidation reveals metastability of β-Bi_2O_3 microislands. *Opt. Mater. Express* **4**, 2133 (2014).
62. Hardcastle, F. D. & Wachs, I. E. The molecular structure of bismuth oxide by Raman spectroscopy. *J. Solid State Chem.* **97**, 319–331 (1992).
63. Trentelman, K. A note on the characterization of bismuth black by Raman microspectroscopy. *J. Raman Spectrosc.* **40**, 585–589 (2009).
64. Kidambi, P. R. *et al.* Observing Graphene Grow: Catalyst–Graphene Interactions during Scalable Graphene Growth on Polycrystalline Copper. *Nano Lett.* **13**, 4769–4778 (2013).
65. Fuchs, D. *et al.* Electrochemical Behavior of Graphene in a Deep Eutectic Solvent. *ACS Appl. Mater. Interfaces* **12**, 40937–40948 (2020).
66. Aktürk, O. Ü. & Tomak, M. Bismuth doping of graphene. *Appl. Phys. Lett.* **96**, 081914 (2010).
67. Huang, H. *et al.* Scanning Tunneling Microscope and Photoemission Spectroscopy Investigations of Bismuth on Epitaxial Graphene on SiC(0001). *J. Phys. Chem. C* **118**, 24995–24999 (2014).
68. Zhang, S. *et al.* Semiconducting Group 15 Monolayers: A Broad Range of Band Gaps and High Carrier Mobilities. *Angew. Chem. Int. Ed.* **55**, 1666–1669 (2016).
69. Mehl, M. J. *et al.* The AFLOW Library of Crystallographic Prototypes: Part 1. *Comput. Mater. Sci.* **136**, S1–S828 (2017).
70. Krivanek, O. L. *et al.* Atom-by-atom structural and chemical analysis by annular dark-field electron microscopy. *Nature* **464**, 571–574 (2010).
71. Nagao, T. *et al.* Nanofilm Allotrope and Phase Transformation of Ultrathin Bi Film on Si(111)-7x7. *Phys. Rev. Lett.* **93**, 105501 (2004).
72. Scott, S., Kral, M. & Brown, S. A crystallographic orientation transition and early stage growth characteristics of thin Bi films on HOPG. *Surf. Sci.* **587**, 175–184 (2005).
73. Kowalczyk, P. J. *et al.* STM and XPS investigations of bismuth islands on HOPG. *Surf. Sci.* **605**, 659–667 (2011).
74. Kowalczyk, P. J. *et al.* Origin of the moiré pattern in thin Bi films deposited on HOPG. *Phys. Rev. B* **91**, 045434 (2015).

Die approbierte gedruckte Originalversion dieser Dissertation ist an der TU Wien Bibliothek verfügbar.
The approved original version of this doctoral thesis is available in print at TU Wien Bibliothek.
TU WIEN Bibliothek Your knowledge hub

75. Scott, S. A., Kral, M. V. & Brown, S. A. Growth of oriented Bi nanorods at graphite step-edges. *Phys. Rev. B* **72**, 205423 (2005).
76. Wang, H., Jing, J. & Henriksen, P. Onset of crystal growth of bismuth on graphite: An atomic force microscopy study. *J. Vac. Sci. Technol. Vac. Surf. Films* **11**, 1987–1991 (1993).
77. Song, F., Wells, J. W., Jiang, Z., Saxegaard, M. & Wahlström, E. Low-temperature growth of bismuth thin films with (111) facet on highly oriented pyrolytic graphite. *ACS Appl. Mater. Interfaces* **7**, 8525–8532 (2015).
78. McCarthy, D. N., Robertson, D., Kowalczyk, P. J. & Brown, S. A. The effects of annealing and growth temperature on the morphologies of Bi nanostructures on HOPG. *Surf. Sci.* **604**, 1273–1282 (2010).
79. Scott, S. A., Kral, M. V. & Brown, S. A. Bi on graphite: Morphology and growth characteristics of star-shaped dendrites. *Phys. Rev. B* **73**, 205424 (2006).
80. Kowalczyk, P. *et al.* Single atomic layer allotrope of bismuth with rectangular symmetry. *Phys. Rev. B* **96**, 205434 (2017).
81. Hu, T. *et al.* Nanostructured Bi Grown on Epitaxial Graphene/SiC. *J. Phys. Chem. Lett.* **9**, 5679–5684 (2018).
82. Song, F., Wells, J. W., Jiang, Z., Saxegaard, M. & Wahlström, E. Low-Temperature Growth of Bismuth Thin Films with (111) Facet on Highly Oriented Pyrolytic Graphite. *ACS Appl. Mater. Interfaces* **7**, 8525–8532 (2015).
83. Wang, H., Jing, J. & Henriksen, P. N. Onset of crystal growth of bismuth on graphite: An atomic force microscopy study. *J. Vac. Sci. Technol. Vac. Surf. Films* **11**, 1987–1991 (1993).
84. Krivanek, O. L. *et al.* Atom-by-atom structural and chemical analysis by annular dark-field electron microscopy. *Nature* **464**, 571–574 (2010).
85. Niggas, A. *et al.* The role of contaminations in ion beam spectroscopy with freestanding 2D materials: A study on thermal treatment. *J. Chem. Phys.* **153**, 014702 (2020).
86. Niggas, A. *et al.* Peeling graphite layer by layer reveals the charge exchange dynamics of ions inside a solid. *Commun. Phys.* **4**, 1–9 (2021).
87. Peppiatt, S. J. The Melting of Small Particles. II. Bismuth. *Proc. R. Soc. Math. Phys. Eng. Sci.* **345**, 401–412 (1975).
88. Hasegawa, M., Watabe, M. & Hoshino, K. A theory of melting in metallic small particles. *J. Phys. F Met. Phys.* **10**, 619–635 (1980).
89. Allen, G. L., Bayles, R. A., Gile, W. W. & Jesser, W. A. Small particle melting of pure metals. *Thin Solid Films* **144**, 297–308 (1986).
90. Kryshtal, A., Minenkov, A. & Dzhus, S. S. Morphology of Islet Systems Formed During Melting of Continuous Bi Films on Ge and SiO2 Substrates. *J. Nano- Electron. Phys.* **7**, (2015).
91. Kryshtal, A. P., Gladkikh, N. T. & Sukhov, R. V. Features of island nanostructures formed by melting Sn, Bi and Sn–Bi thin films on C substrates. *Appl. Surf. Sci.* **257**, 7649–7652 (2011).
92. Olson, E. A., Efremov, M. Yu., Zhang, M., Zhang, Z. & Allen, L. H. Size-dependent melting of Bi nanoparticles. *J. Appl. Phys.* **97**, 034304 (2005).
93. Zayed, M. K. & Elsayed-Ali, H. E. Condensation on (002) graphite of liquid bismuth far below its bulk melting point. *Phys. Rev. B* **72**, 205426 (2005).
94. McCarthy, D. N., Robertson, D., Kowalczyk, P. J. & Brown, S. A. The effects of annealing and growth temperature on the morphologies of Bi nanostructures on HOPG. *Surf. Sci.* **604**, 1273–1282 (2010).

Die approbierte gedruckte Originalversion dieser Dissertation ist an der TU Wien Bibliothek verfügbar.
The approved original version of this doctoral thesis is available in print at TU Wien Bibliothek.
TU Bibliothek Your knowledge hub WIEN

95. Li, J., Wang, Z. & Deepak, F. L. Direct Atomic-Scale Observation of Intermediate Pathways of Melting and Crystallization in Supported Bi Nanoparticles. *J. Phys. Chem. Lett.* **9**, 961–969 (2018).
96. Li, J. *et al.* In Situ Atomic-Scale Study of Particle-Mediated Nucleation and Growth in Amorphous Bismuth to Nanocrystal Phase Transformation. *Adv. Sci.* **5**, 1700992 (2018).
97. Wagner, J. B., Willinger, M.-G., Müller, J.-O., Su, D. S. & Schlögl, R. Surface-Charge-Induced Reversible Phase Transitions of Bi Nanoparticles. *Small* **2**, 230–234 (2006).
98. Ajayan, P. M. & Marks, L. D. Quasimelting and phases of small particles. *Phys. Rev. Lett.* **60**, 585–587 (1988).
99. Li, Y. *et al.* In situ study on atomic mechanism of melting and freezing of single bismuth nanoparticles. *Nat. Commun.* **8**, 14462 (2017).
100. Wu, S. *et al.* Size-dependent crystalline fluctuation and growth mechanism of bismuth nanoparticles under electron beam irradiation. *Nanoscale* **8**, 12282–12288 (2016).
101. Electron beam induced removal of PMMA layer used for graphene transfer | Scientific Reports. https://www.nature.com/articles/s41598-017-18444-1.
102. Wang, L., Wang, Q., Xian, A. & Lu, K. Precise measurement of the densities of liquid Bi, Sn, Pb and Sb. *J. Phys. Condens. Matter* **15**, 777–783 (2003).
103. Gusmão, R., Sofer, Z., Bouša, D. & Pumera, M. Pnictogen (As, Sb, Bi) Nanosheets for Electrochemical Applications Are Produced by Shear Exfoliation Using Kitchen Blenders. *Angew. Chem. Int. Ed.* **56**, 14417–14422 (2017).
104. Oh, S. H., Kauffmann, Y., Scheu, C., Kaplan, W. D. & Rühle, M. Ordered Liquid Aluminum at the Interface with Sapphire. *Science* **310**, 661–663 (2005).
105. Lee, C., Tame, M., Lim, J. & Lee, J. Quantum plasmonics with a metal nanoparticle array. *Phys. Rev. A* **85**, 063823 (2012).
106. Hou, W. & Cronin, S. B. A Review of Surface Plasmon Resonance-Enhanced Photocatalysis. *Adv. Funct. Mater.* **23**, 1612–1619 (2013).
107. Jiang, N., Su, D., Spence, J. C., Zhou, S. & Qiu, J. Volume plasmon of bismuth nanoparticles. *Solid State Commun.* **149**, 111–114 (2009).
108. Powell, C. The origin of the characteristic electron energy losses in ten elements. *Proc. Phys. Soc. 1958-1967* **76**, 593 (1960).
109. Jiménez de Castro, M., Serna, R., Toudert, J., Fernández Navarro, J. M. & Haro-Poniatowski, E. Thermo-optical properties of Bi nanoparticles embedded in germanate glasses and alumina thin films. *Ceram. Int.* **41**, 8216–8222 (2015).
110. Haro-Poniatowski, E., Serna, R., Suárez-García, A. & Afonso, C. N. Thermally driven optical switching in Bi nanostructures. *Nanotechnology* **16**, 3142–3145 (2005).
111. Haro-Poniatowski, E., Castro, M. J. de, Navarro, J. M. F., Morhange, J. F. & Ricolleau, C. Melting and solidification of Bi nanoparticles in a germanate glass. *Nanotechnology* **18**, 315703 (2007).
112. Toudert, J., Serna, R. & Jiménez de Castro, M. Exploring the Optical Potential of Nano-Bismuth: Tunable Surface Plasmon Resonances in the Near Ultraviolet-to-Near Infrared Range. *J. Phys. Chem. C* **116**, 20530–20539 (2012).

Die approbierte gedruckte Originalversion dieser Dissertation ist an der TU Wien Bibliothek verfügbar.
The approved original version of this doctoral thesis is available in print at TU Wien Bibliothek.
TU Bibliothek Your knowledge hub WIEN

Outcome:

Paper II:

"Structural and Plasmonic Evolution in Mixed-Dimensionality Bismuth/Graphene Heterostructures" --finalized

Structural and Plasmonic Evolution in Mixed-Dimensionality Bismuth/Graphene Heterostructures

Tushar Gupta et al.

Die approbierte gedruckte Originalversion dieser Dissertation ist an der TU Wien Bibliothek verfügbar.
The approved original version of this doctoral thesis is available in print at TU Wien Bibliothek.
TU Bibliothek Your knowledge hub WIEN

Chapter 6

Liquid Phase Exfoliation of Bi

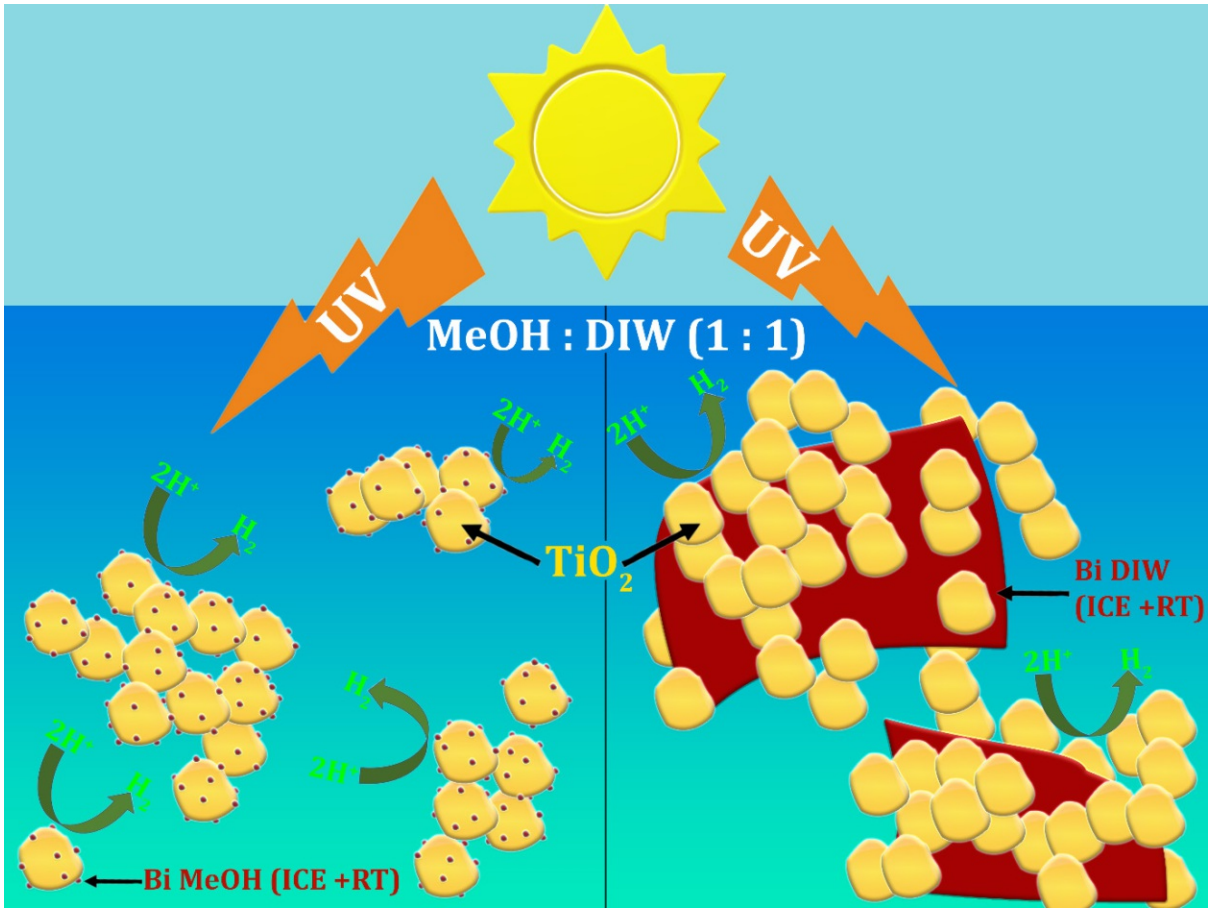

Die approbierte gedruckte Originalversion dieser Dissertation ist an der TU Wien Bibliothek verfügbar.
Your source for knowledge. The approved original version of this thesis is available in print at TU Wien Bibliothek.
TU Bibliothek
WIEN Vourknowledge hub

Chapter Preview

Chapter 6 addresses the second adopted route for the synthesis of 2D pnictogens via wet chemical approach of sonochemical assisted process. Interestingly, carrying out the exfoliation of bismuth under the described conditions led to the synthesis of a different compound of bismuth: namely bismutite.

Laterally large (~3 µm), atomically-thin two-dimensional (2D) $Bi_2O_2CO_3$ nanosheets (2D bismuth oxycarbonate, 2D bismutite) were fabricated via sonochemically-assisted template-free synthesis. Key to the synthesis of the freestanding, laterally large 2D $Bi_2O_2CO_3$ nanosheets from bulk Bi powder is choice of suspension medium, controlled reaction temperatures and several hours processing time. Lateral sizes of 2D $Bi_2O_2CO_3$ can be controlled between µm-sized nanosheets and tens of nm sized nanoflakes solely based on the choice of suspension medium. The here introduced 2D $Bi_2O_2CO_3$ nanosheets/-flakes were then hybridized by a simple mix-and-match approach with TiO_2 nanoparticles for testing in suspension-type photocatalytic hydrogen production via water splitting. This introduces the 2D $Bi_2O_2CO_3$ with TiO_2 as a promising noble-metal-free catalyst component for hydrogen evolution in photocatalytic water splitting.

The findings enrich the fabrication toolbox of emerging 2D pnictogen oxycarbonates towards large 2D nanosheets and demonstrate the promising potential of 2D $Bi_2O_2CO_3$ as a catalyst component for hydrogen evolution in photocatalytic water splitting. The figure caption for chapter 6 is a graphical representation of interfacing of two different morphology of the exfoliated $Bi_2O_2CO_3$ with TiO_2 exhibiting hydrogen evolution activity via photocatalytic water splitting under UV light.

*The contents of this chapter have been submitted for publication. (**see pre-print repository:** https://arxiv.org/ftp/arxiv/papers/2105/2105.09885.pdf)*

Die approbierte gedruckte Originalversion dieser Dissertation ist an der TU Wien Bibliothek verfügbar.
The approved original version of this doctoral thesis is available in print at TU Wien Bibliothek.
TU Bibliothek Your knowledge hub WIEN

6. Liquid Phase Exfoliation of Bi

6.1 Introduction

Two-dimensional (2D) pnictogens such as 2D antimony ("antimonene") and 2D bismuth ("bismuthene") have spurred tremendous interest in electronics, energy applications and catalysis.[1–5] Likewise, more recently, also 2D pnictogen compounds have come into focus because of their combination of unusual, potentially useful properties in electronics, energy and catalysis.[6-13] For the case of bismuth, this includes recent work on binary 2D bismuth oxides[10–13] and 2D ternary and multinary oxygen-containing bismuth compound phases, incl. 2D Bi-oxyhalides, 2D Bi_2WO_6, 2D Bi_2MoO_6 or 2D $BiVO_4$.[2,3,9,14,15]

Amongst the ternary bismuth compound phases, the bismuth oxycarbonate (BOC) $Bi_2O_2CO_3$ phase, also called bismutite and bismuth subcarbonate $(BiO)_2CO_3$, is of particular interest.[16] $Bi_2O_2CO_3$ has an intrinsically layered structure composed of alternating $[Bi_2O_2]^{2+}$ and $[CO_3]^{2-}$ sub-layers and is a semiconductor with a band gap of ~3.1 – 3.5 eV.[16] In nanostructured form, $Bi_2O_2CO_3$ has been shown to have useful properties, particularly towards energy, catalysis and photocatalysis.[16] In particular for photocatalysis, 2D morphology can offer benefits over other morphologies incl. intrinsically high specific surface areas and short migration lengths of photogenerated charge carriers to the reaction fronts on the 2D materials' surfaces. This can reduce recombination losses and thus lead to higher activity of 2D forms of common materials.[17] Synthesis of $Bi_2O_2CO_3$ in atomically-thin 2D morphology remains however underdeveloped, in particular in terms of rational control over lateral sizes and thicknesses.[16,18–49]

Towards filling this gap, a simple method of sonochemically-assisted[50,51] template-free synthesis of laterally large, atomically-thin 2D $Bi_2O_2CO_3$ nanosheets is presented. In particular, the presented synthesis approach readily allows control over lateral 2D $Bi_2O_2CO_3$ size between unusually large, µm-sized nanosheets and small, tens of nm sized nanoflakes solely depending on suspension medium.

Die approbierte gedruckte Originalversion dieser Dissertation ist an der TU Wien Bibliothek verfügbar.
The approved original version of this doctoral thesis is available in print at TU Wien Bibliothek.
TU Bibliothek Your knowledge hub WIEN

While nanostructured $Bi_2O_2CO_3$ is a popular photocatalyst for organic pollutant and NO degradation,[16,18–34,47–49] it has to date received little attention for photocatalytic solar fuel production such as in photocatalytic hydrogen evolution reaction (HER) from water splitting.[35,36,52] This is despite photocatalytic HER being one of the key technologies to meet the demands of the growing energy crisis in a sustainable way.[53,54] Photocatalytic HER critically hinges on the availability of (cost-)efficient, scalable (heterojunction) catalysts and/or (co-)catalysts and the search for these is an ongoing challenge.[53,54]

To this end, here newly introduced 2D $Bi_2O_2CO_3$ nanosheets/-flakes were hybridized by a simple mix-and-match approach with TiO_2 nanoparticles and these hybrids were then tested as heterogeneous photocatalysts in suspension-type photocatalytic HER from water splitting. The results thereby introduce 2D $Bi_2O_2CO_3$ with TiO_2 as a prospective noble-metal-free catalyst component for photocatalytic HER.

6.2 Experimental Procedure

6.2.1 Synthesis of 2D $Bi_2O_2CO_3$ nanosheets/-flakes

The followed sonochemically-assisted synthesis (already been described in section 3.2.2 of chapter 3) first encompasses liquid-phase-exfoliation (LPE)[50,51] type treatment of bulk Bi powder which has a layered, buckled rhombohedral β-Bi/A7 crystal structure[55] and a particle size of up to 150 µm (Figure 6.1). To provide energy to the system ultrasonic bath immersion was employed.[50,51] Sonication was undertaken with air-tight closed sample vials that were immersed in the temperature-controlled sonication bath. Importantly, 5 different suspension media ("solvents") were screened for the Bi during sonochemical treatment, namely: water (H_2O), methanol (MeOH), isopropanol (IPA), ethanol (EtOH) and (motivated by prior literature[56]) IPA:H_2O (4:1) mixture. All solvents were of technical grade and are used without particular purging to remove dissolved gases before synthesis. H_2O was nominally deionized, however resistivity measurements on the order of only ~0.4 MΩ cm indicate significant concentrations of residual ions to be present in

Die approbierte gedruckte Originalversion dieser Dissertation ist an der TU Wien Bibliothek verfügbar.
The approved original version of this doctoral thesis is available in print at TU Wien Bibliothek.
TU Bibliothek Your knowledge hub WIEN

the water incl. carbonate ions from CO_2 dissolution from ambient. Consistent with high content of residual ions in the water, we also find significant traces of Ca and Na from the H_2O preparation in the XPS survey scan (see section 6.3), which we also ascribe to residual ions in the H_2O. A wide screening of solvents is often key in LPE and related techniques as 2D materials' suspendabilities are known to be highly solvent dependent.[50]

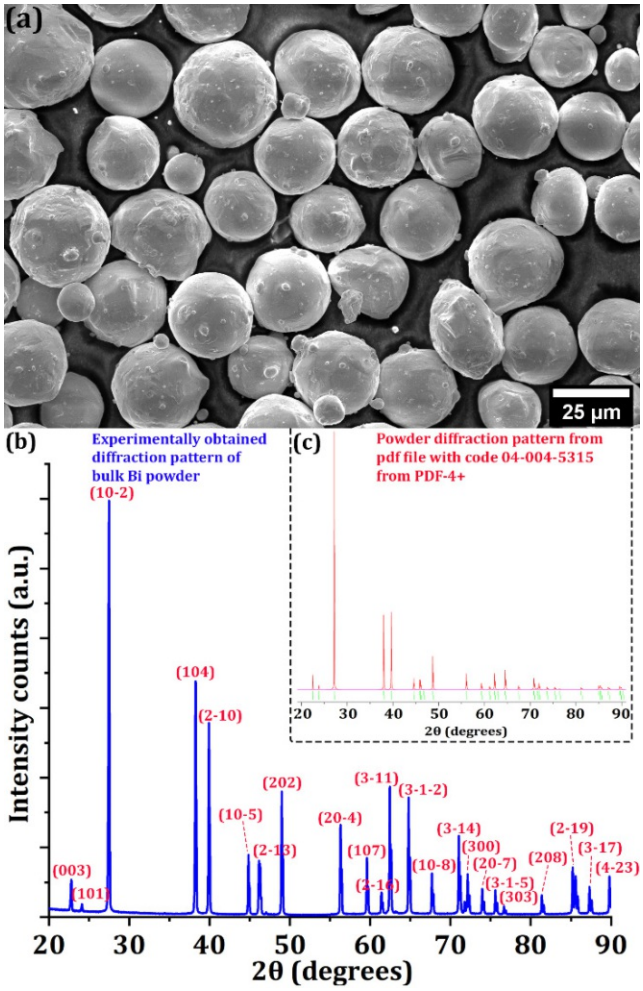

Figure 6.1: (a) SEM image of initial bulk Bi powder. (b) shows the experimentally obtained diffraction pattern of the bulk Bi powder (c) shows the simulated diffraction pattern from the PDF file 04-004-5315 corresponding to rhombohedral β-Bi. The peaks in the obtained diffraction pattern in (b) have been (hkl)-indexed to the simulated pattern in (c). All the peaks obtained in the diffractogram were successfully indexed to β-Bi. This reaffirms the phase purity of bulk Bi powder and verifies the absence of any Bi-oxides in the initial precursor before our sonochemical synthesis.

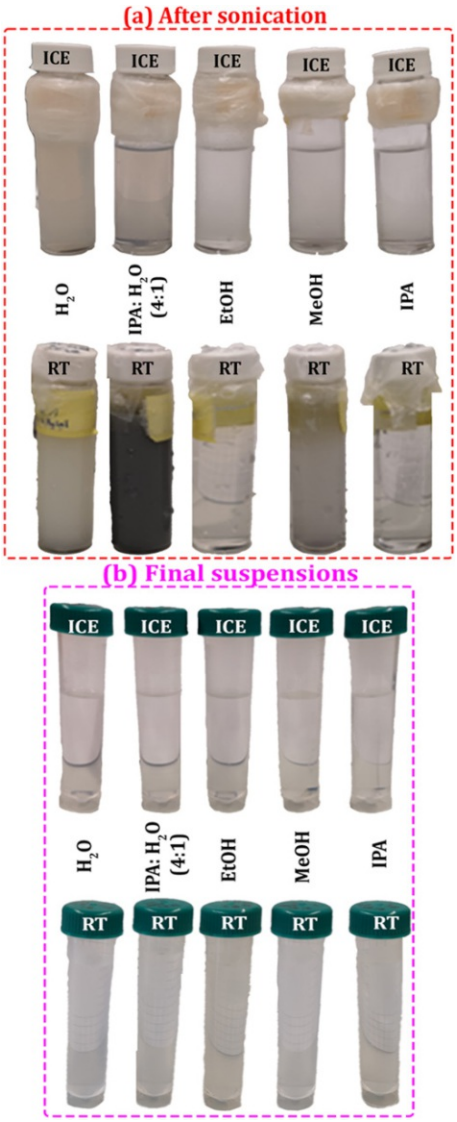

Figure 6.2: Photographs showing the optical appearance of the suspensions of 60 mg of Bi powder in 15 mL of the solvents after 15 h of sonication (a) and of the supernatant collected after subsequent centrifugation (b).

Die approbierte gedruckte Originalversion dieser Dissertation ist an der TU Wien Bibliothek verfügbar.
The approved original version of this doctoral thesis is available in print at TU Wien Bibliothek.
TU Bibliothek Your knowledge hub WIEN

The initial starting concentration of Bi was chosen to be 4 mg mL^{-1} in all solvents, where Bi powder (60 mg) was dispersed in solvent (15 mL). Bi powder was weighed and put into the solvents in vials in ambient air. Then sonication was done by immersion of the air-tight capped vials with the sample solutions in the temperature-controlled sonication water bath. After the sonication, the supernatant in the vials was immediately collected and transferred to the centrifuge tubes without disturbing the sediment. From the initial 15 mL volume of the solution used for the sonication, an approximate volume of 10 mL was safely collected for the next step of centrifugation. After the centrifugation, again the supernatant was immediately separated without disturbing the sediment and transferred to a separate tube. From the initial 10 mL volume of the sonicated sample used for centrifugation, approximately 7.5 mL volume of supernatant was safely recovered after centrifugation. It was this volume of the supernatant (after sonication and centrifugation) that was further utilized for characterization and photocatalytic testing.

To note is that after the sonication step, the suspensions were visibly opaque compared to parent solvents, but after the centrifugation step the suspensions looked virtually as translucent as their parent solvents to the naked eye as depicted in Figure 6.2. This suggests that concentrations of material in centrifuged suspensions is low. Gravimetric quantification of concentration of solid content via solvent evaporation corroborates this and put concentrations in our suspension to a maximum of ~50 mg L^{-1} (which was the detection limit of the balance system).

"Efficacy of 5 different solvents was tested towards exfoliation of bismuth. Important for the recipe development, ultrasonication employed very long processing time (15 h) and very close control of bath temperature during sonication to either "room temperature" (RT, 22 °C to 26 °C) or "ice bath" conditions (ICE, 0.1 °C to 2.2 °C). Subsequent to sonication, suspensions were centrifuged and then supernatant was collected for further characterization and photocatalytic testing"

Die approbierte gedruckte Originalversion dieser Dissertation ist an der TU Wien Bibliothek verfügbar.
The approved original version of this doctoral thesis is available in print at TU Wien Bibliothek.
TU Bibliothek Your knowledge hub WIEN

6.3 Results and Discussion

6.3.1 Morphology and Structure

Figure 6.3 shows scanning electron microscopy (SEM) images of obtained products from sonication and centrifugation (after drop casting onto SiO_2/Si wafer) for MeOH (Figure 6.3a,b) and H_2O (Figure 6.3d,e) from RT and ICE processing. The SEM images confirmed that, despite the visually translucent suspensions, ample solid material was suspended in the sonicated and centrifuged samples. Strikingly, while MeOH (both in ICE and RT) produced small nanoflakes (lateral sizes ~80nm), H_2O resulted in large 2D nanosheets of roughly square shapes with lateral sizes of several µm (ICE: average 3.5 µm ± 2.6 µm standard deviation; RT: average 2.3±1.3 µm) and an apparently low thickness (as flakes appear electron transparent in the SEM images). IPA (RT, ICE), EtOH (RT, ICE) and IPA: H_2O (RT) led to small nanoflakes (Figure 6.4a-e) akin to MeOH, which for IPA and EtOH also appeared to be thicker compared to H_2O and MeOH. IPA:H_2O (ICE) produced thin square nanosheets with µm lateral sizes (Figure 6.4f).

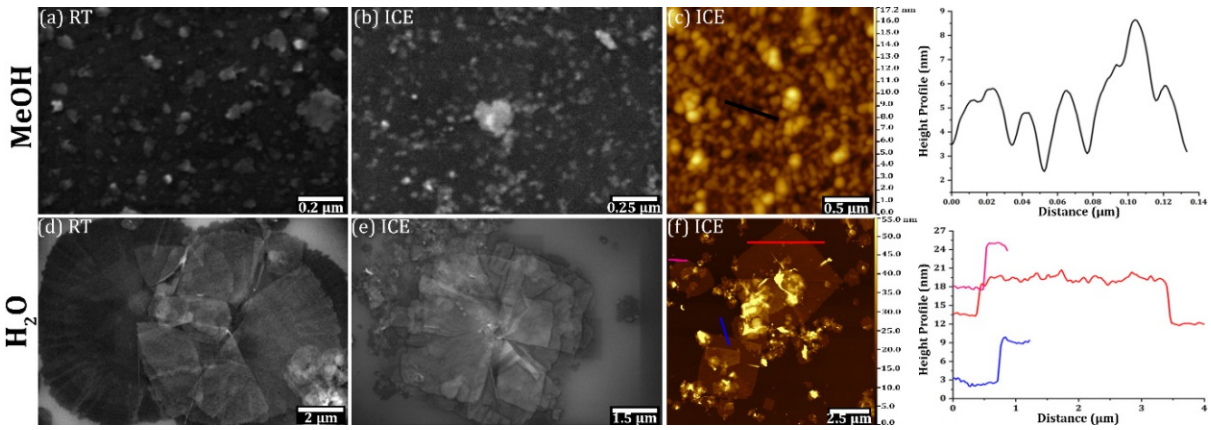

Figure 6.3: (a,b) SEM micrographs of MeOH RT and ICE, (c) AFM image of MeOH ICE. (d,e) SEM images of H_2O RT and ICE (f) AFM image of H_2O ICE. Line profiles over the flakes are plotted alongside the AFM images in (c,f) to obtain thickness measurements of the flakes.

Die approbierte gedruckte Originalversion dieser Dissertation ist an der TU Wien Bibliothek verfügbar.
The approved original version of this doctoral thesis is available in print at TU Wien Bibliothek.
TU Bibliothek Your knowledge hub WIEN

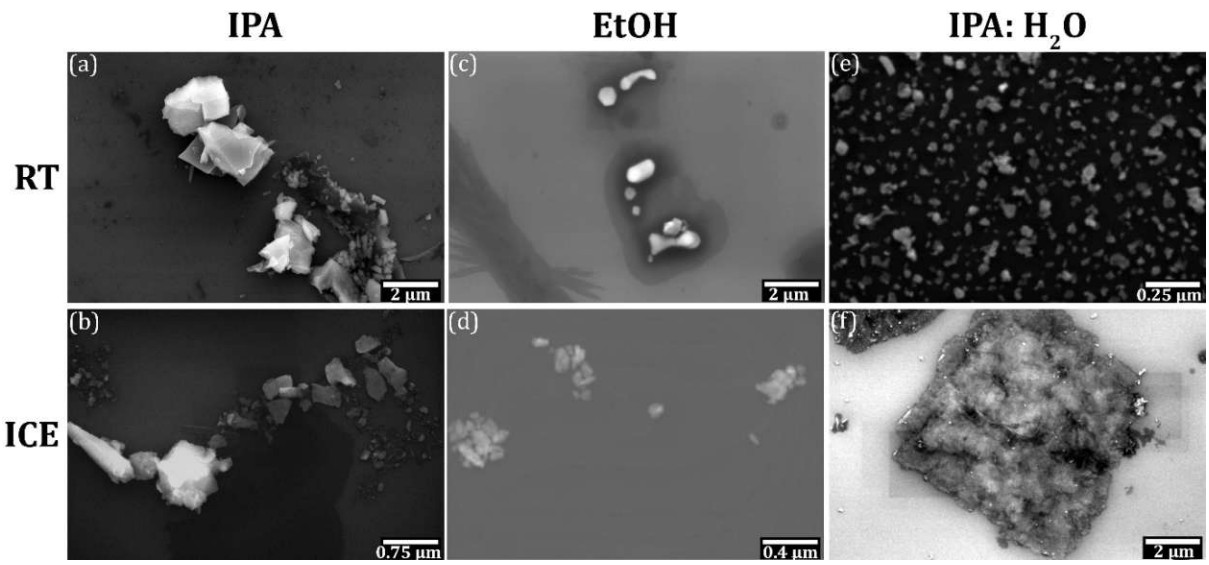

Figure 6.4: SEM images of obtained nanoflakes in IPA (a,b); EtOH (c,d); IPA: H_2O (4:1) (e,f) at RT (a,c,e) and ICE conditions (b,d,f), respectively.

In Figure 6.3c,f atomic force microscopy (AFM) measurements are presented to ascertain the thickness of the laterally small MeOH ICE and laterally large H_2O ICE products. Figure 6.3c confirms that MeOH ICE resulted in thin (~2.5 – 3 nm) but laterally small (only ~ 80 nm) nanoflakes. In very stark contrast, H_2O ICE in Figure 6.3f resulted in approximately squareshaped nanosheets with ultra-high aspect ratios, with lateral sizes of ~3 µm and atomic-scale thicknesses of only 4 – 6 nm. Figure 6.5 shows that MeOH RT resulted in correspondingly small nanoflake morphology and that H_2O RT resulted in correspondingly large, atomically thin 2D nanosheet morphology.

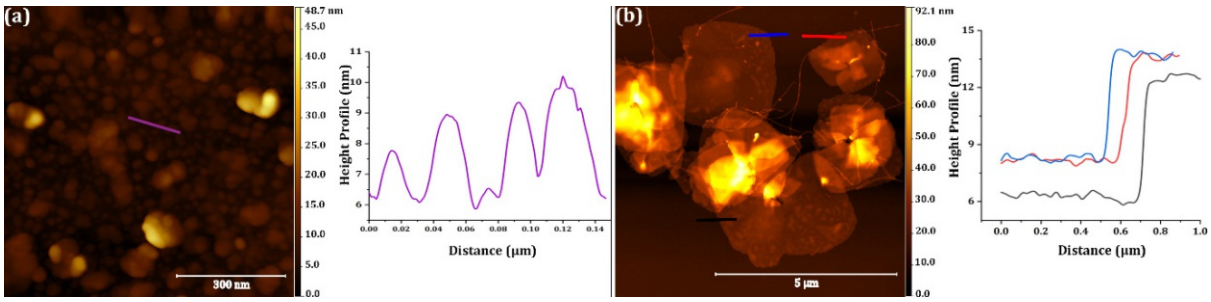

Figure 6.5: AFM images of MeOH RT (a) and H_2O RT (b). Line profiles over the flakes are plotted alongside to measure flake thickness.

Figure 6.6a-c presents a structural characterization of the MeOH ICE products by bright-field (BF) transmission electron microscopy (TEM, overview Figure 6.6a, lattice

Die approbierte gedruckte Originalversion dieser Dissertation ist an der TU Wien Bibliothek verfügbar.
The approved original version of this doctoral thesis is available in print at TU Wien Bibliothek.
TU Bibliothek Your knowledge hub WIEN

resolution side-view in Figure 6.6b and lattice resolution top-view in Figure 6.6c with Fourier Transforms (FTs) in insets). TEM confirmed the small lateral size, atomic thickness of the nanoflakes and additionally proved their crystalline nature. Figure 6.6d-f shows corresponding TEM data for the H_2O ICE products in terms of BF-TEM overview (Figure 6.6d), lattice resolution TEM in topview (Figure 6.6e, FT in inset) and a selected area electron diffraction pattern (SAED) from topview (Figure 6.6f). For the H_2O ICE preparations, TEM confirmed the large lateral size, atomic thickness and approximate square shape, and additionally proved the single crystalline nature of the large nanosheets.

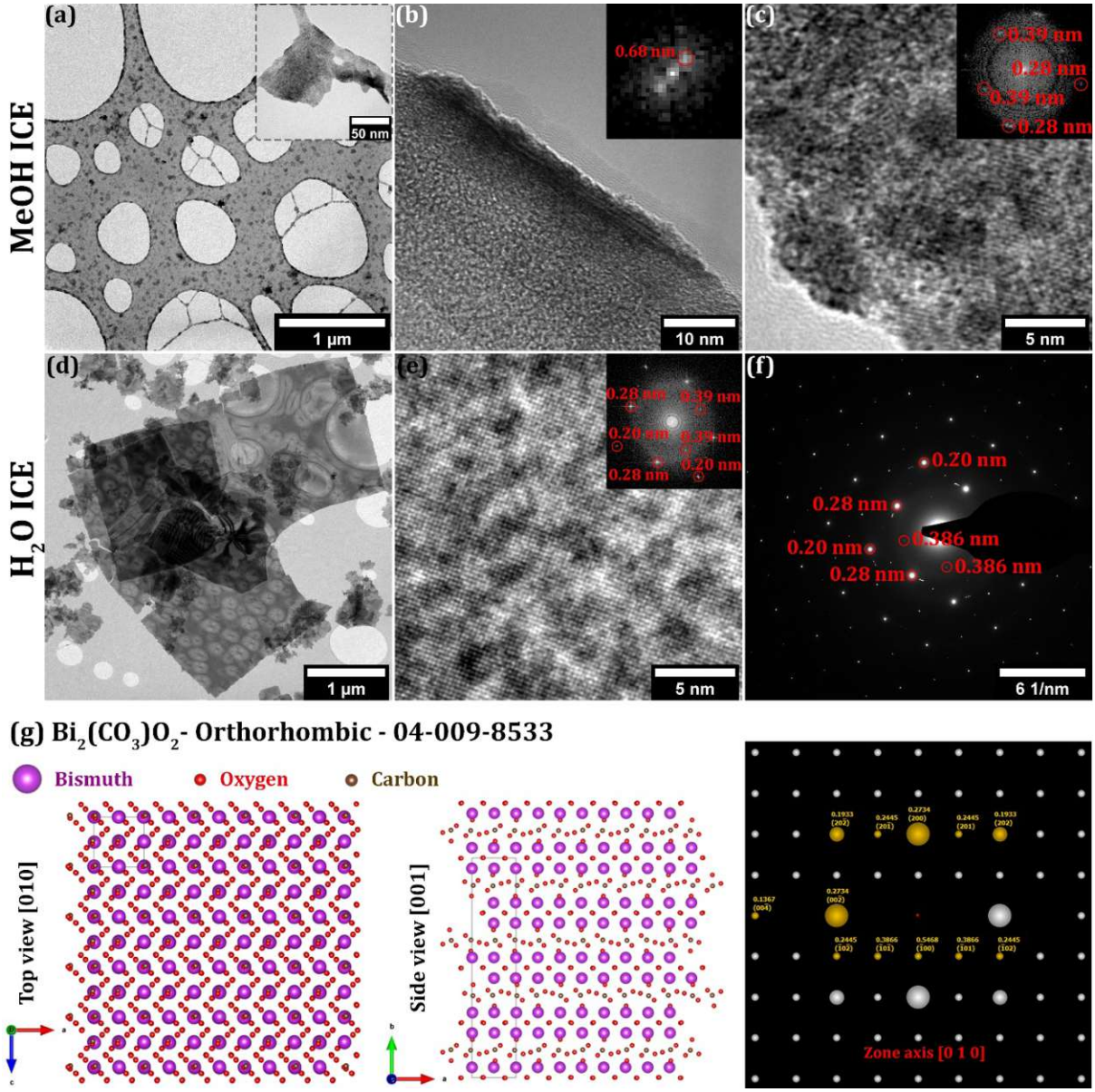

Figure 6.6: (a-c) MeOH ICE studied by overview BF-TEM (a), lattice resolution side-view (b, FT in inset) and lattice resolution top-view (c, FT inset) BF-TEM of nanoflake. (d-f) H_2O ICE studied by

Die approbierte gedruckte Originalversion dieser Dissertation ist an der TU Wien Bibliothek verfügbar.
The approved original version of this doctoral thesis is available in print at TU Wien Bibliothek.
TU Bibliothek Your knowledge hub WIEN

overview (d) and lattice resolution (e, FT in inset, top-view of flake) BF-TEM and top-view SAED (f). (g) shows a structural model of orthorhombic 2D $Bi_2O_2CO_3$ (powder diffraction file: 04-009-8533)[57] in top-view along [010] (left) and side-view along [001] (middle) and a simulated SAED/FT pattern (middle) for $Bi_2O_2CO_3$ along [010] zone axis (i.e. top-view) with salient reflections matches to experimental data in (e,f) highlighted. corresponding SAED/FT simulation of side-view is shown in Figure 6.7.

To identify the crystal structure of the nanoflakes and nanosheets from the lattice resolution TEM and SAED data, it was considered that the starting educt is Bi, and that reactions to Bi_xO_y and $Bi_xO_yC_z$ via oxygen and carbon from MeOH and H_2O decomposition in sonication and via dissolved oxygen and carbonate ions CO_3^{2-} from dissolved CO_2 in the solvents are likely reaction pathways during our long sonication processes. Interestingly, comparing against multiple Bi, Bi_xO_y and $Bi_xO_yC_z$ database structures (see extended discussion in section 6.3.2), consistent best match to the experimental top-view TEM/SAED data (Figure 6.6c,e,f) was found to be orthorhombic $Bi_2O_2CO_3$ viewed along the [010] zone axis (Figure 6.6g, left). (Please note that instead of the orthorhombic unit cell alternatively often a tetragonal unit cell is used to describe $Bi_2O_2CO_3$. The results are discussed using this tetragonal notation.)

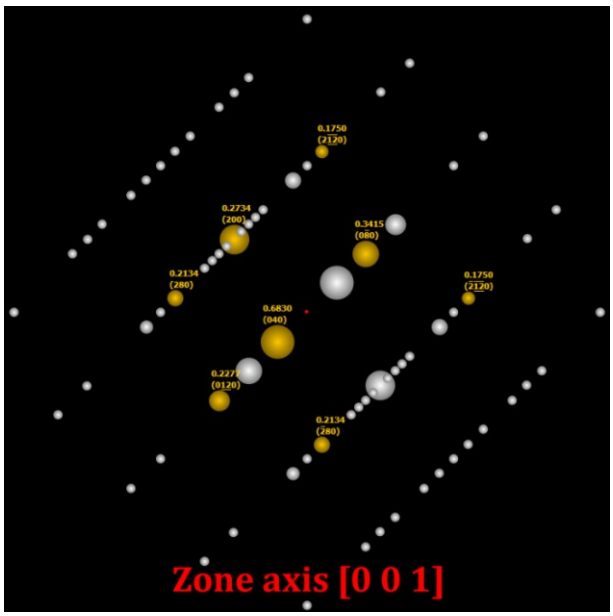

Figure 6.7: Side view FT/SAED simulation for orthorhombic $Bi_2O_2CO_3$ (PDF file orthorhombic 04-009-8533)[57]. Note that FT/SAED simulation is not rotation corrected with respect to side-view, i.e. "basal" (010) plane family parallel to substrate appear inclined at ~45° in this simulation.

The synthesized nanoflakes and nanosheets were thus layered orthorhombic $Bi_2O_2CO_3$ with the alternating Bi_2O_2 and CO_3 sub-layers parallel to the substrate (Figure 6.6g,

Die approbierte gedruckte Originalversion dieser Dissertation ist an der TU Wien Bibliothek verfügbar.
The approved original version of this doctoral thesis is available in print at TU Wien Bibliothek.
TU Bibliothek Your knowledge hub WIEN

middle, orthorhombic $Bi_2O_2CO_3$ with [010] or (010) texture). Beyond structure identification from top-view images, for the MeOH ICE lattice resolved sideview images of the 2D flakes (Figure 6.6b) were also observed. These confirmed their atomically-thin "few-layer" nature and lattice fringes in the side view of ~0.68 nm were measured, which was also in excellent agreement of the layer distance in orthorhombic $Bi_2O_2CO_3$ of ~0.68 nm (corresponding to (040) plane family shown via side-view SAED/FT simulation in Figure 6.7). Thus the side-view TEM data also corroborated 2D $Bi_2O_2CO_3$ with (010) texture.

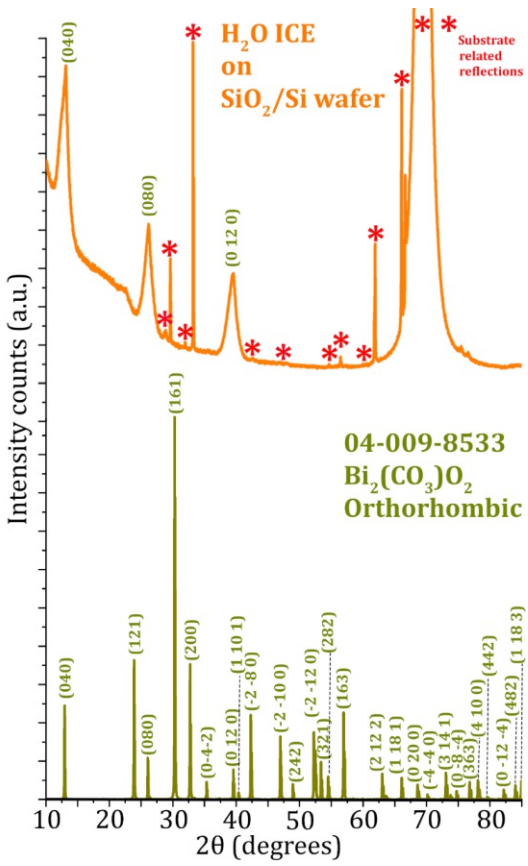

Figure 6.8: XRD pattern (Bragg-Brentano geometry) of H_2O ICE drop cast onto SiO_2/Si substrates. XRD peaks related to the the single-crystalline Si(100) wafer substrate are marked with red asteriks (*). Three reflections (~13°, ~26° and ~40°) are related to the H_2O ICE nanosheets and are consistently indexed to orthorhombic $Bi_2O_2CO_3$ (PDF: 04-009-8533)[57] (040), (080) and (0120) reflections (as labelled), respectively. This is for XRD in Bragg-Brentano geometry exactly the pattern one would expect from 2D $Bi_2O_2CO_3$ with (010) texture, as indicated from TEM data.

The TEM based structural phase assignment was also backed up on a larger scale by Bragg-Brentano X-ray diffractometry (XRD) measurements of nanosheets drop-casted onto SiO_2/Si wafers (Figure 6.8). The measured XRD patterns were highly consistent with $Bi_2O_2CO_3$ with (040) (and equivalently (010)) texture. Notably, XRD was inconsistent with other possible candidate phases, most importantly excluding all Bi_2O_3 polymorphs (see section 6.3.2). Furthermore, XRD did not indicate the presence of any other phases, thus confirming phase purity of the synthesized 2D $Bi_2O_2CO_3$ nanosheets. The phase purity was also corroborated by the number of flakes/sheets observed at lattice resolution in TEM (7 for MeOH, 15 for H_2O) which were all consistently best indexed to 2D $Bi_2O_2CO_3$ along [010] zone axis. Similarly, MeOH RT and H_2O RT synthesis products were found to be best matched by 2D $Bi_2O_2CO_3$ (Figure 6.9). The phase assignment therefore suggested that during 15 h sonication, the Bi has not only transformed to 2D

Die approbierte gedruckte Originalversion dieser Dissertation ist an der TU Wien Bibliothek verfügbar.
The approved original version of this doctoral thesis is available in print at TU Wien Bibliothek.
TU Bibliothek Your knowledge hub WIEN

nanoflake/-sheet morphology[51] but concurrently got oxidized and bridged/intercalated by CO_3^{2-} to form 2D $Bi_2O_2CO_3$.

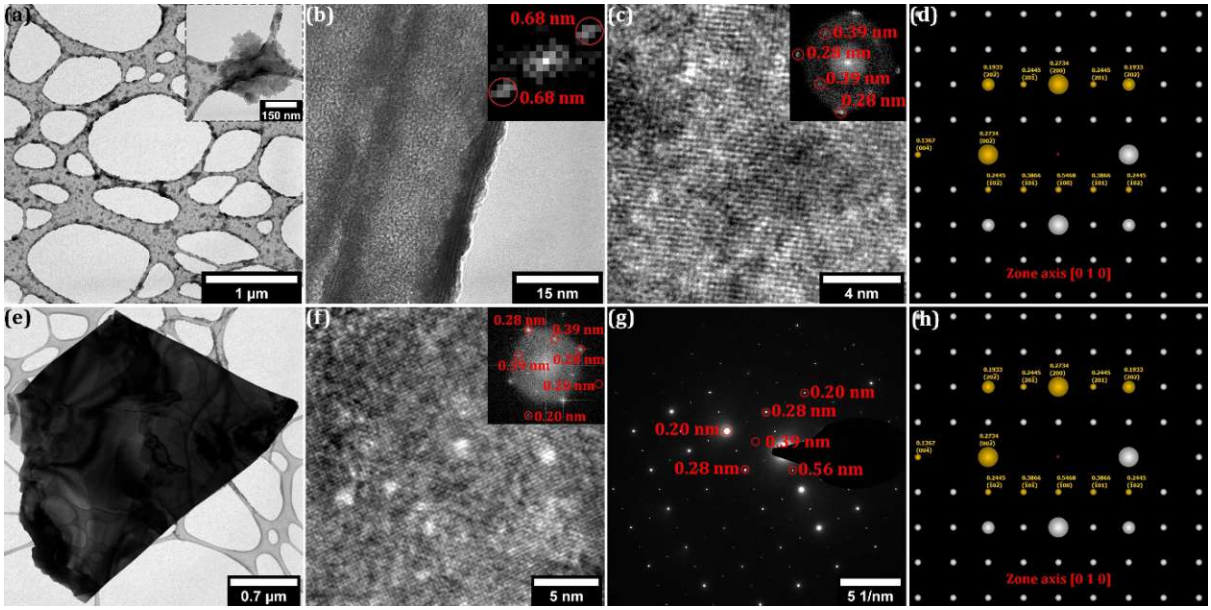

Figure 6.9: (a-d) MeOH RT studied by overview BF-TEM (a), lattice resolution side-view (b, FT inset) and lattice resolution top-view (c, FT inset) of flake. (d) shows a simulated SAED/FT pattern for orthorhombic $Bi_2O_2CO_3$ along [010] zone axis with salient reflections matches to experimental data in (c) highlighted. (e-h) H_2O RT studied by overview (e) and lattice resolution (f, FT in inset, top-view of flake) BF-TEM and top-view SAED (g). (h) shows a simulated SAED/FT pattern for $Bi_2O_2CO_3$ along [010] zone axis with salient reflections matches to experimental data in (f,g) highlighted.

Additional characterization of the synthesized 2D $Bi_2O_2CO_3$ nanoflakes/-sheets was carried out via Energy dispersive X-ray spectroscopy (EDX), X-ray photoelectron spectroscopy (XPS) and Photoluminescence (PL) studies and has been discussed below:

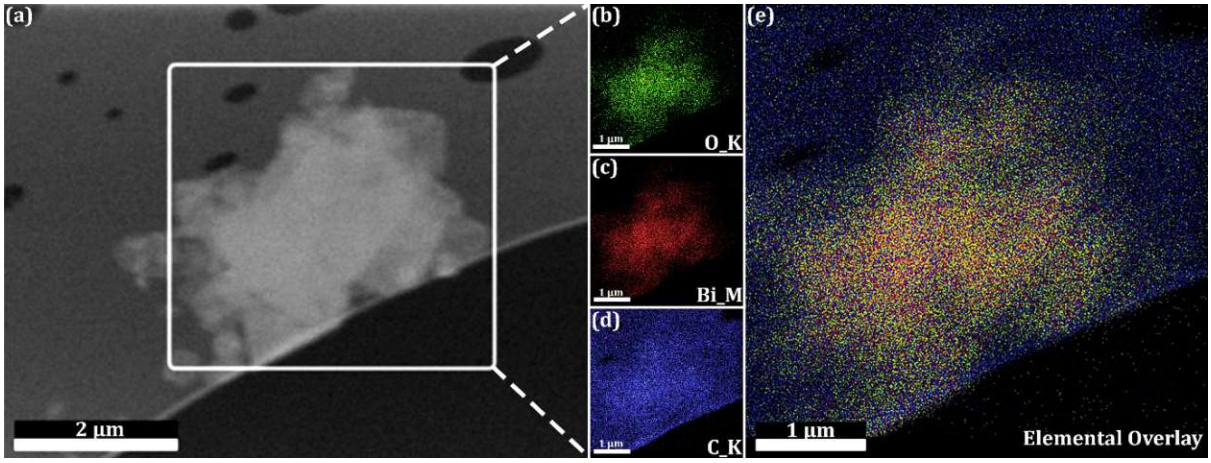

Figure 6.10: Qualitative analysis of Bi H_2O ICE nanosheets via EDX mapping. (a) shows a SEM micrograph of the region of interest in the white square in which EDX mapping was done. (b), (c)

Die approbierte gedruckte Originalversion dieser Dissertation ist an der TU Wien Bibliothek verfügbar.
The approved original version of this doctoral thesis is available in print at TU Wien Bibliothek.
TU Bibliothek Your knowledge hub WIEN

and (d) show the laterally resolved EDX maps for oxygen, bismuth and carbon respectively. A corresponding, elemental overlay composite image of the three elemental maps is presented in (e).

To verify homogeneous presence of Bi, O and C in the nanosheets, EDX mapping of H_2O ICE nanosheets on amorphous carbon TEM membranes was undertaken. Elemental mapping as shown in Figure 6.10 clearly shows the homogeneous presence of Bi, O and C in the nanosheets, corroborating that the nanosheets are 2D $Bi_2O_2CO_3$ (and not metallic 2D bismuthene).

XPS measurements were performed on H_2O ICE nanosheets on SiO_2 (90 nm)/Si wafer. The Bi4f signal has only a single component at a binding energy (BE) of 159.2 eV ($Bi4f_{7/2}$) consistent with Bi^{3+} (as in, e.g., $Bi_2O_2CO_3$, Figure 6.11a).[19] The Bi4f signal in particular excludes the presence of metallic Bi^0 which would be expected at a BE of 156.9 eV.[13,51] Components characteristic of oxycarbonates were correspondingly found in the O1s signal (Figure 6.11b) at a BE of 529.8 eV for Bi-O,[19] at 532.1 eV for C-O[19] (and/or additionally SiO_2 substrate).[58] An intermediate component at 530.9 eV is attributed to carbonate ions[19] and possibly C=O in either the deposit or adventitious carbon contamination. The C1s signal in Figure 6.11c exhibit three components at 285.0 eV, 286.2 eV and 288.6 eV that can be attributed to C-C/C-H, C-O and oxycarbonates respectively, the latter possibly overlapping with the signal of C=O.[19] In particular, the 285.0 eV peak is also consistent with adventitious carbon adsorption from sample storage in ambient air. Survey XPS spectra (Figure 6.12) detected only Bi, O and C plus Si from the substrate as well as traces of Na and Ca, which could be linked to residual ions in the H_2O solvent (as discussed above). In summary, XPS showed signatures consistent with $Bi_2O_2CO_3$[19] and excluded the presence of metallic Bi.[51]

PL mapping (from 532 nm excitation) was performed to study optoelectronic properties of the H_2O ICE nanosheets on SiO_2/Si. Figure 6.13 (left) shows a laterally resolved PL emission intensity map (excitation beam of 532 nm filtered by 550 nm long-pass filter), which indicates the nanosheets to have a PL response well above the "dark" SiO_2/Si substrate. Figure 6.13 (right) shows a PL emission spectrum from the flake circled blue on the map on the left, indicating that the PL emission is predominantly from emission at ~550 nm (confirmed for several flakes, spectrum has been background corrected for

Die approbierte gedruckte Originalversion dieser Dissertation ist an der TU Wien Bibliothek verfügbar.
The approved original version of this doctoral thesis is available in print at TU Wien Bibliothek.
TU Bibliothek Your knowledge hub WIEN

SiO_2/Si background). PL emission at ~550 nm (for 532 nm excitation) is consistent with prior reports of PL from $Bi_2O_2CO_3$.[30,59] Similar PL emission characteristics are also measured for MeOH ICE nanoflakes.

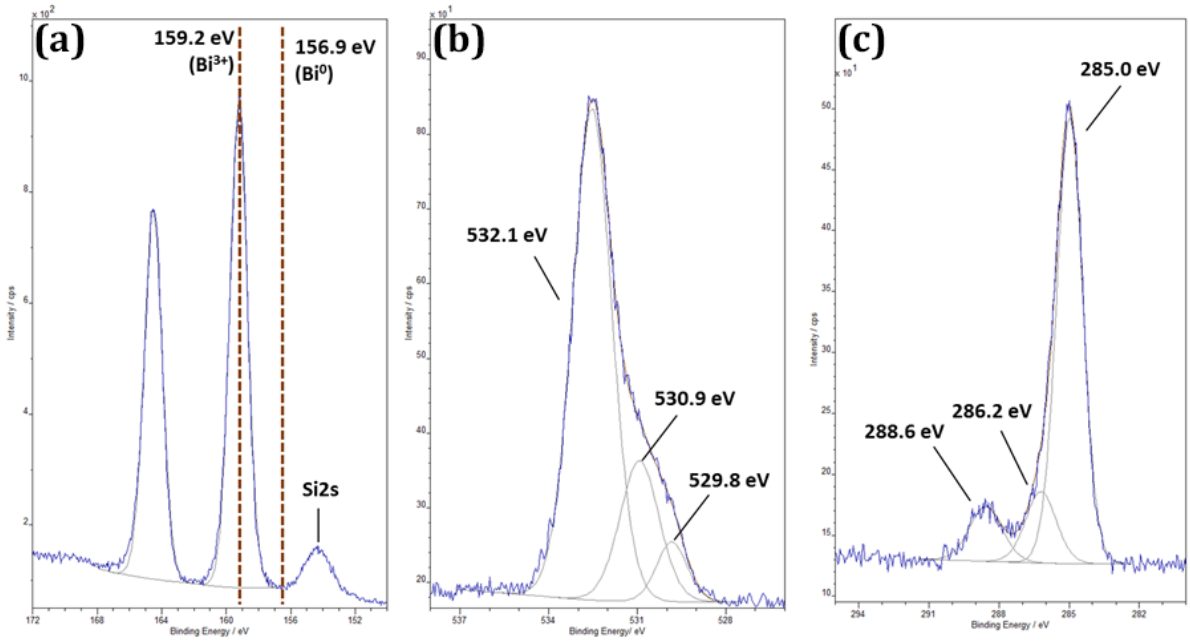

Figure 6.11: (a) Bi4f core-level spectra H_2O ICE nanosheets on SiO_2/Si and (b) corresponding O1s spectra. (c) C1s core-level spectra H_2O ICE nanosheets on SiO_2/Si.

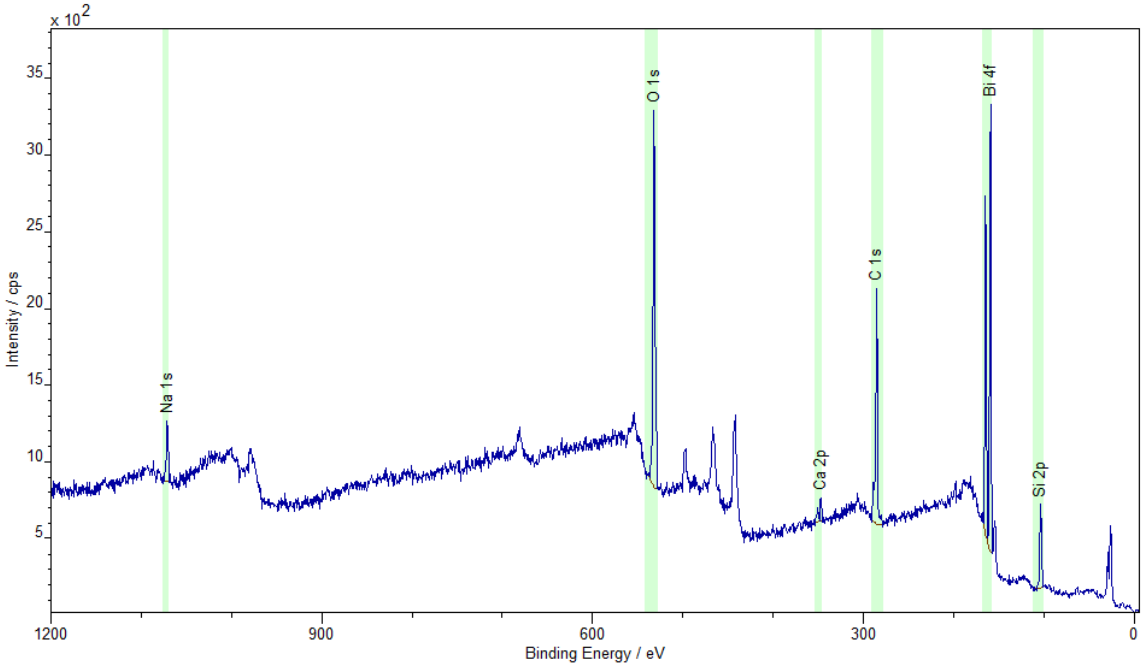

Figure 6.12: XPS survey spectrum of H_2O ICE nanosheets on SiO_2/Si confirming the presence of Bi, O, C and Si (substrate) and additional adventitious C on the samples. Notably minor traces of Na and Ca are also consistently found from the H_2O processing. The Na and Ca signals could be ascribed to

Die approbierte gedruckte Originalversion dieser Dissertation ist an der TU Wien Bibliothek verfügbar.
The approved original version of this doctoral thesis is available in print at TU Wien Bibliothek.
TU Bibliothek Your knowledge hub WIEN

residual ions in the H_2O solvent used, since similar measurements were also obtained for empty H_2O drop-cast onto SiO_2/Si wafers, but not for unprocessed SiO_2/Si wafers. The finding of residual ions in the H_2O also correlates well with the resistivity measurements of the water discussed before.

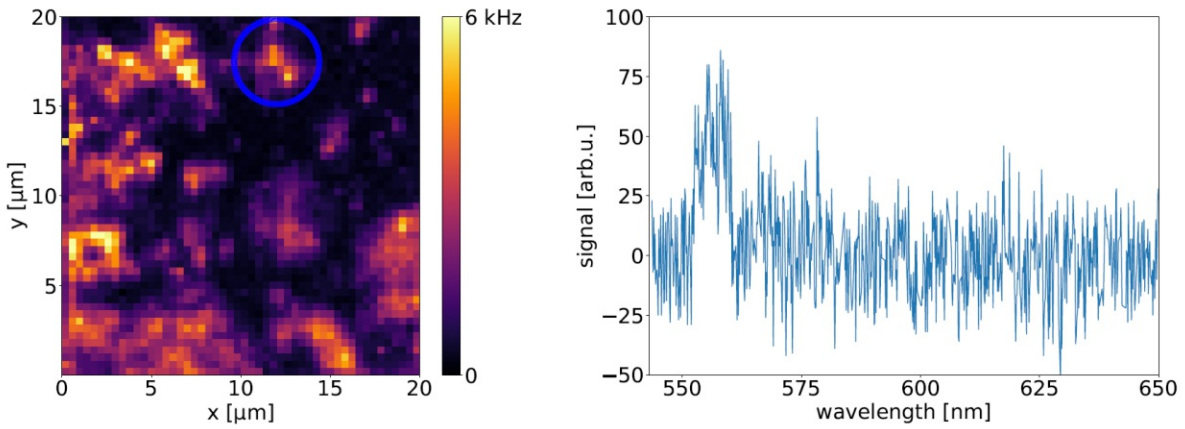

Figure 6.13: (left) latterally resolved PL emission intensity map of H_2O ICE flakes on SiO_2/Si and (left) PL emission spectrum of a flake in the left PL emission map, background corrected over "dark" SiO_2/Si background.

Combined, TEM/SAED, XRD, EDX, XPS and PL all corroborated the assignment of the synthesized H_2O nanosheets and MeOH nanoflakes to 2D $Bi_2O_2CO_3$.

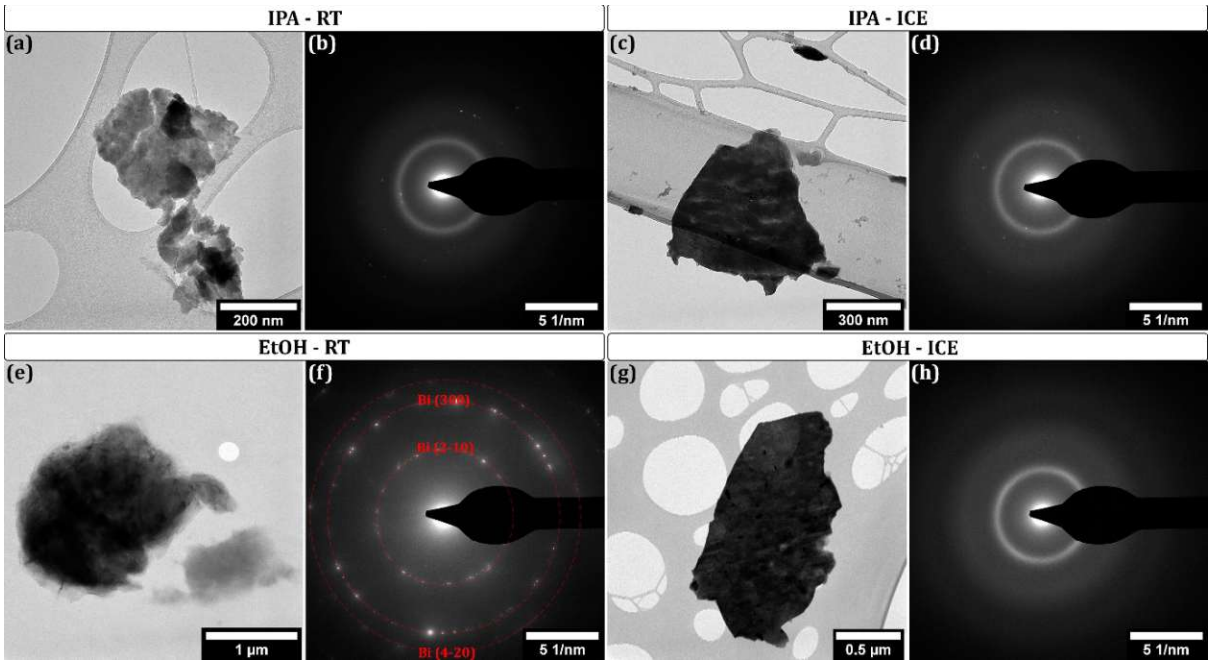

Figure 6.14: BF TEM (a) and SAED (b) of IPA RT and BF TEM (c) and SAED (d) of IPA ICE. SAED in (b) and (d) suggests amorphous structure of the nanoflakes. BF TEM (e) and SAED (f) of EtOH RT. The SAED in (f) indicates that the produced nanoflakes are of metallic β-Bi structure i.e. phase of initial β-Bi powder and no $Bi_2O_2CO_3$ phase was formed in EtOH at RT. BF TEM (g) and SAED (h) of EtOH ICE. SAED in (h) suggests amorphous structure of the nanoflakes.

Die approbierte gedruckte Originalversion dieser Dissertation ist an der TU Wien Bibliothek verfügbar.
The approved original version of this doctoral thesis is available in print at TU Wien Bibliothek.
TU Bibliothek Your knowledge hub WIEN

However, a strong solvent dependence was observed, not only in terms of resulting 2D $Bi_2O_2CO_3$ nanoflake/-sheet morphology as between MeOH vs. H_2O, but also in terms of resulting phase when comparing with IPA, EtOH and IPA:H_2O solvents. While for MeOH and H_2O, 2D $Bi_2O_2CO_3$ nanoflakes/-sheets were obtained, as described above, for IPA (RT, ICE) amorphous nanoflakes were obtained and for EtOH amorphous (ICE) or β-Bi(001) (RT) nanoflakes were obtained (Figure 6.14). In turn for IPA:H_2O (RT) again 2D $Bi_2O_2CO_3$ nanosheets were obtained, while IPA:H2O (ICE) resulted in amorphous nanoflakes (Figure 6.15). This underlines an active role of the solvent in the transformation, oxidation and carbonate bridging/intercalation of initial Bi into the 2D $Bi_2O_2CO_3$ nanoflakes/-sheets, with best results towards crystalline 2D $Bi_2O_2CO_3$ in H_2O for large nanosheets and MeOH for small nanoflakes, respectively.

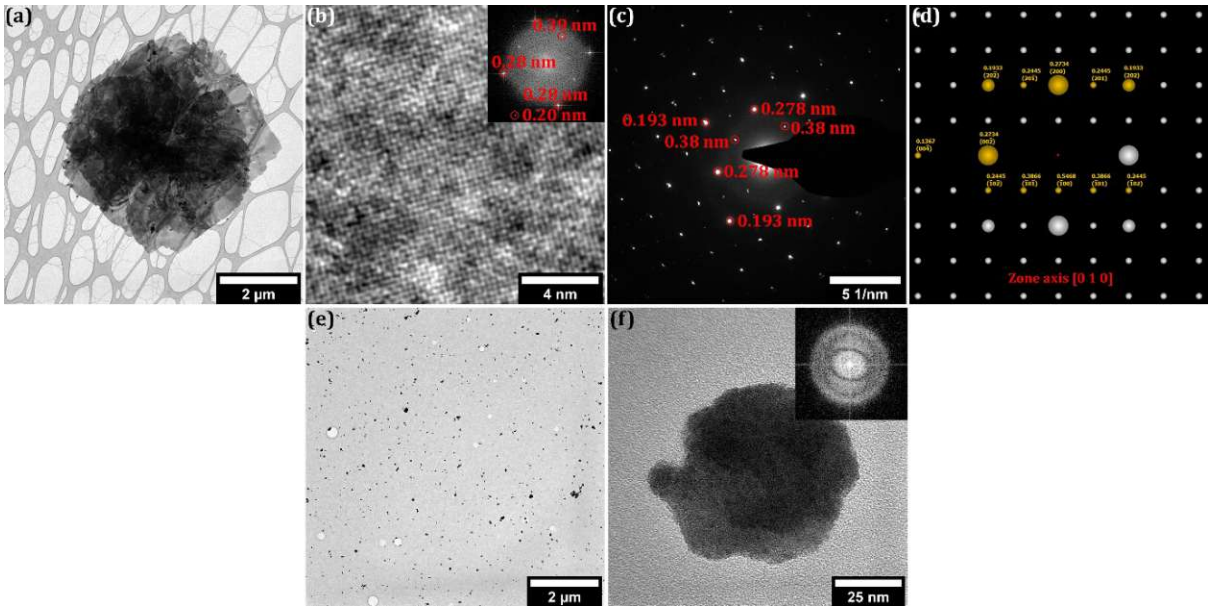

Figure 6.15: (a-d) IPA:H_2O ICE studied by overview (a) and lattice resolution (b, FT in inset, "top view" of flake) BF-TEM and SAED (c). (d) shows a simulated SAED/FT pattern for orthorhombic $Bi_2O_2CO_3$ along [010] zone axis with salient reflections matching to experimental data in (b,c) highlighted. (e-f) IPA:H_2O RT studied by overview (e) and lattice resolution (f) BF-TEM. The FT in inset shows that the obtained nanoflakes from IPA:H_2O RT are amorphous.

6.3.2 Discussion of phase analysis of the nanoflakes/-sheets

The phase analysis of the synthesized nanoflakes/-sheets rests on lattice resolution TEM (FT) and SAED data in top-view and side-view as well as XRD data measured in Bragg-Brentano geometry.

Die approbierte gedruckte Originalversion dieser Dissertation ist an der TU Wien Bibliothek verfügbar.
The approved original version of this doctoral thesis is available in print at TU Wien Bibliothek.
TU Bibliothek Your knowledge hub WIEN

6.3.2.1 Top-view TEM (FT) and SAED

The phase identification is firstly illustrated based on the top-view TEM (FT) and SAED data (Figure 6.6c,e,f and Figure 6.15b,c)

Since the starting bulk material was metallic β-Bi powder without oxides, the initial screening of the phase of the synthesized nanosheets/-flakes was done with all the (semi-)metallic Bi PDF files in the PDF-4+ database. The atomic models along with the simulated diffraction patterns for the two often observed zone axes in 2D bismuth of β-Bi structure ([001] and [2-21]) are presented in Figure 6.16. Both gave worse matching to the d-spacings in the FT patterns of the here synthesized nanosheets/-flakes (Figure 6.6c,e,f and Figure 6.15b,c) compared to $Bi_2O_2CO_3$. A projection along [42-1] has also been presented additionally to underscore the differences in the results with those of the prior work[51,60] with similar but shorter sonication scheme which resulted not in 2D bismuth oxycarbonates but metallic 2D Bi. Also for this β-Bi [42-1] zone axis, the experimental data here was not well matched by β-Bi.

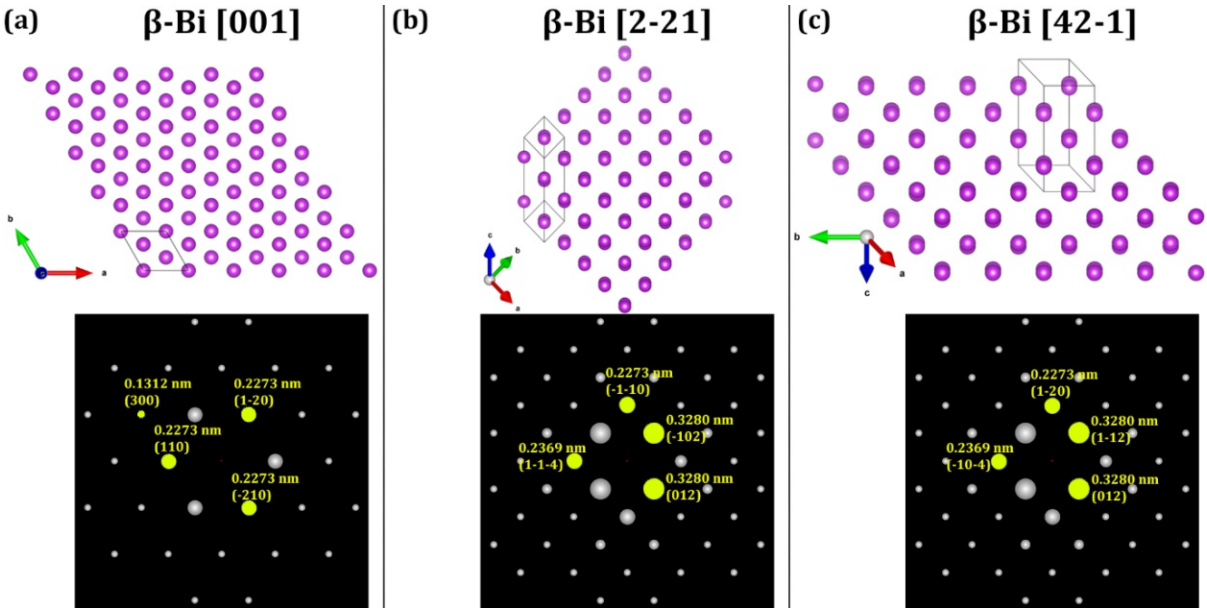

Figure 6.16: The atomic structure (top) and simulated SAED patterns (bottom) for β-Bi along (a) [001], (b) [2-21] and (c) [42-1] zone axes. The PDF file with code 04-007-5315[61] from PDF-4+ crystallographic database was used to construct the atomic and the diffraction models. (b) and (c) also represent the orientations of the β-Bi sheets obtained by Pumera et al.[51,60]

Die approbierte gedruckte Originalversion dieser Dissertation ist an der TU Wien Bibliothek verfügbar.
The approved original version of this doctoral thesis is available in print at TU Wien Bibliothek.
TU Bibliothek Your knowledge hub WIEN

This concludes that the synthesized nanosheets/-flakes are not β-Bi. Similarly worse matches were obtained for other metallic Bi phases, excluding that the obtained nanosheets/-flakes are any allotrope of bismuth. A total of 38 entries in the database were analyzed and no suitable match to the nanosheets/-flakes was found. (Note that for Bi atomic structure models are often described in literature with hexagonal axis (as here) but also with rhombohedral axis. Therefore, numerical (hkl) and [uvw] values need consideration of selected hexagonal or rhombohedral axis system, when comparing between reports. To avoid ambiguity the here used axis have been plotted alongside the atomic models.)

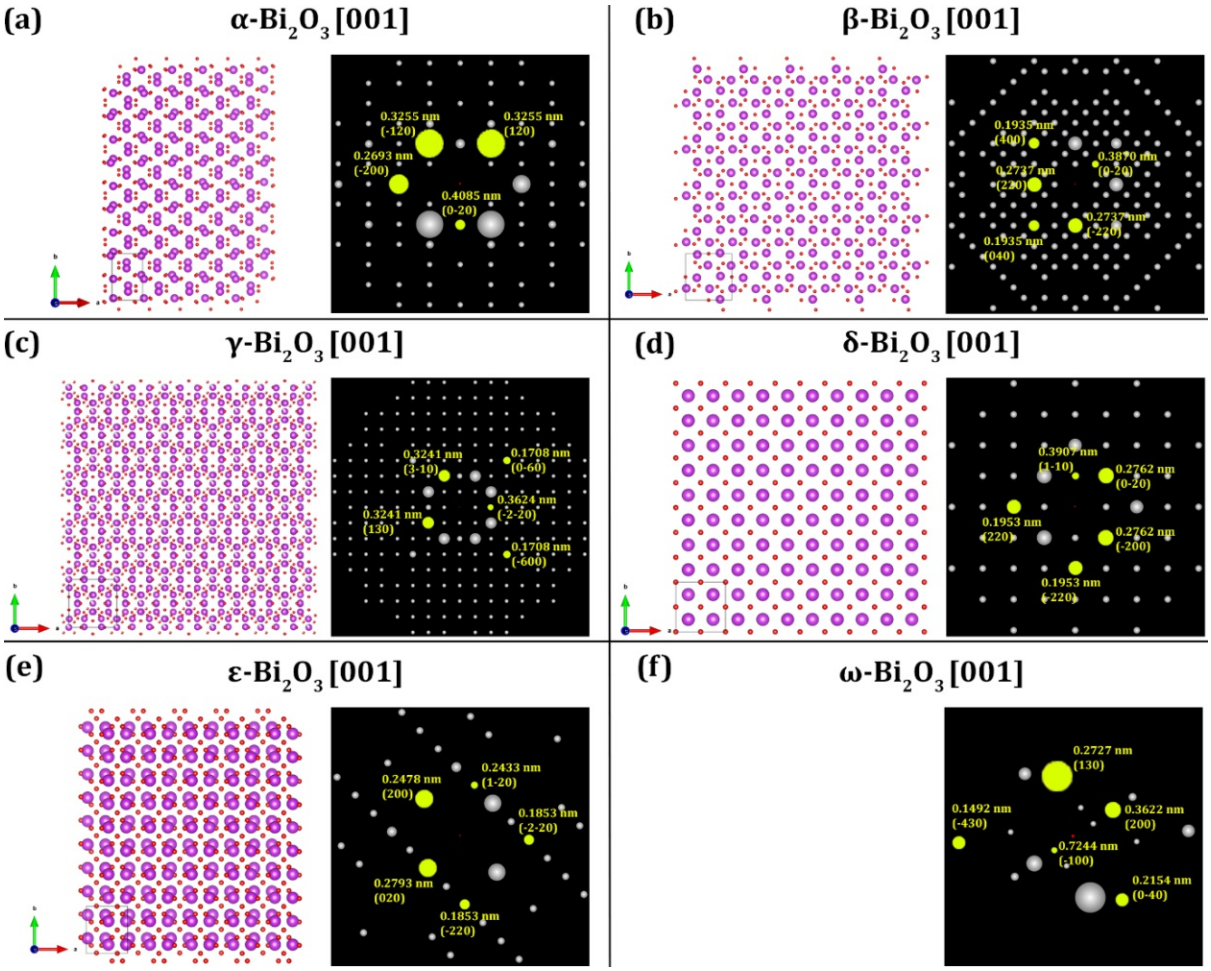

Figure 6.17: Atomic structure (left) and simulated SAED patterns (right) for 6 different allotropes (a-f) of bismuth trioxides along low index [001] zone axes as example. The atomic structure and the SAED pattern for α-Bi_2O_3 with monoclinic crystal system was simulated using the PDF file with code 00-041-1449[64-66] from PDF-4+ crystallographic database. For the case of β-Bi_2O_3 with tetragonal crystal system, PDF file with code 04-007-1443[67] from PDF-4+ database was used to reconstruct atomic and diffraction models. The structure of the γ-Bi_2O_3 is presented via atomic models and equivalent diffraction pattern using PDF file with code 04-007-2395[68]. PDF file with code 04-015-

Die approbierte gedruckte Originalversion dieser Dissertation ist an der TU Wien Bibliothek verfügbar.
The approved original version of this doctoral thesis is available in print at TU Wien Bibliothek.
TU Bibliothek WIEN Your knowledge hub

0028[69–71] was used to project the crystal structure of δ-Bi_2O_3 via atomic and diffraction models. To illustrate the orthorhombic structure of ε-Bi_2O_3 via corresponding atomic coordinates and diffraction profile, PDF file with code 04-013-1463[72] was utilized. For the illustration of triclinic structure of ω-Bi_2O_3, no entry was found in the database. The PDF file with code 00-050-1088[62] could only simulate the SAED profiles based on the powder diffraction data but could not provide the information about the atomic positions. [uvw] denotes the zone axis.

As next possible reaction product, the experimental FT and SAED data was compared to the different oxides of bismuth. A total of 102 PDF files of bismuth oxides available in PDF-4+ database with different stoichiometric ratios of Bi and O were checked. In particular, the thermodynamically most stable Bi_2O_3 phases were checked with respect to the atomic structure and equivalent diffraction patterns along various zone axes. Low index [001] zone axes are shown in Figure 6.17 as examples of this analysis. PDF file with the atomic structure for ω- Bi_2O_3 could not be found. The SAED pattern for ω- Bi2O3 was simulated on the basis of the reflection intensities from the powder diffraction pattern as mentioned by the work[62] cited in the PDF file with code 00-050-1088. δ-Bi_2O_3 along [001] zone axis also gave a very good match to the experimental top-view TEM (FT) and SAED data in Figure 6.6c,e,f and Figure 6.15b,c. For δ-Bi_2O_3, however in side view no lattice distance of 0.68 nm (as experimentally measured in Figure 6.6b) was expected but rather only a much shorter distance of ~0.39 nm. This excludes δ-Bi_2O_3 as possible phase for the here obtained nanosheets/-flakes. Additionally, as discussed below also the measured XRD patterns of the nanosheets (Figure 6.20) were inconsistent with δ-Bi_2O_3. In prior studies[63] particles of β-Bi_2O_3 were also found aligned along [110] zone axis. Therefore, the alignment of nanosheets/-flakes was also cross-checked with respect to β-Bi_2O_3 aligned along [110] zone axis as shown in Figure 6.18. To note is that β-Bi_2O_3 along [110] was also a good match for the top-view TEM and SAED data. However the XRD data in Figure 6.20 is inconsistent with β-Bi_2O_3 (as discussed later), thus excluding β-Bi_2O_3.

After having excluded Bi and Bi-oxides, it was observed that orthorhombic $Bi_2O_2CO_3$ with [010] texture (PDF file: 04-009-8533)[57] matches the TEM data excellently both in top-view and side-view (Figure 6.19a, see also Figure 6.6 and Figure 6.7). Additionally, also the XRD data is perfectly matched by orthorhombic $Bi_2O_2CO_3$ with [010] texture (PDF file: 04-009-8533)[57], as shown in Figure 6.20 and discussed later.

Die approbierte gedruckte Originalversion dieser Dissertation ist an der TU Wien Bibliothek verfügbar.
The approved original version of this doctoral thesis is available in print at TU Wien Bibliothek.
TU Bibliothek Your knowledge hub WIEN

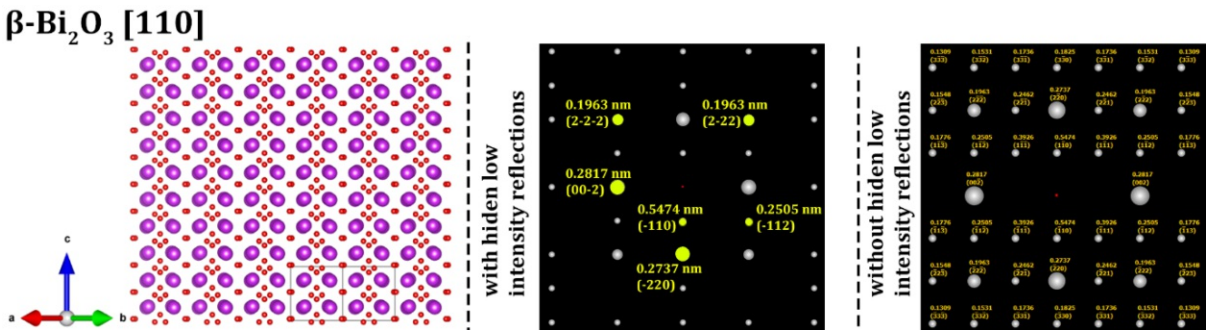

Figure 6.18: Atomic structure (left) and simulated SAED patterns (middle, right) for β-Bi_2O_3 along [110] direction constructed from PDF file with code 04-007-1443 from PDF-4+ database. The simulated FT/SAED profiles are presented in two fashions: (middle) keeping the low intensity reflections hidden and (right) with all the reflections visible to simplify the comparison for phase analysis. [uvw] denotes the zone axis.

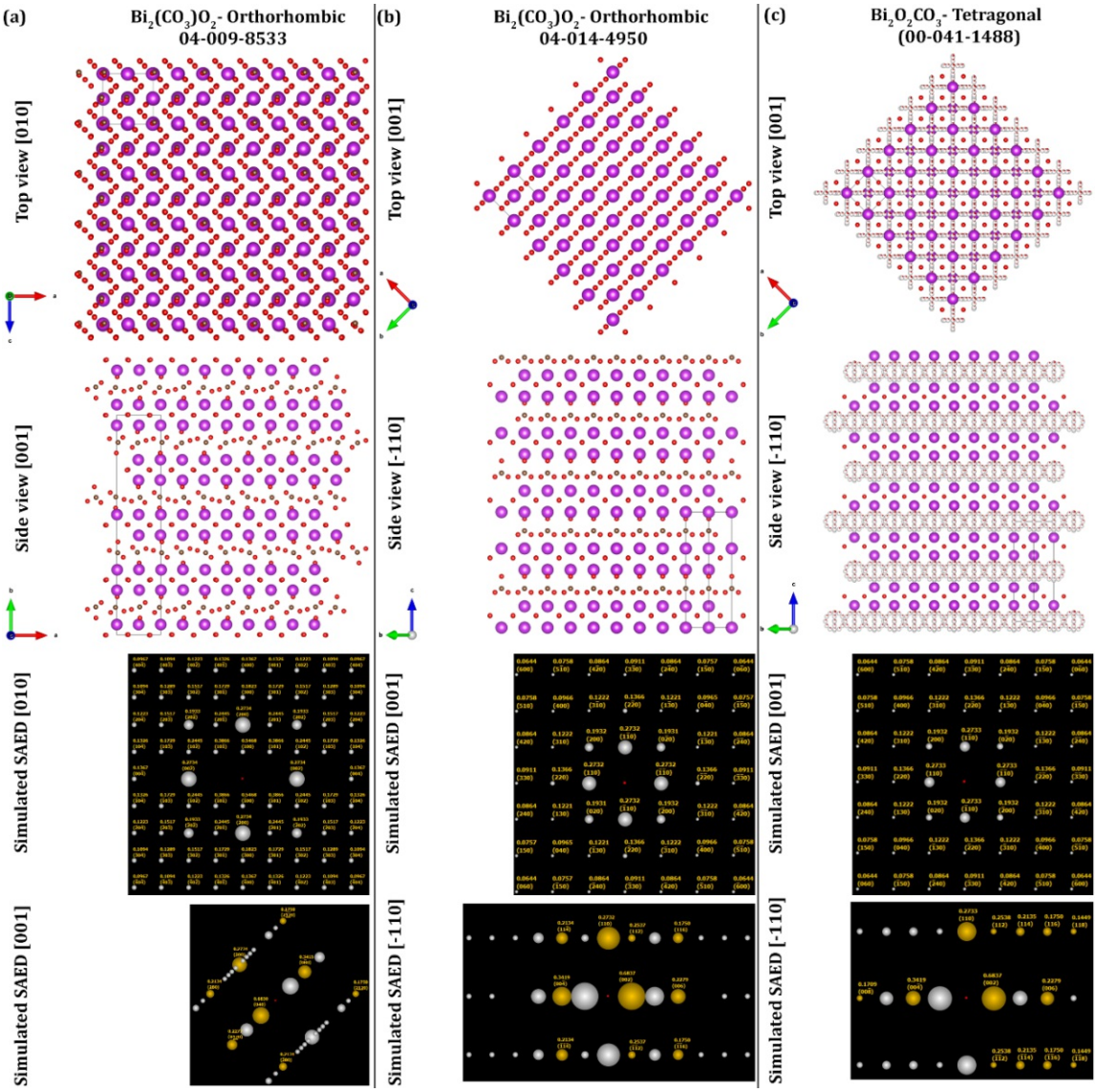

Figure 6.19: From top to bottom: Atomic structure models in top-view and side-view and corresponding simulated FT/SAED for top-view and side-view for the PDF files for $Bi_2O_2CO_3$ (a)

Die approbierte gedruckte Originalversion dieser Dissertation ist an der TU Wien Bibliothek verfügbar.
The approved original version of this doctoral thesis is available in print at TU Wien Bibliothek.
TU Bibliothek Your knowledge hub WIEN

orthorhombic 04-009-8533[57] (the majority file used in this report) and comparison (b) orthorhombic 04-014-4450[73] and (c) tetragonal 00-041-1448.[57] It is to emphasize that, while numerical (hkl)/[uvw] values between PDF files vary due to chosen axis system, all shown PDF entries similarly describe $Bi_2O_2CO_3$ with the Bi_2O_2 sub-layers parallel to the substrate. The reason for choosing orthorhombic 04-009-8533[57] as the best match is the representation of ~0.38 nm reflections that were experimentally observed in FT/SAED data in Figure 6.6 and Figure 6.7 and which are not represented in the other PDF entries.

To note is that $Bi_2O_2CO_3$ unit cell has been described in various orthorhombic and tetragonal notations in the PDF file database. Notably TEM and XRD data is also well matched by other PDF entries for $Bi_2O_2CO_3$ like the orthorhombic PDF file 04-014-4450 (Figure 6.19b)[73] or the often used tetragonal description as in PDF file 00-041-1448 (Figure S19c).[57] The reason for choosing orthorhombic $Bi_2O_2CO_3$ (PDF file: 04-009-8533) as the best description was that the experimentally observed Figure 6.6 and Figure 6.7 ~0.38 nm reflection in FT/SAED data was best represented by the orthorhombic $Bi_2O_2CO_3$ (PDF file: 04-009-8533), while not represented in the other $Bi_2O_2CO_3$ PDF entries. It was also noted that between the different orthorhombic PDF files the axis orientation can be different, and there was likewise also a difference of axis orientation for the tetragonal PDF files. Therefore (hkl) and [uvw] values as used in texture description between the various PDF files vary in numerical values. Hence, for most atomic models sketches in the report always also the axis system used has been plotted. Notably, the stated orthorhombic $Bi_2O_2CO_3$ with [010] texture in PDF file: 04-009-8533[57] is equivalent to [001] texture for orthorhombic PDF file 04-014-4450 and [001] for tetragonal PDF file 00-041-1448. As clearly shown in Figure 6.19, all these descriptions (irrespective of axis system and numerical (hkl) [uvw] values) refer to $Bi_2O_2CO_3$ with the Bi_2O_2 sub-layers parallel to the support.

6.3.2.2 XRD

Finally, the measured XRD data is presented compared to simulated diffraction patterns of all salient metallic Bi and Bi-oxide phases as well as $Bi_2O_2CO_3$ oxycarbonate phases (in both orthorhombic and tetragonal descriptions).

Die approbierte gedruckte Originalversion dieser Dissertation ist an der TU Wien Bibliothek verfügbar.
The approved original version of this doctoral thesis is available in print at TU Wien Bibliothek.
TU Bibliothek Your knowledge hub WIEN

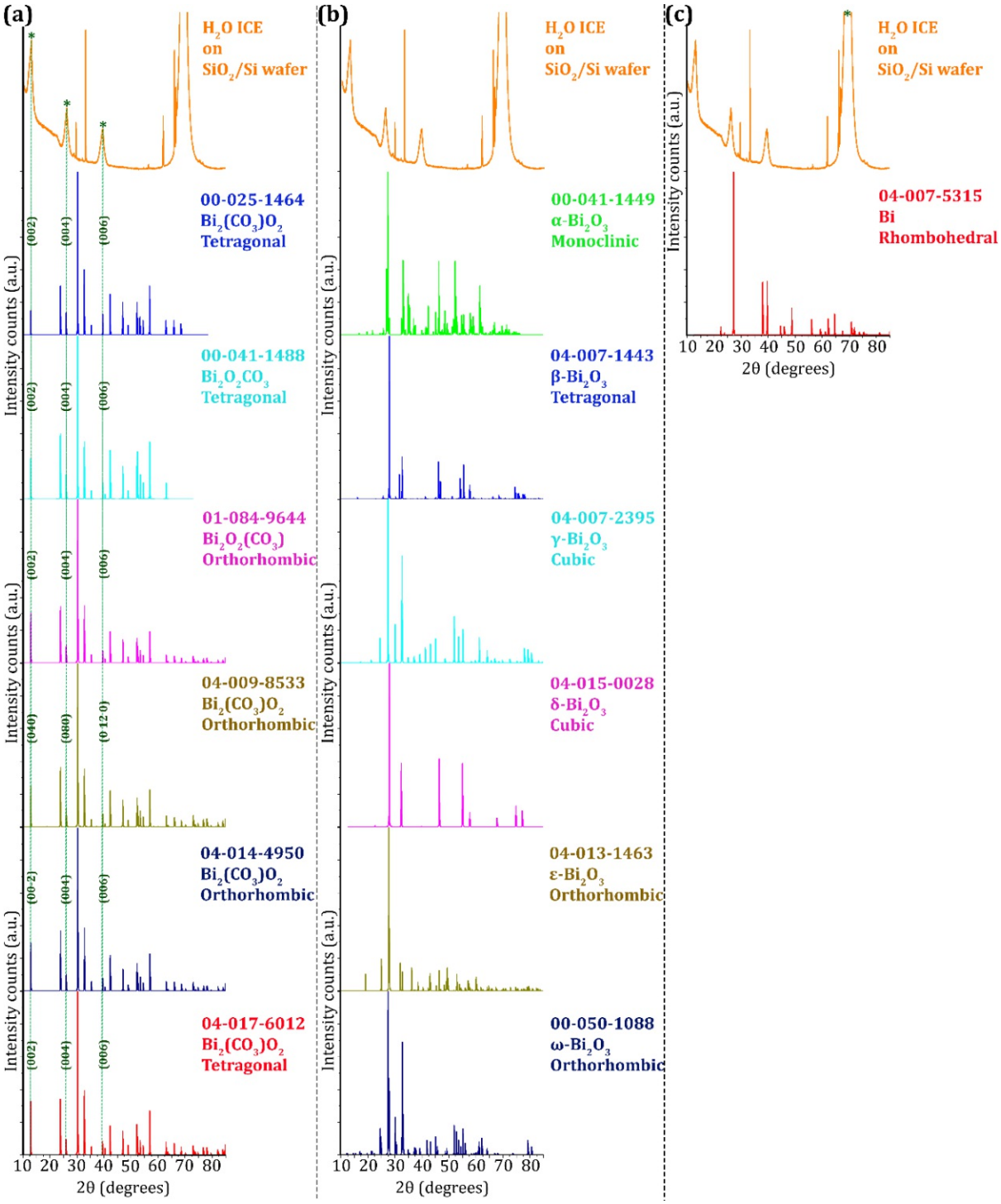

Figure 6.20: Comparison of measured XRD pattern of H_2O ICE nanosheets drop cast onto SiO_2/Si wafers (top patterns in orange) with respect to simulated powder diffraction patterns for various PDF entries (entry numbers in figure) for (a) $Bi_2O_2CO_3$, (b) Bi_2O_3 and (c) Bi phases.

As immediately apparent, the only set of XRD patterns that can account for all peaks observed in the measured XRD data (~13°, ~26° and ~40°) were the $Bi_2O_2CO_3$ patterns. This was most pronounced for the reflection at ~13° which was not consistent with any

Die approbierte gedruckte Originalversion dieser Dissertation ist an der TU Wien Bibliothek verfügbar.
The approved original version of this doctoral thesis is available in print at TU Wien Bibliothek.
TU Bibliothek Your knowledge hub WIEN

of the Bi_2O_3 or Bi phases, but only with $Bi_2O_2CO_3$. Importantly, the three observed peaks were also systematically related to each other as (040), (080) and (0120) reflections of $Bi_2O_2CO_3$ which is for XRD in Bragg Brentano geometry exactly the pattern one would expect from 2D $Bi_2O_2CO_3$ with (010) texture, that was indicated already from the TEM data. Importantly note, that none of the metallic Bi and Bi-oxide phases can account at all for the peak at 13°, thus excluding all these phases.

"In summary, the structural assignment of nanoflakes/-sheets to 2D $Bi_2O_2CO_3$ with (010) texture is fully consistent with TEM (FT) and SAED data in both top-view and side-view and also with Bragg-Brentano XRD data. No other candidate phases such as metallic Bi or Bi-oxides shows similar consistency in top-/side-view and XRD. This reaffirms the assignment of nanoflakes/-sheets to 2D $Bi_2O_2CO_3$ with (010) texture."

6.3.3 Discussion of likely reaction pathways of Bi → $Bi_2O_2CO_3$

Comparing to prior literature, the observation of 2D $Bi_2O_2CO_3$ is surprising: Prior work by Pumera et al.[13,51] found for a similar sonication scheme to the one followed here and also in water, not 2D $Bi_2O_2CO_3$ but large metallic β-Bi[42-1] nanosheets produced while MeOH resulted in small metallic β-Bi(001) nanoflakes. In fact, Pumera et al. explicitely excluded bismuth oxidation in their study. Key differences were however the excitation energy source (tip sonication[13,51] vs. bath sonication here) and in particular a much shorter sonication time (max. 60 min [13,51] vs. 15 h here). Pumera et al. suggested for their 60 min sonication result in H_2O not only physical exfoliation of the parent Bi powder to take place but due to Bi's low melting point (~271 °C) Bi melting under the tip sonicator, dissolution effects and then crystallite growth in suspension to partake in large nanosheet formation.[13,51] In contrast, in MeOH for 60 min Pumera et al. suggested fragmentation (rather than crystallite growth as in H_2O) to be the dominant mechanism for small nanoflake formation. While Pumera et al.'s max. 60 min processing times resulted in metallic β-Bi nanosheets/-flakes, we suggest that for the here followed much longer 15 h processing in addition to the crystallite growth/fragmentation mechanisms

Die approbierte gedruckte Originalversion dieser Dissertation ist an der TU Wien Bibliothek verfügbar.
The approved original version of this doctoral thesis is available in print at TU Wien Bibliothek.
TU Bibliothek Your knowledge hub WIEN

suggested by Pumera et al. also concurrent oxidation and carbonate bridging/intercalation processes of the Bi in H_2O and MeOH take place. Compared to many prior reports on $Bi_2O_2CO_3$ synthesis,[16] notably a dedicated source of oxygen or carbonate ions was not employed in the synthesis but only Bi as dedicated precursor in the various solvents. It is therefore suggested that the sources of the required oxygen and carbon for the here proposed mechanism were coming from solvent decomposition under ultrasound and dissolved atmospheric oxygen and carbonate CO_3^{2-} ions from dissolved atmospheric CO_2 in the solvents.[37–39,41,74] Thus bismuth oxycarbonate nanosheets and -flakes were produced under the adopted conditions in H_2O and MeOH, respectively. This oxidation and carbonate bridging/intercalation process was arrested in the Pumera et al. work due to their shorter processing time.

In prior reports on 2D $Bi_2O_2CO_3$, lateral sizes of atomically-thin 2D $Bi_2O_2CO_3$ were largely limited at ~1 µm,[16,18–49] while this study increases lateral nanosheet sizes to ~3 µm. So far, a controllable synthesis route for laterally large (~3 µm), atomically-thin 2D $Bi_2O_2CO_3$ nanosheets (H_2O ICE and RT) and for laterally small (~ 80 nm), atomically-thin 2D $Bi_2O_2CO_3$ nanoflakes (MeOH ICE and RT), importantly solely based on the choice of solvent was established.

6.3.4 Photocatalytic testing of 2D $Bi_2O_2CO_3$ nanoflakes/nanosheets

Since, nanostructured $Bi_2O_2CO_3$ has been prior reported to have interesting properties as photocatalyst,[16] the here introduced 2D $Bi_2O_2CO_3$ nanosheets and nanoflakes were investigated as heterogeneous (co-)catalysts in suspension-type photocatalytic HER from water splitting under ultra-violet (UV) excitation. To date, $Bi_2O_2CO_3$ has predominantly been screened as a photocatalyst for organic pollutant degradation and NO removal.[16,18–34,47–49] To this end, not only monolithic $Bi_2O_2CO_3$ alone but also various mixed dimensionality hybrids of $Bi_2O_2CO_3$ with metals, metal-oxides, sulfides, Bi-compounds and carbon-nitride (g-C_3N_4) have been investigated.[16,22–24,26,27,36,44,52,75-77] Only very little work has however thus far focused on photocatalytic HER from $Bi_2O_2CO_3$,[16] namely only hybrids consisting of $Bi_2O_2CO_3$ nanoplates/Pt,[35] $Bi_2O_2CO_3$ nanoparticles/g-C_3N_4/Pt[52] and $Bi_2O_2CO_3$ nanoplates/Bi.[36] Further, despite the archetypical importance of TiO_2 as

Die approbierte gedruckte Originalversion dieser Dissertation ist an der TU Wien Bibliothek verfügbar.
The approved original version of this doctoral thesis is available in print at TU Wien Bibliothek.
TU Bibliothek WIEN Your knowledge hub

photocatalyst,[53,54] only very few reports on potentially synergetic performance from $Bi_2O_2CO_3/TiO_2$ hybrids exist.[16,75] Few prior examples are $Bi_2O_2CO_3$ nanoflowers hybridized with TiO_2 nanoparticles on graphene sheets[75] and $Bi_2O_2CO_3$ nanoplates hybrids with TiO_2 nanoparticles and carbon networks,[76] whereby both hybrids showed higher photocatalytic activity in organic dye degradation than their separate components. Notably however, another study reported reduced photocatalytic dye degradation activity from hybridizing $Bi_2O_2CO_3$ to TiO_2 compared to neat TiO_2.[77] In either case, no work has as of yet hybridized atomically-thin 2D $Bi_2O_2CO_3$ with TiO_2 or studied $Bi_2O_2CO_3/TiO_2$ hybrids for photocatalytic HER, as is carried out here.

For photocatalytic HER measurements via water splitting a sacrificial agent, which is often an alcohol, is commonly used as a hole scavenger.[78-81] One of the most commonly used systems in photocatalytic HER is a 1:1 H_2O:MeOH mixture.[78,79] Therefore for the 2D $Bi_2O_2CO_3$ nanoflakes/-sheets exfoliated in MeOH and H_2O, respectively, the respective other solvent was added towards obtaining 2D $Bi_2O_2CO_3$ nanoflakes/-sheets in 1:1 H_2O:MeOH mixture. This consistency of sacrificial agent concentration ensured direct quantitative comparability of HER results for MeOH and H_2O preparations (within limits of the estimated maximum solid content concentrations of maximum of ~50 mg L^{-1}). To elucidate possible roles of the 2D $Bi_2O_2CO_3$ in photocatalysis, HER measurements were undertaken for i. neat 2D $Bi_2O_2CO_3$ nanoflakes/-sheet and ii. 2D $Bi_2O_2CO_3$ nanoflakes/-sheets hybridized with TiO_2 nanoparticles (Degussa P25, particles size ~ 25 nm). TiO_2 nanoparticles are archetypical photocatalysts, but are comparatively inactive towards HER, thus commonly requiring a HER co-catalyst such as expensive Pt.[53,54,78] Thereby combination of 2D $Bi_2O_2CO_3/TiO_2$ to hybrids allows to assess if 2D $Bi_2O_2CO_3$ can act as such HER co-catalyst. Notably most of the few prior reports on HER with $Bi_2O_2CO_3$ hybrids had Pt as additional co-catalyst present in the hybrids,[35,52] thus masking intrinsic $Bi_2O_2CO_3$ HER (co-)catalytic performance.

Figure 6.21a shows that for neat, small 2D $Bi_2O_2CO_3$ nanoflakes (MeOH ICE) no appreciable photocatalytic HER response was observed. This suggested that under the adopted conditions, 2D $Bi_2O_2CO_3$ nanoflakes were not active as a monolithic

Die approbierte gedruckte Originalversion dieser Dissertation ist an der TU Wien Bibliothek verfügbar.
The approved original version of this doctoral thesis is available in print at TU Wien Bibliothek.
TU Bibliothek Your knowledge hub WIEN

photocatalyst for HER. When however, hybridizing these 2D $Bi_2O_2CO_3$ nanoflakes (MeOH ICE) with TiO_2 nanoparticles, notably a significant HER response upon UV illumination (Figure 6.21a) was observed. Most importantly, this HER response was significantly larger than the response from neat TiO_2 alone (Figure 6.21a). This suggested that small 2D $Bi_2O_2CO_3$ nanoflakes here act as useful co-catalysts for photocatalytic HER. TEM of the MeOH ICE 2D $Bi_2O_2CO_3$ nanoflake/TiO_2 nanoparticle hybrids after HER (Figure 6.21b) indicated that TiO_2 nanoparticles have been well adhered to the 2D $Bi_2O_2CO_3$ nanoflakes (MeOH ICE). Notably, the small 2D MeOH ICE nanoflakes are also well size matched to the TiO_2 nanoparticles.

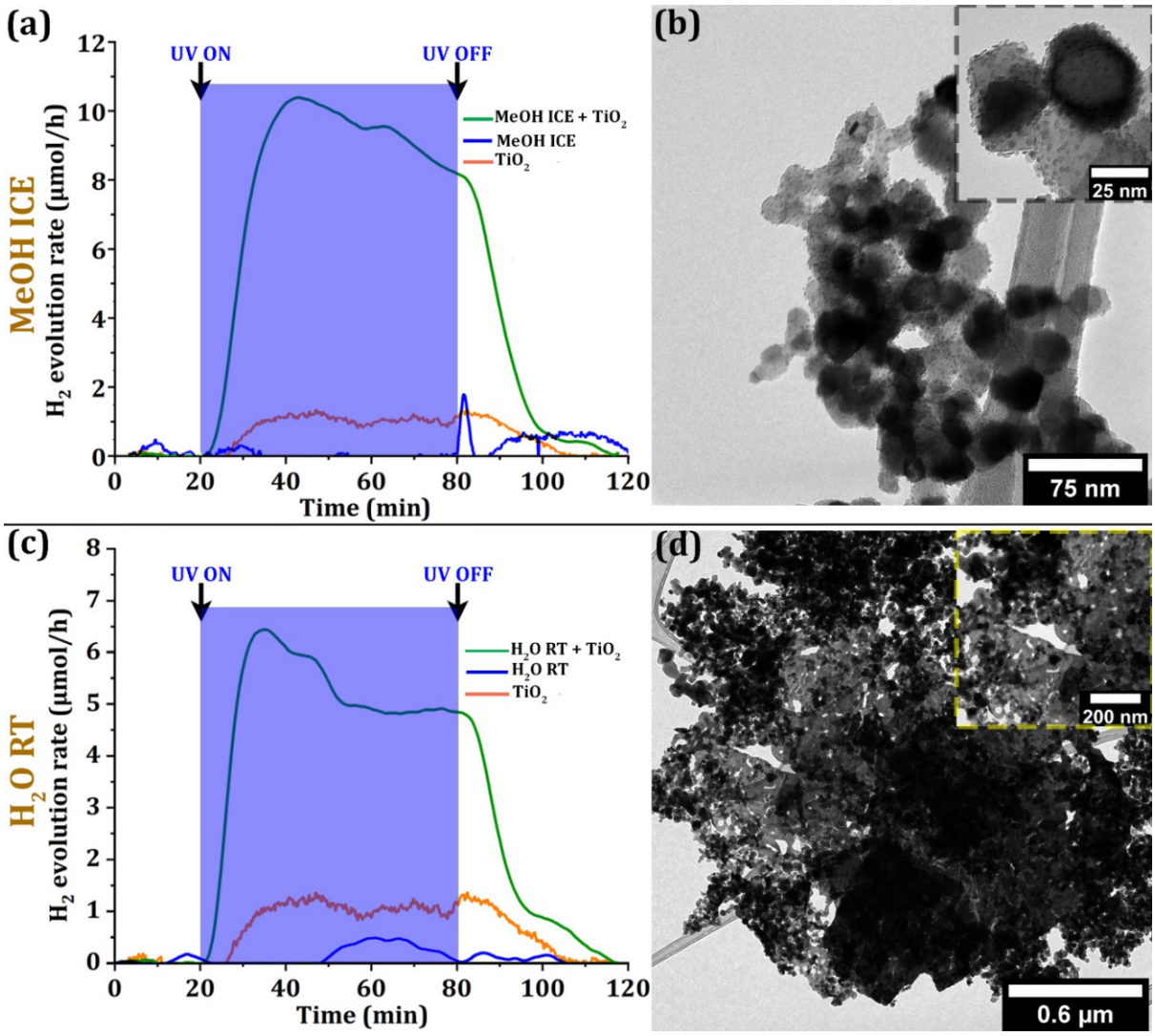

Figure 6.21: (a) Time-resolved hydrogen evolution rate during the photocatalytic HER experiments for neat MeOH ICE nanoflakes, neat TiO_2 nanoparticles and MeOH ICE nanoflakes hybridized with TiO_2 nanoparticles. (b) TEM micrograph of MeOH ICE nanoflakes hybridized with TiO_2 after HER measurements. (c) Time-resolved hydrogen evolution rate for neat H_2O RT nanosheets, neat TiO_2

Die approbierte gedruckte Originalversion dieser Dissertation ist an der TU Wien Bibliothek verfügbar.
The approved original version of this doctoral thesis is available in print at TU Wien Bibliothek.
TU Bibliothek Your knowledge hub WIEN

nanoparticles (replot from (a)) and H_2O RT nanosheets hybridized with TiO_2 nanoparticles. (d) TEM micrograph of H_2O RT nanosheets hybridized with TiO_2 after HER measurements. Start and stop of UV illumination in (a,c) is indicated.

Figure 6.21c shows similar HER photocatalysis data for the large 2D $Bi_2O_2CO_3$ nanosheets (H_2O RT) without/with TiO_2. Similar to the small MeOH ICE nanoflakes, no HER activity for neat, large H_2O RT nanosheets was found. Again, however a significant synergetic effect of 2D $Bi_2O_2CO_3$ nanosheet (H_2O RT)/TiO_2 hybridisation towards a HER photocatalytic response clearly above the performance of neat TiO_2 was observed. Post-HER TEM likewise indicated good interfacing of the large 2D $Bi_2O_2CO_3$ nanosheets with TiO_2 nanoparticles (Figure 6.21d). This thereby introduced 2D $Bi_2O_2CO_3$ nanoflakes/-sheets as noble-metal-free catalyst components with TiO_2 for photocatalytic HER from water splitting. Comparing the obtained specific activities from 2D $Bi_2O_2CO_3$ nanoflakes/-sheets (with TiO_2) towards photocatalytic HER (~25 $\mu mol_{H2} \cdot h^{-1} \cdot mg_{co\text{-}catalyst}^{-1} \cdot (W\ cm^{-2}_{UV})^{-1}$) suggests that the 2D $Bi_2O_2CO_3$ nanoflakes/-sheets facilitated the same order of magnitude of photocatalytic HER activity from UV as recently investigated non-noble co-catalysts such as $Ni(O_x)$ or $Cu(O_x)$ with TiO_2 and were more active than, e.g., $Mn(O_x)$, $Co(O_x)$ and $Fe(O_x)$ with TiO_2 under similar measurement conditions in the same HER setup.[80,81]

6.4 Conclusion

In summary, a fabrication route facilitating template-free synthesis of 2D $Bi_2O_2CO_3$ with good control over lateral 2D size, ranging from unusually large µm nanosheets to few tens of nm small nanoflakes just based on the suspension medium used is presented . This critically adds to the toolbox for 2D pnictogen compound fabrication with emerging applications in (photo-)catalysis, electronics and energy. As one application example, the newly introduced 2D $Bi_2O_2CO_3$ nanosheets/-flakes was tested in photocatalysis for sustainable solar fuel generation. In particular, the study demonstrates that the 2D $Bi_2O_2CO_3$ nanosheets/-flakes can be a promising catalyst component when hybridized with TiO_2 for the important HER in photocatalytic water splitting.

Die approbierte gedruckte Originalversion dieser Dissertation ist an der TU Wien Bibliothek verfügbar.
The approved original version of this doctoral thesis is available in print at TU Wien Bibliothek.
TU Bibliothek Your knowledge hub WIEN

6.5 References

1. Yu, X. *et al.* Emerging 2D pnictogens for catalytic applications: status and challenges. *J. Mater. Chem. A* **8**, 12887–12927 (2020).
2. Liu, X. *et al.* Advances of 2D bismuth in energy sciences. *Chem. Soc. Rev.* **49**, 263–285 (2020).
3. Xu, K. *et al.* Two dimensional bismuth-based layered materials for energy-related applications. *Energy Storage Mater.* **19**, 446–463 (2019).
4. Gupta, T. *et al.* Resolving few-layer antimonene/graphene heterostructures. *Npj 2D Mater. Appl.* **5**, 53 (2021).
5. Yin, Y. *et al.* Anisotropic Transport Property of Antimonene MOSFETs. *ACS Appl. Mater. Interfaces* **12**, 22378–22386 (2020).
6. Wu, Q. *et al.* Two-dimensional semiconducting and single-crystalline antimony trioxide directly-grown on monolayer graphene. *Chem. Commun.* **55**, 2473–2476 (2019).
7. Zhang, S. *et al.* Antimonene oxides: emerging tunable direct bandgap semiconductor and novel topological insulator. *Nano Lett.* **17**, 3434–3440 (2017).
8. Wolff, S., Gillen, R., Assebban, M., Abellán, G. & Maultzsch, J. Two-dimensional antimony oxide. *Phys. Rev. Lett.* **124**, 126101 (2020).
9. Xiong, J., Song, P., Di, J., Li, H. & Liu, Z. Freestanding ultrathin bismuth-based materials for diversified photocatalytic applications. *J. Mater. Chem. A* **7**, 25203–25226 (2019).
10. Chen, S. *et al.* Oxygen vacancy associated single-electron transfer for photofixation of CO 2 to long-chain chemicals. *Nat. Commun.* **10**, 1–8 (2019).
11. Li, J., Wu, X., Pan, W., Zhang, G. & Chen, H. Vacancy-Rich Monolayer BiO2−x as a Highly Efficient UV, Visible, and Near-Infrared Responsive Photocatalyst. *Angew. Chem. Int. Ed.* **57**, 491–495 (2018).
12. Mei, J., Liao, T., Ayoko, G. A. & Sun, Z. Two-dimensional bismuth oxide heterostructured nanosheets for lithium-and sodium-ion storages. *ACS Appl. Mater. Interfaces* **11**, 28205–28212 (2019).
13. Beladi-Mousavi, S. M., Plutnar, J. & Pumera, M. Near-Atomic-Thick Bismuthene Oxide Microsheets for Flexible Aqueous Anodes: Boosted Performance upon 3D → 2D Transition. *ACS Appl. Mater. Interfaces* **12**, 55936–55944 (2020).
14. Chen, S. *et al.* Surface and interface engineering of two-dimensional bismuth-based photocatalysts for ambient molecule activation. *J. Mater. Chem. A* **9**, 196–233 (2021).
15. Ma, H. *et al.* Ultrathin Two-Dimensional Bi-Based photocatalysts: Synthetic strategies, surface defects, and reaction mechanisms. *Chem. Eng. J.* **417**, 129305 (2021).
16. Ni, Z., Sun, Y., Zhang, Y. & Dong, F. Fabrication, modification and application of (BiO) 2CO3-based photocatalysts: A review. *Appl. Surf. Sci.* **365**, 314–335 (2016).
17. Luo, B., Liu, G. & Wang, L. Recent advances in 2D materials for photocatalysis. *Nanoscale* **8**, 6904–6920 (2016).
18. Liang, H., Yang, Y., Tang, J. & Ge, M. Photocatalytic properties of Bi2O2CO3 nanosheets synthesized via a surfactant-assisted hydrothermal method. *Mater. Sci. Semicond. Process.* **16**, 1650–1654 (2013).

Die approbierte gedruckte Originalversion dieser Dissertation ist an der TU Wien Bibliothek verfügbar.
The approved original version of this doctoral thesis is available in print at TU Wien Bibliothek.
TU Bibliothek Your knowledge hub WIEN

19. Selvamani, T., Raj, B. G. S., Anandan, S., Wu, J. J. & Ashokkumar, M. Synthesis of morphology-controlled bismutite for selective applications. *Phys. Chem. Chem. Phys.* **18**, 7768–7779 (2016).
20. Zhou, Y. *et al.* Facile synthesis of surface N-doped Bi2O2CO3: origin of visible light photocatalytic activity and in situ DRIFTS studies. *J. Hazard. Mater.* **307**, 163–172 (2016).
21. Qin, H., Yang, Y., Shi, W. & She, Y. Few-layer Bi 2 O 2 CO 3 nanosheets derived from electrochemically exfoliated bismuthene for the enhanced photocatalytic degradation of ciprofloxacin antibiotic. *RSC Adv.* **11**, 13731–13738 (2021).
22. Yu, C. *et al.* Integrating plasmonic Au nanorods with dendritic like α-Bi2O3/Bi2O2CO3 heterostructures for superior visible-light-driven photocatalysis. *Appl. Catal. B Environ.* **184**, 1–11 (2016).
23. Ran, H. *et al.* Two-dimensional Bi2O2CO3/δ-Bi2O3/Ag2O heterojunction for high performance of photocatalytic activity. *Appl. Surf. Sci.* **525**, 146613 (2020).
24. Li, J., Wu, X., Wan, Z., Chen, H. & Zhang, G. Full spectrum light driven photocatalytic in-situ epitaxy of one-unit-cell Bi2O2CO3 layers on Bi2O4 nanocrystals for highly efficient photocatalysis and mechanism unveiling. *Appl. Catal. B Environ.* **243**, 667–677 (2019).
25. Liu, Y. *et al.* Preparation, electronic structure, and photocatalytic properties of Bi2O2CO3 nanosheet. *Appl. Surf. Sci.* **257**, 172–175 (2010).
26. Zhou, T. *et al.* BiOI/Bi2O2CO3 Two-Dimensional Heteronanostructures with Boosting Charge Carrier Separation Behavior and Enhanced Visible-Light Photocatalytic Performance. *J. Phys. Chem. C* **124**, 20294–20308 (2020).
27. Zhu, G. *et al.* Constructing a 2D/2D Bi2O2CO3/Bi4O5Br2 heterostructure as a direct Z-scheme photocatalyst with enhanced photocatalytic activity for NOx removal. *Appl. Surf. Sci.* **493**, 913–925 (2019).
28. Liu, H. *et al.* Pivotal roles of artificial oxygen vacancies in enhancing photocatalytic activity and selectivity on Bi2O2CO3 nanosheets. *Chin. J. Catal.* **40**, 620–630 (2019).
29. Huang, H. *et al.* Highly efficient Bi2O2CO3 single-crystal lamellas with dominantly exposed {001} facets. *Cryst. Growth Des.* **15**, 534–537 (2015).
30. Yin, P., Kan, P., Liu, M. Q. & Zhao, N. N. Controlled synthesis of Bi2O2CO3 nanorods with enhanced photocatalytic performance. *CrystEngComm* (2021).
31. Cheng, L., Hu, X. & Hao, L. Template-induced Bi2O2CO3 microstructure self-assembled by nanosheets with exposed {001} facets. *Mater. Res. Express* **5**, 065901 (2018).
32. Wu, Y. *et al.* Room-temperature synthesis of BiOCl and (BiO) 2CO3 with predominant {001} facets induced by urea and their photocatalytic performance. *J. Environ. Chem. Eng.* **5**, 987–994 (2017).
33. Xu, J., Wang, K. K., Liu, T., Peng, Y. & Xu, B. G. Br-Doped Bi 2 O 2 CO 3 exposed (001) crystal facets with enhanced photocatalytic activity. *CrystEngComm* **19**, 5001–5007 (2017).
34. Yang, L.-M. *et al.* Mild synthesis of {001} facet predominated Bi 2 O 2 CO 3 clusters with outstanding simulated sunlight photocatalytic activities. *CrystEngComm* **18**, 3683–3695 (2016).
35. Yu, S. *et al.* Readily achieving concentration-tunable oxygen vacancies in Bi2O2CO3: Triple-functional role for efficient visible-light photocatalytic redox performance. *Appl. Catal. B Environ.* **226**, 441–450 (2018).
36. Sun, D. *et al.* Plasma enhanced Bi/Bi2O2CO3 heterojunction photocatalyst via a novel in-situ method. *J. Colloid Interface Sci.* **571**, 80–89 (2020).

Die approbierte gedruckte Originalversion dieser Dissertation ist an der TU Wien Bibliothek verfügbar.
The approved original version of this doctoral thesis is available in print at TU Wien Bibliothek.
TU Bibliothek Your knowledge hub WIEN

37. Zhou, Y. *et al.* Environmentally friendly room temperature synthesis and humidity sensing applications of nanostructured Bi2O2CO3. *Sens. Actuators B Chem.* **188**, 1312–1318 (2013).
38. Dong, F., Bian, J., Sun, Y., Xiong, T. & Zhang, W. The rapid synthesis of photocatalytic (BiO) 2 CO 3 single-crystal nanosheets via an eco-friendly approach. *CrystEngComm* **16**, 3592–3604 (2014).
39. Zhang, W., Dong, F. & Zhang, W. Capture of atmospheric CO2 into (BiO) 2CO3/graphene or graphene oxide nanocomposites with enhanced photocatalytic performance. *Appl. Surf. Sci.* **358**, 75–83 (2015).
40. Yang, H. *et al.* Selective CO2 reduction on 2D mesoporous Bi nanosheets. *Adv. Energy Mater.* **8**, 1801536 (2018).
41. D'Angelo, D. *et al.* β-Bi 2 O 3 reduction by laser irradiation in a liquid environment. *Phys. Chem. Chem. Phys.* **20**, 10292–10301 (2018).
42. Zhou, Y. *et al.* Monolayered Bi 2 WO 6 nanosheets mimicking heterojunction interface with open surfaces for photocatalysis. *Nat. Commun.* **6**, 1–8 (2015).
43. Zhang, Y. *et al.* Controllable synthesis of few-layer bismuth subcarbonate by electrochemical exfoliation for enhanced CO2 reduction performance. *Angew. Chem. Int. Ed.* **57**, 13283–13287 (2018).
44. Tang, S.-F. *et al.* Decorating graphdiyne on ultrathin bismuth subcarbonate nanosheets to promote CO2 electroreduction to formate. *Sci. Bull.* (2021).
45. Ding, J. *et al.* (002) Oriented Bi2O2CO3 Nanosheets with Enhanced Photocatalytic Performance for Toluene Removal in Air. *Catalysts* **10**, 389 (2020).
46. Ortiz-Quiñonez, J. L., Vega-Verduga, C., Díaz, D. & Zumeta-Dubé, I. Transformation of bismuth and β-Bi2O3 nanoparticles into (BiO) 2CO3 and (BiO) 4 (OH) 2CO3 by capturing CO2: the role of halloysite nanotubes and "sunlight" on the crystal shape and size. *Cryst. Growth Des.* **18**, 4334–4346 (2018).
47. Zhao, Z. *et al.* Polyaniline-decorated {001} facets of Bi2O2CO3 nanosheets: in situ oxygen vacancy formation and enhanced visible light photocatalytic activity. *ACS Appl. Mater. Interfaces* **7**, 730–737 (2015).
48. Cheng, H. *et al.* Facile Template-Free Synthesis of Bi2O2CO3 Hierarchical Microflowers and Their Associated Photocatalytic Activity. *ChemPhysChem* **11**, 2167–2173 (2010).
49. Xiong, T. *et al.* Single precursor mediated-synthesis of Bi semimetal deposited N-doped (BiO) 2CO3 superstructures for highly promoted photocatalysis. *Acs Sustain. Chem. Eng.* **4**, 2969–2979 (2016).
50. Backes, C. *et al.* Guidelines for exfoliation, characterization and processing of layered materials produced by liquid exfoliation. *Chem. Mater.* **29**, 243–255 (2017).
51. Beladi-Mousavi, S. M., Ying, Y., Plutnar, J. & Pumera, M. Bismuthene Metallurgy: Transformation of Bismuth Particles to Ultrahigh-Aspect-Ratio 2D Microsheets. *Small* **16**, 2002037 (2020).
52. Yang, C. *et al.* Visible light-driven photocatalytic H2 generation and mechanism insights into Bi2O2CO3/G-C3N4 Z-scheme photocatalyst. *J. Phys. Chem. C* **123**, 4795–4804 (2019).
53. Kampouri, S. & Stylianou, K. C. Dual-Functional Photocatalysis for Simultaneous Hydrogen Production and Oxidation of Organic Substances. *ACS Catal.* **9**, 4247–4270 (2019).
54. Ahmad, H., Kamarudin, S. K., Minggu, L. J. & Kassim, M. Hydrogen from photocatalytic water splitting process: A review. *Renew. Sustain. Energy Rev.* **43**, 599–610 (2015).

Die approbierte gedruckte Originalversion dieser Dissertation ist an der TU Wien Bibliothek verfügbar.
The approved original version of this doctoral thesis is available in print at TU Wien Bibliothek.
TU Bibliothek Your knowledge hub WIEN

55. Nagao, T. *et al.* Nanofilm Allotrope and Phase Transformation of Ultrathin Bi Film on Si(111)-7x7. *Phys. Rev. Lett.* **93**, 105501 (2004).
56. Martínez-Periñán, E. *et al.* Antimonene: a novel 2D nanomaterial for supercapacitor applications. *Adv. Energy Mater.* **8**, 1702606 (2018).
57. Greaves, C. & Blower, S. Structural relationships between Bi2O2CO3 and β-Bi2O3. *Mater. Res. Bull.* **23**, 1001–1008 (1988).
58. Pitts, J., Thomas, T., Czanderna, A. & Passler, M. XPS and ISS of submonolayer coverage of Ag on SiO2. Appl. Surf. Sci. **26**, 107–120 (1986)
59. Huang, Y. *et al.* Visible light Bi2S3/Bi2O3/Bi2O2CO3 photocatalyst for effective degradation of organic pollutions. *Appl. Catal. B Environ.* **185**, 68–76 (2016).
60. Huang, Y. *et al.* Ultrathin Bismuth Nanosheets for Stable Na-Ion Batteries: Clarification of Structure and Phase Transition by in Situ Observation. *Nano Lett.* **19**, 1118–1123 (2019).
61. Cucka, P. & Barrett, C. S. The crystal structure of Bi and of solid solutions of Pb, Sn, Sb and Te in Bi. *Acta Crystallogr.* **15**, 865–872 (1962)
62. Gualtieri, A. F., Immovilli, S. & Prudenziati, M. Powder X-ray diffraction data for the new polymorphic compound ω-Bi2O3. *Powder Diffr.* **12**, 90–92 (1997).
63. Dreyer, J. A. H. *et al.* Decrease of the required dopant concentration for δ-Bi $_2$ O $_3$ crystal stabilization through thermal quenching during single-step flame spray pyrolysis. *CrystEngComm* **18**, 2046–2056 (2016).
64. Malmros, G. The crystal structure of a-Bi2O3. Acta Chem Scand **24**, e396 (1970).
65. Harwig, H. A. On the Structure of Bismuthsesquioxide: The α, β, γ, and δ-phase. Z. Für Anorg. Allg. Chem. **444**, 151–166 (1978).
66. Winchell, A. N. & Winchell, H. Optical Properties of Artificial Minerals. 410.
67. Blower, S. K. & Greaves, C. The structure of β-Bi2O3 from powder neutron diffraction data. *Acta Crystallogr. C* **44**, 587–589 (1988)
68. Radaev, S. F., Simonov, V. I. & Kargin, Y. F. Structural features of γ-phase Bi2O3 and its place in the sillenite family. *Acta Crystallogr. B* **48**, 604–609 (1992).
69. Sillén, L. G. X-Ray Studies on Bismuth Trioxide. (Almqvist & Wiksell, 1937).
70. Bohannan, E. W., Jaynes, C. C., Shumsky, M. G., Barton, J. K. & Switzer, J. A. Low-temperature electrodeposition of the high-temperature cubic polymorph of bismuth(III) oxide. Solid State Ion. **131**, 97–107 (2000).
71. Medernach, J. W. & Snyder, R. L. Powder Diffraction Patterns and Structures of the Bismuth Oxides. J. Am. Ceram. Soc. **61**, 494–497 (1978).
72. Cornei, N., Tancret, N., Abraham, F. & Mentré, O. New ε-Bi2O3 Metastable Polymorph. Inorg. Chem. **45**, 4886–4888 (2006).
73. Grice, J. D. A solution to the crystal structures of bismutite and beyerite. *Can. Mineral.* **40**, 693–698 (2002).
74. Moré, R. *et al.* Bi2O2CO3 growth at room temperature: in situ x-ray diffraction monitoring and thermal behavior. *ACS Omega* **2**, 8213–8221 (2017).
75. Ao, Y. *et al.* Graphene and TiO2 co-modified flower-like Bi2O2CO3: A novel multi-heterojunction photocatalyst with enhanced photocatalytic activity. *Appl. Surf. Sci.* **355**, 411–418 (2015).
76. Lin, K., Qian, J., ZhaO, Z., Wu, G. & Wu, H. Synthesis of a carbon-loaded Bi2O2CO3/TiO2 photocatalyst with improved photocatalytic degradation of methyl orange dye. *J. Nanosci. Nanotechnol.* **20**, 7653–7658 (2020).
77. Bogusz, K. *et al.* TiO 2/(BiO) 2 CO 3 nanocomposites for ultraviolet filtration with reduced photocatalytic activity. *J. Mater. Chem. C* **6**, 5639–5650 (2018).

Die approbierte gedruckte Originalversion dieser Dissertation ist an der TU Wien Bibliothek verfügbar.
The approved original version of this doctoral thesis is available in print at TU Wien Bibliothek.
TU Bibliothek Your knowledge hub WIEN

78. Haselmann, G. M. & Eder, D. Early-stage deactivation of platinum-loaded TiO2 using in situ photodeposition during photocatalytic hydrogen evolution. *ACS Catal.* **7**, 4668–4675 (2017).
79. Wang, J. *et al.* Ti-based MOFs: New insights on the impact of ligand composition and hole scavengers on stability, charge separation and photocatalytic hydrogen evolution. *Appl. Catal. B Environ.* **283**, 119626 (2021).
80. Schubert, J. S. *et al.* Immobilization of Co, Mn, Ni and Fe oxide co-catalysts on TiO 2 for photocatalytic water splitting reactions. *J. Mater. Chem. A* **7**, 18568–18579 (2019).
81. Ayala, P. *et al.* Isolation Strategy towards Earth-Abundant Single-Site Co-Catalysts for Photocatalytic Hydrogen Evolution Reaction. *Catalysts* **11**, 417 (2021).

Die approbierte gedruckte Originalversion dieser Dissertation ist an der TU Wien Bibliothek verfügbar.
The approved original version of this doctoral thesis is available in print at TU Wien Bibliothek.
TU Bibliothek Your knowledge hub WIEN

Outcome:

Paper III:

"Sonochemical synthesis of large two-dimensional $Bi_2O_2CO_3$ nanosheets for hydrogen evolution in photocatalytic water splitting"--submitted

Sonochemical Synthesis of Large Two-Dimensional $Bi_2O_2CO_3$ Nanosheets for Hydrogen Evolution in Photocatalytic Water Splitting†

Tushar Gupta,[a] Nicole Rosza,[a] Markus Sauer,[b] Alexander Goetz,[c] Maximilian Winzely,[d] Jakob Rath,[a] Shaghayegh Naghdi,[a] Dogukan H. Apaydin,[a] Alexey Cherevan,[a] Gernot Friedbacher,[d] Annette Foelske,[b] Sarah M. Skoff,[c] Bernhard C. Bayer,[*a] Dominik Eder[*a]

Die approbierte gedruckte Originalversion dieser Dissertation ist an der TU Wien Bibliothek verfügbar.
The approved original version of this doctoral thesis is available in print at TU Wien Bibliothek.
TU Bibliothek Your knowledge hub WIEN

Chapter 7

Epilogue

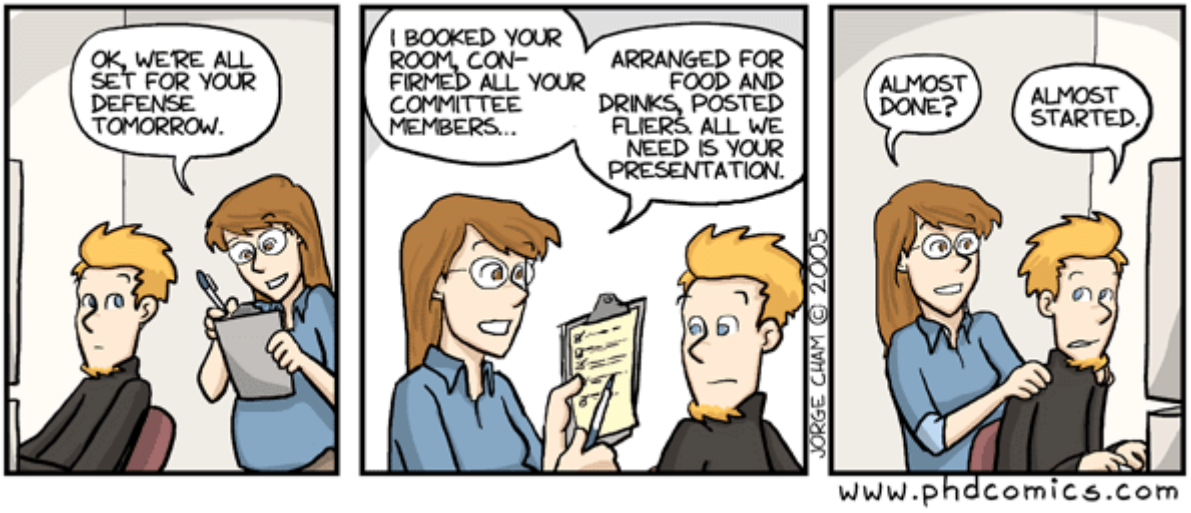

Die approbierte gedruckte Originalversion dieser Dissertation ist an der TU Wien Bibliothek verfügbar.
Die approbierte gedruckte Originalversion dieser Dissertation ist an der TU Wien Bibliothek verfügbar.
TU Bibliothek, WIEN Vorsprung durch Technik

Chapter Preview

Chapter 7 *provides a brief summary of the key research findings of this study. This study was based on exploring cost effective and intrinsically scalable routes of physical vapor deposition and liquid phase exfoliation for the synthesis of 2D pnictogens particularly antimonene and bismuthene and their graphene-based heterostructures. 2D pnictogens and their graphene-based heterostructures remain an attractive candidate for several energy and electronics related applications. The results presented in this thesis delineate the phase wealth and epitaxial relations readily existing in these heterostructures. Not only that but several other interesting properties like oxidation susceptibility, probing plasmonic associated electron beam dynamics have been explored in this work. Starting from the synthesis of these pnictogens, the study progressed towards their numerous intrinsic property characterization and finally demonstrated the application perspective of the synthesized pnictogens based compounds in the form of photocatalytic water splitting.*

A short summary of all the experimental chapters has been provided and wherever possible the characteristics of the fellow pnictogens in their varied response to the same stimuli have been juxtaposed to further highlight the multitude of different element specific properties of pnictogens (particularly antimonene and bismuthene).

*The figure caption for chapter 7 is again an illustration adopted from "**http://phdcomics.com**".*

Die approbierte gedruckte Originalversion dieser Dissertation ist an der TU Wien Bibliothek verfügbar.
The approved original version of this doctoral thesis is available in print at TU Wien Bibliothek.
TU Bibliothek Your knowledge hub WIEN

7. Epilogue

7.1 Conclusions

The rich allotropic wealth of two-dimensional (2D) pnictogens lately garnered a lot of attention, owing to the possibility of their structural modifications via adoption of different synthesis strategies coupled with the multitude of applications where the different allotropes/ structural modified versions of these 2D pnictogens can be best placed in. Equal interest in 2D antimony and bismuth arises from the prediction of layer dependent transition in their opto-electronic properties[1,2]. Along this direction, the work in this thesis has disentangled several factors crucial for the scalable synthesis of 2D pnictogens (antimonene (Sb) and bismuthene (Bi)) by unravelling the role of substrate temperature, nature of direct support underneath the 2D substrate upon employing a physical vapor deposition (PVD) route of thermal evaporation. Several interesting properties of the investigated 2D pnictogens including the effect of external stimuli have been probed via ex-situ (through ambient oxidation) as well as in-situ (e-beam induced crystallization and associated plasmonics) approaches.

Along with the 2D pnictogens, a facile synthesis protocol for obtaining phase-pure 2D $Bi_2O_2CO_3$ has also been presented in this thesis. A two-step facilitated process of liquid phase exfoliation (LPE) has been presented as an effective method for the synthesis of ultra-large and thin flakes/nanosheets of $Bi_2O_2CO_3$ solely based on the choice of solvent employed as a medium in the process of LPE (particularly sonication). Later, a photo-reactor system was developed by immobilizing the obtained exfoliated flakes/ nano-sheets of $Bi_2O_2CO_3$ on a photocatalyst material TiO_2 and the efficacy of the obtained $Bi_2O_2CO_3$ as an efficient UV-driving photocatalyst has been established. This adopted facile scheme of synthesis of catalytically active 2D pnictogen compounds thus offers promising approach in tackling two major challenges in the field of photocatalysis: (1) in terms of material's property (i.e. their suitability towards exhibiting catalytic properties) and (2) in terms of their scalable synthesis.

Die approbierte gedruckte Originalversion dieser Dissertation ist an der TU Wien Bibliothek verfügbar.
The approved original version of this doctoral thesis is available in print at TU Wien Bibliothek.
TU WIEN Bibliothek Your knowledge hub

Importantly, the dimensions of the 2D pnictogen based heterostructures explored in this thesis readily emulates and thereby critically enables study at atomic resolution by (S)TEM of the prior investigated antimony-carbon hybrids and bismuth-carbon hybrids which have already outlined their potential towards battery applications expanding the horizon of the 2D pnictogens and based compounds in a sustainable energy landscape.

The findings of this thesis subsequently establish a noteworthy impression of the 2D pnictogens, particularly antimonene and bismuthene (including their compounds) from the perspective of their atomic structures, fundamental properties and unmasking their promising potential to outlined applications. These aftermaths will certainly help instigate and understand phase and epitaxial relations in any 2D pnictogen based 2D heterostructures.

7.2 Sb Vs Bi on Graphene

An enriching outcome of this work was to observe and establish the different growth morphological characteristics of antimonene and bismuthene on graphene under the same adopted synthesis and processing conditions of PVD route. Figure 7.1 sums up several parameters on which the characteristics of grown antimonene and bismuthene on graphene of 10nm nominal thickness was evaluated. These parameters will now be captured:

1. Morphology:

Sb: Amorphous films were obtained at 10nm room temperature (RT) depositions which transformed to single crystalline 2D and 1D structures for depositions at higher temperatures (HT: 150 °C and 250 °C). Areal coverage by Sb deposits also reduced from RT to HT depositions.

Bi: Crystalline films were obtained at 10nm RT depositions which showed a drastic transition to amorphous spherical nanoparticles for depositions at HT. Bi deposits also exhibited lower areal coverage at HT depositions than at RT.

Die approbierte gedruckte Originalversion dieser Dissertation ist an der TU Wien Bibliothek verfügbar.
The approved original version of this doctoral thesis is available in print at TU Wien Bibliothek.

2. Phase:

Sb: Sb was found to exist in two different phases in its crystalline 2D and 1D structures at 10nm HT depositions. while 2D Sb was best phase matched to β-Sb(001), two equi-probable matches were found for indexing 1D Sb, namely: β-Sb[2-21] and also cubic-Sb(001).

Bi: Bi exhibited two different phases in its 10nm crystalline films at RT. First was the β-Bi(001) natural rhombohedral phase, second was the β-Bi[2-21] phase. The nearing crystallization amorphous regions also exhibited β-Bi[2-21]-like phase.

3. Oxidation susceptibility:

Sb: Antimonene showed presence of superficial surface oxide in its crystalline 2D and 1D structures after a period of 8 months.

Bi: No such discrete signs of any type of oxidation were found for Bismuthene.

4. Epitaxy: β-(001) and β-[2-21] phases exhibited two different epitaxial relation per phase in the case of bismuthene on graphene where as for the case of antimonene only one preferred epitaxial relation per phase was found.

Sb: Both crystalline 2D and 1D structures of Sb showed visible signs of rotational van-der-Waals epitaxial relationship with graphene underneath. Following relationships were established for the two phases:

- β-Sb(001)||graphene(001) / β-Sb[110]||graphene [120]
- cubic-Sb(001)||graphene (001) / cubic-Sb[110]||graphene[120]
- β-Sb[2-21]⊥graphene(001) / β-Sb[1-1-1]||graphene[120]

Bi: The two phases of the Bi observed in RT depositions as well as upon crystallization of amorphous nanoparticles under electron beam also exhibited the following rotational van-der-Waals epitaxial relationship with respect to graphene underneath:

- β-Bi(001)||graphene(001) / β-Bi[110]||graphene[120]
- β-Bi(001)||graphene(001) / β-Bi[110] ∠30° graphene[120]
- β-Bi[2-21]⊥graphene(001) / β-Bi[-201]||graphene[120]

Die approbierte gedruckte Originalversion dieser Dissertation ist an der TU Wien Bibliothek verfügbar.
The approved original version of this doctoral thesis is available in print at TU Wien Bibliothek.
TU Bibliothek WIEN Your knowledge hub

- β-Bi[2-21]⊥graphene(001) / β-Bi[-201] ∠30° graphene[120]

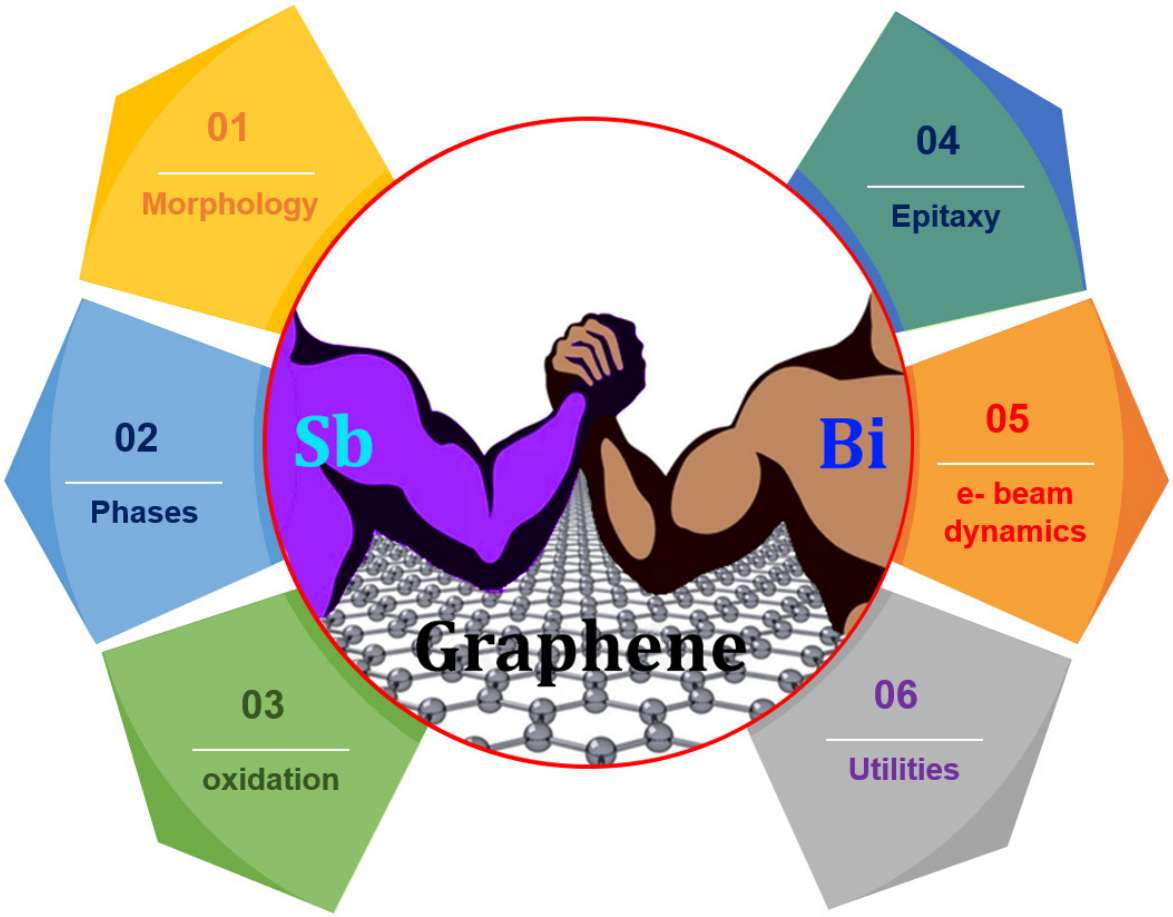

Figure 7.1: Parameter space explored for the growth of antimonene and bismuthene via PVD on graphene in this study. **clip art adapted from www.slidemodel.com and www.wdrfree.com

5. <u>e- beam Dynamics</u>:

Sb: No visible signs of any structural/ atomic dynamics were observed for Sb deposits as they were found to be stable under the e-beam.

Bi: HT Bi deposits in the form of amorphous nanoparticles showed electron beam induced crystallization and also showed associated surface plasmon shift.

6. <u>Applications</u>:

Die approbierte gedruckte Originalversion dieser Dissertation ist an der TU Wien Bibliothek verfügbar.
The approved original version of this doctoral thesis is available in print at TU Wien Bibliothek.
TU Bibliothek Your knowledge hub WIEN

Sb: Sb-Carbon hybrids have been studied as promising next generation electrode materials for batteries[3,4] and for electronic applications towards better contact resistances[5–7] by prior works.

Bi: Bi-Carbon hybrids have also been studied as potential electrode materials for electrochemical applications[8,9] and also for electronic applications by mitigating contact resistances[10] by earlier works.

7.3 Key findings

Chapter 4,5,6 constitute the key findings of the work carried out and presented in this thesis. Figure 7.2 explains the various outcomes of this thesis in a nutshell. On that note, following are the brief recaps of the main constituent chapters of this thesis:

- ***Chapter 4*** explored the model system 1: antimonene-graphene heterostructures. The studies highlighted the role of high substrate temperature in governing the growth of single crystalline 2D pnictogens on graphene. These 2D pnictogens were identified as natural rhombohedral phase of antimony in β-Sb(001) texture. Along with these 2D structures, co-existing were the 1D structures of antimonene, where exclusively in this study two equi-probable assignment of the 1D phase were suggested: first was β-Sb[2-21] texture and the second was seldom reported meta stable high pressure cubic-Sb(001) texture. In the next phase, via the epitaxial relationships, the preferential orientation of the 2D and 1D structures of Sb on graphene was established followed by outlining the presence of superficial surface oxidation in 8 months aged samples. Particularly, the armchair direction of graphene was found to promote the growth of 1D Sb along it. Towards the end, the studies highlighted the pivotal role of graphene in driving the epitaxial growth of Sb on it as non-faceted Sb depositions were obtained on annealed Copper tapes.

- ***Chapter 5*** explored the model system 2: bismuthene-graphene heterostructures. The studies here also highlighted the role of substrate temperature in governing

Die approbierte gedruckte Originalversion dieser Dissertation ist an der TU Wien Bibliothek verfügbar.
The approved original version of this doctoral thesis is available in print at TU Wien Bibliothek.
TU Bibliothek Your knowledge hub WIEN

the morphology of the Bi deposits on graphene. HT depositions were found to be detrimental to realize crystalline Bi structures but lead to amorphous Bi instead.

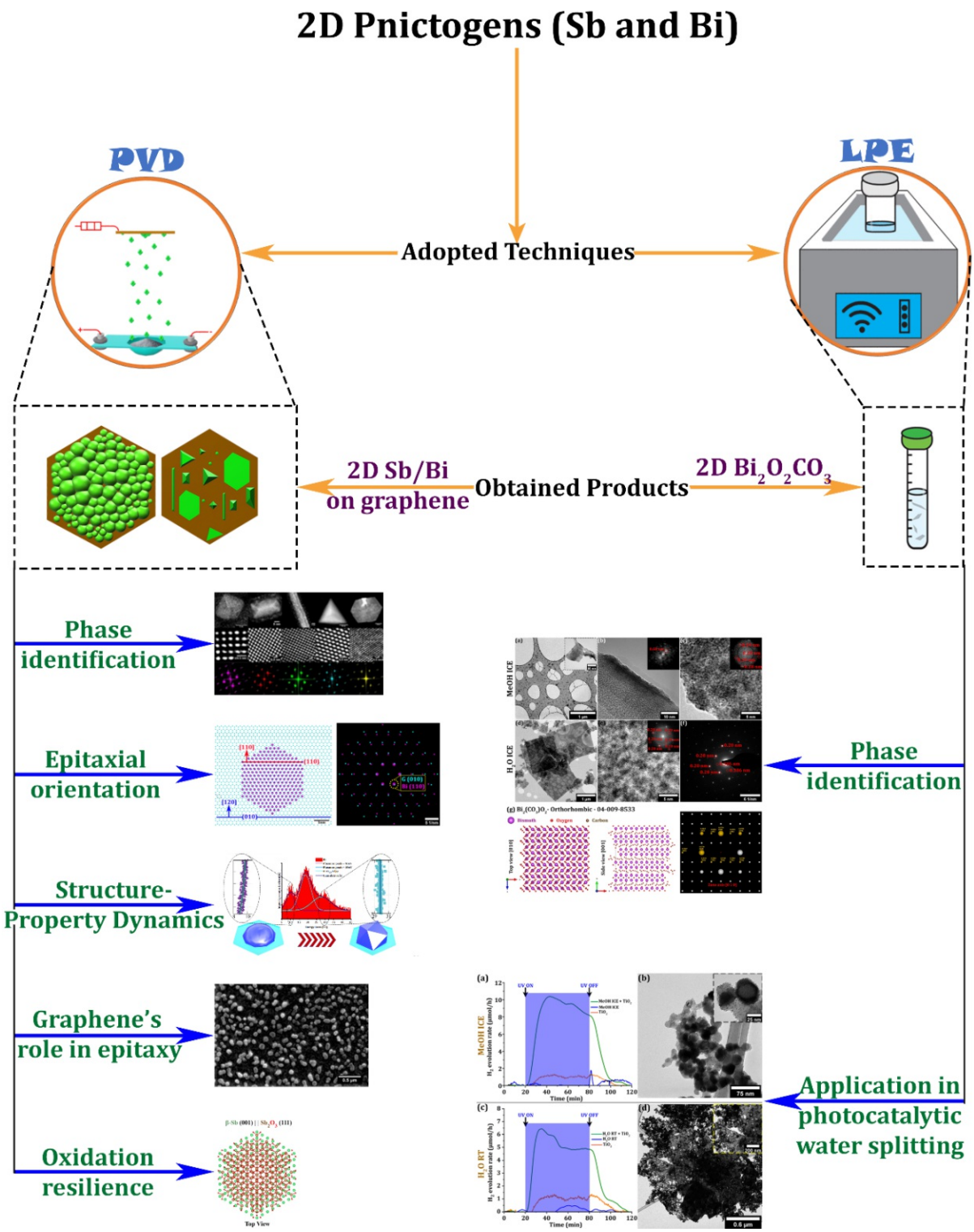

Figure 7.2: Schematic representation of the key findings of this work.

Die approbierte gedruckte Originalversion dieser Dissertation ist an der TU Wien Bibliothek verfügbar.
The approved original version of this doctoral thesis is available in print at TU Wien Bibliothek.
TU Bibliothek Your knowledge hub WIEN

The RT deposits in the form of films were crystalline and consisted of two different phases which were best matched to β-Bi(001) and β-Bi[2-21] respectively, with β-Bi being the natural rhombohedral phase of Bi. Both these phases were found to exist in two preferred orientations with respect to graphene as established by epitaxial relations outlined in Section 7.2. The HT deposits had spherical nanoparticle like morphology with amorphous nature. These nanoparticles underwent complete crystallization upon extended electron beam exposure. The studies alongside this structural change also probe the associated plasmon dynamics that help establish a sort of structure-property correlation.

- ***Chapter 6*** explored the second adopted route of liquid phase exfoliation to obtain low-dimensional pnictogens. The studies highlight the role of solvent in governing the morphology of the exfoliated produce. Five commonly used lab solvents namely: H_2O, Iso-propanol (IPA), methanol (MeOH), ethanol (EtOH) and IPA: H_2O (4:1) were utilized to exfoliate Bi which under the adopted processing conditions (particularly long sonication time of 15 h) yielded a ternary compound of Bi called as Bismutite or Bismuth-oxy-carbonate with chemical formula $Bi_2O_2CO_3$. The work stresses on the role of dissolved atmospheric O_2 and CO_2 to be responsible for this phase change. The adopted protocol resulted in the synthesis of laterally large sheets 2D $Bi_2O_2CO_3$ with average lateral size of 3 μm using H_2O as solvent. While exfoliation in MeOH resulted in the synthesis of small flakes of 2D $Bi_2O_2CO_3$. The studies towards the end exhibited the potential of these exfoliated 2D $Bi_2O_2CO_3$ as catalyst components by hybridizing them with archetypical photocatalyst TiO_2 and testing the hybrid for hydrogen evolution via photocatalytic water splitting. The hybrid exhibited better performance than the individual components respectively with comparable activity to other non-noble non-noble co-catalysts such as $Ni(O_x)$ or $Cu(O_x)$.

Die approbierte gedruckte Originalversion dieser Dissertation ist an der TU Wien Bibliothek verfügbar.
The approved original version of this doctoral thesis is available in print at TU Wien Bibliothek.
TU WIEN Bibliothek Your knowledge hub

7.4 Outlook

Among all the 9 different theoretically projected structures of the pnictogens in 2D forms via prior studies[2,11], only 2 of them namely α- and β- have been scalably realized. However, a major question still remains whether these are actually the allotropes or just the surface modifications and that is why the term "allotropes/ structural modified versions" have been used in this section. As observed in our case presented here for the case of antimonene and bismuthene, where α-phase was found to be the natural rhombohedral β-phase but in [2-21] projection implying β[2-21] = α[001]. This anonymity in the precise phase assignments opens a plethora of uncertainties regarding the accurate indexing of the obtained structural polymorphs and thus readily concerns any potential scenario involving their phase-pure synthesis in a scalable fashion, especially for the case of non-thermodynamically preferred allotropic forms. A major highlight in this regard was the absence of low-indexed basal planes parallel to the substrate in the β[2-21] configuration as emphasized by studies here, further questioning the experimental realization of such polymorphs of 2D pnictogens.

The present state of the art in 2D pnictogens research often tends to assign the observed square-symmetry and the hexagonal-symmetry of Sb and Bi atoms to be arising from α- and β- phases respectively, which is also correct in its own right. However, as shown in studies here on antimonene/graphene heterostructures, where the close call between the alpha and the meta-stable cubic phase which might result from the induced surface stresses was outlined, summons a strong need to consider wider possibilities in terms of structural interpretations. Such strong close correlations are rather scarce in the available literature which restrict the possibility of further investigation to the safe assignments of the observed thermodynamically non-preferred structures. Apparently, the literature dating back to the late 90's has assigned the square-symmetry of Sb atoms in Sb nanostructures deposited on graphite to be high pressure cubic phase and not the α-phase. Since graphite is an AB stacking of graphene, investigating the effects of the layer stacking of graphite in directing the morphology, growth dynamics and atomic structure of the grown Sb/ Bi nanostructures, constitutes a theme for future investigations which was unfortunately beyond the scope of this thesis thereby helping establishing a

Die approbierte gedruckte Originalversion dieser Dissertation ist an der TU Wien Bibliothek verfügbar.
The approved original version of this doctoral thesis is available in print at TU Wien Bibliothek.
TU Bibliothek Your knowledge hub WIEN

wholesome picture in elucidating the role of substrate in governing the morphology and atomic structure modifications of the Sb/Bi nanostructures grown atop.

The growth parameter space for obtaining 2D pnictogens is wide however importantly as per the current state-of-the-art, exploited deposition/ growth technique, temperature and type of substrate employed for the deposition has found to play a crucial role in influencing the growth and behavior dynamics of the grown 2D pnictogens, with nature/ type of the substrate employed being the prominent factor.
Similarly results from the prior studies dealing with different vapor techniques to grow/ deposit antimony nanostructures on graphene/ graphite via PVD[12], CVD[13] and MBE[14] have reported different proportions of Sb nanostructures with cubic-symmetry and natural hexagonal symmetry. Understanding and outlining their growth mechanisms are paramount to establishing control over the phase-selective synthesis of 2D-pnictogens which would provide momentum in designing the novel pnictogens based 2D materials and 2D heterostructures towards advanced energy applications.

Analogous challenges exist in the field of 2D pnictogens based compounds whose vast allotropic diversity calls for the close control on the morphology and atomic structure in any potential synthesis scenario. Particularly, establishing them as a promising alternative to expensive noble metal-based catalyst components remains a challenge that merits attention.

The thesis aimed at providing wider insights into the rich allotropic wealth of 2D pnictogens and based heterostructures and also on 2D pnictogen-based compounds. The key foresights on the synthesis and application perspective of the 2D pnictogens and based heterostructures were also provided in this study via characterizing their diverse properties, all of which surely summon efforts on (1) probing a cost effective and more scalable route to phase-pure synthesis of the different 2D allotropes of pnictogens on graphene and (2) on further deep investigations on clear outlining of the properties of different allotropes to provide them a suitable application perspective → a feat that may inspire future works to follow to revolutionize the role of 2D pnictogens and their based heterostructures and also of 2D pnictogens-based compounds in the area of sustainable

Die approbierte gedruckte Originalversion dieser Dissertation ist an der TU Wien Bibliothek verfügbar.
The approved original version of this doctoral thesis is available in print at TU Wien Bibliothek.
TU WIEN Bibliothek Your knowledge hub

energy research and applications, given the multitude of exciting properties that these pnictogens in their low dimensional form possess.

7.5 References

1. Zhang, S., Yan, Z., Li, Y., Chen, Z. & Zeng, H. Atomically Thin Arsenene and Antimonene: Semimetal–Semiconductor and Indirect–Direct Band-Gap Transitions. *Angew. Chem. Int. Ed.* **54**, 3112–3115 (2015).
2. Wang, G., Pandey, R. & Karna, S. P. Atomically thin group-V elemental films: theoretical investigations of antimonene allotropes. *ACS Appl. Mater. Interfaces* **7**, 11490–11496 (2015).
3. Cui, C. *et al.* Antimony Nanorod Encapsulated in Cross-Linked Carbon for High-Performance Sodium Ion Battery Anodes. *Nano Lett.* **19**, 538–544 (2019).
4. Cheng, Y. *et al.* Nanostructured Carbon/Antimony Composites as Anode Materials for Lithium-Ion Batteries with Long Life. *Chem. – Asian J.* **11**, 2173–2180 (2016).
5. Chen, H.-A. *et al.* Single-Crystal Antimonene Films Prepared by Molecular Beam Epitaxy: Selective Growth and Contact Resistance Reduction of the 2D Material Heterostructure. *ACS Appl. Mater. Interfaces* **10**, 15058–15064 (2018).
6. Li, W., Wang, X. & Dai, X. Tunable Schottky contacts in the antimonene/graphene van der Waals heterostructures. *Solid State Commun.* **254**, 37–41 (2017).
7. Phuc, H. V. *et al.* Out-of-plane strain and electric field tunable electronic properties and Schottky contact of graphene/antimonene heterostructure. *Superlattices Microstruct.* **112**, 554–560 (2017).
8. Liu, S. *et al.* Bismuth nanosheets grown on carbon fiber cloth as advanced binder-free anode for sodium-ion batteries. *Electrochem. Commun.* **81**, 10–13 (2017).
9. Xiong, P. *et al.* Bismuth Nanoparticle@Carbon Composite Anodes for Ultralong Cycle Life and High-Rate Sodium-Ion Batteries. *Adv. Mater.* **31**, 1904771 (2019).
10. Guo, Y. *et al.* Monolayer Bismuthene-Metal Contacts: A Theoretical Study. *ACS Appl. Mater. Interfaces* **9**, 23128–23140 (2017).
11. Zhang, S. *et al.* Semiconducting Group 15 Monolayers: A Broad Range of Band Gaps and High Carrier Mobilities. *Angew. Chem. Int. Ed.* **55**, 1666–1669 (2016).
12. Yan, Z., Kushvaha, S. S., Xiao, W. & Wang, X.-S. Different-dimensional structures of antimony formed selectively on graphite. *Appl. Phys. A* **88**, 299–307 (2007).
13. Sun, X. *et al.* van der Waals Epitaxy of Antimony Islands, Sheets, and Thin Films on Single-Crystalline Graphene. *ACS Nano* (2018) doi:10.1021/acsnano.8b02374.
14. Fortin-Deschênes, M. *et al.* Dynamics of Antimonene–Graphene Van Der Waals Growth. *Adv. Mater.* **31**, 1900569 (2019).

Die approbierte gedruckte Originalversion dieser Dissertation ist an der TU Wien Bibliothek verfügbar.
The approved original version of this doctoral thesis is available in print at TU Wien Bibliothek.
TU Bibliothek Your knowledge hub WIEN

Curriculum Vitae: Tushar Gupta

CURRENT POSITION

06/2017-present

University Assistant (Pre doctoral)

Growth, Characterization and Application of 2D Pnictogens - Graphene Heterostructures

Supervisors: Prof. Dominik Eder & Dr. Bernhard C. Bayer

Institute of Material Chemistry, TU Wien, Austria

EDUCATION

2010-2015

Bachelor + Master of Nanotechnology (Dual Degree)

Amity Institute of Nanotechnology,

Amity University, Noida, India.

PREVIOUS SHORT TERM RESEARCH POSITIONS

01/2015 - 07/2015

Project Research Intern

2D materials and devices for advanced electronic applications

Primary Tasks: Mechanical exfoliation of 2D materials, Optical identification of the exfoliated 2D flakes and characterization of FETs based on exfoliated 2D materials

Organization: Indian Institute of Technology-Bombay, India

05/2014 - 07/2014

Summer Research Intern

Development of Fe-CNT Nanocomposites

Primary Tasks: Synthesis of composites via Ball milling, preparation of samples (cutting, grinding, polishing) and characterizing them via SEM, Vickers hardness, Raman, Carbon Analysis etc.

Die approbierte gedruckte Originalversion dieser Dissertation ist an der TU Wien Bibliothek verfügbar.
The approved original version of this doctoral thesis is available in print at TU Wien Bibliothek.
TU Bibliothek Your knowledge hub WIEN

Organization: ARCI-Hyderabad, India

05/2013 - 07/2013 & 05/2012 - 07/2012

Summer Intern

Synthesis, characterization and testing of the self-propagating nanoenergetic composite materials

Primary Tasks: Synthesis and characterization of nanoenergetic composite material for their ignition properties, pulse pressure etc.

Organization: Indian Institute of Technology-Kanpur, India

EXPERIENCE

Materials fabrication: chemical vapour deposition (CVD), physical vapour deposition (PVD) and mechanical exfoliation of 2D-based heterostructures

Materials characterisation incl. analysis: high-resolution transmission electron microscopy (TEM) and atomically resolved scanning transmission electronic microscopy (STEM), optical spectroscopy (Raman, UV-vis, photoluminescence), scanning electron microscopy (SEM), atomic force microscopy (AFM), Photo-catalysis (Hydrogen Evolution Reaction)

PUBLICATIONS

15. **T. Gupta**, et al. *Structural and plasmonic evolution in few layered mixed-dimensionality Bismuthene / Graphene heterostructures*, in preparation**[**]**

14. S. Naghdi, Md. Zendehbad, **T. Gupta,** M. Weil, A. Cherevan, P. R. A. A. Leiva, C. Stumpp, D. Eder: *Synthesis of Highly Water Stable Cu-based Metal-Organic Frameworks for Efficient Adsorption of Nitrate from Aqueous Solutions*, in preparation

Die approbierte gedruckte Originalversion dieser Dissertation ist an der TU Wien Bibliothek verfügbar.
The approved original version of this doctoral thesis is available in print at TU Wien Bibliothek.
TU Bibliothek Your knowledge hub WIEN

13. S. Naghdi, A. Cherevan, A. Giesriegl, R. G. Nicolas, J. Wang, S. Biswas, **T. Gupta**, B. C. Bayer, M. C. Toroker, G. Rupprechter, F. Kleitz, D. Eder: *Selective ligand removal to improve accessibility of active sites in hierarchical MOFs for heterogeneous photocatalysis*, submitted

12. R. Kaindl, **T. Gupta**, A. Blümel, S. Pei, P. Hou, J. Du, C. Liu, P. Patter, K. Popovic, D. Dergez, K. Elibol, J. Liu, D. Eder, D. Kieslinger, W. Ren, P. Hartmann, W. Waldhauser, B. C. Bayer: *Aerosol jet printing of graphene and carbon nanotube patterns on realistically rugged substrates*, submitted

11. **T. Gupta,** N. Rosza, M. Sauer, A. Goetz, M. Winzely, J. Rath, S. Naghdi, D. H. Apaydin G. Friedbacher, A. Foelske, S. M. Skoff, B. C. Bayer, D. Eder: *Sonochemical synthesis of large two-dimensional $Bi_2O_2CO_3$ nanosheets for hydrogen evolution in photocatalytic water splitting*, submitted (pre-print repository: https://arxiv.org/ftp/arxiv/papers/2105/2105.09885.pdf)**[**]**

10. A. Niggas, S. Creutzburg, J. Schwestka, B. Wöckinger, **T. Gupta**, P. Grande, D. Eder, J. Marques, B. C. Bayer, F. Aumayr, R. Bennett, R. Wilhelm: *Peeling graphite layer by layer reveals the charge exchange dynamics of ions inside a solid*, Commun Phys 4, 180 (2021); https://doi.org/10.1038/s42005-021-00686-1

09. **T. Gupta**, K. Elibol, S. Hummel, M. Stöger-Pollach, C. Mangler, G. Habler, J. C. Meyer, D. Eder, B. C. Bayer: *Resolving Few Layer Antimonene/Graphene Heterostructures*, npj 2D Mater Appl 5, 53 (2021); https://doi.org/10.1038/s41699-021-00230-3**[**]**

08. R. Kaindl, B. C. Bayer, **T. Gupta**, S. Pei, P. Hou, J. Du, C. Liu 3, W. Ren, A. Blümel, P. Patter, K. Popovic, D. Dergez, W. Waldhauser: *Aerosol Jet Printed Nanocarbons on*

Die approbierte gedruckte Originalversion dieser Dissertation ist an der TU Wien Bibliothek verfügbar.
The approved original version of this doctoral thesis is available in print at TU Wien Bibliothek.
TU Bibliothek Your knowledge hub WIEN

Heat Sink Materials, Proceedings, 56(1), 30 (2020); https://doi.org/10.3390/proceedings2020056030

07. J. Wang, A. S. Cherevan, C. Hannecart, S. Naghdi, S. P Nandan, **T. Gupta**, D. Eder: *Ti-based MOFs: new insights on the impact of ligand composition and hole scavengers on stability, charge separation and photocatalytic hydrogen evolution,* Applied Catalysis B: Environmental, 283, 119626 (2021) https://doi.org/10.1016/j.apcatb.2020.119626

06. A. Niggas, J. Schwestka, S. Creutzburg, **T. Gupta**, D. Eder, B. C. Bayer, F. Aumayr, R. A. Wilhelm: *The role of contaminations in ion beam experiments with freestanding 2D materials: a study on thermal treatment,* J. Chem. Phys., 153, 014702 (2020), https://doi.org/10.1063/5.0011255

05. D. Fuchs, B. C. Bayer, **T. Gupta**, D. Eder, J. C. Meyer, S. Steiner, B. Gollas: *The Electrochemical Behavior of Graphene in a Deep Eutectic Solvent*, ACS Appl. Mater. Interfaces, 12, 40937 (2020), https://doi.org/10.1021/acsami.0c11467

04. K. Elibol, C. Mangler, **T. Gupta**, G. Zagler, D. Eder, J. C. Meyer, J. Kotakoski, B. C. Bayer: *Process Pathway Controlled Evolution of Phase and Vander-Waals Epitaxy in In/In2O3 on Graphene Heterostructures*, Adv. Funct. Mater., 30, 2003300 (2020), https://doi.org/10.1002/adfm.202003300

03. G. M. Haselmann, B. Baumgartner, J. Wang, K. Wieland, **T. Gupta**, C. Herzig, A. Limbeck, B. Lendl, D. Eder: *In Situ Pt Photodeposition and Methanol Photooxidation on Pt/TiO2: Pt-Loading-Dependent Photocatalytic Reaction Pathways Studied by Liquid-Phase Infrared Spectroscopy,* ACS Catalysis, 10, 2964 (2020), https://doi.org/10.1021/acscatal.9b05588

Die approbierte gedruckte Originalversion dieser Dissertation ist an der TU Wien Bibliothek verfügbar.
The approved original version of this doctoral thesis is available in print at TU Wien Bibliothek.
TU WIEN Bibliothek Your knowledge hub

02. B. C. Bayer, R. Kaindl, M. R. A. Monazam, T. Susi, J. Kotakoski, **T. Gupta**, D. Eder, W. Waldhauser, J. C. Meyer: *Atomic-Scale in Situ Observations of Crystallization and Restructuring Processes in Two-Dimensional MoS_2 Films*, ACS Nano, 12, 8758 (2018), http://dx.doi.org/10.1021/acsnano.8b04945C

01. R. Castro-Amoedo, Z. Csendes, J. Brünig, M. Sauer, A. Foelske-Schmitz, N. Yigit, G. Rupprechter, **T. Gupta**, A. Margarida Martins, K. Bica, H. Hoffmann, K. Kirchner: *Carbon-based SILP catalysis for the selective hydrogenation of aldehydes using a well-defined Fe(II) PNP complex*, Catal. Sci. Technol., 8, 4812 (2018), https://doi.org/10.1039/C8CY00818

[*Article is based on work in this thesis*]**

CO-SUPERVISION OF GRADUATE STUDENTS

06/2020 - 07/2020	One Bachelor Thesis (Framing the work plan and supervising day-to-day activities)
03/2018	One short-term intern (Framing the work plan and supervising day-to-day activities)

TEACHING RESPONSIBILITIES

04/2021 - 05/2021	Laboratory coordinator for 1st year masters Ceramics and Electrochemistry lab course
07/2020	Laboratory coordinator for 1st year masters Ceramics and Electrochemistry lab course

Die approbierte gedruckte Originalversion dieser Dissertation ist an der TU Wien Bibliothek verfügbar.
The approved original version of this doctoral thesis is available in print at TU Wien Bibliothek.
TU Bibliothek Your knowledge hub WIEN

05/2019	Laboratory coordinator for 1st year masters Ceramics and Electrochemistry lab course
05/2018	Laboratory coordinator for 1st year masters Ceramics and Electrochemistry lab course

HONOURS

11/2015 **Gold Medal**

First Division with Distinction. First in Academic performance in graduation.

Amity Institute of Nanotechnology, Amity University, Noida, India.

08/2008 **Science Student Honour**

Scoring the highest [100%] marks in the subject of mathematics under the science honour year 2007-2008

Department of Science & Technology, Government of Uttar Pradesh, India.

07/2007 **Certificate of Merit**

Outstanding academic performance and for being among the top 0.1% of successful candidates of All India Secondary School Examination [AISSE]

2007 in mathematics.

Central Board of Secondary Education, Delhi, India.

AWARDS & SCHOLARSHIPS

04/2015 **Amity Merit Scholarship**

Consecutively third time in a row for exhibiting academic excellence in the academic session 2014-2015. Amity Institute of Nanotechnology, Amity University, Noida, India.

Die approbierte gedruckte Originalversion dieser Dissertation ist an der TU Wien Bibliothek verfügbar.
The approved original version of this doctoral thesis is available in print at TU Wien Bibliothek.
TU Bibliothek Your knowledge hub WIEN

10/2014 **IIT-B IRCC Research Internship Award**
Project Research Intern
Indian Institute of Technology-Bombay, India

06/2014 **ARCI Summer Research Fellowship**
ARCI-Hyderabad, India

04/2014 **Amity Merit Scholarship**
Outstanding Academic performance in the academic session 2013-2014. Amity Institute of Nanotechnology, Amity University, Noida, India.

04/2013 **Amity Merit Scholarship**
Outstanding Academic performance in the academic session 2012-2013. Amity Institute of Nanotechnology, Amity University, Noida, India.

MEMBERSHIPS

Student Member **Austrian Society for Electron Microscopy (ASEM)**

Student Member **European Microscopy Society (EMS)**

Student Member **Erwin Schrödinger Society for Nanosciences (ESG NANO)**

CONFERENCE PARTICIPATION

Oral Presentation: **1.** Title: Resolving Few Layer Antimonene/Graphene Heterostructures
Conference: Graphene 2020 International Online Conference (October 19-23, 2020)

Die approbierte gedruckte Originalversion dieser Dissertation ist an der TU Wien Bibliothek verfügbar.
The approved original version of this doctoral thesis is available in print at TU Wien Bibliothek.
TU Bibliothek Your knowledge hub WIEN

2. Title: Resolving Few Layer Antimonene/Graphene Heterostructures
   Conference: International Online Conference on Functional Nanomaterials (September 6, 2021)

3. Title: Resolving Few Layer Antimonene/Graphene Heterostructures
   Conference: EUROMAT-2021, European Congress and Exhibition on Advanced Materials and Processes (September 13-17, 2021)

Poster Presentation:

1. Title: Resolving Few Layer Antimonene/Graphene Heterostructures
   Conference: 34th International Winter on Electronic Properties of Novel Materials (March 7-14, 2020), Austria.

Volunteer:

1. Conference: 17th International Workshop on The Physics of Semiconductor Devices (December 10-13, 2013), India.

REVIEWERSHIP OF JOURNALS

- Referring for Molecules (MDPI)

Die approbierte gedruckte Originalversion dieser Dissertation ist an der TU Wien Bibliothek verfügbar.
The approved original version of this doctoral thesis is available in print at TU Wien Bibliothek.
TU Bibliothek Your knowledge hub WIEN